

JYU DISSERTATIONS 722

Arpan Dutta

Weak and Strong Coupling between Organic Molecules and Confined Light



UNIVERSITY OF JYVÄSKYLÄ
FACULTY OF MATHEMATICS
AND SCIENCE

JYU DISSERTATIONS 722

Arpan Dutta

Weak and Strong Coupling between Organic Molecules and Confined Light

Esitetään Jyväskylän yliopiston matemaattis-luonnontieteellisen tiedekunnan suostumuksella
julkisesti tarkastettavaksi Ylistönrinteen auditoriossa FYS1
joulukuun 1. päivänä 2023 kello 12.

Academic dissertation to be publicly discussed, by permission of
the Faculty of Mathematics and Science of the University of Jyväskylä,
in Ylistönrinne, auditorium FYS1, on December 1, 2023, at 12 o'clock.



JYVÄSKYLÄN YLIOPISTO
UNIVERSITY OF JYVÄSKYLÄ

JYVÄSKYLÄ 2023

Editors

Ilari Maasilta

Department of Physics, University of Jyväskylä

Päivi Vuorio

Open Science Centre, University of Jyväskylä

Copyright © 2023, by the author and University of Jyväskylä

ISBN 978-951-39-9835-6 (PDF)

URN:ISBN:978-951-39-9835-6

ISSN 2489-9003

Permanent link to this publication: <http://urn.fi/URN:ISBN:978-951-39-9835-6>

ABSTRACT

Dutta, Arpan

Weak and strong coupling between organic molecules and confined light

Interaction between organic molecules and confined light can influence the molecular responses in the weak coupling regime and can even alter the molecular properties when the coupling is strong. The latter is crucial to achieve a leap in organic photovoltaics, material science, and modern organic nanophotonics to name a few. Optical nanostructures are usually employed to obtain the confined light and this dissertation focuses on optimization of such nanostructures in order to attain effective light-matter coupling resulting in a modification of the photochemical properties of the coupled molecules. Three kinds of optical nanostructures, namely plasmonic, photonic, and excitonic nanostructures have been studied. Computational and experimental studies reveal that in the weak coupling regime, subradiant plasmonic modes supported by metallic Fano-resonant oligomers and gratings can optimally enhance the molecular Raman response, while planar metallic Fabry-Pérot cavities with a reflective geometry, i.e., a leaky top and a non-transparent bottom mirrors, can optimally enhance the molecular emission. In the strong coupling regime, similar cavities sustaining hybrid light-matter states, cavity polaritons, can modify the emission yield of an ultra-fast photochemical reaction. The dissertation also studies fully organic nanostructures made of polymer doped with excitonic molecules. The findings show that optical properties of such excitonic nanostructures can be tuned via molecular concentration of the dopants and in the weak coupling regime, they can provide equivalent or even better confinement of light compared to the plasmonic systems. However, in the strong coupling regime, in most of the cases, excitonic nanostructures can only support the strong coupling induced transparency and cannot sustain the hybrid polaritonic states due to spectrally limited operation range. The findings reported in this dissertation are important for development of novel nanodevices and for facilitation of engineered light-matter coupling in order to manipulate material properties. This dissertation contains six chapters, six published articles, and two preprints that are currently in the peer review phase.

Keywords: light-matter interaction, plasmonics, Raman spectroscopy, strong coupling, polaritons, surface excitons

TIIVISTELMÄ (ABSTRACT IN FINNISH)

Dutta, Arpan

Vangitun valon vahva ja heikko kytkeytyminen orgaanisiin molekyyliin

Heikkokin vuorovaikutus orgaanisten molekyylien ja vangitun (confined) valon välillä voi vaikuttaa molekyylien kemialliseen vasteeseen, mutta se voi myös jopa muuntaa molekyylin kemiallisia ominaisuuksia, kun vuorovaikutusta kasvataan vahvan kytkennän alueelle. Näistä erityisesti jälkimmäinen, eli kemiallisten ominaisuuksien muokkaus on tärkeä ominaisuus, koska se voi mahdollistaa merkittävän kehitysloikan muun muassa orgaanisissa aurinkokennoissa, materiaalitieteissä sekä orgaanisen nanofotoniikan sovellutuksissa. Tiedeyhteisö käyttää optisia nanorakenteita vangitsemaan valoa. Tämä tutkielma keskittyy tällaisten rakenteiden optimointiin kyllin tehokkaan kytkennän aikaansaamiseksi, jotta kytkettyjen molekyylinen kemiallisiin ominaisuuksiin kyettäisiin vaikuttamaan. Tutkielma keskittyy kolmen tyyppisiin optisiin nanorakenteisiin: plasmonisiin-, fotonisiin- ja eksitonisiin. Työssä käytetyt laskennalliset ja kokeelliset menetelmät paljastavat, että heikon kytkennän rajalla pimeät (subradiant) plasmoniset värähtelymoodit metallisissa Fano-resonoivissa oligomeereissä sekä hiloissa voivat parantaa molekulaarista Raman vastetta, kun taas täysin heijastavalla pohjapeilillä varustetut metalliset Fabry-Pérot -tyyppiset kaviteetit kykenevät vahvistamaan molekyylien emissiota. Vahvan kytkennän rajalla vastaavanlaisia kaviteetteja voidaan käyttää luomaan hybridisoituneita valon ja materian superpositiotiloja polaritoneja, joilla voidaan muokata ultranopean fotokemiallisen reaktion kvantitisaantoa. Väitöskirjan tutkimus perehtyy myös täysin orgaanisiin nanorakenteisiin, jotka on valmistettu eksitonisilla molekyyliellä seostetusta polymeeriseoksesta. Löydökset osoittavat, että tällaisten rakenteiden optisia ominaisuuksia voidaan säätää seostuksessa käytettävän molekyylin konsentraatiolla ja, että heikon kytkennän alueella ne voivat tarjota yhtä hyvän tai jopa paremman keinon vangita valoa kuin vastaavat plasmoniset rakenteet. Useimmat tutkituista orgaanisista nanorakenteista eivät kuitenkaan pystyneet ylläpitämään vahvan kytkennän aikaansaamia polariton-tiloja, rajallisen spektraalisen toiminta-alueensa takia, mutta vahva kytkentä oli silti havaittavissa sen aiheuttaman läpinäkyvyyden kautta. Tutkielmassa esiin tulleet löydökset ovat merkittäviä uudenlaisten nanolaitteiden kehitystyössä ja edesauttavat ponnisteluuksia kohti materiaaliominaisuuksien muokkaamista vahvan kytkennän avulla. Tämä tutkielma sisältää kuusi lukua, kuusi julkaistua artikkelia sekä kaksi esivedosta (preprint), jotka ovat parhaillaan vertaisarvioitavana.

Avainsanat: valon ja aineen vuorovaikutus, plasmoniikka, Raman spektroskopia, vahva kytkentä, polaritoni, pintaeksitoni

Author Arpan Dutta
Department of Physics
Nanoscience Center
University of Jyväskylä
Finland

Supervisor Professor Jussi Toppari
Department of Physics
Nanoscience Center
University of Jyväskylä
Finland

Reviewers Professor Humeyra Caglayan
Faculty of Engineering and Natural Sciences
Tampere University
Finland

Professor Markku Vainio
Department of Chemistry
University of Helsinki
Finland

Opponent Professor Karl Börjesson
Department of Chemistry and Molecular Biology
University of Gothenburg
Sweden

PREFACE

The research included in this dissertation was performed at the University of Jyväskylä from August 2018 to August 2023 and funded by Academy of Finland (projects 289947, 323995). I consider myself highly privileged to have such financial support, which eases my journey as a researcher and aids my professional as well as personal growth.

I would like to express my deepest gratitude to my supervisor, Prof. Jussi Toppari, for letting me prosper in research, for guiding me through the uphill and downhill of doctoral studies, for creating countless unfading moments in my life, for engulfing me in positivity, and for being a lot more than just my supervisor. I am very grateful to my esteemed opponent, Prof. Karl Börjesson, and the pre-examiners, Prof. Humeyra Caglayan and Prof. Markku Vainio. The dissertation would not have been possible without their guidance and generous support.

During my doctoral studies in Jyväskylä, I immensely enjoyed the excellent courses offered by the university and the borderless atmosphere in Nanoscience Center without feeling any hierarchy. I am thankful to Prof. Gerrit Groenhof, Prof. Tero Heikkilä, Prof. Mika Pettersson, Dr. Eero Hulkko, Dr. Pasi Myllyperkiö, Dr. Heikki Häkkänen, Dr. Kimmo Kinnunen, and Dr. Andreas Johansson for their generous support. I really enjoyed the supportive, encouraging, and stimulating environment in Nanoscience Center, which helped me a lot to stay productive. I am lucky to be surrounded by so many great people, like Fabiola, Hanan, Marko, Johanna, Kamila, and Efstratios. I especially thank the current and former members of my group, Dr. Robrecht Vergauwe, Dr. Abhishek Pathak, Johannes Parikka, Ville Tiainen, Dr. Nemanja Markešević, and Dr. Luís Duarte, for their kind assistance and for all the fun moments. Specifically, I thank Ville Tiainen, for his friendship and for all our exciting conversations, which are, in my opinion, the best antidepressants in the world. I also thank Kristiina and Sonja (and the kids) for knitting many beautiful moments in my and my partner's lives.

I am especially thankful to my wife, Kausani, for her love and support during my scientific progress and for her irreplaceable presence in my life.

I came to Finland in 2016 for higher studies, and since then, my mom was waiting to see me as a doctorate. Unfortunately, I lost her in November 2021. I hope she will see me graduating from eternity. I dedicate this thesis to her.

Jyväskylä, December 2023

Arpan Dutta

LIST OF INCLUDED ARTICLES

- PI A. Dutta, K. Alam, T. Nuutinen, E. Hulkko, P. Karvinen, M. Kuittinen, J. J. Toppari, and E. M. Vartiainen, *Influence of Fano resonance on SERS enhancement in Fano-plasmonic oligomers*. *Optics Express*, **27** 30031 (2019).
- PII A. Dutta and E. M. Vartiainen, *Spatial localization of hotspots in Fano-resonant plasmonic oligomers for surface-enhanced coherent anti-Stokes Raman scattering*. *Journal of the European Optical Society-Rapid Publications*, **16** 8 (2020).
- PIII A. Dutta, T. Nuutinen, K. Alam, A. Matikainen, P. Li, E. Hulkko, J. J. Toppari, H. Lipsanen, and G. Kang, *Fabrication-friendly polarization-sensitive plasmonic grating for optimal surface-enhanced Raman spectroscopy*. *Journal of the European Optical Society-Rapid Publications*, **16** 022 (2020).
- PIV A. Dutta, V. Tiainen, and J. J. Toppari, *Optimizing geometry of low-Q all-metal Fabry-Pérot microcavity for fluorescence spectroscopy*. *IOPSciNotes*, **2** 015205 (2021).
- PV A. Dutta, V. Tiainen, H. A. Qureshi, L. Duarte, and J. J. Toppari, *Modeling optical constants from the absorption of organic thin films using a modified Lorentz oscillator model*. *Optical Materials Express*, **12** 2855 (2022).
- PVI A. Dutta, V. Tiainen, L. Duarte, N. Markešević, D. Morozov, H. A. Qureshi, G. Groenhof, and J. J. Toppari, *Ultra-fast photochemistry in the strong light-matter coupling regime*. *Research Square*, **Preprint** 10.21203/rs.3.rs-3237899/v1 (2023).
- PVII A. Dutta and J. J. Toppari, *Effect of molecular concentration on excitonic nanostructure based refractive-index sensing and near-field enhanced spectroscopy*. *Optical Materials Express*, **13** 2426 (2023).
- PVIII A. Dutta and J. J. Toppari, *Weak and strong coupling properties of surface excitons*. *ChemRxiv*, **Preprint** 10.26434/chemrxiv-2023-ldwcs (2023).

Author's contribution

In all publications, the author performed the electromagnetic simulations and related data analysis. In all publications, the author wrote the first version of the manuscript and prepared the figures except in [PVI] where the author wrote only the experimental parts and prepared the associated figures. Some of the cavities as well as thin film samples in [PV] and [PVI] are entirely fabricated by the author. The author carried out Raman and angle-resolved measurements in [PI], bright-field measurements in [PIII], the angle-resolved measurements of some of the samples in [PV, PVI], and participated in the data analysis of all of them.

OTHER PUBLICATIONS TO WHICH THE AUTHOR HAS CONTRIBUTED

- API A. Dutta, V. Tiainen, and J. J. Toppari, *Numerical study on the limit of quasi-static approximation for plasmonic nanosphere*. AIP Conference Proceedings, **2220** 050012 (2020).
- APII A. Dutta, A. Matikainen, S. Andoh, and T. Nuutinen, *SERS activity of photo-reduced silver chloride crystals*. AIP Conference Proceedings, **2220** 050004 (2020).
- APIII A. Dutta, *Ytterbium-doped fibers for high-power fiber lasers*. AIP Conference Proceedings, **2352** 020071 (2021).

CONTENTS

ABSTRACT

TIIVISTELMÄ (ABSTRACT IN FINNISH)

PREFACE

LIST OF INCLUDED ARTICLES

OTHER PUBLICATIONS TO WHICH THE AUTHOR HAS CONTRIBUTED

CONTENTS

| | | |
|-----|--|----|
| 1 | INTRODUCTION | 11 |
| 1.1 | Confined light using photonic nanostructures | 12 |
| 1.2 | Confined light using plasmonic nanostructures | 14 |
| 1.3 | Confined light using excitonic nanostructures | 17 |
| 2 | DESIGN, FABRICATION, AND CHARACTERIZATION OF OPTICAL NANOSTRUCTURES | 19 |
| 2.1 | Design of nanostructures | 19 |
| 2.2 | Fabrication of nanostructures | 27 |
| 2.3 | Characterization of nanostructures | 35 |
| 3 | WEAK COUPLING BETWEEN ORGANIC MOLECULES AND PLAS- MONIC NANOSTRUCTURES | 41 |
| 3.1 | Raman scattering | 41 |
| 3.2 | Weak coupling: surface enhancement | 43 |
| 3.3 | Plasmonic nanostructures for SERS | 44 |
| 3.4 | Plasmonic nanostructures for SECARS | 49 |
| 4 | WEAK AND STRONG COUPLING BETWEEN ORGANIC MOLECULES AND PHOTONIC NANOSTRUCTURES | 54 |
| 4.1 | Criteria for weak and strong light-matter coupling | 54 |
| 4.2 | Role of optical cavity | 59 |
| 4.3 | Polariton chemistry | 61 |
| 4.4 | Photochemistry in strong coupling regime | 62 |
| 5 | WEAK AND STRONG COUPLING BETWEEN ORGANIC MOLECULES AND EXCITONIC NANOSTRUCTURES | 70 |
| 5.1 | Modeling of excitonic materials | 70 |
| 5.2 | Origin of surface excitons | 73 |
| 5.3 | Weak coupling properties of surface excitons | 74 |
| 5.4 | Strong coupling properties of surface excitons | 78 |
| 6 | CONCLUSION | 84 |
| | REFERENCES | 87 |

INCLUDED ARTICLES

1 INTRODUCTION

Light-matter coupling is a thriving topic in science, especially in physics and chemistry, since fifth century BC. The term *light-matter coupling* is usually used to imply any interaction between light and matter considering them as two distinct entities. Studies on light-matter coupling evolved through time and gave birth of seminal theories in physics such as ancient corpuscular theory, wave theory, theory of relativity, and quantum theory to name a few. It also shaped our understanding on a broad arena of physical phenomena happening in nature and in the universe ranging from astrophysical occurrences to subatomic processes. Scientific research on light-matter coupling results in technological advancements such as invention of lasers, telescopes, and consumer optical products which are industrialized and utilized in daily life. Eventually, exploring the rich physics behind light-matter coupling to reveal the mysteries of the universe and to engineer such coupling for practical applications becomes pivotal in modern science and technology [1].

Light-matter coupling can be *weak* or *strong* depending on the physical conditions. In *weak* light-matter coupling, the light and matter can be considered as two different entities where the matter (e.g., a molecule) experiences the light, i.e., an electromagnetic field, as a perturbation. In weak coupling regime, the exchange of energy between the molecule and the electromagnetic field is slower than their individual decays. Examples of such phenomena are absorption and spontaneous emission of a molecule influenced (enhanced or suppressed) by the presence of an electromagnetic field. In *strong* light-matter coupling, the light and matter cannot be considered as two different entities anymore and the energy exchange between them is faster than their individual decays. In strong coupling regime, the excitation energy is virtually transferred from the molecule to the electromagnetic field and reabsorbed by the molecule again. Thus, the system consisting of the molecule and the electromagnetic field shows an oscillatory behaviour of the expectation value of the energy (Rabi oscillations), i.e., a cycle of the virtual energy transfer and reabsorption processes. Consequently, new energy states, polaritons, emerge which are hybrid light-matter states, i.e., superpositions of the eigenstates of the light and the matter. Such *half-light-half-matter*

hybrid states can absorb and emit light at different energies than the molecule and the coupled electromagnetic mode. This has led to a fully new field called *polariton chemistry* [2,3]. Therefore, electromagnetic environment, i.e., available light modes, can merely influence the interaction between light and matter (e.g., enhancing the emission rate of a molecule) when weakly coupled, and to modify the properties of light and matter, the coupling needs to be strong.

In light-matter coupling studies at nanoscale, organic molecules are a popular choice as *matter* [4–7]. Influencing or modifying physical and chemical properties of organic molecules through weak [4, 5] or strong [6–10] coupling has essential significance in organic photovoltaics [11–14] and organic optoelectronics [15–18]. Consequently, realization of novel optical nanodevices involving organic molecules is one of the thrust area in modern nanophotonics.

The quality of coupling between light and matter, i.e., how well they are coupled to each other, can be quantified by a parameter called coupling strength. The higher the coupling strength, the stronger the coupling, and it is inversely proportional to the physical volume of an optical mode, i.e., an electromagnetic resonance. In other words, the more confined the light, the higher the coupling strength. Optical nanostructures, i.e., structures with subwavelength dimensions, having engineered electromagnetic resonances or modes are frequently used to achieve such *confined light* [3]. Hence, it is vital to develop novel and customized optical nanostructures to optimize the confinement of light and thereby, the light-matter coupling.

Optical nanostructures can be photonic, plasmonic, or excitonic depending on the underlying mechanism of confining light. These different mechanisms are briefly discussed in the following subsections.

1.1 Confined light using photonic nanostructures

Light can be confined using photonic nanostructures and the simplest example of it is a planar Fabry-Pérot (FP) optical cavity having two mirrors facing each other at a suitable distance [19]. Figure 1(a) illustrates the schematic of such a cavity where M1 and M2 are the two parallelly aligned planar mirrors and the distance between them is the cavity length (L_c). A cavity can be considered as a nanostructure (nanocavity) for a subwavelength cavity length, i.e., when L_c is smaller or same length as the wavelength of the excitation light.

In a planar FP cavity, light enters through one of the mirrors (e.g., M1), and reflects back and forth between the mirrors resulting in a formation of standing waves inside the cavity. The cavity mode (or resonance) implies the scenario when the light is in-phase after one round trip and an enhanced transmission of light is obtained through M2. In the case of an ideal cavity with fully non-transparent mirrors, the spectral position of a cavity mode depends on the cavity

length L_c as

$$L_c = \frac{m\lambda}{2n_c}, \quad (1)$$

where λ and n_c are the wavelength of light and refractive index of the cavity medium, respectively, while m is an integer [19, 20]. Considering air ($n_c = 1$) as the cavity medium and both mirrors to be identical, for $m = 1$, we get the fundamental (first order) mode of the cavity having a single antinode inside the cavity region as shown by the blue curve in Figure 1(a). For $m = 2$ and 3, we get the second (green curve) and third (dark red curve) order cavity modes having two and three antinodes, respectively.

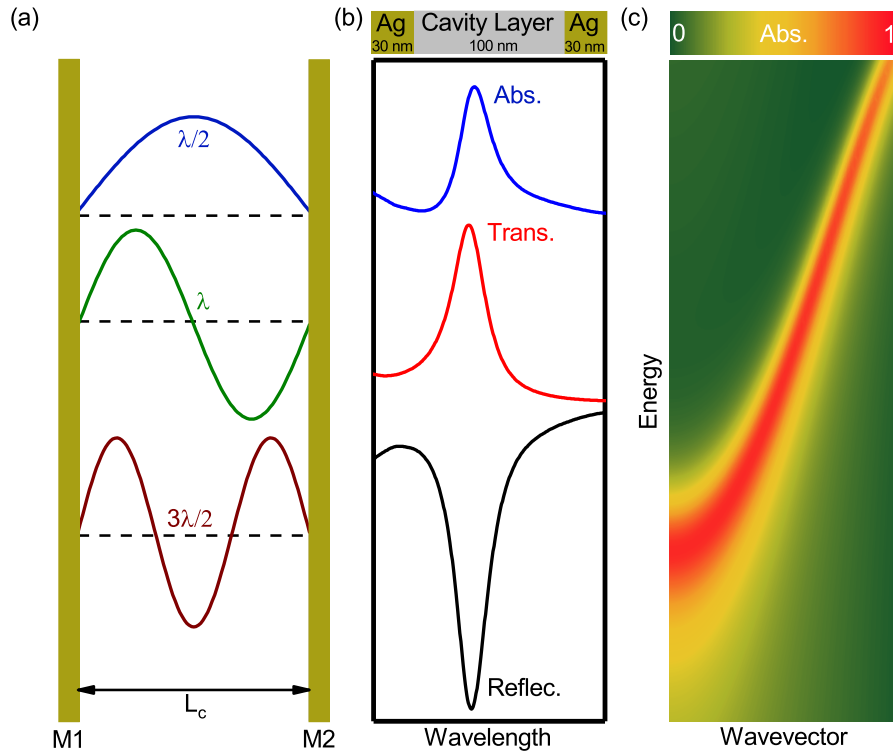


FIGURE 1 (a) Schematic of a planar Fabry-Pérot (FP) optical cavity having two parallelly aligned planar mirrors (M1 and M2) facing each other at a distance L_c (cavity length). The blue, green, and dark red curves represent the first, second, and third order cavity modes, respectively, according to Eq. (1). (b) Reflection (Reflec.), transmission (Trans.), and absorption (Abs.) spectra of the first order cavity mode of a planar FP cavity with its schematic on top. (c) Dispersion in the absorption of the same cavity plotted as a contour map.

A planar FP cavity can be implemented as a multilayer structure having two metallic thin films as mirrors and a polymer layer sandwiched between them as the cavity region [19, 20]. Figure 1(b) illustrates the schematic of such cavity having a 100 nm thick cavity layer ($L_c = 100$ nm) sandwiched between two identical 30 nm silver (Ag) mirrors. The first order cavity mode is profound in the reflection (Reflec.), transmission (Trans.), and absorption (Abs.) spectra of the cavity as shown in Figure 1(b). The spatial distribution of the electric field inside the

cavity layer at resonance (absorption peak) represents the confinement of light within the cavity and it follows the profile shown by the blue curve in Figure 1(a) for the first order mode.

Confinement of light inside a cavity can be quantified by the quality factor (Q) in temporal domain and by the mode volume (V_m) in spatial domain [21]. The quality factor (Q) of a cavity mode is defined as

$$Q = \frac{\lambda_c}{\Delta\lambda}, \quad (2)$$

where λ_c and $\Delta\lambda$ are the peak wavelength and the full width at half maximum (FWHM) of the cavity mode, respectively [22]. The mode volume can be calculated as

$$V_m = \frac{\int \epsilon \mathbf{E}^2 dV}{\max[\epsilon \mathbf{E}^2]}, \quad (3)$$

where ϵ is the dielectric constant and \mathbf{E} is the electric-field amplitude inside the interaction volume V [21]. Finally, the light confinement can be estimated by a field-confinement factor defined as Q/V_m [23].

The optical responses of a cavity strongly depend on the incident angle of the excitation light. The energy of a cavity mode E_c follows an in-plane dispersion expressed as

$$E_c(k_{\parallel}) = \frac{\hbar c}{n_c} \sqrt{\left(\frac{m\pi}{L_c}\right)^2 + (k_{\parallel})^2}, \quad (4)$$

with the in-plane wavevector k_{\parallel} defined as

$$k_{\parallel} = \left(\frac{2\pi}{\lambda}\right) \sin \theta. \quad (5)$$

Here, c is the velocity of light in vacuum, θ is the angle of incidence of the excitation light, and \hbar is the reduced Planck's constant. From Eqs. (4) and (5) we can see that the spectral position (E_c) of the cavity mode (absorption peak) can be tuned by changing the incident angle (θ) of the excitation light and thereby, the in-plane wavevector (k_{\parallel}) [19]. Such dispersion in the cavity absorption is plotted as a contour map in Figure 1(c) for the cavity shown in Figure 1(b).

In light-matter coupling studies, the organic molecules are doped in the polymer layer sandwiched between the cavity mirrors and the cavity mode is spectrally tuned with the molecular absorption or emission. The weak [PIV] and strong [PVI] coupling between organic molecules and optical cavities are covered in Chapter 4.

1.2 Confined light using plasmonic nanostructures

Light can also be confined using plasmonic nanostructures which are metallic systems with subwavelength dimensions. The collectively oscillating conduction electrons in metals, i.e., plasmons, can be excited by shining light on such

metallic nanostructures. The resulting plasmonic modes are visible in the optical spectra of the metallic system and usually manifest a strong enhancement of electromagnetic field in the vicinity of the structure [24]. In other words, the confinement of light (Q/V_m) in plasmonic nanostructures is often better compared to the planar FP cavities. The type of the excited plasmonic mode depends on the nanostructure geometry. For example, surface plasmon polariton (SPP) and localized surface plasmon (LSP) modes can be excited at a flat metal/dielectric interface and in a metal nanoparticle (NP), respectively, [24] while periodic structures such as metal NP arrays can sustain plasmonic surface lattice resonance (PSLR) mode [25].

In a metal-dielectric interface, if the dielectric has a positive and real permittivity while the metal has a complex dielectric function with a negative real part, the SPP modes can be excited using the transverse magnetic (TM or p) polarized excitation light coupled through a prism [24, 26] as depicted in Figure 2(a). The excited SPP modes are electromagnetic surface waves hybridized with the oscillating electrons in the metal, i.e., plasmons. They are propagating at the metal-dielectric interface with a decay in the transverse direction like an evanescent field [24] as shown by the near-field ($|\mathbf{E}|^2$) profile (dark red curve) in Figure 2(a) for gold (Au). Such modes can be excited and detected in angular scheme, i.e., using p -polarized monochromatic light for excitation and recording the attenuated total reflection (ATR) over a broad range of incident angles higher than the critical angle of total internal reflection [26]. The blue curve in Figure 2(b) depicts such angle-dependent reflectivity where the SPP mode is profound as a dip. The SPP modes can also be excited and recorded in spectral scheme, i.e., using a broadband white light source (p -polarized) for excitation at a fixed incident angle while the reflectivity is measured over a wide spectral range [26]. The dark red curve in Figure 2(b) represents such wavelength-dependent reflectivity (spectral reflectance) where the dip in the curve is the signature of the SPP mode. Like the FP cavity mode, the SPP mode (reflectance dip) shows in-plane dispersion [24] as shown in Figure 2(c) and its spectral position can be tuned by changing the excitation angle [26].

Interaction of light with a metal nanoparticle (NP) having a subwavelength size can excite the LSP mode without any phase-matching condition (e.g., prism coupling) and hence, via direct illumination [24]. For a Au NP (radius r), signature of such LSP mode is profound as a peak in the extinction spectrum as shown in Figure 2(d) and the near-field ($|\mathbf{E}|^2$) around the NP enhances at the LSP peak due to the *localized* nature of such mode [24].

The optical response of a NP array drastically differs from the response of the individual NPs present in that array. Figure 2(e) schematically illustrates a square array of Au NPs (radius r) having a period D in both x and y directions. The choice of lattice period D is important here since the PSLR mode can only be excited if $D > \lambda_{RA}$ where $\lambda_{RA} = n_s \lambda_{LSP}$ is the spectral position of the Rayleigh anomaly with n_s as the refractive index of the surrounding medium, and λ_{LSP} as the extinction peak (LSP mode) of the individual NPs [27]. Eventually, the PSLR mode is always found as a sharp peak in the extinction spectrum at a

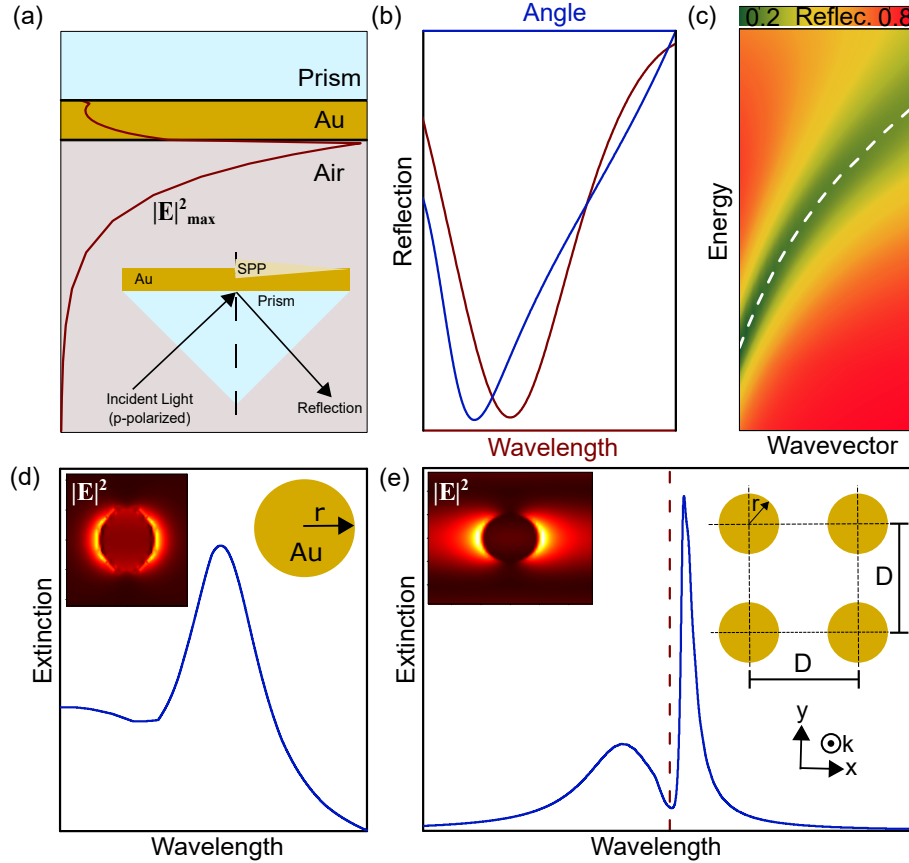


FIGURE 2 (a) Near-field ($|E|^2$) profile of the SPP mode with a schematic of the prism-coupled excitation. (b) Angular (blue) and spectral (dark red) reflectivity of the prism where the dip is due to the excitation of a SPP mode. (c) Dispersion in the attenuated total reflection (ATR) of the SPP mode plotted as a contour map. (d) Schematic of a metal NP (radius r) along with its extinction spectrum and the near-field ($|E|^2$) distribution around it at the extinction peak. (e) Schematic of a square array (period D) of metal NPs (radius r) along with the extinction spectrum of the array and the near-field ($|E|^2$) distribution around a NP in that array at the sharp PSLR peak. The vertical dashed line depicts the spectral position of the Rayleigh anomaly.

higher wavelength than the LSP mode of the individual NPs (broad peak) and the Rayleigh anomaly (vertical dashed line) [25,27] as shown in Figure 2(e). Like the LSP mode, the PSLR mode can be excited by direct illumination and the near-field ($|E|^2$) around the NPs present in the array enhances at the PSLR peak [25] as depicted in Figure 2(e). In general, the near-field enhancement ($|E|^2$) due to the PSLR mode is stronger than that of the LSP mode [25].

In light-matter coupling applications, the organic molecules are deposited on the plasmonic nanostructures while the plasmonic modes are spectrally tuned with the molecular responses. The study on the *localized* [PI, PII] and *propagating* [PIII] plasmonic modes when weakly coupled to the organic molecules is summarised in Chapter 3.

1.3 Confined light using excitonic nanostructures

Even though plasmonic nanostructures outperform photonic nanostructures in confining and enhancing light, they exhibit absorption losses which limit their optical performance. In this regard, Frenkel exciton based organic thin films are a potential alternative. Such thin films are usually made of polymer doped with excitonic molecules and can possess *plasmon-like* modes in the visible wavelengths with low losses when the doping concentration is high enough [28, 29]. This type of organic excitonic materials can support surface exciton polariton (SEP, analogous to SPP), localized surface exciton (LSE, analogous to LSP), and excitonic surface lattice resonance (ESLR, analogous to PSLR) modes at the organic film/dielectric interfaces [28, 29], in the excitonic NPs [29], and in the excitonic NP arrays [30], respectively.

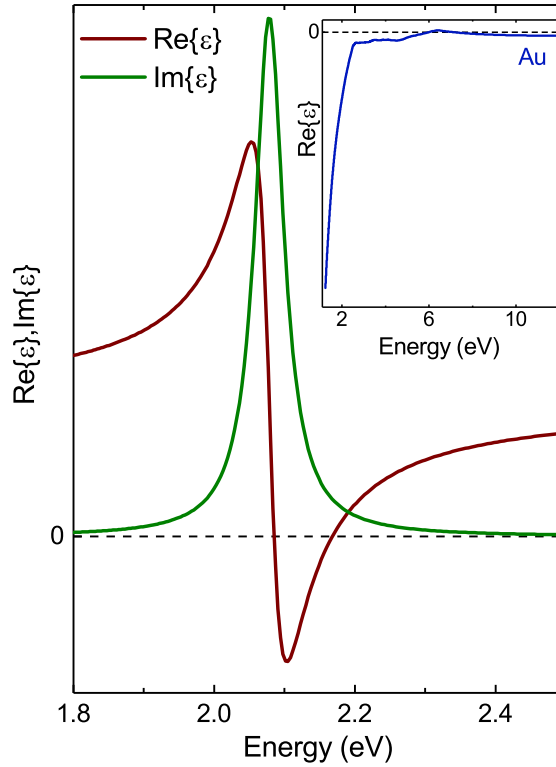


FIGURE 3 Real ($\text{Re}\{\epsilon\}$) and imaginary ($\text{Im}\{\epsilon\}$) parts of the dielectric function (ϵ) of TDBC J-aggregates with $\text{Re}\{\epsilon\}$ of Au in the inset.

To understand how surface excitonic modes originate in excitonic nanostructures, we should look into the complex-dispersive permittivity, $\epsilon(\omega)$, of the excitonic materials. The surface plasmon modes originate in metals when their permittivity has a negative real part, i.e., $\text{Re}\{\epsilon(\omega)\} < 0$. The criteria for the SPP and the LSP modes are $\text{Re}\{\epsilon(\omega)\} < -1$ and $\text{Re}\{\epsilon(\omega)\} < -2$, respectively [29]. For Au, spectral region where $\text{Re}\{\epsilon(\omega)\} < 0$ covers the entire visible spectrum [31] as shown in the inset of Figure 3. Therefore, to support any surface exciton mode, the excitonic materials should have at least $\text{Re}\{\epsilon(\omega)\} < 0$. Only

few organic molecules that have strong transition dipole moment along with narrow absorption linewidth can sustain such surface excitonic modes [28]. Their negative $\text{Re}\{\epsilon(\omega)\}$ regime is always spectrally located at energies just above their strong excitonic absorption band [28,29]. Figure 3 illustrates an example of such scenario for TDBC J-aggregates [29] where its $\text{Re}\{\epsilon(\omega)\}$ is negative only in a narrow spectral regime at energies higher than its material absorption.

Optical properties of the surface excitonic modes (SEP, LSE, and ESLR) are mostly similar to their plasmonic analogs (SPP, LSP, and PSLR). For example, if we replace the material of the nanostructures presented in Figure 2 from Au to TDBC J-aggregates, we will get almost similar results, however, with better confinement of light (Q/V_m) and less material losses [PVII]. Chapter 5 summarizes the findings on how the surface excitonic modes can be implemented [PV] in light-matter coupling applications [PVII], and how such modes behave in weak and strong coupling regimes [PVIII].

Chapter summary

To summarise, this thesis reports weak and strong coupling between organic molecules and *confined light* achieved through different optical nanostructures. Chapter 2 briefly explains the methods to design, fabricate, and characterize such nanostructures. Chapter 3, Chapter 4, and Chapter 5 summarize findings on the plasmonic, photonic, and excitonic nanostructures, respectively, when weakly and/or strongly coupled to the organic molecules. Chapter 6 concludes the thesis followed by a list of cited references and the appended publications included in this thesis.

2 DESIGN, FABRICATION, AND CHARACTERIZATION OF OPTICAL NANOSTRUCTURES

Optical nanostructures can be photonic, plasmonic, or excitonic depending on what type of electromagnetic or optical resonance they possess. Realization of such nanostructures in application-specific purposes requires optimal design or modelling, precise fabrication, and accurate characterization. In this chapter, methods and techniques relevant to design, fabrication, and characterization of nanostructures are briefly discussed.

2.1 Design of nanostructures

In this thesis, nanostructures are designed and optimized using transfer matrix method (TMM) [32–34], Mie theory [35–37], coupled dipole method [30], finite-difference time-domain (FDTD) method [38,39], and finite element method (FEM) [40,41]. The methods are briefly explained in the following subsections.

2.1.1 Transfer matrix method (TMM)

Nanofilms, i.e., thin films with sub-wavelength thicknesses, are an important class of nanostructures. In this thesis, nanofilms are used to develop optical coatings [PV], planar microcavities [PIV, PVI], and resonant substrates [PVII] while TMM [32–34] implemented in MATLAB [42] is used to model those nanofilm based systems and to optimize their optical responses (reflection, transmission, and absorption).

To understand the basic formalism of TMM [32], let's consider a simple model of a stratified medium, i.e., a multilayer stack consisting of two nanofilms on a substrate in air (Figure 4). The refractive index of the j -th layer is n_j while the four layers are substrate ($j = 1$), film-X ($j = 2$), film-Y ($j = 3$), and air ($j = 4$) from right to left in Figure 4. For simplicity, let's assume normal incidence of light

from air. To calculate the reflection/transmission coefficients, one has to consider the continuity of the electric field amplitudes and their derivatives at all interfaces [32]. From the continuity equations one can form transfer matrices for each interface to calculate the total reflection/transmission. For the interface z_3 (Air to film-Y), the transfer-matrix relation takes a form as

$$\mathbf{M}(n_4, z_3) \begin{bmatrix} 1 \\ r \end{bmatrix} = \mathbf{M}(n_3, z_3) \begin{bmatrix} C \\ D \end{bmatrix}, \quad (6)$$

where the transfer-matrix $\mathbf{M}(n_j, z_q)$ is

$$\mathbf{M}(n_j, z_q) = \begin{bmatrix} e^{-ik_0 n_j z_q} & e^{+ik_0 n_j z_q} \\ n_j e^{-ik_0 n_j z_q} & -n_j e^{+ik_0 n_j z_q} \end{bmatrix} \quad (7)$$

with k_0 as the wave vector in free space. For the interface z_2 (film-Y to film-X), the transfer-matrix relation becomes

$$\mathbf{M}(n_3, z_2) \begin{bmatrix} C \\ D \end{bmatrix} = \mathbf{M}(n_2, z_2) \begin{bmatrix} A \\ B \end{bmatrix}, \quad (8)$$

while for the last interface z_1 (film X to substrate), it is

$$\mathbf{M}(n_2, z_1) \begin{bmatrix} A \\ B \end{bmatrix} = \mathbf{M}(n_1, z_1) \begin{bmatrix} t \\ b \end{bmatrix}, \quad (9)$$

where r and t are the reflection and transmission coefficients, respectively [32]. The field amplitudes at different layers are A , B , C , D , and b as shown in Figure 4.

Considering the whole multilayer structure (four layers) as a cascaded system and using Eqs. (6) to (9), one can derive

$$\begin{bmatrix} 1 \\ r \end{bmatrix} = \mathbf{M} \begin{bmatrix} t \\ b \end{bmatrix}, \quad (10)$$

where \mathbf{M} represents the transfer matrix of the whole system described as

$$\mathbf{M} = [\mathbf{M}(n_4, z_3)]^{-1} \mathbf{M}(n_3, z_3) [\mathbf{M}(n_3, z_2)]^{-1} \mathbf{M}(n_2, z_2) [\mathbf{M}(n_2, z_1)]^{-1} \mathbf{M}(n_1, z_1). \quad (11)$$

Since the excitation is considered coming from air, the backside incidence coefficient (b) is zero. Hence, Eq. (10) becomes

$$\begin{bmatrix} 1 \\ r \end{bmatrix} = \mathbf{M} \begin{bmatrix} t \\ 0 \end{bmatrix} = \begin{bmatrix} M_{11} & M_{12} \\ M_{21} & M_{22} \end{bmatrix} \begin{bmatrix} t \\ 0 \end{bmatrix}. \quad (12)$$

Solving Eq. (12) for r and t yields

$$t = \frac{1}{M_{11}} \quad (13)$$

and

$$r = \frac{M_{21}}{M_{11}}. \quad (14)$$

The total reflection (R) and transmission (T) of the multilayer are then

$$R = |r|^2 \quad (15)$$

and

$$T = \frac{n_1}{n_4} |t|^2, \quad (16)$$

while the absorption (A) is calculated as $A = 1 - R - T$ [32].

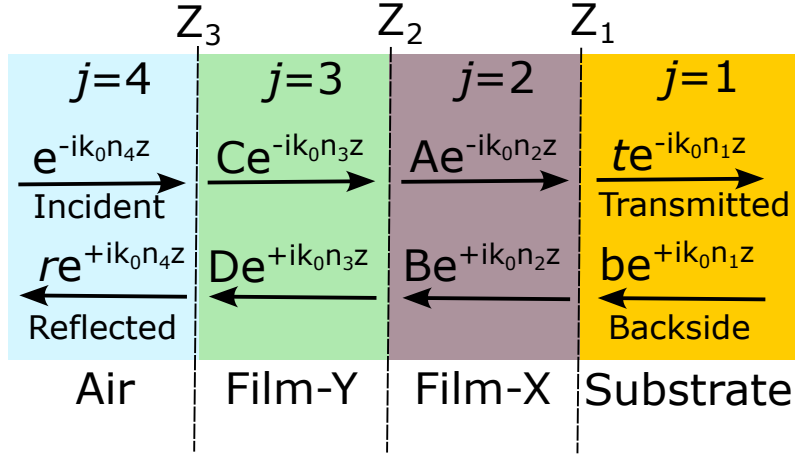


FIGURE 4 Transfer matrix method (TMM) for a stratified medium.

2.1.2 Mie theory

Nanoparticles are another important class of nanostructures. In this thesis, sensors and resonators are developed using nanoparticles with spherical shape, i.e., using homogeneous [PVII] and core-shell [PVIII] nanospheres. In both cases, Mie theory [35–37] implemented in MATLAB is used to model those nanospheres and to optimize their optical responses (scattering, extinction, and absorption).

To understand the basic formulation of Mie theory, let's consider a homogeneous nanosphere first. The radius of the nanosphere is r while its complex-dispersive refractive index is $n_m(\lambda)$. The nanosphere is surrounded by a dielectric medium of refractive index n_d (non-dispersive). For an excitation wavelength λ , the wave vector (k_d) is then $k_d = 2\pi n_d / \lambda$. The Mie parameters used in the following formulation are $m = n_m(\lambda) / n_d$, $v = k_d r$, and $w = mv$. The scattering (σ_{sca}), extinction (σ_{ext}), and absorption (σ_{abs}) cross-sections of the nanosphere can be derived as

$$\sigma_{sca} = \frac{2\pi}{k_d^2} \sum_{j=1}^{\infty} (2j+1) (|a_j|^2 + |b_j|^2), \quad (17)$$

$$\sigma_{ext} = \frac{2\pi}{k_d^2} \sum_{j=1}^{\infty} (2j+1) \text{Re}\{a_j + b_j\}, \quad (18)$$

and

$$\sigma_{abs} = \sigma_{ext} - \sigma_{sca}, \quad (19)$$

where a_j and b_j are the Mie coefficients. To attain numerical convergence, it is sufficient to consider the sum over j from $j = 1$ to $j = N$ where $N = v + 4v^{1/3} + 2$ [36,37]. The scattering (Q_{sca}), extinction (Q_{ext}), and absorption (Q_{abs}) efficiencies are then $Q_{sca} = \sigma_{sca}/c_{geo}$, $Q_{ext} = \sigma_{ext}/c_{geo}$, and $Q_{abs} = \sigma_{abs}/c_{geo}$, respectively, where c_{geo} is the geometrical cross-section of the nanosphere, i.e., $c_{geo} = \pi r^2$ for a spherical NP [36,37].

The Mie coefficients a_j and b_j in Eqs. (17) and (18) can be described as

$$a_j = \frac{m\psi_j(w)\psi'_j(v) - \psi_j(v)\psi'_j(w)}{m\psi_j(w)\xi'_j(v) - \xi_j(v)\psi'_j(w)} \quad (20)$$

and

$$b_j = \frac{\psi_j(w)\psi'_j(v) - m\psi_j(v)\psi'_j(w)}{\psi_j(w)\xi'_j(v) - m\xi_j(v)\psi'_j(w)}, \quad (21)$$

where

$$\psi_j(x) = \sqrt{\frac{\pi x}{2}} J_{j+1/2}(x), \quad (22)$$

$$\xi_j(x) = \sqrt{\frac{\pi x}{2}} [J_{j+1/2}(x) + iY_{j+1/2}(x)], \quad (23)$$

$$\psi'_j(x) = \psi_{j-1}(x) - \frac{j}{x}\psi_j(x), \quad (24)$$

and

$$\xi'_j(x) = \xi_{j-1}(x) - \frac{j}{x}\xi_j(x). \quad (25)$$

In Eqs. (22) and (23), J_j and Y_j are the Bessel functions of the first and second kind, respectively. In Eqs. (20) to (25), ψ_j and ξ_j are the Riccati-Bessel functions while ψ'_j and ξ'_j are their first order derivatives [36,37].

For a core-shell nanosphere, however, the Mie theory becomes a bit cumbersome. Lets consider a core-shell nanosphere having a core with radius r_1 and a shell (coating) with thickness t . The shell outer radius is then $r_2 = r_1 + t$. The complex-dispersive refractive indices for the core and shell are n_1 and n_2 , respectively. The coated nanosphere is surrounded by a dielectric medium of refractive index n_d (non-dispersive). For an excitation wavelength λ , the wave vector (k_d) is again $k_d = 2\pi n_d/\lambda$. The Mie parameters used in the formulation are $m_1 = n_1/n_d$, $m_2 = n_2/n_d$, $v_1 = k_d r_1$, $v_2 = k_d r_2$, $w_1 = m_1 v_1$, $w_2 = m_2 v_1$, and $w_3 = m_2 v_2$ [36].

The scattering (σ_{sca}), extinction (σ_{ext}), and absorption (σ_{abs}) cross-sections of the core-shell nanosphere can still be calculated from Eqs. (17) to (19) where only the Mie coefficients a_j and b_j are now changed. The sum over j is now restricted from $j = 1$ to $j = N$ where $N = v_2 + 4v_2^{1/3} + 2$. The scattering (Q_{sca}), extinction (Q_{ext}), and absorption (Q_{abs}) efficiencies can also be calculated similarly like the case for homogeneous nanosphere except the fact that c_{geo} is now πr_2^2 [36].

The Mie coefficients a_j and b_j for core-shell nanosphere are now

$$a_j = \frac{\psi_j(v_2)[\psi'_j(w_3) - A_j\chi'_j(w_3)] - m_2\psi'_j(v_2)[\psi_j(w_3) - A_j\chi_j(w_3)]}{\xi_j(v_2)[\psi'_j(w_3) - A_j\chi'_j(w_3)] - m_2\xi'_j(v_2)[\psi_j(w_3) - A_j\chi_j(w_3)]} \quad (26)$$

and

$$b_j = \frac{m_2 \psi_j(v_2) [\psi_j'(w_3) - B_j \chi_j'(w_3)] - \psi_j'(v_2) [\psi_j(w_3) - B_j \chi_j(w_3)]}{m_2 \xi_j(v_2) [\psi_j'(w_3) - B_j \chi_j'(w_3)] - \xi_j'(v_2) [\psi_j(w_3) - B_j \chi_j(w_3)]}, \quad (27)$$

where

$$A_j = \frac{m_2 \psi_j(w_2) \psi_j'(w_1) - m_1 \psi_j'(w_2) \psi_j(w_1)}{m_2 \chi_j(w_2) \psi_j'(w_1) - m_1 \chi_j'(w_2) \psi_j(w_1)} \quad (28)$$

and

$$B_j = \frac{m_2 \psi_j(w_1) \psi_j'(w_2) - m_1 \psi_j(w_2) \psi_j'(w_1)}{m_2 \chi_j'(w_2) \psi_j(w_1) - m_1 \psi_j'(w_1) \chi_j(w_2)} \quad (29)$$

with an additional Riccati–Bessel function χ_j and its first order derivative χ_j' as

$$\chi_j(x) = -x Y_j(x) \quad (30)$$

and

$$\chi_j'(x) = \chi_{j-1}(x) - \frac{j}{x} \chi_j(x). \quad (31)$$

The other Riccati–Bessel functions and their first order derivatives, i.e., ψ_j , ξ_j , ψ_j' , and ξ_j' are identical with the case for homogeneous nanosphere, i.e., as described in Eqs. (22), (23), (24), and (25), respectively [36].

Considering $m_1 = m_2$ gives $A_j = B_j = 0$ leading to the scenario where Eqs. (26) and (27) reduce to Eqs. (20) and (21) which is the case for the homogeneous sphere [36].

2.1.3 Coupled dipole method

Nanoparticle arrays with well-defined periodicity are also an important class of nanostructures. In this thesis, sensors and resonators are developed using spherical nanoparticle arrays, i.e., using nanosphere arrays [PVII] where the coupled dipole method [30] implemented in MATLAB is used to model those arrays and to optimize their optical responses (scattering, absorption, extinction, and transmittance).

To realize the coupled dipole approach [30], let's start from an individual dipole, i.e., a single nanosphere with its radius as r and its complex-dispersive dielectric function as ϵ_m . The nanosphere is surrounded by a non-dispersive medium having a dielectric constant ϵ_d . In quasi-static limit [API], i.e., when the excitation wavelength (λ) is very large compared to the nanoparticle size ($2r$), the polarizability of the nanosphere can be written as

$$\alpha_0 = \frac{4\pi}{3} r^3 \frac{\epsilon_m - \epsilon_d}{\epsilon_d + L(\epsilon_m - \epsilon_d)}, \quad (32)$$

where L is a geometrical shape factor and for a sphere, $L = 1/3$. To obtain a more generalized version of the polarizability beyond the quasi-static limit [API] (i.e., when $\lambda \gg 2r$ is not valid), one has to consider corrections on the quasi-static

polarizability (α_0) for dynamic depolarization and retardation. In modified long-wavelength approximation (MLWA), the corrected polarizability (α_1) becomes

$$\alpha_1 = \alpha_0 \left[1 - \frac{ik_d^3}{6\pi} \alpha_0 - \frac{k_d^2}{4\pi r} \alpha_0 \right]^{-1} \quad (33)$$

with $k_d = 2\pi n_d / \lambda$ and $n_d = \sqrt{\epsilon_d}$ [30].

Now, let's assume a two dimensional array of such nanospheres with a lattice period D in both x and y directions. In coupled dipole method, nanoparticles present in an array are collectively considered as coupled dipoles where each nanoparticle is treated as a single dipole. The collective polarizability of such array, i.e., the array polarizability (α_2) can be described as

$$\alpha_2 = \frac{1}{\alpha_1^{-1} - S} \quad (34)$$

with the lattice sum S as

$$S = \frac{1}{4\pi} \sum_j e^{ik_d r_j} \left[\frac{(1 - ik_d r_j)(3 \cos^2 \theta_j - 1)}{r_j^3} + \frac{k_d^2 \sin^2 \theta_j}{r_j} \right], \quad (35)$$

where r_j and θ_j are the polar coordinates of the j -th nanoparticle (dipole) from the central nanoparticle (origin) in an array [30].

The absorption (σ_{abs}), scattering (σ_{sca}), and extinction (σ_{ext}) cross-sections of the array are then calculated as [36]

$$\sigma_{abs} = k_d \text{Im}\{\alpha_2\}, \quad (36)$$

$$\sigma_{sca} = \frac{k_d^4}{6\pi} |\alpha_2|^2, \quad (37)$$

and

$$\sigma_{ext} = \sigma_{abs} + \sigma_{sca}, \quad (38)$$

while the transmittance (T) of the array can be calculated from the extinction [43] using the relation

$$\sigma_{ext} = D^2(1 - T). \quad (39)$$

2.1.4 Finite-difference time-domain (FDTD)

Nanostructures with arbitrary shapes, aperiodic arrangements, and complex designs cannot be modelled using TMM, Mie theory, or coupled dipole method. Moreover, these methods are often unable to provide information on the electric and magnetic fields, such as enhancement and confinement of the near-field, in a straightforward way. In these cases, Maxwell equations need to be solved rigorously and FDTD [38, 39] is a common approach to do it. In this thesis, FDTD is used to design optimal gratings [PIII], planar cavities [PIV, PVI], and resonant substrates [PVII, PVIII] by using the method implemented in Ansys Lumerical FDTD solver [44].

To understand the basic formalism of FDTD [38], lets consider the Maxwell equations in differential form as

$$\nabla \times \mathbf{H} = \frac{\partial \mathbf{D}}{\partial t} + \mathbf{J}, \quad (40)$$

$$\nabla \times \mathbf{E} = -\frac{\partial \mathbf{B}}{\partial t}, \quad (41)$$

$$\nabla \cdot \mathbf{D} = \rho, \quad (42)$$

and

$$\nabla \cdot \mathbf{B} = 0, \quad (43)$$

where \mathbf{J} is the source current and ρ is the charge density. In FDTD approach, Eqs. (40) to (43) are solved using Yee algorithm [39] by discretizing the time and space. The cartesian space (x , y , and z) is discretized as a grid of rectangular cells with side lengths Δx , Δy , and Δz while the time (t) is discretized in steps of Δt . In Yee algorithm, the field components take a form as

$$\mathbf{E}(x, y, z, t) = \mathbf{E}^n(j, k, l), \quad (44)$$

where $x = j\Delta x$, $y = k\Delta y$, $z = l\Delta z$, and $t = n\Delta t$ with $j, k, l, n \in \mathbb{N}$. Using this notation one can write the x -component of Eq. (41) in a discretized form as

$$\begin{aligned} B_x^{n+0.5}(j+0.5, k, l) &= B_x^{n-0.5}(j+0.5, k, l) \\ &- \frac{\Delta t}{\Delta y} \left[E_z^n(j+0.5, k+0.5, l) - E_z^n(j+0.5, k-0.5, l) \right] \\ &+ \frac{\Delta t}{\Delta z} \left[E_y^n(j+0.5, k, l+0.5) - E_y^n(j+0.5, k, l-0.5) \right]. \end{aligned} \quad (45)$$

In Eq. (45), the magnetic field (B) at the time step $n+0.5$ is updated from the magnetic field (B) at the time step $n-0.5$ and the electric field (E) at the time step n in a leapfrog manner. For other components of Eq. (41), the electric field (E) at the time step $n+1$ can be updated from the electric field (E) at the time step n and the magnetic field (B) at the time step $n+0.5$. Such procedure can be generalized to compute the electromagnetic field at all times over the whole computational grid [38].

Proper discretization of time and space is essential in FDTD to attain highly accurate results. The finer the discretization, the higher the accuracy in results, however, in expense of long computation time and demanding computational resources. As a thumb rule, the spatial discretization Δx , Δy , and Δz should be smaller than $\lambda/20$ where λ is the excitation wavelength. The temporal discretization should satisfy the Courant condition described as

$$c\Delta t \leq \frac{1}{\sqrt{\frac{1}{(\Delta x)^2} + \frac{1}{(\Delta y)^2} + \frac{1}{(\Delta z)^2}}}, \quad (46)$$

where c is the velocity of light [38].

The basic workflow of FDTD method contains multiple steps. At first, a nanostructure and its surroundings (substrate and superstrate) are designed as geometrical objects. Then, the material properties (permittivity and refractive index) are added to the objects. After that, the computational region is defined and suitable boundary conditions are added to the design. For periodic structures, periodic boundary conditions are used. For single nanostructures and aperiodic structures, perfectly matched layers are used. The next step is meshing, i.e., discretizing the computational region uniformly or non-uniformly, i.e., finer mesh in the region of interest and relatively coarse mesh elsewhere. Then, a light source is added depending on the type of the excitation, i.e., a plane wave source for broadband illumination, a Gaussian wave source to mimic a laser pulse, and dipole sources for quantum emitters. The last step is adding power monitors for collecting spectra and field monitors for extracting electromagnetic field information. The near-field information can be collected by placing a field monitor very close to the nanostructure [45].

2.1.5 Finite element method (FEM)

Maxwell equations can be solved rigorously also by using FEM [40, 41] as an alternative of FDTD method. The basic workflow of FEM is similar to FDTD except the fact that Maxwell equations are solved in frequency domain [38]. In this thesis, FEM is used to model and optimize oligomer nanostructures [PI, PII] implemented in COMSOL Multiphysics FEM solver [46].

To grasp a simple picture of FEM, let's consider the one dimensional Poisson's equation expressed as

$$-u''(x) = f \quad (47)$$

in $(0, 1)$ where the boundary condition is $u(0) = u(1) = 0$. To find a solution of u using FEM for a source function f , one has to consider a weak form of Eq. (47) described as

$$\int_0^1 u'(x)v'(x) dx = \int_0^1 f v(x) dx \quad (48)$$

where v is a test function defined in a domain Λ . The solution of Eq. (48) can be approximated by truncating the problem into a *finite element* (subdomain) $\Lambda_h \subset \Lambda$. In other words, to find a solution of $u_h \in \Lambda_h$ for a source function f , we need to solve

$$\int_0^1 u_h'(x)v'(x) dx = \int_0^1 f v(x) dx \quad (49)$$

for all $v \in \Lambda_h$ [40, 41].

In order to numerically solve Eq. (49), one needs to define u_h and v_h in terms of basis functions as

$$u_h = \sum_{j=1}^n \beta_j \varphi_j \quad (50)$$

and

$$v_h = \sum_{i=1}^n \varphi_i \quad (51)$$

where φ_j and φ_i are the basis functions while β_j is the basis coefficient. Inserting the basis forms of u_h and v_h in Eq. (49) yields

$$\sum_{j=1}^n \beta_j \int_0^1 \varphi_j' \varphi_i' dx = \int_0^1 f \varphi_i dx \quad (52)$$

for each $i = 1, \dots, n$. From this point, a system of linear equations for β_j can be developed and can be expressed in a matrix form as

$$\boldsymbol{\beta} = \mathbf{A}^{-1} \mathbf{b} \quad (53)$$

with

$$A_{ij} = \int_0^1 \varphi_j' \varphi_i' dx \quad (54)$$

and

$$b_i = \int_0^1 f \varphi_i dx \quad (55)$$

where \mathbf{A} is the system matrix and $\boldsymbol{\beta}$ is the solution vector. The majority of the elements in the system matrix (\mathbf{A}) are zero since each subdomain is connected to only a few neighboring subdomains (finite elements). In other words, \mathbf{A} is a sparse matrix and can be solved numerically using a sparse matrix solver. For two and three dimensional cases, the subdomains can be triangles and tetrahedrons, respectively [40,41].

In practice, FEM and FDTD are equivalent for designing nanostructures. However, FEM can provide triangular and tetrahedral mesh cells which are often better to model anisotropy and critical geometries compared to the rectangular and cubic cells of FDTD method [38].

2.2 Fabrication of nanostructures

Practical implementation of nanostructures requires precise fabrication of such structures as per their optimized design parameters. In this thesis, fabricated nanostructures can be classified into two categories - multilayer structures, i.e., coatings [PV] and planar cavities [PVI], and patterned structures, i.e., oligomers [PI] and gratings [PIII]. The fabrication techniques used to develop these nanostructures are thermal evaporation [47], spin coating [47], electron-beam lithography [48,49], and etching [47,50], which are briefly explained in the following subsections.

2.2.1 Thermal evaporation

Thermal evaporation is a physical vapor deposition (PVD) technique typically used to fabricate thin films (nanofilms) of metals on top of a desired substrate (e.g., glass or silicon). Figure 5 depicts a schematic diagram of the thermal evaporation process. In thermal evaporation, a source material in solid form (melt)

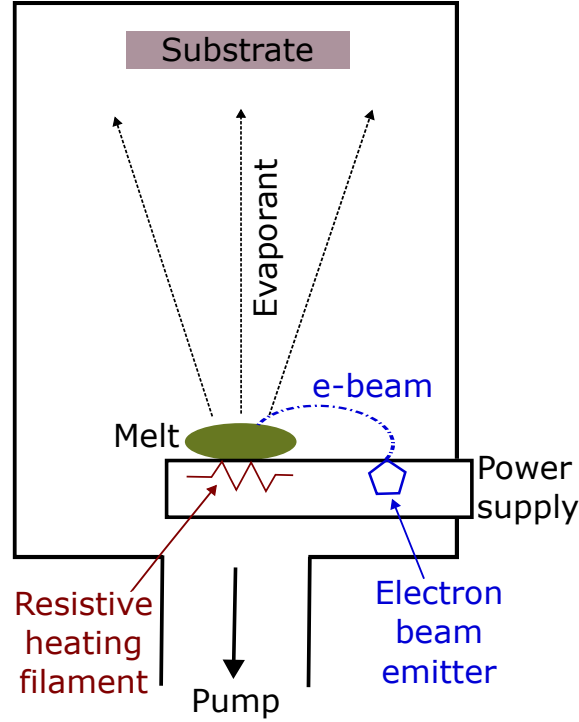


FIGURE 5 Schematic diagram of a thermal evaporator.

is vaporized atom by atom to deposit on the substrate. The deposition happens at a controlled rate to attain a target thickness of the deposited thin film. The source material is vaporized using thermal energy provided either by resistive heating (filament) or by a tightly focused electron beam (e-beam). The temperature of the melt is increased up to a point where it starts to evaporate. A high vacuum environment ($10^{-8} - 10^{-9}$ mbar pressure) is maintained inside the evaporation chamber using a vacuum pump to avoid formation of any oxides or nitrides due to the presence of any background gases. In addition, the substrate is kept at a distance from the melt no longer than the mean free path of the evaporated atoms (evaporant) to ensure no collision between the evaporant and the background gas molecules during transit from melt to substrate. The substrate is usually positioned above the melt so that the vapor (evaporant) produced during evaporation can condense on the substrate to form a uniform thin film [47].

The evaporation rate (Z_A), i.e., the number of atoms leaving the melt surface depends on the binding energy of the source material as well as its temperature and can be expressed as

$$Z_A \propto \frac{P}{\sqrt{M \times T}}, \quad (56)$$

where P is the vapor pressure, T is the vapor temperature, and M is the molar mass. The deposition rate (r) on the substrate can be calculated from Z_A as

$$r = \frac{Z_A}{\frac{\rho}{M} \times N_A}, \quad (57)$$

where ρ is the density of the source material (melt) and N_A is the Avogadro number. In practice, thermal evaporation systems contain a quartz crystal control unit

for monitoring the deposition rate in real time to obtain the target thickness of the deposited film [47].

In resistance-heated evaporation, the thermal energy is provided through a resistive heating filament where a flow of large direct current through the filament (controlled by a power supply) is used to increase the temperature. The pellets of melt are kept on a cup made of materials with high melting points (tungsten or molybdenum) to ensure that the cup will not deform or evaporate during the evaporation of melt. In resistive heating, the temperature is highest at the filament and at the bottom of the melt while its lowest at the melt surface which is the actual region of interest. Eventually, such approach is cheap, simple but less efficient [47].

Electron-beam evaporation is a more sophisticated way of providing thermal energy to the melt. In this process, an electron-beam emitter (controlled by a power supply) is used to generate an electron beam (e-beam) which is then guided to the top of the melt (melt surface) with the help of several beam forming plates, deflectors and electromagnets. The magnets are used to adjust the beam spot and to sweep the beam. The pellets of melt are kept on a crucible which is water cooled. In e-beam heating, the temperature is highest at the melt surface while lower in the bulk material and crucible. Consequently, this approach provides better material purity than the resistive heating, however, is more expensive to operate [47].

In this thesis, thermal e-beam evaporation is used to develop thin metallic layers for fabrication of nanoparticles [PI], gratings [PIII], and cavity mirrors [PVI].

2.2.2 Spin coating

Spin coating is a common procedure to develop polymer based organic thin films (nanofilms) on top of a substrate from the spin solution containing the polymer dissolved in a liquid solvent. In this process, the substrate is placed inside the spinner on a motorized rotating stage and kept there by a vacuum chuck. After that spin coating happens in four phases, i.e., dispense, spreading, thin-out, and evaporation. Figure 6 shows the first three phases of the spin coating process. In the dispense phase, the spin solution is dispensed on top of the substrate through a pipette or syringe. The amount of the dispensed solution has no effect on the film thickness as far as the amount is ample to cover the substrate area in the following phases. In the spreading phase, the substrate is spun with a low speed to ensure spreading of the dispensed fluid covering its entire surface. Spinning with low speed will incur angular acceleration and the fluid will experience a tangential force. In addition, due to the angular velocity, the fluid will also experience a centrifugal force acting radially. As a result, the fluid will flow in a spiral trajectory towards the edge opposite to the rotation as shown in Figure 6. In thin-out phase, the substrate is spun at full speed. Consequently, the angular acceleration drops to zero so as the tangential forces resulting in a radially outward motion of the fluid (Figure 6). Eventually, the film will thin out and its thickness will

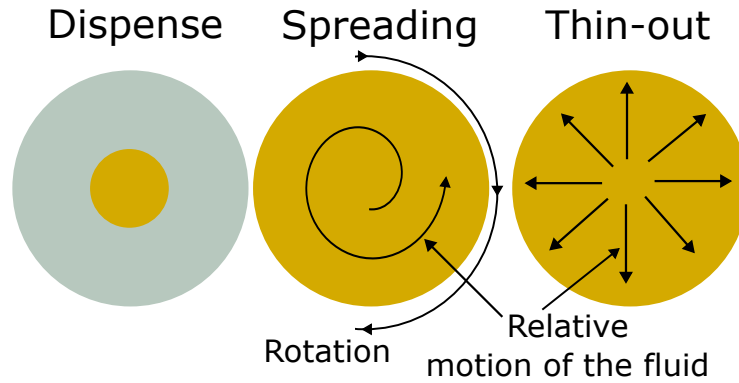


FIGURE 6 Different phases of the spin coating process.

reach a steady-state. In the evaporation phase, the rest of the solvent will evaporate (solvent evaporation happens in all phases of spin coating) and hence, the film viscosity will increase. At this stage, the film thickness will saturate and will not change even if the spinning continues. After the evaporation phase, often the spin-coated film is baked at a high temperature to harden the polymer [47].

The thickness of a spin-coated film depends on the spin speed and the viscosity of the spin solution [47]. To achieve a target thickness, the spin speed should be optimized with the help of a calibration curve, i.e., a plot of film thickness as a function of spin speed. Figure 7 illustrates an example of a calibration curve for a generic polymer film. To construct such a calibration curve, multiple spin-coated films should be produced using different spin speeds with identical spin solution (same viscosity) and their thicknesses should be measured to plot the trend. From Figure 7, it is clear that for a constant viscosity of the spin solution, the coated films will be thick if the spin speed is very low and the thickness will drop rapidly if the spin speed increases. However, after a certain spin speed, the thickness will saturate and further reduction in thickness is only possible by reducing the viscosity of the spin solution (i.e., diluting the polymer in solvent).

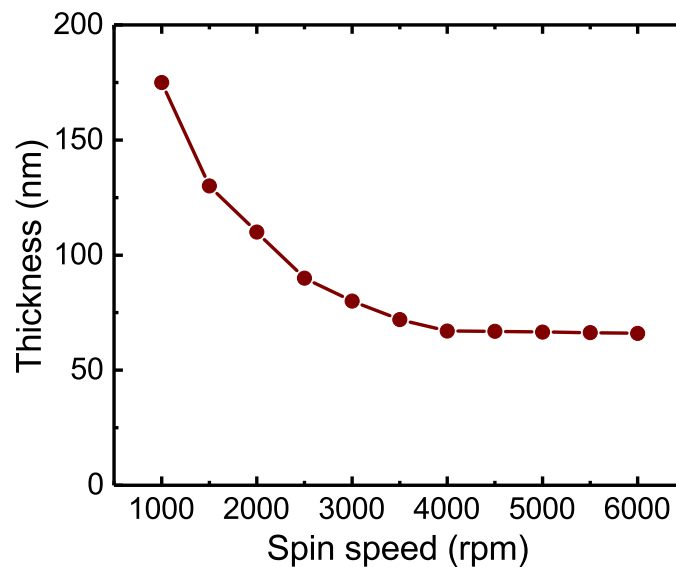


FIGURE 7 Calibration curve of the spin coating process for a generic polymer.

In this thesis, spin coating is used to coat resists before e-beam patterning for oligomers [PI] and gratings [PIII], and to produce molecular films [PV] and doped cavities [PVI].

2.2.3 Electron-beam lithography and lift-off process

Electron-beam lithography (EBL) is a fabrication technique to pattern nanostructures on top of a substrate using a focused electron-beam (e-beam). The substrate is coated with an electron-sensitive material called resist and after exposure to the e-beam, the solubility of the resist changes in the exposed areas. For a positive resist (e.g., polymethyl methacrylate or PMMA), the polymer chains break due to exposure in the exposed areas and the exposed part of the resist will dissolve during the development process. Therefore, only the resist in the unexposed areas will remain after development. For a negative resist (e.g., SU-8 from Microchem), the polymer chains cross-link due to exposure in the exposed areas and the unexposed part of the resist will dissolve during the development process. Hence, only the resist in the exposed areas will remain after development. The e-beam scans the coated substrate guided by the pattern generator where the desired design parameters are loaded.

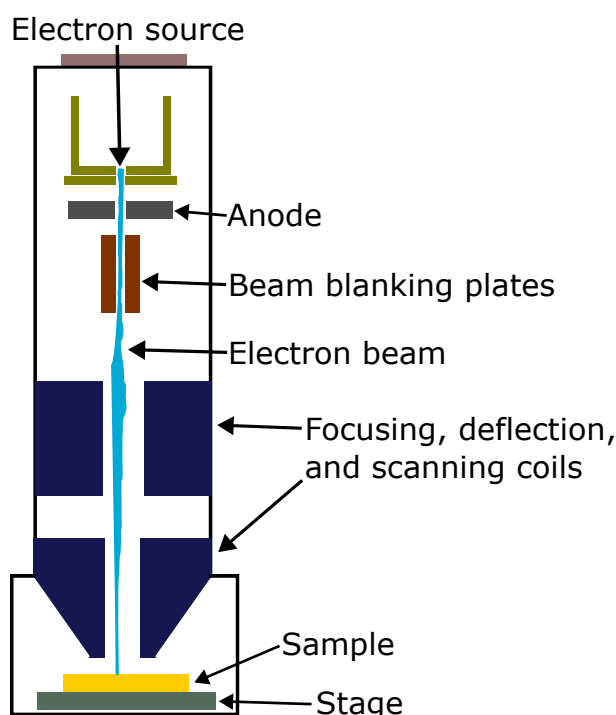


FIGURE 8 Schematic diagram of an electron beam lithography (EBL) system.

An EBL system consists a chamber, an electron gun, and a column with electro-optic elements. Figure 8 depicts a simplified schematic diagram of an EBL system. The e-beam generated by the electron source (gun) traverses through an anode and a pair of beam blanking plates. After that, electro-optics elements, i.e., focusing, deflection, and scanning coils are used to accelerate, control, focus, and deflect the e-beam to write the pattern on the sample (resist-coated substrate).

The sample is usually inserted into the EBL chamber through a loadlock, and placed on a stage equipped with accurate positioning and precise movements. A high vacuum is maintained inside the EBL chamber using vacuum pumps and the EBL system is operated by computers containing the control unit, the pattern generator and the operator interface [48].

In e-beam patterning, the important EBL parameters to consider are the size of the writing field (largest exposed area without any movement of the stage), the size of the exposure elements (subdivisions of the writing field), the stitching conditions (stitching of areas exposed to include totally more than one writing fields), the exposure dose (energy in terms of current applied per unit area), the system clock (writing speed), and the beam current (number of electrons hitting the sample per second). Calibration and optimization of these parameters are essential to obtain high accuracy in the patterning. However, these parameters often vary pattern to pattern depending on the desired resolution, resist type, and density/dimension/fineness of the pattern. Another important factor to consider in EBL is the proximity effect, i.e., creation of unwanted features during patterning due to multiple elastic and inelastic scattering of electrons after hitting the sample surface. Usually, high acceleration voltage is used to minimize the proximity effect [48].

To pattern a nanostructure, the optimized design is imported into the EBL system through a CAD tool. A fracturing process is employed to convert the design into a pattern data file containing patterning instructions required by the pattern generator for directing and scanning the e-beam. The drawing substrate (sample) is usually conducting or semiconducting to conduct the electrons from the e-beam to ground. For insulating substrates, to avoid charging of the sample during exposure which might incur inaccuracy in patterning, a thin layer of metal or conducting polymer is added on top of the resist. At this point, performing a calibration sequence is essential to optimize the EBL parameters. Such sequence includes electron gun and column alignment, writing field calibration, and adjustment of beam current, beam focus, and astigmatism. After that the sample can be exposed to the e-beam. During patterning, the EBL software moves the stage and separates the pattern in corresponding writing fields as per requirements [48].

In EBL, the so-called lift-off process usually involves the patterning, the subsequent development phase, deposition, and the final lift-off. Figure 9 illustrates a flowchart for fabrication of metal nanostructures on a dielectric substrate. The process starts with a cleaned substrate (e.g., fused silica). First, the substrate is coated with a positive e-beam resist, e.g., PMMA, by spin coating (see Section 2.2.2). Then, the coated substrate is exposed to the e-beam for patterning. After that, the patterned substrate is developed by submerging it into a developer solution. Consequently, only the PMMA in the unexposed area will be left after the development. The next step is metallization, i.e., depositing metal (e.g., gold) on top of the developed substrate by thermal evaporation (see Section 2.2.1). The last step of the lift-off process is submerging the metallized substrate into a resist stripper (e.g., acetone for PMMA). Eventually, the PMMA with the metal on

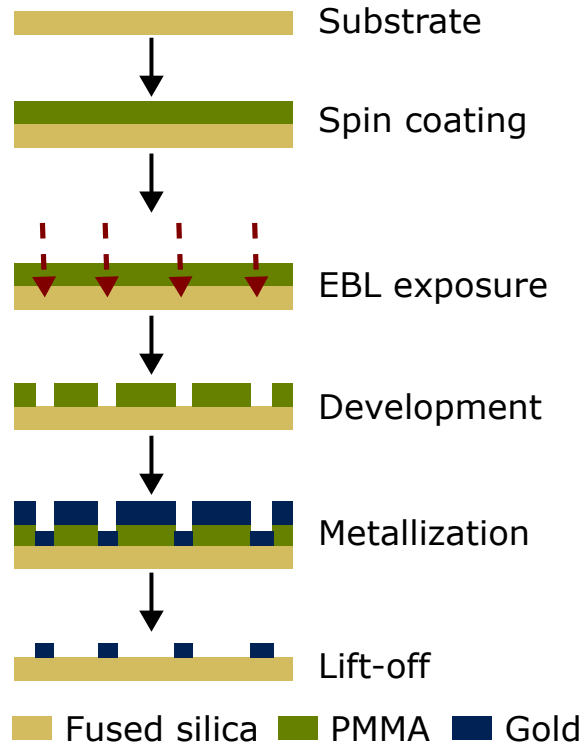


FIGURE 9 Flowchart for fabrication of metal nanostructures on a dielectric substrate.

top of it will dissolve and only the metal directly on top of the substrate will remain [49].

In this thesis, EBL and the lift-off process are used to fabricate oligomers [PI] and gratings [PIII].

2.2.4 Wet and reactive-ion etching

Etching is a method of patterning substrate by removing material from it through chemical or/and physical processes. The etching process is purely chemical in wet etching, while in dry etching, it can be more like a physical process. In wet etching, a resist-coated and lithographically patterned substrate is immersed into an etch solution and during that chemical bath, the etch liquid reaches to the substrate material through the openings in the resist pattern to etch it. The etch solution should be selected such a way that it will only etch the target material but neither the resist on top nor the bulk substrate underneath and hence, the resist will work as an etch mask. The etch selectivity is defined as

$$\text{Selectivity} = \frac{\text{Etch rate of the target material}}{\text{Etch rate of the etch mask}} \quad (58)$$

and an etch solution with high selectivity is required to achieve desired etched pattern. In wet etching, the etch selectivity is usually very high [47].

Wet etching can be isotropic or anisotropic in nature as illustrated in Figure 10. In anisotropic etching, the etching rates are different for different crystal planes of the target material. For example, the etch rates for $\langle 100 \rangle$, $\langle 110 \rangle$, and $\langle 111 \rangle$ planes of crystalline silicon are different in potassium hydroxide (KOH) so-

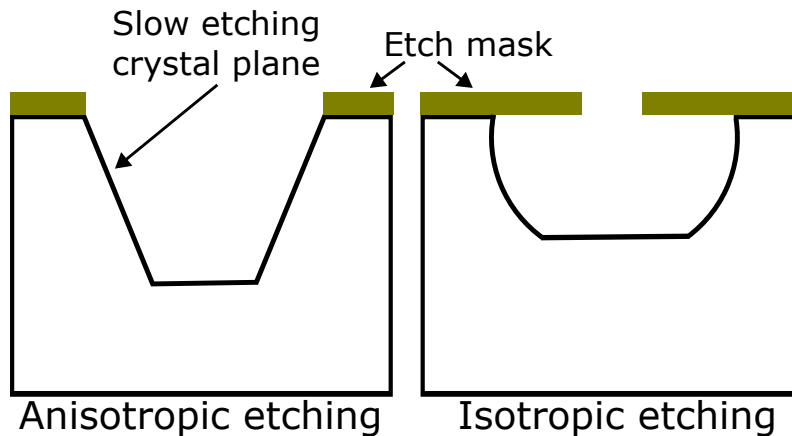


FIGURE 10 Anisotropic and isotropic wet etching processes.

lution. The $\langle 100 \rangle$ and $\langle 110 \rangle$ crystal planes are etched much faster than the $\langle 111 \rangle$ plane which is the etch-stop plane. Consequently, the anisotropically etched pattern results in a hole with tapered sidewalls (see Figure 10). Such orientation-dependent etching is often useful to maintain the resolution of the desired pattern. For most amorphous or polycrystalline materials, however, wet etching is isotropic in nature, i.e., the etch rate is same in all directions. Such etching often narrows the etched line and affects the resolution of the desired pattern. The scenario becomes more severe when the thickness of the target material (to be etched) is in the same order of magnitude as the dimensions of the desired pattern, which is often the case in practice [47].

A more sophisticated way to perform etching is the inductively coupled plasma reactive ion etching (ICP-RIE). It is a dry etching technique and often preferred over wet etching for patterns with demanding resolution [47, 50]. Figure 11 presents a simplified schematic diagram of the ICP-RIE system.

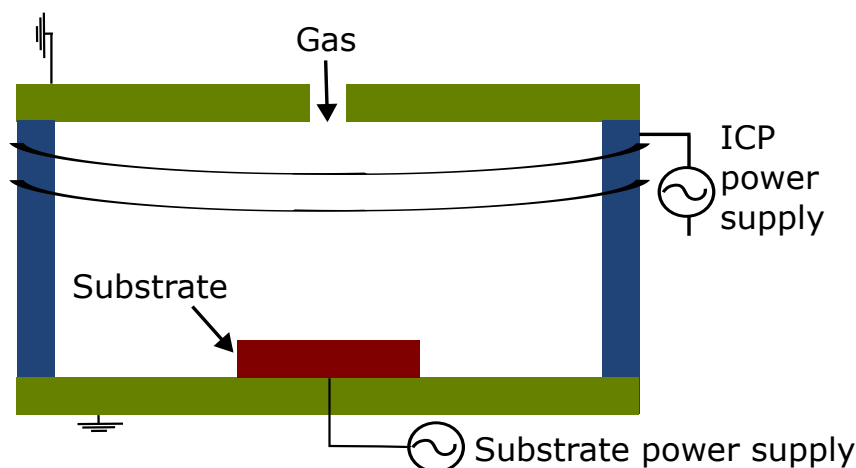


FIGURE 11 Schematic diagram of an ICP-RIE system.

In an ICP-RIE system, an inductive coil is looped around the outer walls of the etching chamber and excited by a time-varying current controlled via ICP power supply. The gas used for etching (e.g., oxygen or sulfur hexafluoride) enters into the chamber from above through a nozzle with a controlled in-flow

rate. A vacuum environment is maintained inside the chamber by controlling the chamber pressure using pumps. Inside the vacuum chamber, the substrate being etched is placed on a wafer electrode (cathode), while the chamber wall at the bottom works as the grounded anode. A separate substrate power supply is used to apply a negative DC bias voltage on the wafer electrode. The time-varying magnetic field provided by the ICP power supply ionizes the gas and sustains a plasma (containing positive ions and excited molecules) generated inside the chamber. The excited pieces act as radicals and easily react and thus etch the substrate. The negative DC bias at the wafer electrode attracts the ions towards the substrate and the etching is enhanced by the energy due to the ion bombardment on the surface of the substrate. The process can be tuned to only physical etching also by removing the chemically reacting component/gas and using only inert gas like Argon to have only the Ar^+ ions to bombard the substrate away. This process is usually called sputter etching. During etching, a flow of helium gas is often used for cooling the substrate, while volatile species produced in the process are pumped out from the chamber. The etching parameters, i.e., ICP power, substrate power, chamber pressure, and gas flow rate should be optimized to attain anisotropic etching with a high etch rate [47,50]. In this thesis, gratings [PIII] are fabricated using wet and ICP-RIE etching.

2.3 Characterization of nanostructures

Fabricated nanostructures are characterized to verify the accordance between the fabricated version and the targeted optimal design. The geometry of the fabricated version is assessed by structural characterization, i.e., profilometry [51] for measuring the thickness and scanning electron microscopy (SEM) [52] for verifying the morphology. Optical characterization is employed to check the optical responses (reflection, transmission, and emission) of the fabricated nanostructures, while Raman characterization is used to test their performance as a resonant substrate in Raman spectroscopy [53].

2.3.1 Structural characterization

Stylus profilometry is a structural characterization method used to measure the thickness and surface roughness of a fabricated nanofilm. Figure 12 shows a schematic diagram of the stylus profilometer. In the profilometer, the vibration isolation frame is used to isolate the measurement from external vibrations that incur inaccuracy in the measured data. The base plate connected to the control system with line scanning system is used to scan the substrate. The substrate is kept on the substrate holder and both of them move during the line scan. To incorporate a change in surface height, the substrate often contains an artificially made scratch (e.g., made by a scalpel) on a sacrificial region of the film (e.g., close to the edges). During a line scan, the stylus scans the rough substrate surface and

any change in stylus height is recorded by the displacement sensor. The computerized control system is used for controlling the line scanning (speed and length), converting the displacement sensor data (analog to digital), and data processing. The vertical resolution of the measurement depends on the sensitivity of the displacement sensor but the horizontal resolution is determined by the tip diameter of the stylus. The surface profile (thickness and roughness) is evaluated from the changes in stylus height in terms of arithmetical mean deviation of roughness, maximum height of roughness, and root mean square deviation of roughness. An optical microscope is often combined with the profilometer to facilitate selective local measurements [51]. In this thesis, profilometry is used for thickness characterization of nanofilms in [PV] and [PVI]. Examples of profilometric data can be found in [PV].

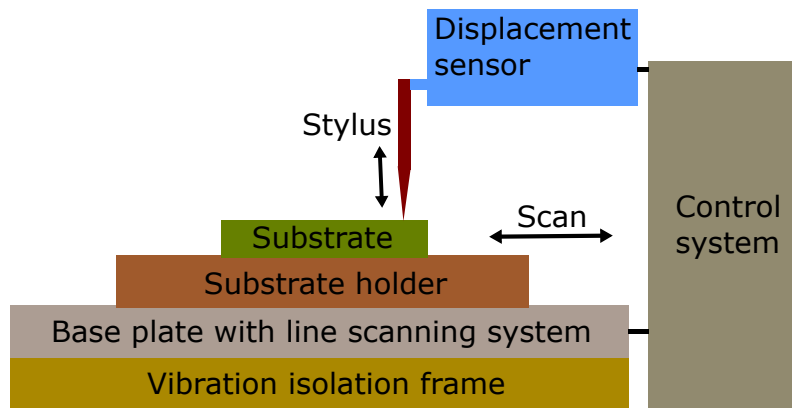


FIGURE 12 Schematic diagram of a stylus profilometer.

Scanning electron microscope (SEM) [52] imaging is another structural characterization method used to explore the morphology, i.e., shape, size, and structure of a fabricated nanostructure. The working principle and schematic of a SEM is identical with an EBL system (see Section 2.2.3) except the fact that in SEM, the focused e-beam is used for imaging with subnanometer resolution instead of patterning. During the imaging, the e-beam is continuously scanned along the substrate as stated by the name of the method. Consequently, often SEM and EBL systems are combined to a single e-beam system operated either in the patterning mode (EBL) or in the imaging mode (SEM).

In SEM, multiple signals are produced due to an interaction between the focused e-beam and the substrate being imaged. Figure 13 schematically shows such an interaction where the produced signals are secondary electrons (SEs), backscattered electrons (BSEs), Auger electrons (AEs), and X-rays, while PE refers to the primary electrons impinging on the substrate surface. The SEs are recorded by a dedicated detector and their yield heavily depends on the incident angle of the e-beam. Therefore, they are utilized to image the shape. The yield of the BSEs depends on the atomic number of the specimen being imaged and hence, they are utilized to determine the composition, i.e., to observe the material contrast. In addition to the shape and composition, elemental analysis can also be done in SEM by recording the characteristic X-rays through an energy-dispersive X-ray

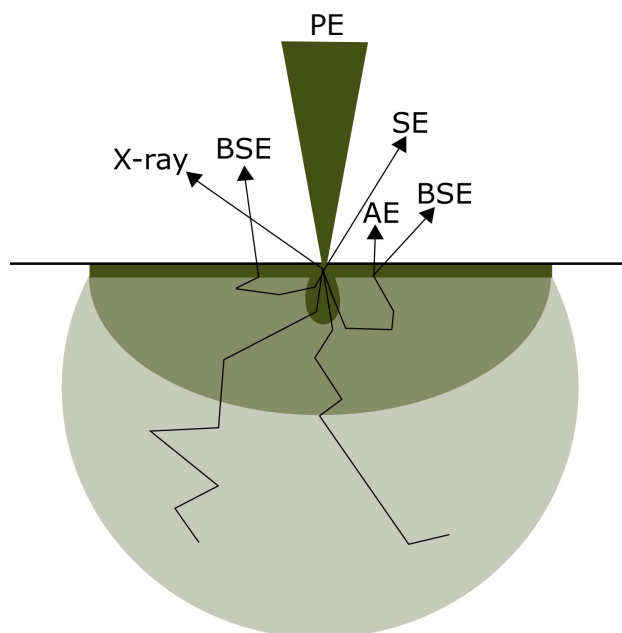


FIGURE 13 Interaction between the focused e-beam and the substrate being imaged where the produced signals are secondary electrons (SEs), backscattered electrons (BSEs), Auger electrons (AEs), and X-rays, while PEs refer to the primary electrons impinging on the substrate surface.

spectrometer (EDS) attached with the SEM [52]. In this thesis, SEM is used to characterize the morphology of the oligomers [PI] and gratings [PIII] where the corresponding SEM images can be found.

2.3.2 Optical characterization

Bright-field reflection spectroscopy is a straightforward method to measure the reflectivity of a nanostructure and a schematic of such set up is shown in Figure 14. In this method, the sample (nanostructure) is kept on a movable microscopic stage and illuminated by a white light source (lamp). A polarizer is used to select the polarization of the excitation. After passing through a beam splitter, the polarized incident light is tightly focused on the sample through an objective. The same objective is used to collect the reflected light where an analyzer is used to select the polarization of the reflected signal. The reflected light is then fed to an optical fiber via a fiber coupler and guided to a CCD spectrometer system to collect the reflection spectrum.

The experimental set up in Figure 14, however, fails to provide any angle-resolved information of the optical responses. That is because, the incident light through an objective comes at all angles and hence, precise control on the excitation angle is not possible in such set up. To accurately measure the angle-resolved reflection, transmission, and emission, a customized goniometric set up depicted in Figure 15 is used along with a suitable light source.

In angle-resolved steady-state reflection and transmission measurements, a white light source (lamp) is used to shine light on the samples, i.e., the nanos-

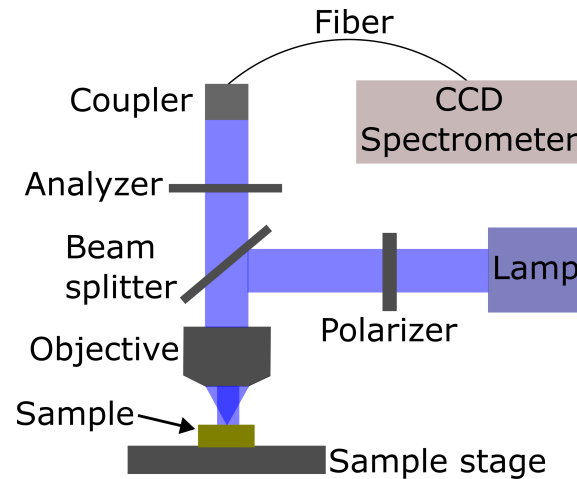


FIGURE 14 Experimental set up for the bright-field reflection spectroscopy.

structures. The pseudo-collimated incident light passes two pinholes (P_1 and P_2) and reaches the sample. The sample is kept on the rotation axis of a 360° rotating stage facing towards the incident light and the prism polarizer axis is set to the vertical or s -polarization. By rotating the sample stage and the rotational arm, the excitation (θ) and detection (ϕ) angles are regulated, respectively. When collecting reflection, $\theta = \phi$, while for transmission, the rotational arm is always kept at the transmission position as shown in Figure 15 for all θ . The reflected and transmitted signals are collected using a fiber coupler connected to an optical fiber. The collected light is then guided to a spectrometer having a monochromator and CCD to obtain the corresponding spectra.

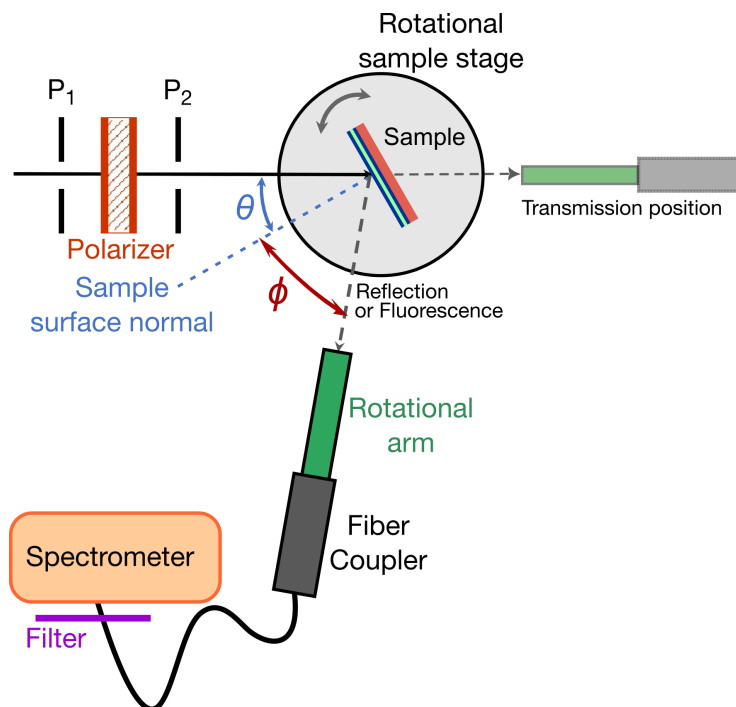


FIGURE 15 Experimental set up for the angle-resolved optical spectroscopy. Adapted from [PVI] under the license CC BY 4.0.

In angle-resolved steady-state emission measurement, the sample is excited by a tunable pulse laser where the temporal length of the excitation pulses (pulse length or pulse width) is ~ 5 ns, while the repetition rate, i.e., the number of emitted pulses per second (inverse temporal pulse spacing) is 100 Hz. Care has been taken on pulse energy to keep everything in a linear regime, so that the laser can be treated as a continuous wave excitation. The laser beam is collected into a fiber, guided to the experimental setup, and used to excite the sample with pseudo-collimation. The other experimental settings (sample position, polarization, regulation of θ and ϕ , and the pinhole sizes) are kept exactly similar to the reflection and transmission studies. In this work, the emission at the sample surface normal is detected, i.e., $\phi = 0^\circ$ for all θ . The collection path for the sample emission is similar to the reflection/transmission measurements except a long pass filter placed before the spectrometer to exclude the laser excitation (see Figure 15).

In this thesis, the bright-field reflection spectroscopy is used to measure the reflectance of the gratings [PIII], while the angle-resolved approach is employed to measure reflection, transmission, and/or emission of the oligomers [PI], nanofilms [PV], and doped cavities [PVI].

2.3.3 Raman characterization

Confocal Raman microscopy [53] is a common approach to evaluate the performance of a nanostructure when employed as a resonant substrate in Raman spectroscopy. A confocal Raman microscope as schematically shown in Figure 16 is usually used to carry out such measurements.

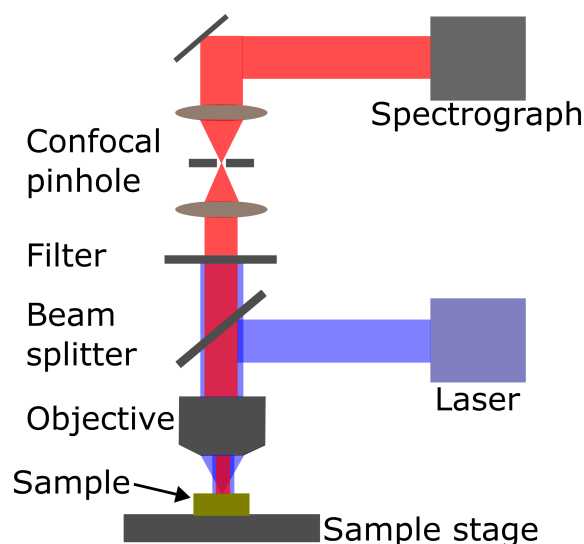


FIGURE 16 Schematic diagram of a confocal Raman microscope.

In Raman characterization, the sample is placed on a movable microscopic stage and excited by a laser. The excitation light (blue) passes a beam splitter and is tightly focused on the sample through a high numerical aperture objective. The same objective is used to collect the scattered light, i.e., the Rayleigh component

of the excitation light (blue) and the Raman-shifted (Stokes) signal (red). A notch filter is used to exclude the Rayleigh component of the excitation light (blue) and only the Raman signal (red) is collected via a confocal path. The collected light is then guided to the spectrograph for recording the Raman spectrum [53]. In this thesis, the confocal Raman microscopy is used to measure the Raman responses of the oligomers [PI] and gratings [PIII].

Chapter summary

To summarise, this chapter briefly explains how the optical nanostructures reported in this dissertation are designed, fabricated, and characterized for light-matter coupling applications. To design nanofilms, nanospheres, and nanosphere arrays, transfer matrix method, Mie theory, and coupled dipole method are used, respectively, while for modelling complex and arbitrary nanostructure geometries, rigorous approaches such as finite-difference time-domain and finite element methods are employed. To fabricate planar multilayer structures (nanofilms and nanocavities), thermal evaporation and spin coating are used, while for patterned nanostructures (oligomers and gratings), electron-beam lithography, lift-off process, and etching are further employed. The structural properties of the fabricated nanostructures are explored using stylus profilometry and scanning electron microscopy, while the optical properties are investigated through bright-field and angle-resolved optical spectroscopy, and Raman spectroscopy.

3 WEAK COUPLING BETWEEN ORGANIC MOLECULES AND PLASMONIC NANOSTRUCTURES

In *weak* light-matter coupling, as mentioned in Chapter 1, molecular responses can be influenced using *confined light*. In line with that this chapter summarizes how Raman responses of the organic molecules can be enhanced using plasmonic nanostructures possessing subradiant plasmonic modes.

3.1 Raman scattering

The size of an organic molecule is usually smaller or comparable to the wavelength of light and consequently, they scatter light when illuminated. When a monochromatic light (e.g., a laser beam) is used as an excitation, the light scattered from the molecule contains the excitation frequency (ν_{ex}) at the center of its spectrum along with a higher and a lower frequencies. The scattered light having the frequency ν_{ex} is called the Rayleigh signal originated due to the Rayleigh scattering of light, while the higher and lower frequencies are called the anti-Stokes and Stokes signal, respectively, emerged due to the Raman scattering (RS) [54–56].

To understand the origin of RS, one can consider a simple energy diagram as shown in Figure 17. Lets assume that an organic molecule has two vibrational energy states m and n with an energy difference between them as $\Delta E = h\Delta\nu$ where h is the Planck's constant and $\Delta\nu$ is the frequency difference of the states. When the molecule is illuminated by a laser with a frequency of ν_{ex} (green arrows), majority of the incident photons elastically collide with it and the scattered photons have the same frequency (ν_{ex}) as the excitation light (green). As if the molecule goes through a transition from m or n state to a corresponding virtual state (m^* or n^*) and relaxes to the same state, i.e., the net energy difference between the initial and final states is zero. This is the case of Rayleigh scattering [54–56] as shown in

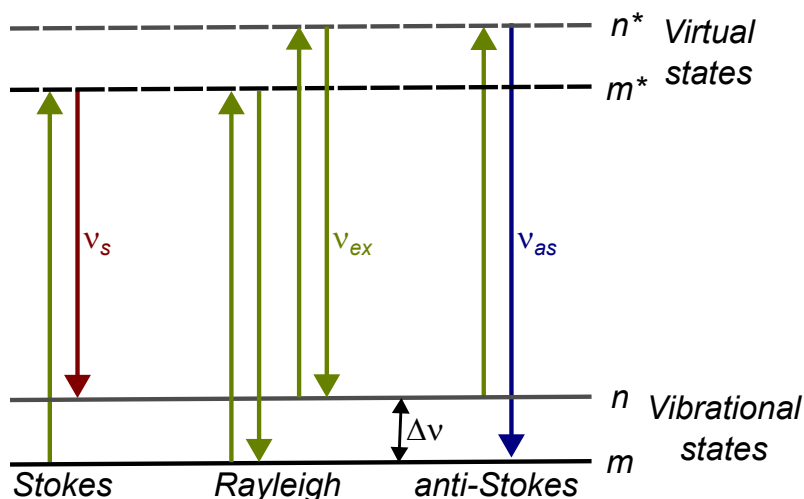


FIGURE 17 Energy diagram for Raman scattering (RS).

the middle part of Figure 17.

There is, however, a small fraction of incident photons present that inelastically collide with the molecule. In that case, the scattered photons can have a frequency (ν_s , red) lower than the excitation light. The lost energy ($\Delta\nu$) will result in a molecular transition from the vibrational state m to the virtual state (m^*) where the molecule relaxes to the upper vibrational state n . Such scenario originates the Stokes part of the Raman signal [54–56] as shown in the left part of Figure 17. It can also be possible that after the inelastic collision, the scattered photons have a frequency (ν_{as} , blue) higher than the excitation light. The photons gain this extra energy ($\Delta\nu$) from a molecular transition where the molecule is pumped from the vibrational state n to the virtual state (n^*) while relaxes to the lower vibrational state m . This explains the emergence of the anti-Stokes part of the Raman signal [54–56] as shown in the right part of Figure 17.

Raman response of an organic molecule can be considered as a chemical *fingerprint* since Raman spectrum contains information about the vibrational or rotational energy levels of the molecule which can further be used to determine its atomic arrangements and bond strengths. Eventually, Raman spectroscopy is widely used as an analytical tool in material science. In practice, however, RS is a weak process since the Raman cross-sections ($10^{-29} - 10^{-31} \text{ cm}^2/\text{molecule}$) are quite lower than the fluorescence cross sections ($10^{-16} \text{ cm}^2/\text{molecule}$) even when the excitation light is in resonance with a real molecular transition [54–56].

One approach to enhance the RS is coherent anti-Stokes Raman scattering (CARS) which involves a third-order nonlinear effect called four-wave mixing (FWM) process. In CARS, an organic molecule is excited by three laser beams, i.e., a pump (ν_p), a Stokes (ν_s), and a probe (ν_{prb}) beam. The CARS signal (ν_{CARS}) is the enhanced anti-Stokes response of the molecule generated at the four-wave mixed frequency as

$$\nu_{CARS} = \nu_p + \nu_{prb} - \nu_s, \quad (59)$$

where the beat frequency ($\nu_p - \nu_s$) is tuned with a vibrational transition (ν_{vib}) of the molecule [57–59]. Figure 18 shows a simple energy diagram of the CARS

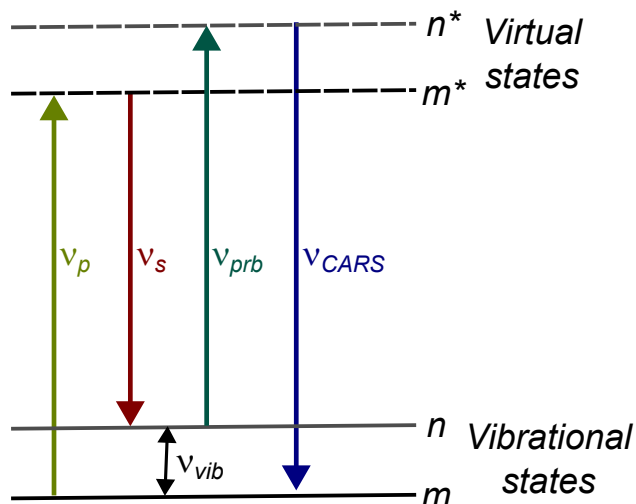


FIGURE 18 Energy diagram for coherent anti-Stokes Raman scattering (CARS).

process. In general, CARS signal is stronger than the RS signal, however, both RS and CARS processes need to be enhanced for optimal Raman analysis of organic molecules.

3.2 Weak coupling: surface enhancement

The RS and CARS signals of the organic molecules can be enhanced via *surface enhancement*, i.e., an enhancement due to the presence of a resonant *surface* underneath [4,55,56,60]. From Chapter 1 we know that in metallic nanostructures, the supported plasmonic modes can enhance and confine light at the near-field, i.e., very close to or around the structure (see Section 1.2). Therefore, the surface of the plasmonic nanostructure underneath the organic molecules can be the resonant *surface* having the plasmonic modes coupled to the molecular responses [4, 55, 56, 60]. Surface enhancement is a weak coupling process since it only enhances the Raman responses without inducing any change in the molecular energy levels. In other words, the light (plasmonic modes) and the matter (molecular responses) can still be considered as two different entities where the molecules experience the confined light (plasmonic mode) as a perturbation aiding the amplification of the molecular Raman response without forming any hybrid light-matter states.

The surface enhancement can have a chemical or an electromagnetic origin [56]. Here, we only focus on the electromagnetic enhancement which can be quantified by an enhancement factor (G). In surface enhanced Raman scattering (SERS), the enhancement factor can be formulated as

$$G_{SERS} = \left| \frac{\mathbf{E}_{loc}(\nu_{ex})}{\mathbf{E}_0(\nu_{ex})} \right|^2 \times \left| \frac{\mathbf{E}_{loc}(\nu_s)}{\mathbf{E}_0(\nu_s)} \right|^2 \quad (60)$$

with \mathbf{E}_0 and \mathbf{E}_{loc} as the electric field amplitudes of the incident light and the local field (near-field), respectively. From Eq. (60) it is clear that to significantly

enhance the SERS signal, the underlying plasmonic surface should support plasmonic modes at the excitation (ν_{ex}) and Stokes (ν_s) frequencies [60]. In surface enhanced coherent anti-Stokes Raman scattering (SECARS), Eq. (60) extends to

$$G_{SECARS} = \left| \frac{\mathbf{E}_{loc}(\nu_p)}{\mathbf{E}_0(\nu_p)} \right|^4 \times \left| \frac{\mathbf{E}_{loc}(\nu_s)}{\mathbf{E}_0(\nu_s)} \right|^2 \times \left| \frac{\mathbf{E}_{loc}(\nu_{CARS})}{\mathbf{E}_0(\nu_{CARS})} \right|^2 \quad (61)$$

and it is apparent from Eq. (61) that the plasmonic modes need to be present at the pump (ν_p), Stokes (ν_s), and CARS (ν_{CARS}) frequencies [61]. The near-field intensity enhancement (NFIE) of a plasmonic mode is defined as $|\mathbf{E}_{loc}/\mathbf{E}_0|^2$ and it is a key parameter here since the higher the NFIE at the excitation (ν_{ex} and ν_p) and Raman (ν_s and ν_{CARS}) frequencies, the higher the G , and the stronger the Raman signals [60, 61]. Considering $\nu_{ex} \approx \nu_s$ we get $|\mathbf{E}|^4$ enhancement of the Raman signal in SERS [60] and assuming $\nu_p \approx \nu_s \approx \nu_{CARS}$ we get $|\mathbf{E}|^8$ enhancement in SECARS [61]. Therefore, it is crucial to develop plasmonic nanostructures that can provide an optimal NFIE.

3.3 Plasmonic nanostructures for SERS

The optical properties of a plasmonic nanostructure both at near- and far-field are important for SERS. A plasmonic mode can strongly enhance and tightly confine light at the near-field (i.e., around the structure), and hence, can provide high NFIE leading to a large value of G_{SERS} . On the other hand, a strong peak in the scattering spectrum of such nanostructure enhances the intensity of the scattered light at the far-field and hence, improves the collection of the Raman signal with a high signal to noise ratio. Therefore, it is essential to engineer a plasmonic mode which ensures intense interaction between the molecules and the excitation light at ν_{ex} along with a strong far-field intensity at the targeted Stokes frequency (ν_s) [61]. Realizing Fano resonance [62] in a coupled plasmonic system is one way to engineer such plasmonic modes and in [PI], it is used to facilitate SERS.

Fano resonance (FR) is an asymmetric non-Lorentzian resonance [62] and it can be supported by a plasmonic oligomer, i.e., a cluster of metallic NPs [63–70]. In such oligomer, the size, shape, and material of the NPs as well as the interparticle distance are carefully chosen so that the structure can sustain FR at the desired spectral range. In a Fano-plasmonic oligomer, the LSP modes of the individual NPs hybridize when the interparticle distance is very small. Such hybridization can be a constructive interference resulting in an increase in the net dipole moment of the structure when the plasmon oscillations in all particles are in phase. This scenario yields a broad peak in the scattering spectrum known as the superradiant mode. When the plasmon oscillations in the NPs are not in phase, a destructive interference occurs and the net dipole moment decreases. Consequently, a subradiant mode emerges as a dip in the scattering profile. The depth of this Fano dip indicates how strongly the LSP modes of the NPs are coupled and it can be modulated by varying the interparticle distance. For a large interparticle

gap, such dip starts to disappear while it can reach even to a plasmon-induced transparency for a very small gap [63–71].

The subradiant mode (Fano dip) can provide a large NFIE within the nanostructure due to its non-radiative nature and capability to trap energy at the interparticle gaps, while the superradiant mode (Fano peak) can ensure a strong far-field intensity [69,70]. Therefore, it is desirable to tune the Fano dip mainly at the excitation frequency and match the Fano peak more with the targeted Stokes region. Such strategy ensures an enhanced collection of the Raman signal at the far-field along with an optimal interaction between the molecules and the excitation energy at the near-field [61].

In [PI], two plasmonic oligomers - a trimer and a pentamer having disk shaped NPs are used for SERS. The nanostructures are designed by FEM (see Section 2.1.5) and fabricated using EBL followed by a lift-off process (see Section 2.2.3). The fabricated nanostructures are characterized by an angle-resolved optical setup (see Section 2.3.2). Figure 19(a) shows the simulated and measured optical responses of the fabricated trimer with its SEM image on top. The green markings on the SEM image show its geometrical parameters where $s_1 = 200$ nm, $s_2 = 100$ nm, and $d_1 = 20$ nm so as is the thickness of the nanodisks. The signature of FR is profound in the simulated (blue curve) and experimental (red curve) scattering spectra of the trimer where the Fano dip is at 800 nm in between two Fano peaks, one at 700 nm and another one beyond 900 nm as one can see in Figure 19(a). The reported spectra are truncated at 900 nm since the collection efficiency of the measurement setup beyond that region is really poor. Unfortunately, that excludes the second Fano peak (> 900 nm) except its rising tail.

The green curve in Figure 19(a) shows the simulated NFIE profile of the trimer where the NFIE is maximum at the Fano dip due to the non-radiative nature of the subradiant mode. In Figure 19(b), the optical responses (simulated and measured) of the fabricated pentamer are reported along with the SEM image of the structure on top. The geometrical parameters of the pentamer marked in green on the SEM image are: $s_3 = 150$ nm, $s_4 = 125$ nm, and $d_2 = 20$ nm so as is the disk thickness. Like in the trimer, simulated (blue curve) and experimental (red curve) scattering profiles of the pentamer clearly show the signature of FR with a Fano dip (800 nm) and two Fano peaks (700 nm and > 900 nm). Here also, the NFIE profile (green curve) has its maximum at the Fano dip.

In Figures 19(a)-(b), the orange, magenta, and violet dashed vertical lines depict the excitation wavelength (785 nm), 734 cm^{-1} Raman line of adenine [72], and 1360 cm^{-1} Raman line of rhodamine 6G [73]. The FR in the trimer and pentamer is optimized such a way that in both cases, the Fano dip is tuned with the excitation wavelength (785 nm) while the Fano peak on the red side of the dip is overlapping with the targeted Stokes region (833 nm and 879 nm). From the NFIE profiles (green curves) in Figures 19(a)-(b) it is clear that for both structures, the NFIE is maximum at the excitation wavelength and reasonably high at the targeted Stokes region. This ensures an intense near-field interaction (i.e., large NFIE) between the molecules and light at the desired frequencies (excitation and Stokes) resulting in an optimal G_{SERS} . On the other hand, in both oligomers, the

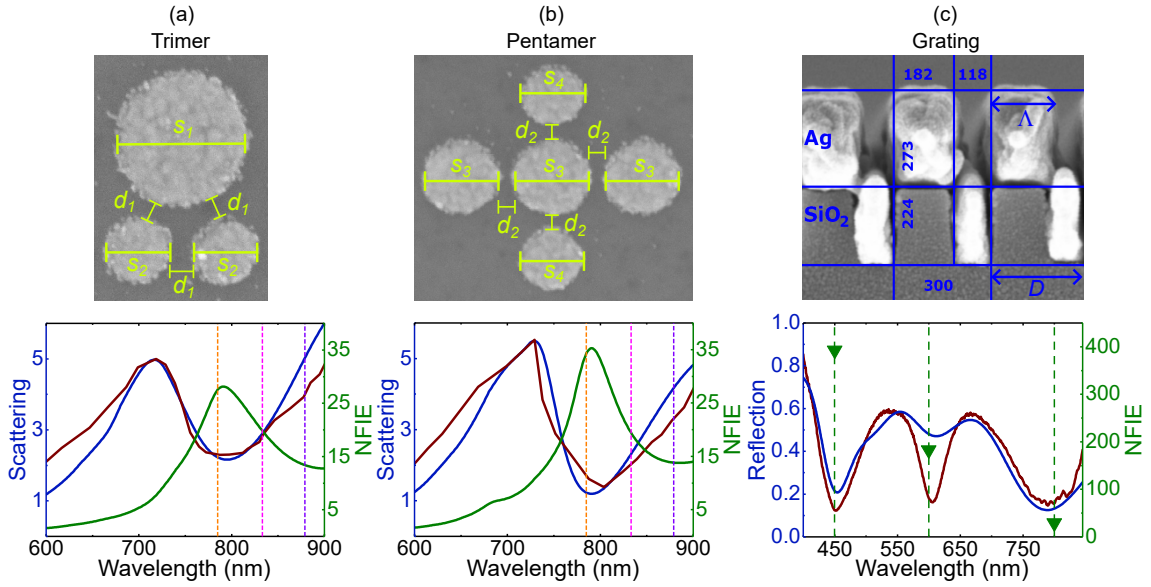


FIGURE 19 Optical responses of the fabricated (a) trimer and (b) pentamer with their SEM images on top. The green markings on the SEM images show the geometrical parameters of the structures where $s_1 = 200$ nm, $s_2 = 100$ nm, $s_3 = 150$ nm, $s_4 = 125$ nm, and $d_1 = d_2 = 20$ nm. The thickness of the nanodisks in both structures is 20 nm. In (a)-(b), the blue and red curves (left vertical axis) present the simulated and experimental (scaled) scattering spectra, respectively, while the green curve (right vertical axis) shows the simulated NFIE. The orange, magenta, and violet dashed vertical lines depict the excitation wavelength (785 nm), the targeted Raman line of adenine (734 cm^{-1} or 833 nm), and the targeted Raman line of rhodamine 6G (1360 cm^{-1} or 879 nm), respectively. (c) Spectral reflectance of the grating with the SEM image of a fabricated grating on top. The blue markings on the SEM image show the geometrical parameters of the structure where the fill factor (ff) is defined as Λ/D with D as the grating period and Λ as the top groove width. The blue and red curves (left vertical axis) present the simulated and experimental reflection spectra, respectively, for a grating with $ff = 0.47$ while the green dashed vertical lines show the spectral position of the SPP modes manifested as dips. The green triangles (right vertical axis) are the simulated average NFIE values calculated for a grating with $ff = 0.47$ at the position of the SPP modes and plotted as a scatter diagram. The SEM images of the trimer and pentamer are adapted with permission from [PI] © The Optical Society. The SEM image of the fabricated grating ($ff = 0.61$) is modified from [PIII] under the license CC BY 4.0.

targeted Stokes region overlaps with the rising tail of the Fano peak (at > 900 nm) in the scattering profile (blue and red curves) which confirms a strong intensity of the Stokes signal at the far-field. This way one can fully utilize the near- and far-field properties of FR for SERS [61, 63].

Another approach to attain subradiant modes with large NFIE is to excite SPP modes in plasmonic gratings. The SPP modes in such gratings manifest as reflectance dips at the resonant energies when excited by regular transverse-magnetic (TM) polarized light [74–78]. In [PIII], such SPP modes are used to enhance SERS. The gratings are designed by FDTD method (see Section 2.1.4) while fabricated using EBL followed by the lift-off (see Section 2.2.3) and etching (see Section 2.2.4) processes. The fabricated gratings are characterized by bright-field reflection spectroscopy (see Section 2.3.2). Figure 19(c) depicts the spectral reflectance (simulated and measured) of the grating with the SEM image of a fabricated grating on top. The blue markings on the SEM image show the geometrical parameters of the structure where a fill factor (ff) is defined as Λ/D with D as the grating period and Λ as the top groove width. The simulated (blue curve) and measured (red curve) reflection spectra of the grating ($ff = 0.47$) clearly depict the signature of three SPP modes as reflectance dips with their spectral positions marked by the green dashed vertical lines. The green triangles in the figure report the simulated NFIE values for the same grating ($ff = 0.47$) calculated at the position of the SPP modes and plotted as a scatter diagram. From the right vertical axis (green) in Figure 19(c) it is clear that the SPP modes at 450 nm and at 800 nm provide the highest and lowest NFIE, respectively, having the NFIE from the mode at 600 nm in between. Eventually, the *bluest* SPP mode at 450 nm is chosen for SERS and by varying the ff , it is spectrally tuned at the excitation wavelength (488 nm).

The SERS performance of the trimer, pentamer, and gratings are evaluated through Raman characterization (see Section 2.3.3). Even though both oligomers support FR, the pentamer provides higher depth in the Fano dip (blue vertical axis on left) and hence, higher NFIE (green vertical axis on right) at the excitation wavelength compared to the trimer as one can see by comparing the spectra in Figures 19(a)-(b). Consequently, in Figures 20(a)-(b), we see that the SERS intensities of adenine (Ade) and rhodamine 6G (R6G) at the targeted Raman lines are much higher with the presence of the pentamer (red curves) than the trimer (blue curves). Such finding clearly indicates that the higher the strength (depth and NFIE) of a subradiant mode (Fano dip) at the excitation wavelength, the stronger the SERS response.

For the gratings, 1321 cm^{-1} and 1345 cm^{-1} Raman lines of riboflavin [79] are targeted for an excitation at 488 nm. Four gratings are designed and fabricated with different ff (0.47, 0.50, 0.55, and 0.61) to incorporate different amounts of detunings between the *bluest* SPP mode (reflectance dip at 450 nm) and the excitation wavelength (488 nm). An increase in ff red shifts the *bluest* SPP mode [PIII]. Therefore, when the ff increases from 0.47 to 0.61, the spectral detuning between the *bluest* SPP mode and the excitation reduces. In other words, the higher the ff (within 0.47 – 0.61), the better the spectral match between the subradiant mode

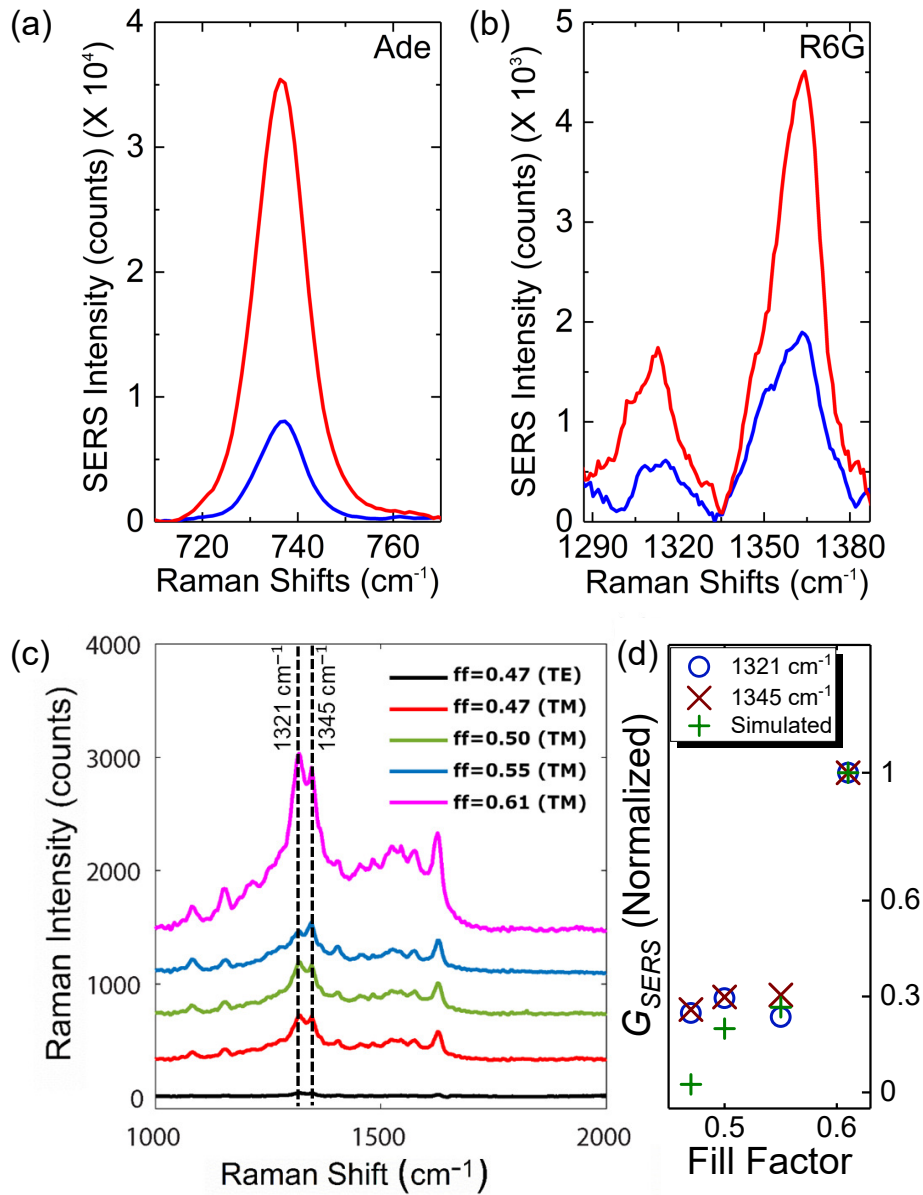


FIGURE 20 SERS intensity spectra of the Raman lines (a) 734 cm^{-1} of adenine (Ade) and (b) 1360 cm^{-1} of rhodamine 6G (R6G). In (a)-(b), the blue and red curves show the Raman spectra with the presence of the trimer and pentamer, respectively. Reprinted with permission from [PI] © The Optical Society. (c) SERS spectra of riboflavin on top of the fabricated gratings with an excitation at 488 nm . Reproduced from [PIII] under the license CC BY 4.0. (d) Scatter diagram of the simulated and experimental SERS enhancement factors (G_{SERS}) for 1321 cm^{-1} and 1345 cm^{-1} Raman lines as a function of fill factor (ff). The experimental G_{SERS} values are calculated from the data reported in (c). In (d), the G_{SERS} values are normalized (divided by maximum) for qualitative comparison.

(reflectance dip) and the Raman excitation. The SERS spectra of riboflavin on the fabricated gratings are reported in Figure 20(c) where the Raman signal intensity rises with an increase in ff .

The G_{SERS} values of the gratings are computed for the targeted Raman lines (1321-1345 cm^{-1} , 522 nm) using Eq. (60). The experimental G_{SERS} values for the targeted Raman lines are the *relative* SERS enhancement estimated by the ratio between the SERS intensities for TM (I_{TM}) and transverse-electric or TE (I_{TE}) polarizations, i.e., I_{TM}/I_{TE} . When excited by TE-polarized light, no SPP modes are present in the reflectance of the gratings and eventually, the Raman signal intensity is very weak as shown by the black curve in Figure 20(c). This is the non-resonant signal (I_{TE}). When the polarization is set to TM, SPP modes are profound in the reflectance of the gratings resulting in prominent SERS enhancement and hence, that is the resonant signal (I_{TM}). The ratio between the resonant (I_{TM}) and non-resonant (I_{TE}) signals gives a qualitative picture for G_{SERS} since the black curve (I_{TE}) in Figure 20(c) is identical for all ff and hence, can be used as a reference. The simulated and estimated G_{SERS} (normalized values) are reported in Figure 20(d), and they show almost identical qualitative trend as a function of ff . From Figures 20(c)-(d) one can infer that as ff increases from 0.47 to 0.61, the spectral match between the strongest subradiant mode (bluest reflectance dip) and the Raman excitation improves resulting in an increase of the Raman intensities and G_{SERS} values. Such outcome confirms that the better the spectral tuning between a subradiant mode (reflectance dip) and the Raman excitation, the stronger the SERS response. Therefore, in this case, the grating with $ff = 0.61$ (SEM image in Figure 19(c)) is optimal for SERS.

From the results in [PI] and [PIII], and from the Figures 19 and 20, we can conclude that an optimal plasmonic nanostructure for SERS should have a subradiant mode possessing a large NFIE at the Raman excitation.

3.4 Plasmonic nanostructures for SECARS

Developing plasmonic nanostructures for SECARS is challenging since CARS is a multi-excitation based spectroscopic method [61,80,81]. The SECARS substrate (nanostructure) needs to be engineered such a way that the supported plasmonic mode should have large NFIE at the pump (ν_p), Stokes (ν_s), and CARS (ν_{CARS}) frequencies as one can see from Eq. (61). Plasmonic oligomers possessing FR are suitable as SECARS substrates since one can tune the subradiant Fano dip with the pump frequency while overlapping the superradiant Fano peaks with the *fingerprint* region, i.e., the Stokes and CARS frequencies. Like in SERS, such strategy ensures a far-field CARS enhancement with an efficient near-field coupling between the pump energy and the organic molecules [61,81].

Ensuring large NFIE at the pump, Stokes, and CARS frequencies is not enough to attain a high value for G_{SECARS} . The spatial distribution of the NFIE *hot spots* over the oligomer geometry at those frequencies is also an important

factor to consider. These *hot spots* tightly confine the highly localized electromagnetic energy and for a large G_{SECARS} , they need to be at the exact same location at all intended frequencies. Usually, spatial distribution of *hot spots* over the oligomer geometry is random, i.e., *hot spot* locations change when the wavelength is changed [81]. Moreover, in disk-type NP based oligomers like in [PI], only a few *hot spots* can be achieved. Consequently, plasmonic substrates possessing a large number of *hot spots* with identical spatial localization at multiple frequencies are favorable for SECARS [81]. Such substrates are developed in [PII] based on the hexagonal shaped NPs as schematically shown in Figure 21.

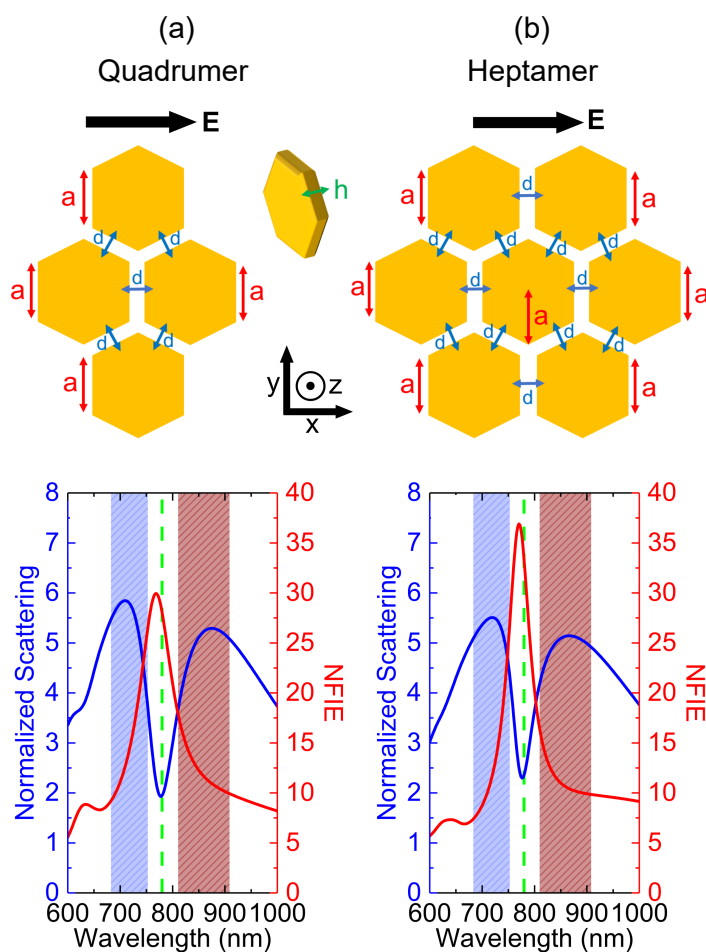


FIGURE 21 Optical responses of the (a) quadrumer and (b) heptamer with their schematics on top. The geometrical parameters for the quadrumer are $a = 80$ nm, $d = 15$ nm, and $h = 40$ nm while for the heptamer, $a = 62.5$ nm with identical values for d and h . The black arrows on top of the schematics present the polarization of the excitation light. In (a)-(b), the blue and red curves present the simulated scattering and NFIE spectra, respectively, where the blue (red) vertical axis corresponds to the blue (red) curve. The green dashed vertical line and the red (blue) shaded rectangular region depict the pump wavelength (780 nm) and the Stokes (CARS) window of the fingerprint region, respectively. Reproduced from [PII] under the license CC BY 4.0.

The proposed oligomers, a quadrumer and a heptamer, are modelled and optimized using FEM (see Section 2.1.5). Figure 21(a) shows the optical responses of the quadrumer with its schematics on top while Figure 21(b) reports the same for the heptamer. The geometrical parameters for the quadrumer are $a = 80$ nm, $d = 15$ nm, and $h = 40$ nm while for the heptamer, $a = 62.5$ nm with identical values for d and h . Both oligomers are excited by normal incidence of light with a polarization indicated by the black arrows on top of their schematics. The signature of FR is clear in their simulated scattering spectra (blue curves) and the corresponding NFIE profiles (red curves) have the maxima at the Fano dips. The designed oligomers are optimized for SECARS where the pump wavelength is 780 nm and the targeted *fingerprint* region is the favorable Raman signature zone of the organic molecules, i.e., $500 - 1800$ cm^{-1} [82]. Consequently, in both structures, the Fano dip is tuned at the pump wavelength (green dashed vertical lines) while the Fano peaks at the blue and red sides of the dip are tuned with the CARS (blue shaded areas, 683 – 753 nm) and the Stokes (red shaded areas, 810 – 908 nm) regimes, respectively.

The NPs present in the proposed quadrumer and heptamer are chosen as hexagons since the hexagonal geometry offers a higher area of nanogaps as potential *hot spots* than that in the disk-type geometry. To verify this, the hot spots in oligomers with hexagons and disks are compared by visualizing them through the spatial distribution of the NFIE. For 740 cm^{-1} Raman line of adenine [61], the NFIE maps are computed at CARS (738 nm), pump (780 nm), and Stokes (828 nm) wavelengths along with the resulting SECARS maps, i.e., spatial distribution of G_{SECARS} calculated using Eq. (61). Figures 22(a) and 22(b) show the results for the quadrumer and heptamer, respectively, where the *hot spot* positions are labelled as i, ii, . . . vi. From Figure 22 it is clear that hexagon based oligomers provide higher number of spatially localized *hot spots* and hence, are better SECARS substrates than their disk based analogs.

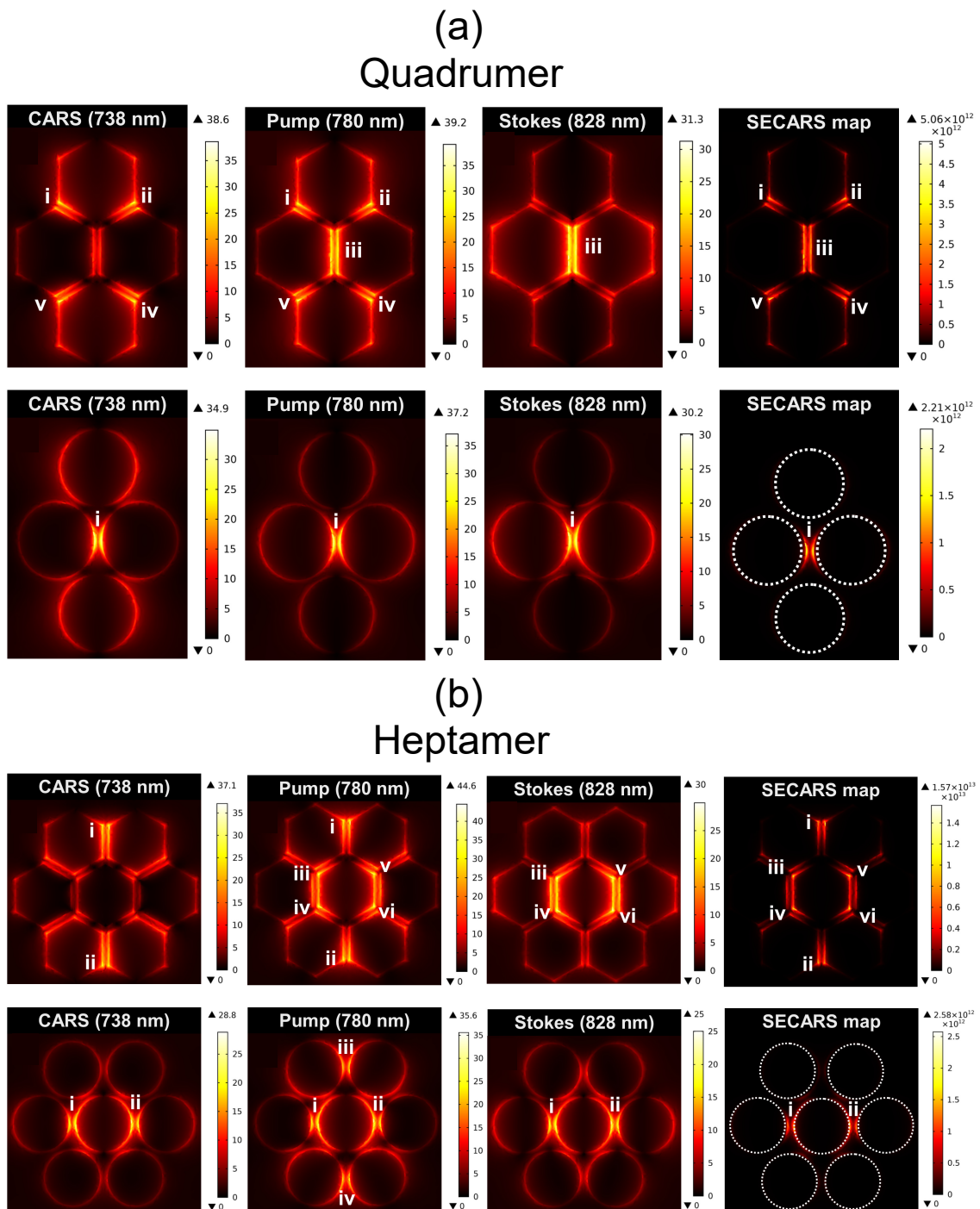


FIGURE 22 NFIE maps for the (a) quadramer and (b) heptamer computed at CARS (738 nm), pump (780 nm), and Stokes (828 nm) wavelengths along with the corresponding SECARS maps for 740 cm^{-1} Raman line of adenine. Reproduced from [PII] under the license CC BY 4.0.

Chapter summary

In summary, we can conclude from [PI, PII, PIII] that weak coupling between organic molecules and confined light can enhance the Raman responses of the molecules. Plasmonic nanostructures like Fano-resonant oligomers and gratings can provide such confined light where the plasmonic modes have subradiant and superradiant natures. For an optimal Raman enhancement, the subradiant mode should be tuned at the Raman excitation and it should have a large NFIE at that frequency. The superradiant modes with strong scattering nature should overlap with the Raman or CARS fingerprint regions of the molecules. Furthermore, the nanostructure geometry (e.g., NP shapes) should be optimized to attain a high number of spatially localized hotspots for efficient Raman enhancement.

4 WEAK AND STRONG COUPLING BETWEEN ORGANIC MOLECULES AND PHOTONIC NANOSTRUCTURES

Implementation of optical nanostructures may become too sophisticated if the fabrication demands advanced lithography processes. In this regard, planar multilayer photonic nanostructures such as metallic Fabry-Pérot (FP) cavities are extremely useful since such cavities doped with organic molecules are relatively easy to fabricate and study by spectroscopy [83,84]. Moreover, chemical properties of organic molecules are modified when they are strongly coupled to such FP cavities [8]. In line with that, this chapter summarizes how weak and strong coupling between planar metallic FP cavities and organic molecules can be utilized to influence molecular emission and photochemistry happening in an ultrafast (femtosecond) time scale.

4.1 Criteria for weak and strong light-matter coupling

To understand the criteria for weak and strong light-matter coupling, we first need to understand the basics of such interaction. Light-matter coupling can be figuratively described in a classical picture considering the *light* and *matter* as harmonic oscillators [3, 19]. Let us assume two harmonic oscillators having masses m_A and m_B with corresponding spring constants k_A and k_B as shown in Figure 23(a). The oscillators are coupled to each other through a spring constant k_C . In Newtonian mechanics, the system can be described using the laws of motion

$$m_A \ddot{x}_A + k_A x_A + k_C (x_A - x_B) = 0 \quad (62)$$

and

$$m_B \ddot{x}_B + k_B x_B - k_C (x_A - x_B) = 0 \quad (63)$$

with x_A and x_B as the corresponding displacements. The solution of Eqs. (62) and (63) yields

$$\omega_{\pm} = \frac{1}{2} \left[\omega_A + \omega_B \pm \sqrt{(\omega_A - \omega_B)^2 + 4\Omega^2} \right] \quad (64)$$

where ω_A and ω_B are the natural frequencies of the uncoupled oscillators, and Ω is the frequency splitting causing the generation of two new frequencies (ω_{\pm}) in the coupled system. For a resonant condition ($\omega_A = \omega_B = \omega$), i.e., at zero detuning ($\omega_A - \omega_B = 0$), the solution reduces to $\omega_{\pm} = \omega \pm \Omega$. These new frequencies (ω_{\pm}) show an avoided crossing by being separated with a frequency difference of 2Ω [3,19] as shown in Figure 23(a). The strength of the coupling directly depends on the magnitude of k_C . The higher the k_C , the higher the Ω , and the wider the avoided crossing [3,19].

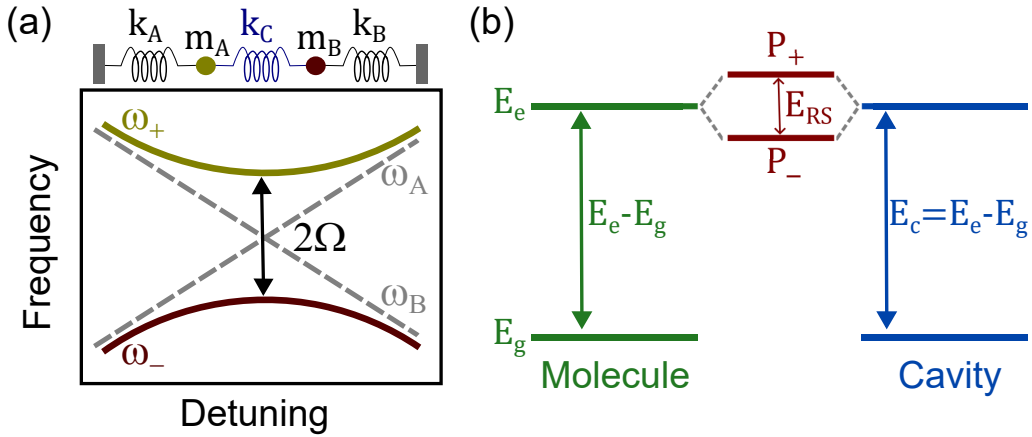


FIGURE 23 (a) Classical picture of light-matter interaction in terms of two harmonic oscillators. (b) Quantum mechanical picture of a coupling between an optical cavity and a molecule.

The above-mentioned formulation considers the oscillators as undamped. To incorporate damping, we need to insert the frictional terms $\gamma_A \dot{x}_A$ and $\gamma_B \dot{x}_B$ in Eqs. (62) and (63), respectively. In such formulation, when $\Omega < (\gamma_A/m_A + \gamma_B/m_B)$ the coupling is considered as *weak*, while in the case of *strong* coupling, $\Omega > (\gamma_A/m_A + \gamma_B/m_B)$. Other definitions also exist, but only the details of the definition vary. A wider view on this topic can be found in Reference [3]. In strong coupling regime, the coupling strength outperforms the energy dissipation or loss in the system and new eigenfrequencies (ω_{\pm}) are generated with an anticrossing (2Ω). In weak coupling, no such new frequency states are generated since the loss is larger than the coupling strength [3,19].

The classical picture of light-matter coupling fails to describe the *vacuum energy*, i.e., the ground state energy of a quantized field as deduced from Heisenberg's uncertainty principle. To address this, one has to consider the quantum picture of light-matter coupling where molecules can weakly or strongly couple with the *vacuum* field of an optical cavity *without any light*. Such *vacuum* field

(ε_{vac}) of a cavity can be described as

$$\varepsilon_{vac} = \sqrt{\frac{\hbar\omega_c}{2\varepsilon_0 V_m}} \quad (65)$$

where \hbar is the reduced Planck's constant, ω_c is the cavity mode frequency, ε_0 is the permittivity of vacuum, and V_m is the cavity mode volume [3,8,19] as described by Eq. (3) in Chapter 1.

In a quantum mechanical picture, the strength of a molecular transition between a ground (E_g) state and an electronic excited state (E_e) depends on the transition dipole moment (d) of the molecule. According to the Fermi's golden rule, the rate (Γ) of such transition can be defined as

$$\Gamma = \frac{2\pi}{\hbar} |\mathbf{d} \cdot \boldsymbol{\varepsilon}|^2 \rho(E) \quad (66)$$

where $\boldsymbol{\varepsilon}$ is the electric field vector and $\rho(E)$ is the density of states (DOS) at energy E . When the coupling between a molecule and a cavity is *weak*, the confinement of light inside the cavity can significantly improve $\rho(E)$ and $\boldsymbol{\varepsilon}$ at the molecular emission energy causing an enhancement of the molecular spontaneous emission rate (Γ). Such cavity induced emission enhancement is known as Purcell effect [19] and the associated enhancement factor (Purcell factor) is directly proportional to the field-confinement factor (see Section 1.1) of the cavity [23]. In other words, when a molecule is weakly coupled to a cavity, the molecular emission rate is influenced (e.g., enhanced) due to the presence of confined light (cavity field) while the molecular energy states remain intact.

The scenario is drastically different when the coupling between a molecule and a cavity is *strong*. In this case, if the cavity mode energy ($E_c = \hbar\omega_c$) matches with the molecular transition energy, i.e., $E_c = E_e - E_g$, new energy states (P_{\pm}) are generated due to the energy splitting also known as the vacuum Rabi splitting (E_{RS}), as shown in Figure 23(b). The new energy states (P_{\pm}) are hybrid light-matter states called the upper (P_+) and lower (P_-) polaritons. The energy difference between the upper polariton (UP) P_+ and the lower polariton (LP) P_- is the vacuum Rabi splitting (E_{RS}) formulated as

$$E_{RS} = 2\hbar\Omega_R = 2g \propto 2\sqrt{N} |\mathbf{d} \cdot \boldsymbol{\varepsilon}_{vac}| \quad (67)$$

where Ω_R is the Rabi frequency, g is the coupling strength, and N is the number of molecules coupled to the cavity mode. The coupling parameters E_{RS} and g quantify the intensity of the cavity-molecule interaction, i.e., how strongly they are coupled to each other. From Eqs. (65) and (67) it is apparent that E_{RS} and g are directly proportional to d , N , and $\varepsilon_{vac} \propto V_m^{-1/2}$. Therefore, when $N = 1$ (single molecule), a molecule with large d and a cavity with small V_m are favourable to attain strong coupling. Furthermore, for an ensemble of molecules (large N), it is desirable to have a large number of molecules residing inside the volume of the cavity mode, i.e., a large value of $\sqrt{N/V_m}$ [3,6,7,19].

The hybrid nature of the polariton states (P_{\pm}) can be understood from a quantum description of light-matter coupling based on the Jaynes–Cummings

(JC) model. In such model, the system is described by a JC Hamiltonian expressed as

$$\hat{H}_{JC} = \hat{H}_m + \hat{H}_c + \hat{H}_{int} \quad (68)$$

where \hat{H}_m , \hat{H}_c , and \hat{H}_{int} are the Hamiltonians for molecule, cavity, and cavity-molecule interaction, respectively, within the rotating wave approximation. The polariton states (P_{\pm}) are the eigenstates of \hat{H}_{JC} deducible via diagonalization and can be expressed as

$$|P^+\rangle = \alpha|e, 0\rangle + \beta|g, 1\rangle \quad (69)$$

and

$$|P^-\rangle = \beta|e, 0\rangle - \alpha|g, 1\rangle \quad (70)$$

where $|g\rangle$ and $|e\rangle$ render the ground and excited states of the molecule, respectively, with the absence ($|0\rangle$) and presence ($|1\rangle$) of a cavity photon. From Eqs. (69) and (70) it is clear that P_{\pm} states are linear combination of light and matter states, and hence, have a half-light-half-matter nature. The ratio between photonic and molecular components of a polariton state yields the Hopfield coefficients $|\alpha|^2$ and $|\beta|^2$ which are the probabilities of polariton to have photonic or molecular properties, respectively. For large N (ensemble of molecules), the JC model has to be extended to the Tavis–Cummings model to consider the collective coupling [6,7,19].

The spectroscopic signature of strong coupling can easily be observed by shining light on a cavity having the organic molecules embedded in it [7, 19]. Let us assume a cavity with a cavity mode at energy E_c as shown by the blue curve in Figure 24(a). If we dope such cavity with molecules having a strong absorption at energy E_m (green dashed vertical line) and ensure that these two entities are spectrally tuned, i.e., $E_c = E_m$, we would see two new polariton peaks (P_{\pm}) and a transparency at $E_c = E_m$ in the absorption of the doped cavity as shown by the red curve in Figure 24(a). This is an indication that the molecules are strongly coupled with the cavity mode [7,19]. However, to confirm this, one should measure the absorption of the doped cavity for different excitation angles, i.e., as a function of in-plane wavevector k_{\parallel} since like the cavity mode, the cavity polaritons (P_{\pm}) possess an in-plane dispersion [3,6,7,19]. Similarly, the Hopfield coefficients also depend on in-plane wavevector k_{\parallel} , i.e., $\alpha(k_{\parallel})$ and $\beta(k_{\parallel})$. The red curves in Figure 24(b) show such dispersion of P_{\pm} states where E_{RS} is defined as the minimum energy difference between them in k -space (k_{\parallel}). In the figure, the blue dashed curve depicts the dispersion of the cavity mode energy (E_c) as discussed in Section 1.1, while the green dashed horizontal line represents the dispersionless molecular absorption (E_m). In the dispersion of the uncoupled absorption, the undoped cavity (blue dashed curve) and the bare molecules (green dashed line) cross each other. However, when they are strongly coupled, the cavity polaritons (P_{\pm}) show an avoided crossing (E_{RS}) like we see in the classical picture in Figure 23(a).

Figure 24(a) shows the absorption of the doped cavity, undoped cavity, and bare molecules for one excitation angle (or k_{\parallel}) while Figure 24(b) depicts the

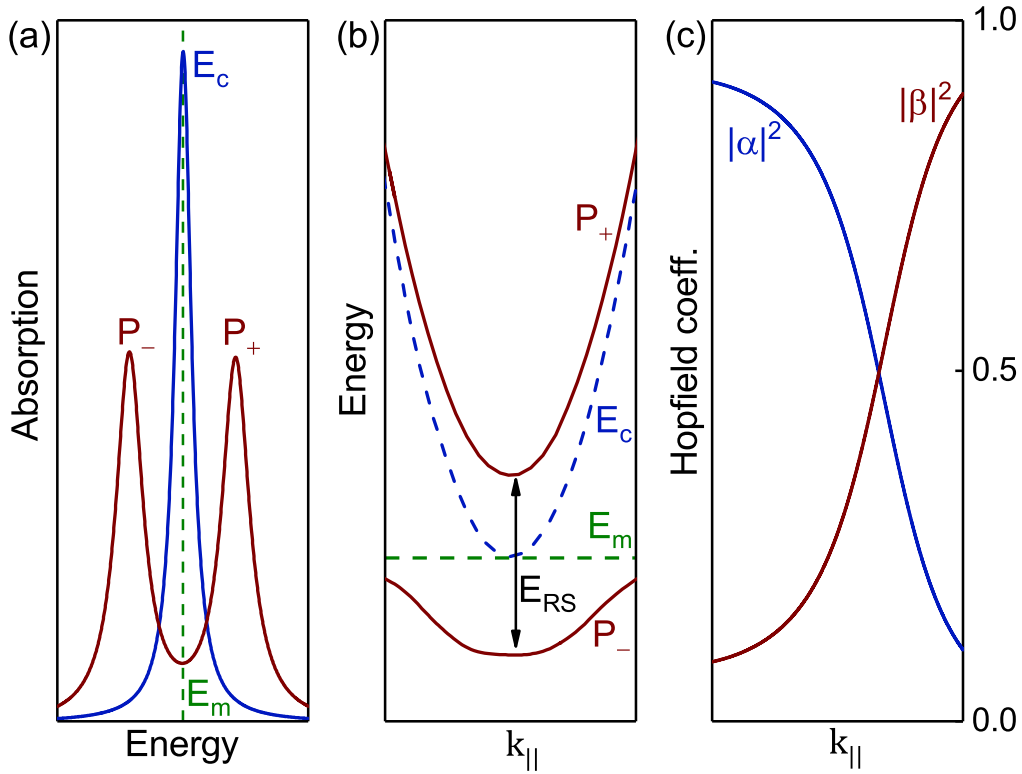


FIGURE 24 (a) Absorption spectra of the undoped cavity (blue curve) having a cavity mode at E_c and the doped cavity (red curve) possessing two polariton (P_{\pm}) states. The cavity is doped with molecules having a strong absorption at energy E_m (green dashed vertical line) and spectrally tuned with the molecular absorption ($E_c = E_m$). (b) Dispersion of P_{\pm} states (red curves), undoped cavity energy E_c (blue dashed curve), and molecular absorption E_m (green dashed horizontal line) as a function of in-plane wavevector (k_{\parallel}). The vacuum Rabi split (E_{RS}) is defined as the minimum energy difference between the polaritons (P_{\pm}) in k_{\parallel} -space. (c) Hopfield coefficients $|\alpha|^2$ and $|\beta|^2$ (ranges from 0 to 1) for P_- as a function of k_{\parallel} .

same for all incident angles (k_{\parallel} space). From these information one can evaluate whether the cavity and the embedded molecules are strongly coupled or not using the condition for strong coupling [3,7,19]. A cavity-molecular system can be considered as *strongly coupled* if the coupling strength $g > (\kappa, \gamma)$ where κ and γ are the FWHM of the cavity mode and the molecular absorption, respectively. When $g < (\kappa, \gamma)$, the system can be considered as *weakly coupled*. The system enters into the strong coupling regime for $g > (\gamma + \kappa)/4$, and in that regime, g outperforms the system losses in time scale. In other words, a coherent interaction happens between the cavity photon and the molecules through the virtual emission and reabsorption cycles (Rabi oscillations) till the cavity photon decays. During this phase, energy is delocalized in the system [3,7,19].

The probabilities of polariton to express molecular and photonic properties [85], i.e., the Hopfield coefficients ($|\alpha|^2$ and $|\beta|^2$) [86] can be calculated from the

dispersion of the cavity polaritons P_{\pm} shown in Figure 24(b) using a coupled harmonic oscillators model (CHOM) [19]. In such model, the coupled molecules are treated as a single strong oscillator or absorber and the coupling between this molecular absorption (exciton) and the cavity mode (photon) is expressed by a Hamiltonian similar to the JC-model. This can be expressed in the form of a 2×2 matrix as

$$\begin{bmatrix} E_c(k_{\parallel}) & \frac{\hbar\Omega_R}{2} \\ \frac{\hbar\Omega_R}{2} & E_m(k_{\parallel}) \end{bmatrix} \begin{bmatrix} \alpha \\ \beta \end{bmatrix} = E \begin{bmatrix} \alpha \\ \beta \end{bmatrix} \quad (71)$$

where $E_c(k_{\parallel})$ and $E_m(k_{\parallel})$ are the dispersions of the undoped cavity and the molecular absorption (blue and green dashed lines in Figure 24(b), respectively) while $\hbar\Omega_R$ is the half of the Rabi split E_{RS} . The deducible eigenvectors of the Hamiltonian are the same as in Eqs. (69) and (70) [19], with the Hopfield coefficients ($|\alpha|^2$ and $|\beta|^2$). Figure 24(c) shows their dependency on k_{\parallel} for the LP (P_-). These coefficients are actually probabilities (ranging from 0 to 1) stating the photonic ($|\alpha|^2$) and molecular ($|\beta|^2$) contribution in a polariton, i.e., how much is *light* ($|\alpha|^2$) and how much is *matter* ($|\beta|^2$) in a hybrid light-matter state [19,85]. For example, from Figure 24(c) we can infer that the nature of the LP (P_-) is more photonic (light) for small values of k_{\parallel} ($|\alpha|^2 > |\beta|^2$) while it is more molecular (matter) when k_{\parallel} is large ($|\alpha|^2 < |\beta|^2$). For a certain value of k_{\parallel} , the red and blue curves in Figure 24(c) intersect ($|\alpha|^2 = |\beta|^2$) implying P_- is *half-light-half-matter* at that k_{\parallel} .

4.2 Role of optical cavity

Optimizing the optical properties of a cavity is essential to attain efficient light-matter coupling. As discussed in the previous section, a cavity with high Q and small V_m is optimal to facilitate effective coupling since in the weak coupling regime, the Purcell factor scales as $F_P \propto Q/V_m$ [23], while in the strong coupling regime, the coupling strength scales as $g \propto V_m^{-1/2}$ [3]. In [PIV], the optical properties of a planar metallic FP cavity are optimized for fluorescence spectroscopy of sulforhodamine 101 (SR101) dye in the weak coupling regime.

In planar metallic FP cavities, the organic molecules are usually embedded in a polymer matrix sandwiched between the two metallic mirrors [83, 84] as schematically shown in Figure 25 inset. The embedded molecules are excited and the corresponding Stokes-shifted off-resonant emission is detected through one of the mirror by making it leaky (semi-transparent). Increasing the cavity mirror thicknesses (L_1 and L_2) is one way to achieve high Q , small V_m (since the modes *leak* outside the mirrors in the case of *leaky* mirrors), and hence, a large F_P . However, such approach is unfavourable in fluorescence spectroscopy since exciting molecules and detecting their emission through the thick mirrors are challenging. Therefore, one needs to consider an optimal trade-off between the Purcell factor (F_P) and the fluorescence measurability (I_{FL}), i.e., the fluorescence intensity measurable outside of the cavity. Such fluorescence measurability (I_{FL}) can

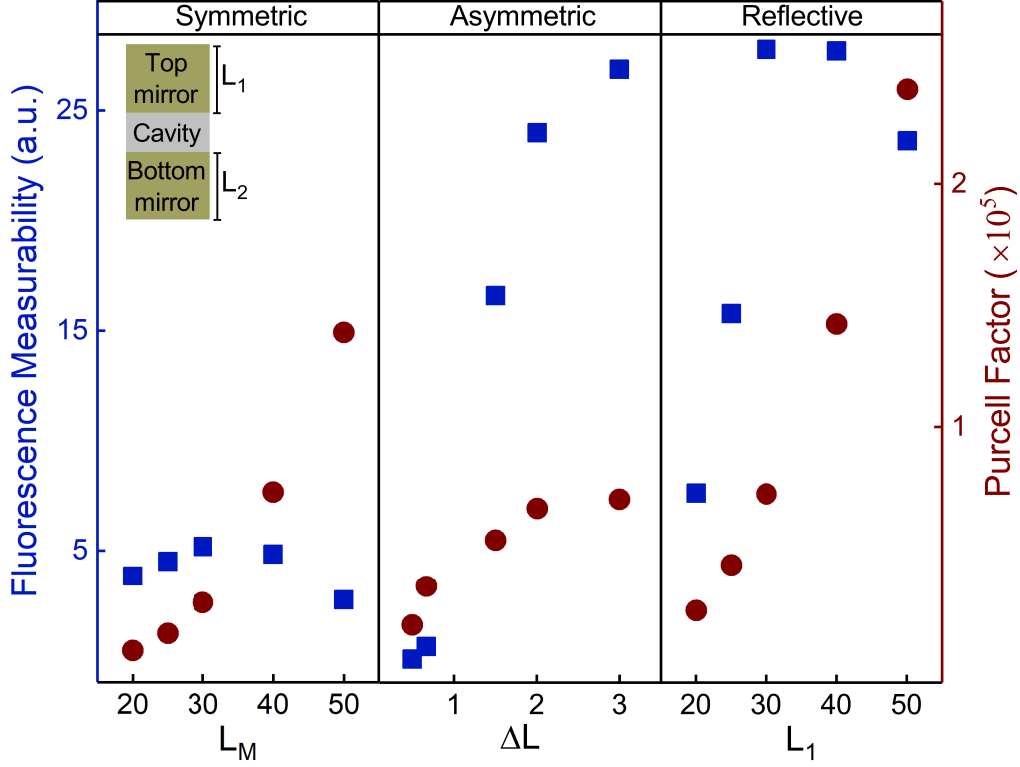


FIGURE 25 Plot of fluorescence measurability and Purcell factor for FP cavities having symmetric, asymmetric, and reflective geometries with the cavity schematic on the top left corner. The top and bottom mirror thicknesses are L_1 and L_2 , respectively, while $L_M = L_1 = L_2$ and $\Delta L = L_2/L_1$. The blue and red vertical axes correspond to the discrete data points blue squares and red circles, respectively.

be formulated as

$$I_{FL} = F_P T_{avg} \Phi_E \Phi_A \quad (72)$$

where T_{avg} is the average transmissivity of the leaky mirror through which the emission is collected, Φ_E is the spectral overlap between the molecular emission $PL(\lambda)$ and the cavity absorption $A_c(\lambda)$, i.e., $\Phi_E = \int A_c(\lambda) \cap PL(\lambda) d\lambda$, and Φ_A is the spectral overlap between the molecular absorption $A_m(\lambda)$ and $A_c(\lambda)$, i.e., $\Phi_A = \int A_c(\lambda) \cap A_m(\lambda) d\lambda$. Considering the fact that F_P and I_{FL} can not be optimal simultaneously for a certain cavity, it is crucial to attain an optimal trade-off between them. In [PIV], such trade-off has been achieved by optimizing the cavity geometry in terms of cavity mirror thicknesses, while the optical properties of the cavities are calculated by TMM (see Section 2.1.1) and FDTD method (see Section 2.1.4).

Figure 25 shows a plot of fluorescence measurability (I_{FL}) and Purcell factor (F_P) as a function of cavity geometry. A FP cavity is *symmetric* when the top and bottom mirrors have equal thicknesses, i.e., $L_1 = L_2 = L_M$. In that case, as we see in the figure, an increase in L_M results in a rise in F_P with a drop in I_{FL} . Hence, a symmetric cavity geometry fails to attain a good balance between F_P and I_{FL} . By making a thick top mirror and a thin bottom mirror or vice versa, one can design an *asymmetric* cavity. In such a case, the geometry can be quantified by

a parameter $\Delta L = L_2/L_1$ where $\Delta L > 1$ implies a thin top and a thick bottom mirrors, while $\Delta L < 1$ means the opposite. From Figure 25 it is clear that an increase in ΔL beyond 1 incurs a simultaneous rise in F_P and I_{FL} . Such outcome indicates that a cavity geometry having a thin (leaky) top mirror for fluorescence collection and a thick bottom mirror can assure a reasonable trade-off between F_P and I_{FL} .

Inspired by the aforementioned finding, one can consider a *reflective* cavity geometry having a leaky top mirror (L_1) for emission collection and a non-transparent thick bottom mirror (e.g. $L_2 = 200$ nm). Such cavity has zero transmission and hence, is fully *reflective*. As we see in Figure 25, an increase in L_1 for such cavity improves F_P and I_{FL} simultaneously. Moreover, among the three geometries, only a reflective geometry ($L_1 = 50$ nm) yields the largest F_P while maintaining a reasonably high I_{FL} . Therefore, from [PIV] we can conclude that reflective FP cavities are optimal for fluorescence spectroscopy in the weak coupling regime since such cavities can ensure high Purcell enhancement of molecular emission inside the cavity along with a reasonably efficient collection of the enhanced emission.

4.3 Polariton chemistry

Weak coupling between organic molecules and optical cavities, as discussed in the previous sections, can merely influence the molecular responses (e.g., enhancing the spontaneous emission rate), but is unable to create new energy states in the coupled system. Eventually, the molecules experience the cavity field as a small perturbation only (e.g., a surge in local DOS), while the individuality of the *light* (cavity field) and the *matter* (molecules) remains intact [3, 6, 7, 19]. Essentially, to affect the energy landscape of the molecules [8] and thereby, modifying their material properties [10, 87], the cavity-molecular coupling needs to be *strong* enough, i.e., $g > (\gamma + \kappa)/4$ [19].

Formation of hybrid light-matter states or polaritons in strong coupling regime can modify the photochemical properties of organic molecules by influencing the reaction rate [8, 9, 88, 89], by enabling the energy transfer [90–92], by affecting the kinetics [87], and/or by changing the optoelectronic properties [93–95] to name a few. Consequently, a new branch has emerged called as *polariton chemistry* to grow more insights on the effects of polaritons and how to exploit them to alter material properties [2, 6, 96]. In this regard, polariton chemistry is crucial to achieve a leap in modern organic photovoltaics by influencing, modifying, and controlling the photochemical properties of organic molecules via strong coupling.

4.4 Photochemistry in strong coupling regime

In a strongly coupled cavity-molecular system, polaritons supplant the electronic excited state of the molecules coupled to the cavity mode (see Figure 23(b)). Such event can incur modifications in the molecular potential energy surfaces leading to a change in the photochemical reactivity of the molecules [89]. However, to optimally affect the reaction, the polariton lifetime needs to be comparable with the reaction timescale, i.e., the evolution time of the reactants. In practice, polariton lifetime is limited by the cavity photon lifetime [97, 98]. Therefore, to study the influence of strong coupling on a photochemical reaction, one should choose a cavity-molecular system where the reaction timescale and the cavity photon lifetime are comparable, i.e., in the same orders of magnitude. In [PVI], such study has been performed to investigate the effect of strong coupling on ultrafast photochemistry.

To study photochemistry, 10-hydroxybenzo[h]quinoline (HBQ) molecule is selected since it possesses an ultrafast photochemical reaction, excited-state intramolecular proton transfer (ESIPT), with a reaction timescale of ~ 15 fs [99, 100]. In order to facilitate strong coupling with a comparable cavity photon lifetime, a planar metallic FP cavity is chosen with a reflective geometry as optimized in [PIV]. Figure 26(a) shows a schematic of the cavity-molecular system where HBQ molecules are embedded in a polymethyl methacrylate (PMMA) matrix (thickness ~ 100 nm) sandwiched between a leaky (20 nm) and a non-transparent (120 nm) aluminium (Al) mirrors on a glass substrate. Figure 26(b) depicts the absorption (violet curve) and emission (red curve) spectra of HBQ along with its chemical structures in *enol* (violet) and *keto* (red) forms.

The ESIPT in HBQ can be elucidated from Figure 26(c) which illustrates how the potential energy profiles of the electronic ground state S_0 (black curve) and the first singlet electronic excited state S_1 (violet curve) of HBQ evolve over the reaction coordinate, i.e., the difference between oxygen-hydrogen (d_{O-H}) and nitrogen-hydrogen (d_{N-H}) distances ($d_{O-H} - d_{N-H}$) [PVI]. When S_1 state of HBQ in *enol* form is excited by ultraviolet ($\lambda_{ex} = 375$ nm) light, it undergoes the ESIPT process, i.e., transfers the hydrogen from the phenol oxygen to the nitrogen, and reaches to its *keto* form within ~ 15 fs. After that, HBQ decays back to its S_0 state by emitting red ($\lambda_{em} = 620$ nm) light and after that returns to its *enol* form.

The ESIPT process in bare HBQ molecules is barrierless as one can see in Figure 26(c). However, if we embed such molecules in a cavity having a cavity mode spectrally tuned with the $S_0 \rightarrow S_1$ transition of HBQ at 375 nm, then the LP would replace the S_1 state of the molecule when the cavity-molecule coupling is strong. In such a case, the potential energy profile of the LP shows a barrier which increases with an increase in Rabi split resulted due to a rise in the number of molecules (N) inside the cavity mode volume. As depicted in Figure 26(c), the higher the N ($256 \rightarrow 512 \rightarrow 1024$), the higher the Rabi split (250 meV $\rightarrow 356$ meV $\rightarrow 502$ meV), and the higher the barrier in LP (red \rightarrow green \rightarrow blue), which reaches to 157 meV for the highest Rabi split (502 meV). Such a high barrier can

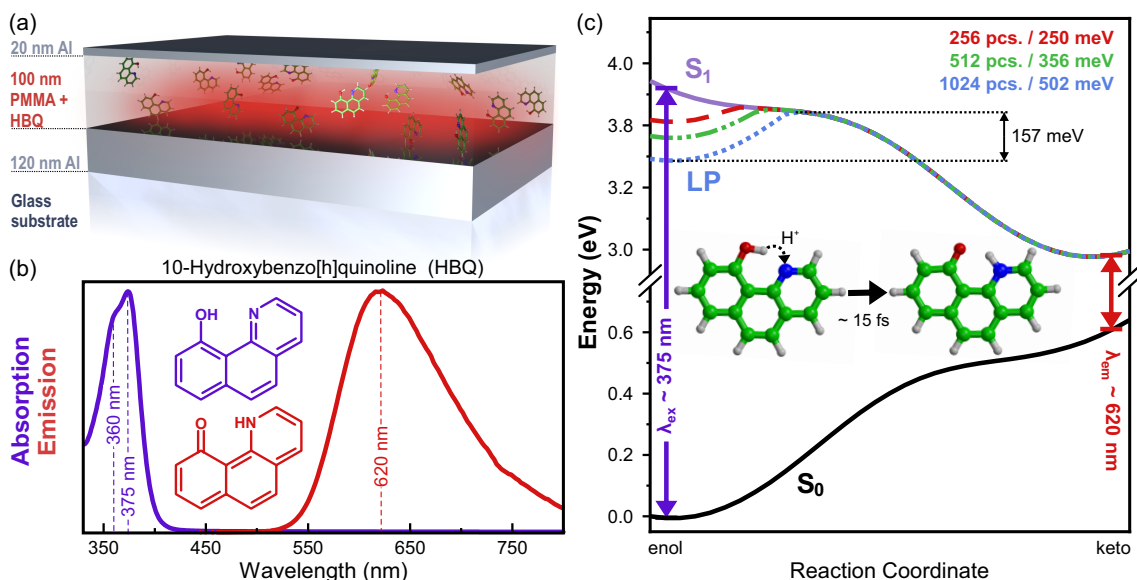


FIGURE 26 (a) Schematic diagram of the HBQ doped cavity. (b) HBQ absorption and emission in PMMA. (c) Potential energy surfaces for the molecular ground state S_0 (in black) and excited state S_1 (in purple). The red dashed, green dashed, and blue dotted lines show the lower polariton (LP) for 256, 512, and 1024 HBQ molecules (pcs.), respectively, originated due to a strong cavity-molecular coupling, and resulting in Rabi split of 250, 356 and 502 meV. The cavity mode is spectrally tuned with the $S_0 \rightarrow S_1$ transition. In the upper right, the corresponding Rabi splits are reported. The potential barrier for ESIPT present in LP is shown by the double-arrow for the Rabi split of 502 meV. Reproduced from [PVI] under the license CC BY 4.0.

hinder the ESIPT process resulting in a low emission yield at 620 nm in steady-state.

To verify the theoretical findings mentioned above, three HBQ-doped cavities were fabricated with increasing HBQ/PMMA ratios (doping concentration C) as 0.5 (low C), 1.0 (mid C), and 1.6 (high C). The HBQ-doped PMMA layers are prepared by spin-coating (see Section 2.2.2) while the mirrors are deposited via thermal evaporation (see Section 2.2.1). The cavity thicknesses are tuned via profilometry (see Section 2.3.1) to attain a spectral match between the first-order cavity mode and the HBQ absorption (375 nm). For each concentration, an identical HBQ:PMMA film is prepared without the top Al mirror as a *reference* sample. The fabricated films and cavities are optically characterized by angle-resolved reflection and fluorescence spectroscopy (see Section 2.3.2).

The angle-resolved absorption of the doped cavities, reported in Figure 27 as contour map, shows profound signature of strong coupling with extracted coupling strengths (g) of 140 meV, 170 meV, and 190 meV for low, mid, and high C cavities, respectively. In the figure, the left axes show the bare HBQ/PMMA film (reference samples) absorption spectra, while the CHOM fitted polariton branches (upper, middle, and lower) are depicted by the white dashed curves. The black crosses represent the spectral positions of the polaritons measured and used in CHOM fitting. The undoped cavity dispersion is shown by the black dot-

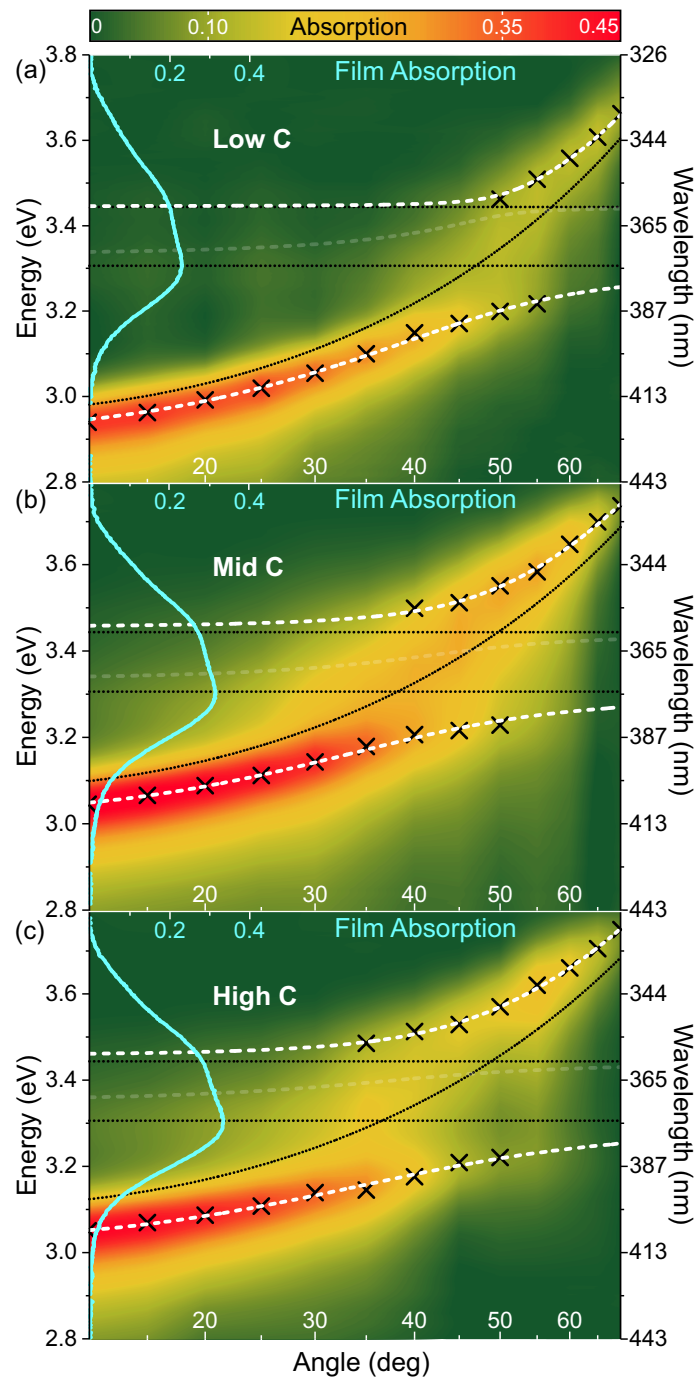


FIGURE 27 Dispersion in the absorption of the HBQ doped cavities plotted as a contour map for (a) low, (b) mid, and (c) high doping concentrations (C). The left axes show the corresponding bare HBQ/PMMA film (reference samples) absorption spectra, while the CHOM fitted polariton branches (upper, middle, and lower) are depicted by the white dashed curves. The black crosses represent the spectral positions of the polaritons measured and used in CHOM fitting. The undoped cavity dispersion is shown by the black dotted curves, while the HBQ absorption peaks (360 nm and 375 nm) are depicted by the horizontal black dotted lines. Reproduced from [PVI] under the license CC BY 4.0.

ted curves, while the HBQ absorption peaks (360 nm and 375 nm) are depicted by the horizontal black dotted lines. The minimum energy difference between the UP and LP, i.e., the *resonance* angle, is obtained around 40° to 50° for the doped cavities. From the figure it is apparent that due to an increase in molecular concentration (C) and absorption, g increases, as also reported in the earlier findings [3,7,19].

Figure 27 confirms that the HBQ molecules are strongly coupled to the first order cavity mode for all concentrations (C), and the higher the C, the larger the g . As previously discussed and shown in Figure 26(c), strong coupling induces a barrier in the LP energy surface hindering the ESIPT process and thus resulting in a lower ESIPT emission. To verify this, the steady-state emission intensity at 620 nm is measured for the doped cavities (and reference films) at different excitation angles as a function of excitation wavelength sweeping the molecular absorption band (350-400 nm). The cavities and films are excited by a tunable pulsed laser with ~ 5 ns pulses at a 100 Hz repetition rate and the ESIPT emission (620 nm) is collected at the sample surface normal. Such measurements construct the excitation spectra as reported in Figures 28(c) and 28(d) for the mid and high C cavities, respectively.

In the uncoupled system, i.e., in reference HBQ films, the absorption (curves on the left axis in Figure 27) and excitation (grey curves in Figures 28(c)-(d)) spectra are very similar. However, in the strongly coupled system, i.e., in HBQ doped cavities, the absorption and excitation profiles differ drastically as one can see by comparing Figures 28(a) and 28(c) for the mid C cavity, and Figures 28(b) and 28(d) for the high C cavity. By hypothesizing that all the excitations from excited polariton states end up into HBQ molecules undergoing ESIPT according to the earlier predicted behavior [98,101], the ESIPT reaction yield inside a cavity should depend on the *probability to absorb a photon* determined by the cavity absorption and the *probability to undergo ESIPT* determined by the density of molecular states, i.e., the excitation spectrum of the bare molecules [PVI]. To verify this, the film excitation and the cavity absorption are multiplied, which yields profiles very similar to the cavity excitation as one can see in Figures 28(e) and 28(f). Similarly, dividing the cavity excitation by the film excitation yields the polaritonic absorption profiles as shown in Figures 28(g) and 28(h). Such outcomes confirm that the reaction efficiency is mainly governed by the excitation transfer from the bright polaritonic states (polaritonic absorption) into the molecular dark states (molecular absorption). In other words, when the coupling is strong, the bright cavity polaritons become a pathway of accessing the reactive bare molecular dark states. How efficient this pathway is depends on how much the polaritonic absorption and the molecular density of states (molecular absorption or excitation) overlap [98].

As a collaborator, Prof. Groenhof's group performed quantum mechanics molecular mechanics (QM/MM) simulations to model the system. The results of these simulations are presented in Figure 29 and strongly support the above-mentioned findings. The QM/MM simulations show that no matter which polariton state is excited, a single HBQ molecule soon obtains all the excitation en-

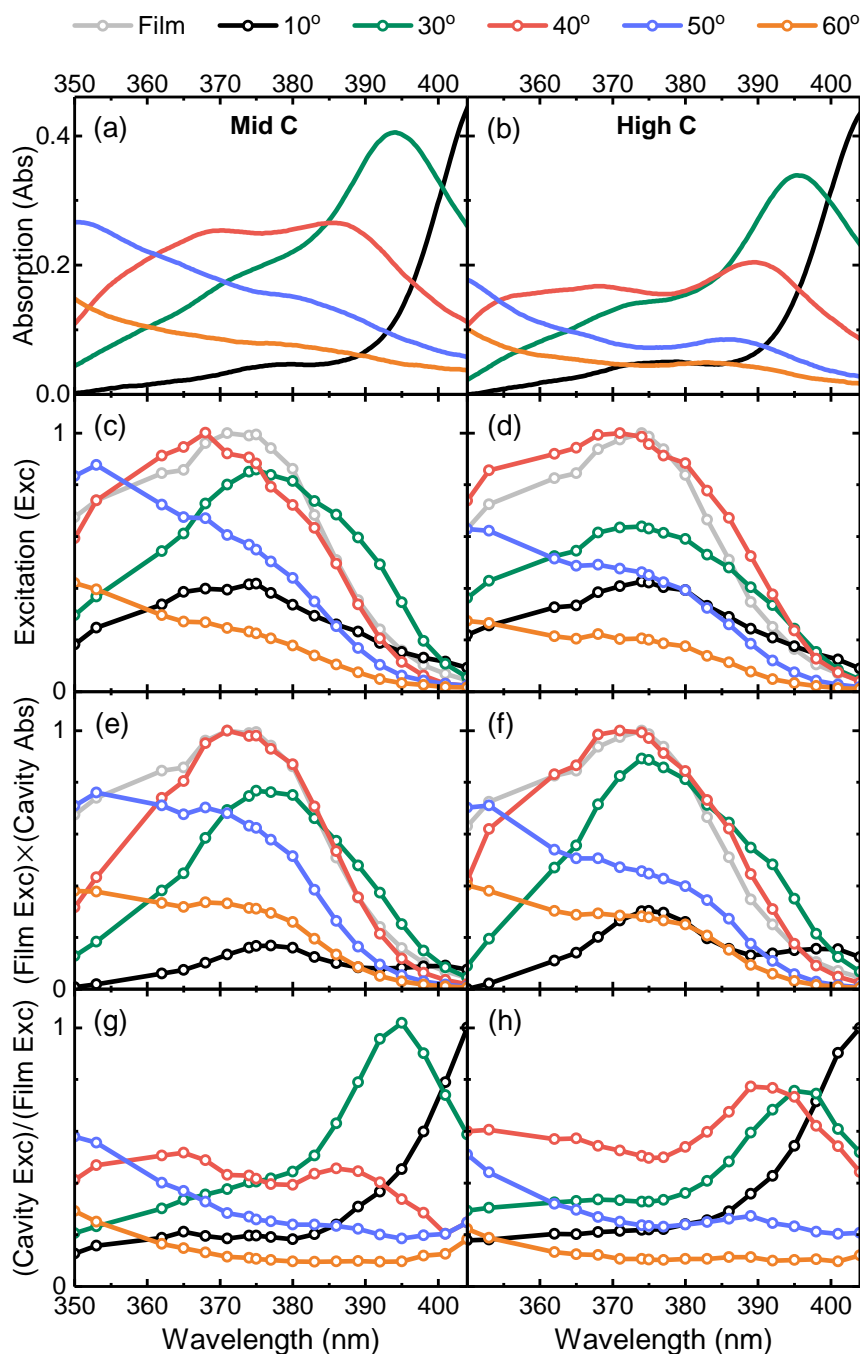


FIGURE 28 Absorption of HBQ doped cavities for different excitation angles when the doping concentration (C) is (a) mid and (b) high. Excitation profiles of HBQ doped cavities for different excitation angles when the doping C is (c) mid and (d) high. The excitation spectra are constructed for 620 nm emission of HBQ. The light grey curves show the film excitation profiles (scaled down for comparison). The results of the spectral multiplication between the cavity absorption and the film excitation are reported for (e) mid C and (f) high C cavities. The results of the spectral division between the cavity excitation and the film excitation are reported for (g) mid C and (h) high C cavities. Reproduced from [PVI] under the license CC BY 4.0.

ergy and undergoes ESIPT as depicted in Figure 29(d). This is due to the unavoidable (thermal) disorder of the coupled molecules, which dilute the photonic contribution among almost all the possible states as shown in Figure 29(b). This also allows the direct transition from any polariton state into a dark localized molecular state which then undergoes ESIPT [PVI].

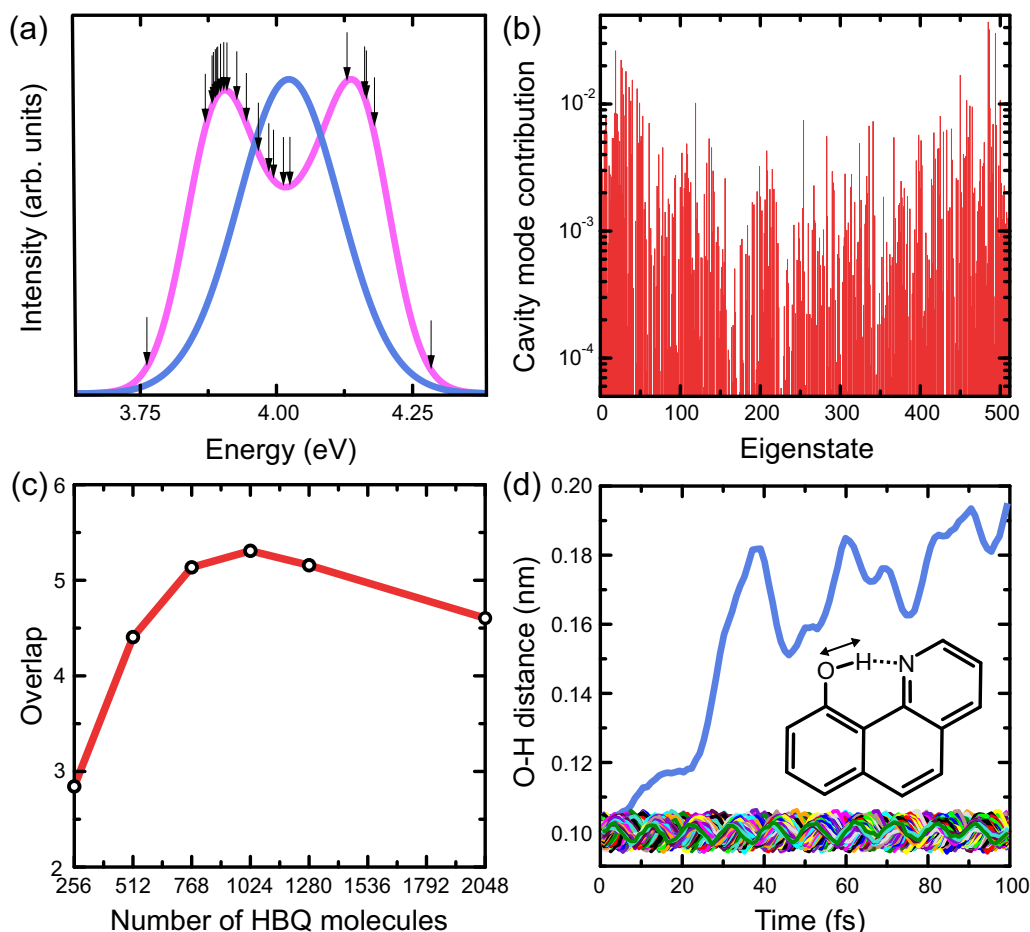


FIGURE 29 (a) QM/MM simulated HBQ absorption with (magenta) and without (blue) the presence of a resonant cavity mode with $\epsilon_{vac} = 0.77 \text{ MVcm}^{-1}$ where the number of HBQ molecules $N = 512$. The eigenstates used as starting points of the simulations are shown by the arrows. (b) The photonic contribution ($|\alpha|^2$) in the eigenstates of the strongly coupled cavity-molecular system for all the 513 eigenstates. (c) Plot of how much the polaritonic absorption and the molecular density of states overlap for a varying number of strongly-coupled molecules. (d) The plot of how the oxygen-proton distance evolved temporally in HBQ molecules ($N = 512$, all colors) when a bright polariton is excited where $\sim 0.10 \text{ nm}$ distance means that the proton is bound with the oxygen, while $\sim 0.19 \text{ nm}$ distance means that the proton is bound with the nitrogen. Reproduced from [PVI] under the license CC BY 4.0.

The aforementioned findings suggest that cavity polaritons provide an efficient pathway to excite molecular states while still inducing a barrier in LP energy surface. To see how these affect the ESIPT reaction, the yield (η) of the ESIPT emission is evaluated for the doped cavities and reference films. Such yield (η)

can be quantified as

$$\eta = I(\lambda_{em}) / A(\theta_{ex}, \lambda_{ex}) \quad (73)$$

where $I(\lambda_{em})$ is the intensity at the emission maximum ($\lambda_{em} = 620$ nm) and $A(\theta_{ex}, \lambda_{ex})$ is the absorption at the excitation wavelength (λ_{ex}) and angle (θ_{ex}). To obtain similar and comparable η , the cavities are excited at their LP wavelength (low C: 385 nm, mid C: 386 nm, and high C: 390 nm) at their resonance angle (low C: 50°, mid C: 40°, and high C: 40°), while the reference HBQ/PMMA films are always excited at their absorption maximum (375 nm). Figure 30 depicts the emission yield (η) of the doped cavities and reference films as a function of HBQ concentration, i.e., HBQ/PMMA doping ratio.

Since strong coupling creates a potential barrier in the LP energy surface as a hindrance for the ESIPT process to occur and as such barrier increases with a rise in $g \propto \sqrt{N}$ (see Figure 26(c)), one would expect a drop in η for a doped cavity when the doping concentration is high. However, as shown in Figure 30, η increases for the cavity with a rise in HBQ concentration and hence, with an increase in g . The reason for this cannot be the HBQ film concentration since for the reference films, η is almost constant except at higher concentrations where it drops because of quenching [102].

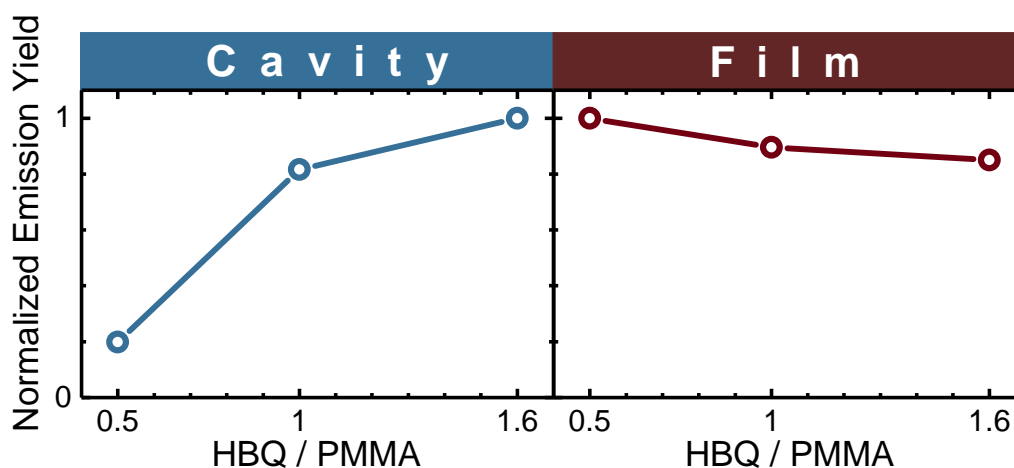


FIGURE 30 Yield (η) of the ESIPT emission in HBQ doped cavities and reference films when the doping concentration is varied. Reproduced from [PVI] under the license CC BY 4.0.

The theoretical prediction on how strong coupling can affect an ultrafast photochemical reaction, as shown in Figure 26(c), strikingly differs from the experimental findings reported in Figure 30. Such a discrepancy can be understood considering the role of reactive molecular dark states in a strongly coupled cavity-molecular system. As previously discussed and depicted in Figure 28, the ESIPT reaction yield inside a cavity depends on the probabilities of photon absorption and the DOS of reactive molecular dark states. Hence, the reaction efficiency directly depends on how much the bright polaritons and the molecular dark states spectrally overlap. Increasing HBQ concentration and thereby g , increases also the density of dark states and eventually enhances such overlap at the resonance

angle resulting in a surge in η for the doped cavities. As the coupling becomes stronger due to a rise in concentration, it decreases and even surpasses the predicted suppression (due to the barrier). That is because the rate of the population transfer from the polaritons to the dark states is accelerated [PVI, 98]. Nevertheless, the findings in [PVI] show that strong coupling can influence the photochemistry in organic molecules, e.g., by affecting the reaction yield of the ESIPT process in this case. However, the findings in [PVI] also reveal that the original hypothesis of polariton chemistry for chemical reaction happening along the polariton's modified potential energy surface, is hard or in many cases even impossible, to achieve. The observed effects are mainly due to efficient energy transfer into the dark states [89], which here produced exactly opposite effect than the original hypothesis would suggest.

Chapter summary

In summary, we can conclude from [PIV, PVI] that planar metallic FP cavities doped with organic molecules can facilitate efficient cavity-molecule coupling and hence, can be utilized to engineer the photochemical properties of molecules. When such cavity-molecule coupling is weak, *confined light* provided by the cavity enhances the spontaneous emission rate of the molecules (Purcell effect). In this regard, a reflective cavity geometry is optimal for achieving such Purcell enhancement and for collecting the enhanced emission. When similar cavity geometry is employed to attain strong cavity-molecule coupling for a molecule possessing a photochemical reaction with a reaction timescale comparable to the cavity photon lifetime, the emission yield of the reaction enhances due to the cavity polaritons efficiently transferring the energy to the reactive molecular states. This modifies significantly the excitation spectrum of the molecules, but does not modify the reaction itself via modified potential energy surfaces as predicted. This means that the bright polaritons provide an efficient pathway of accessing the molecular dark states depending on how much the polaritons and the molecular states spectrally overlap.

5 WEAK AND STRONG COUPLING BETWEEN ORGANIC MOLECULES AND EXCITONIC NANOSTRUCTURES

Optical nanostructures can be purely organic and excitonic (Frenkel excitons), i.e., made of organic dye doped polymers. Such excitonic nanostructures possess surface excitonic modes similar to the plasmonic modes when the doping concentration is very high. Excitonic materials are considered as a potential alternative for plasmonics since they can provide confinement of light in the visible range while exhibiting low material losses compared to the metals [28,29]. This chapter briefly explains the modeling of excitonic materials and the origin of surface excitons followed by a summary of weak and strong coupling properties of surface excitons.

5.1 Modeling of excitonic materials

To develop novel excitonic nanostructures one first needs to model the absorption of the excitonic materials [103]. Such modeling requires knowledge on the complex-dispersive dielectric function of the materials [104–106]. In [PV], a simple and straightforward spectral fitting is proposed for estimation of such optical constants.

In dye-doped polymer based excitonic materials, the local excitonic absorption bands ideally show a Lorentzian profile and hence, Lorentz oscillator model (LOM) is generally used to model the associated optical constants [29, 105]. In such framework, the complex-dispersive permittivity (ϵ) takes the form as a function of energy (E) as

$$\epsilon(E) = \epsilon_{\infty} + \frac{fE_0^2}{E_0^2 - E^2 - i\gamma E} \quad (74)$$

for an excitonic absorption band (peak energy: E_0 , oscillator strength: f , spectral linewidth: γ) when the dielectric constant of the host polymer is ϵ_{∞} [29]. In

practice, however, when the doping concentration is very high which is the case for excitonic nanostructures, the absorption profile broadens inhomogeneously (unlike a Lorentzian or Gaussian). Consequently, in such a case, LOM becomes inaccurate in estimating the optical constants and a modified Lorentz oscillator model (MLOM) needs to be considered [105, 107, 108].

In MLOM, a frequency-dependent adjustable broadening function (ABF) is incorporated as a modification to address the inhomogeneous broadening. The ABF is considered as

$$\gamma'(E) = \gamma \exp \left[-\alpha \left(\frac{E - E_0}{\gamma} \right)^2 \right] \quad (75)$$

where α is an adjustable broadening parameter. Any arbitrary lineshape can be fitted by varying α ($\alpha = 0$: Lorentzian, $\alpha = 0.3$: Gaussian, $0 < \alpha < 0.3$: Voigt, and $\alpha > 0.3$: asymmetric or inhomogeneous lineshapes). The damping term γ in Eq. (74) is replaced by the frequency-dependent ABF γ' in MLOM. Therefore, MLOM is a convenient method of obtaining dielectric function by fitting absorption bands with non-Lorentzian broadening [105, 107, 108].

In MLOM fitting, f , E_0 , γ , and α are the fitting parameters. They are optimized to reduce the value of an objective function (Θ) which indicates the difference between the experimental (A_{exp}) and the calculated (A_{cal}) absorption. The value of Θ is calculated as

$$\Theta = \sum_E [A_{exp}(E) - A_{cal}(E)]^2 \quad (76)$$

with $A = 1 - R - T$ (R : reflection and T : transmission) [106]. In the fitting, A_{cal} is calculated using the optical constants derived from MLOM.

In [PV], thin films of poly-vinyl alcohol (PVA) doped with rhodamine 6G (R6G) molecules are considered as the excitonic material and the doping concentration is varied. The thin films are prepared on top of glass substrates using spin coating (see Section 2.2.2) and optically characterized (R and T measurements) by an angle-resolved optical setup (see Section 2.3.2). The theoretical absorption (A_{cal}) is calculated using the transfer-matrix method (see Section 2.1.1). Figure 31(a) reports the R6G film absorption spectra for four different doping concentrations: 0.2 mol/L (blue), 0.6 mol/L (green), 1.7 mol/L (red), and 5.2 mol/L (grey). The vibronic shoulder (503 nm) of R6G (dashed vertical line) becomes prominent with an increase in concentration resulting in a merging of two separate peaks (540 nm and 503 nm) leading to a flat top profile (grey curves) for highest doping (5.2 mol/L) as one can see in Figure 31(a).

The effect of R6G concentration on the fitted f and γ for the vibronic shoulder (503 nm) of R6G can be understood from Figure 31(b). From the figure, we can see that when the R6G concentration increases, f and γ rises, and as a result, the vibronic shoulder intensifies and broadens as reported in Figure 31(a). Such trend validates the dominance of the shoulder peak (503 nm) at high concentrations.

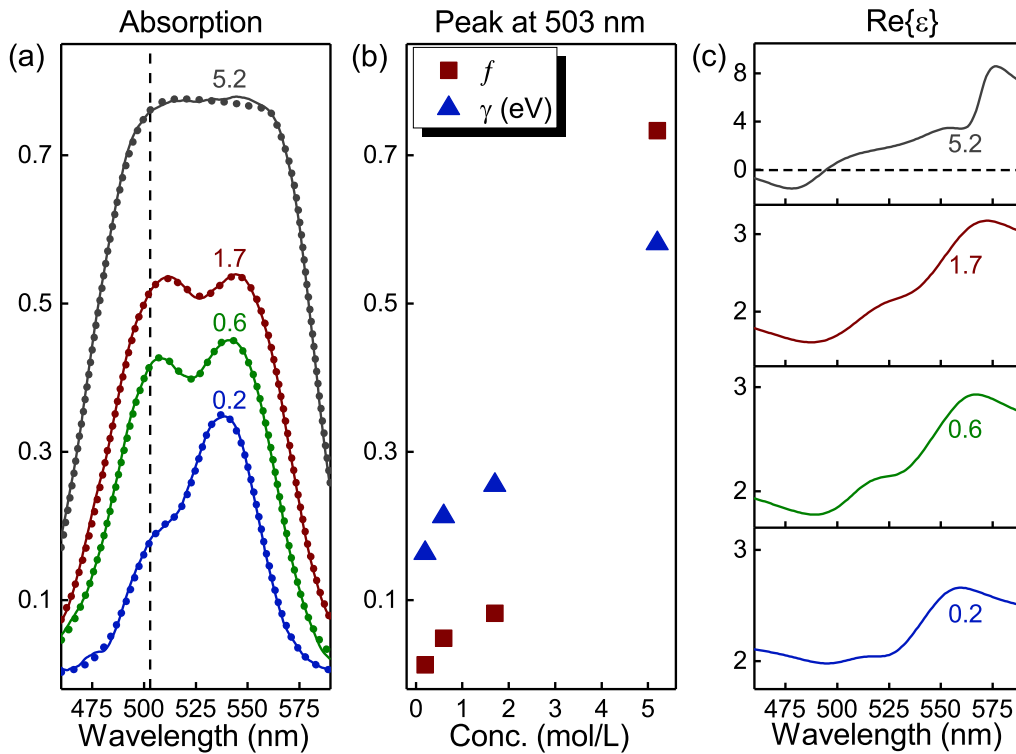


FIGURE 31 (a) Measured (solid curves) and fitted (dotted curves) absorption spectra of the R6G films for four target concentrations: 0.2 mol/L (blue), 0.6 mol/L (green), 1.7 mol/L (red), and 5.2 mol/L (grey). The dashed vertical line in the figure depicts the spectral position of the vibronic shoulder (503 nm) of R6G. (b) Evolution of the fitted oscillator strength (f) and Lorentz linewidth (γ) as a function of R6G concentration (Conc.) for the vibronic shoulder (503 nm) of R6G. The red squares and blue triangles are the discrete data points plotted as a scatter diagram. (c) Real part of the complex dielectric function ($\text{Re}\{\epsilon\}$) of the R6G films for four target concentrations: 0.2 mol/L (blue), 0.6 mol/L (green), 1.7 mol/L (red), and 5.2 mol/L (grey).

The real component of the permittivity ($\text{Re}\{\epsilon\}$) calculated by Eq. (74) using the optimized fitting parameters for the R6G films are reported in Figure 31(c). We can clearly see in the figure that the gap between $\text{Re}\{\epsilon\}$ values below 475 nm and above 575 nm increases with concentration. This results in negative values of $\text{Re}\{\epsilon\}$, implying a plasmon-like behavior [28, 29], in a small spectral window (460-500 nm) when the doping is highest (5.2 mol/L) as one can see in the grey curve in Figure 31(c).

From Figure 31 and from [PV] in general, we can infer that the effect of molecular concentration can be modelled by varying f and γ of an excitonic material. Moreover, simultaneous rise in f and γ due to an increase in concentration can induce negative values of $\text{Re}\{\epsilon\}$ which is an essential prerequisite to realize surface excitonic modes in excitonic nanostructures.

5.2 Origin of surface excitons

The origin of surface exciton (SE) in excitonic materials can be explained in terms of $\text{Re}\{\epsilon\}$ [29] as also discussed in Chapter 1 (see Section 1.3). To support any surface exciton mode, the excitonic materials should have at least $\text{Re}\{\epsilon(\omega)\} < 0$. The criteria for sustaining the surface exciton polariton (SEP) mode in an excitonic thin film and the localized surface exciton (LSE) mode in an excitonic NP are $\text{Re}\{\epsilon(\omega)\} < -1$ and $\text{Re}\{\epsilon(\omega)\} < -2$, respectively [29]. In [PVII], the effect of molecular concentration on the generation of SE modes is investigated numerically by considering PVA doped with TDBC J-aggregates as the excitonic material since such system can sustain SE modes in room temperature [29,30,109–114].

To determine how molecular concentration can affect the negative-real permittivity regime, i.e., $\text{Re}\{\epsilon(\omega)\} < 0$, for a TDBC-PVA system, f and γ are varied in Eq. (74) during the calculation of $\epsilon(\omega)$ for a TDBC-PVA thin film (thickness: 60 nm). Other Lorentz parameters ($\epsilon_\infty = 2.1025$, $E_0 = 2.08$ eV) are realistic values taken from the existing literature [115]. Figure 32(a) reports the calculated $\epsilon(\omega)$ (real: solid and imaginary: dashed) spectra where f and γ are varied. In the figure inset, the associated absorption computed using the transfer-matrix method (see Section 2.1.1) is shown.

Figure 32(a) shows how molecular concentration can affect the existence of SE modes. In the case of a 60 nm TDBC-PVA film with low concentration ($f = 0.05$ and $\gamma = 0.05$ eV), $\text{Re}\{\epsilon(\omega)\} > 0$ (green solid curve) and therefore, no SE mode exists. By increasing the value of f with the same γ , i.e., $f = 0.20$ and $\gamma = 0.05$ eV, one can partially mimic an increase in concentration. In such a case, $\text{Re}\{\epsilon(\omega)\} < 0$ around 575-595 nm (green spot in red solid curve) and hence, SE modes can exist in the TDBC-PVA film. By increasing the value of f and γ together, one can fully mimic an increase in concentration as we infer from [PV]. Therefore, when $f = 0.20$ and $\gamma = 0.15$ eV, we see the more accurate scenario of high concentration where again $\text{Re}\{\epsilon(\omega)\} > 0$ (blue solid curve) and therefore, no SE mode exists. At this point, it is apparent that broadening (rise in γ) negates the consequences of an increase in f without broadening.

By calculating the spectral window of $\text{Re}\{\epsilon(\omega)\} < -1$ and $\text{Re}\{\epsilon(\omega)\} < -2$ for various f and γ where the loss is low, i.e., $|\text{Im}\{\epsilon(\omega)\}| < |\text{Re}\{\epsilon(\omega)\}|$ [116] one can estimate the bandwidth (BW) sustaining the SE modes. Figure 32(b) reports the BW (solid: $\text{Re}\{\epsilon\} < -1$ and dashed: $\text{Re}\{\epsilon\} < -2$). From the figure it is clear that without broadening (at $\gamma = 0.05$ eV), the higher the f ($0.40 \rightarrow 0.50 \rightarrow 0.75$), the higher the BW (green \rightarrow blue \rightarrow red in the vertical axis). If we now consider broadening, i.e., a rise in γ (0.05 eV \rightarrow 0.20 eV) for a constant f , we observe a rapid fall in BW. Again, we see that a rise in γ (broadening) negates the consequences of an increase in f .

From Figure 32(b) we also see that the BW vanishes after a threshold value of γ . For example, the threshold value is 0.14 eV for the LSE mode at $f = 0.75$ (dashed red curve). This threshold is actually a broadening tolerance ($\Delta\gamma$) and to sustain the SE modes, the broadening needs to be $< \Delta\gamma$. The tolerance ($\Delta\gamma$) also

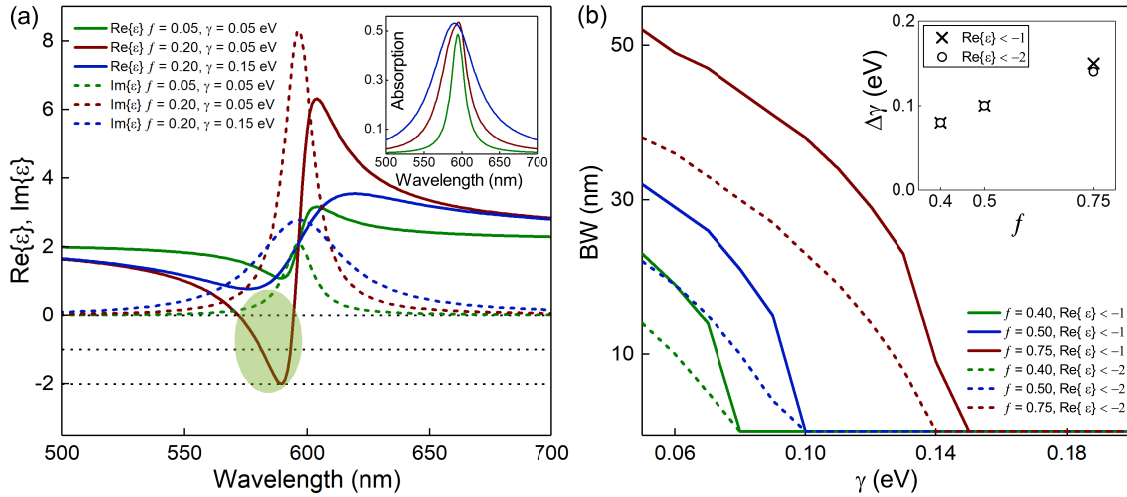


FIGURE 32 (a) Permittivity $\epsilon(\omega)$ (real: solid and imaginary: dashed) of a TDBC-PVA thin film (thickness: 60 nm) for various f and γ . In the inset, the associated absorption spectra are reported in the corresponding colors. In the red curve of $\text{Re}\{\epsilon\}$, the spectral region of $\text{Re}\{\epsilon\} < 0$ and $|\text{Im}\{\epsilon\}| < |\text{Re}\{\epsilon\}|$ is marked by the green spot. (b) Spectral window or bandwidth (BW) sustaining SE modes for various f and γ . The f -dependent profile of the broadening tolerance ($\Delta\gamma$) is plotted in the inset. Reprinted with permission from [PVII] © The Optical Society.

increases with f as we see in the inset of Figure 32(b). Therefore, if we attain a very high concentration, f will be very high resulting in a BW of $\text{Re}\{\epsilon(\omega)\} < 0$ with a large $\Delta\gamma$. Consequently, the associated obvious broadening can be mitigated and the TDBC layer will support the SE modes.

5.3 Weak coupling properties of surface excitons

From the results reported in previous sections it is apparent that we can model the variation in molecular concentration by varying f and γ , and these parameters can directly affect the generation of SE modes in excitonic materials. In line with that weak coupling properties of SE modes are also studied in [PVII], i.e., how molecular concentration affects the SE mode based sensing and spectroscopy. For the previously discussed TDBC-PVA system, the weak coupling properties, i.e., spectral sensitivity (S_λ), spectral figure of merit (F_λ) in sensing, NFIE, Purcell enhancement, and field confinement are evaluated for varying concentration. Three types of TDBC-PVA nanostructures are studied, i.e., a thin film (SEP), a nanosphere (LSE), and a nanosphere array (ESLR) identical to the schematics shown in Figures 2(a), 2(d), and 2(e), respectively, if we change the material from Au to TDBC-PVA. The resulting SE modes have optical responses and near-field profiles similar to their plasmonic analogs shown in Figure 2.

Refractive-index (RI) sensing performance of SEP, LSE, and ESLR modes

can be quantified in terms of S_λ and F_λ where

$$S_\lambda = \frac{\Delta\lambda_r}{\Delta n_s} \quad (77)$$

and

$$F_\lambda = \frac{S_\lambda}{\Delta\lambda} \quad (78)$$

with $\Delta\lambda_r$ as the shift in the spectral position of the SE mode (λ_r) due to a change in refractive index (Δn_s) of the sensing medium (n_s) and $\Delta\lambda$ as the spectral full-width at half-maximum (FWHM) of the SE mode in air ($n_s = 1$) [26, 27, 110]. The optical spectra (and thus subsequently λ_r and $\Delta\lambda$) of the SEP, LSE, and ESLR modes are computed using the transfer-matrix method (see Section 2.1.1), Mie theory (see Section 2.1.2), and coupled dipole method (see Section 2.1.3), respectively, for n_s varying from 1 to 1.01 with a step size of 0.001. Figure 33 reports the evolution of S_λ and F_λ as a function of molecular concentration implemented by varying f (at $\gamma = 0.05$ eV) and by varying γ (at $f = 0.5$).

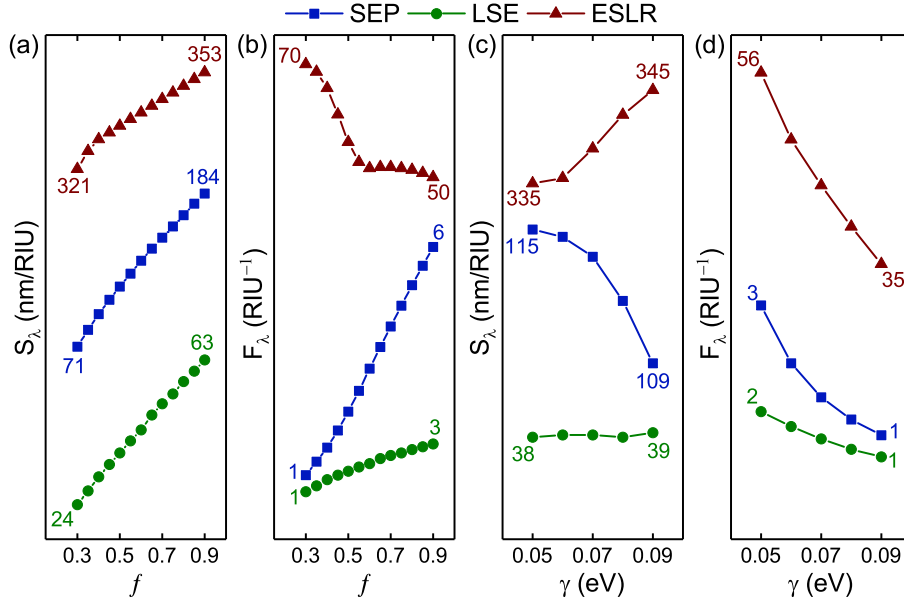


FIGURE 33 Sensing properties of SEP, LSE, and ESLR modes. The f -dependent (at $\gamma = 0.05$ eV) profiles of the spectral (a) sensitivity (S_λ) and (b) figure of merit (F_λ). The γ -dependent (at $f = 0.5$) profiles of the spectral (c) sensitivity (S_λ) and (d) figure of merit (F_λ). In all figures, the discrete data points are depicted by the blue squares, dark red triangles, and green circles, while the numbers in corresponding color show the obtained minimum and maximum values of the parameters.

From Figures 33(a) and 33(b) it is clear that for all SE modes, S_λ and F_λ increase with f except F_λ of ESLR (dark red triangles) which drops drastically as one can see in Figure 33(b). This is the case of no broadening, i.e., $\gamma = 0.05$ eV where an increase in f induces broadening in the ESLR mode ($\Delta\lambda$ increases) and eventually, F_λ drops [PVII]. When broadening is included at $f = 0.5$, we see a fall in S_λ for SEP (blue squares) and a rise in S_λ for ESLR (dark red triangles), while

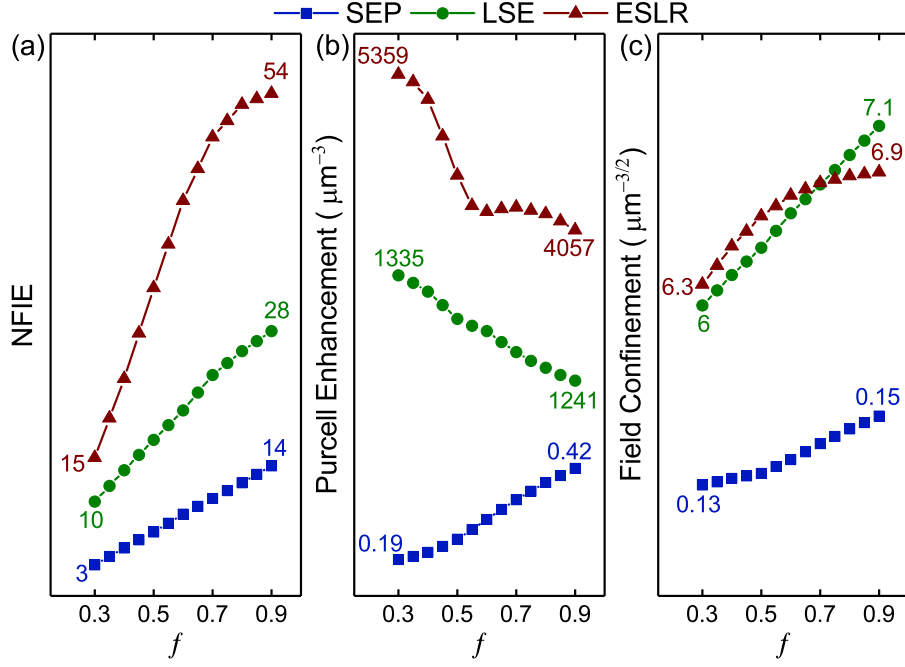


FIGURE 34 The f -dependent (at $\gamma = 0.05$ eV) profiles of (a) NFIE, (b) Purcell enhancement, and (c) field confinement of SEP, LSE, and ESLR modes. In all figures, the discrete data points are depicted by the blue squares, dark red triangles, and green circles, while the numbers in corresponding color show the obtained minimum and maximum values of the parameters.

no change in S_λ for LSE (green circles) as reported in Figure 33(c). However, such rise in γ ($f = 0.5$) causes a drop in F_λ for all SE modes as shown in Figure 33(d). Such findings imply that the performance of SE modes in RI sensing is tunable via molecular concentration since an increase in f and γ induces counterbalancing effects.

In spectroscopy, the effectiveness of the SEP, LSE, and ESLR modes are assessed by the NFIE, Purcell enhancement, and field confinement. As discussed in Section 3.2, the NFIE ($|E|^2$) is relevant to the surface enhancement [60, 61]. In fluorescence spectroscopy, the Purcell enhancement $\propto Q/V_m$ accounts for the amount of emission enhancement [23]. Here, Q and V_m are the confinement of light in temporal and spatial domains, respectively, [21] as described in Section 1.1. In strong coupling regime, the field-confinement ($V_m^{-1/2}$) is relevant to the coupling strength [3]. All the TDBC-PVA nanostructures are simulated using FDTD method (see Section 2.1.4) to compute NFIE, Q , and V_m . The evolution of NFIE, Purcell enhancement, and field confinement is shown in Figure 34 for a varying f with $\gamma = 0.05$ eV and is illustrated in Figure 35 for a varying γ with $f = 0.5$.

From Figures 34(a) and 34(c) it is evident that the NFIE and field confinement increase with f . However, the Purcell enhancement drops except for SEP (blue squares) where it is rising as we see in Figure 34(b). A rise in f causes an increase in $\Delta\lambda$ of the LSE and ESLR modes causing a drop in Q [PVII]. Consequently, the Purcell enhancement drops. If we now include broadening at $f = 0.5$,

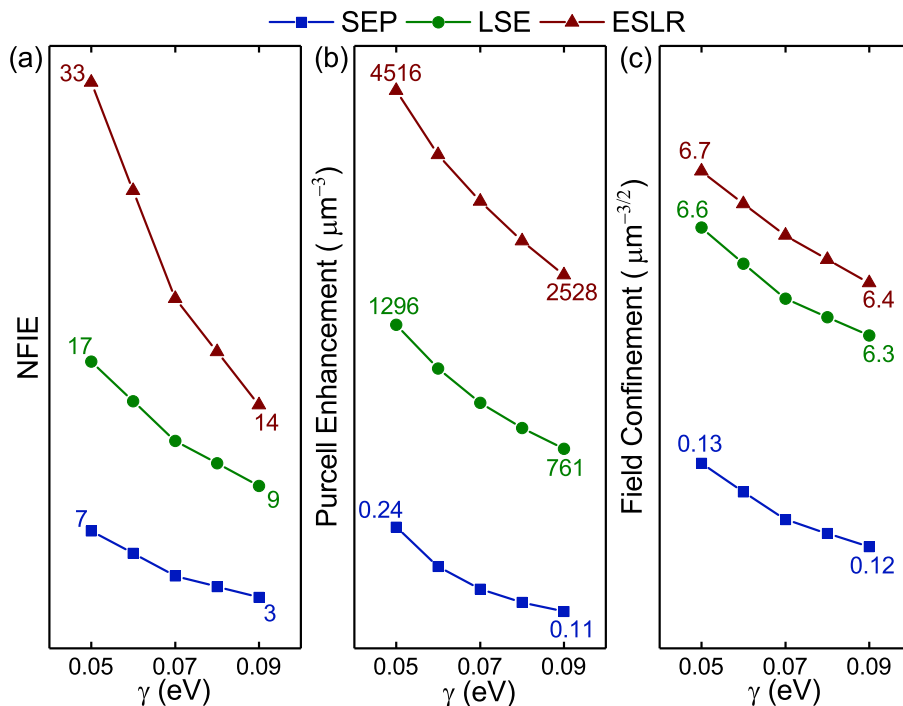


FIGURE 35 The γ -dependent (at $f = 0.5$) profiles of (a) NFIE, (b) Purcell enhancement, and (c) field confinement of SEP, LSE, and ESLR modes. In all figures, the discrete data points are depicted by the blue squares, dark red triangles, and green circles, while the numbers in corresponding color show the obtained minimum and maximum values of the parameters.

all the parameters drop as one can see in Figure 35. Therefore, the performance of SE modes in spectroscopy is tunable through molecular concentration and an increase in f and γ induces counterbalancing effects.

In [PVII], the TDBC-PVA nanostructures are also compared with their plasmonic analogs, i.e., with identical gold (Au) nanostructures when used as sensors and resonant substrates in spectroscopy. The most surprising and important finding revealed through such comparison is that the SE modes outperform the plasmonic modes in enhancing and confining light, and hence, can supplant the conventional plasmonic systems as a potential alternative.

We can conclude from [PVII] that the SE modes in the excitonic nanostructures possess concentration-dependent and thus, tunable optical properties unlike the conventional plasmonics. Most of their weak coupling (sensing and spectroscopy) parameters increase with f when no broadening is allowed. However, broadening negates that effect by incurring a drop in those parameter values. Such findings also suggest that the chosen excitonic molecule should have a strong transition dipole moment (large f) and a narrow spectral linewidth (small γ).

5.4 Strong coupling properties of surface excitons

So far we have seen how SE modes having tunable optical properties can be exploited in weak coupling applications. In [PVIII], the study extends to investigate how we can utilize such SE modes in excitonic nanostructures for strong coupling.

A core-shell NP geometry depicted in Figure 36(a) is considered as the platform for strong coupling where a TDBC-PVA core (radius: $r_{core} = 50$ nm, permittivity: $\epsilon_{core}(\omega)$) possessing LSE mode is surrounded by a generic dye shell (thickness: $t_{shell} = 25$ nm, permittivity: $\epsilon_{shell}(\omega)$). Mie theory (see Section 2.1.2) is used to calculate the optical responses of such system since the effective size of the NP ($r_{shell} = 75$ nm) is beyond the quasi-static scenario [API]. The core permittivity $\epsilon_{core}(\omega)$ is obtained from Eq. (74) with ϵ_{∞} as 1.45^2 , γ as 0.05 eV, f as 0.5, and E_0 as 2.08 eV. The shell permittivity $\epsilon_{shell}(\omega)$ is calculated using the same equation with ϵ_{∞} as 1.45^2 , γ as 0.10 eV, and E_0 as 2.15 eV for a varying f , i.e., f_{dye} as 0.01, 0.03, 0.05, 0.10, 0.15, and 0.20. The variation in f_{dye} renders the variation in the shell concentration, while the shell absorption peak is spectrally tuned with the LSE mode (E_c) in core at 2.15 eV.

At this point, we should keep in mind that the modelled NP is fully organic having the core and shell made of Lorentz materials described by Eq. (74). However, only the core sustains a LSE mode (E_c) in the spectral regime where $\text{Re}\{\epsilon(\omega)\} < -2$ in addition to its material absorption (E_m). The shell has a positive $\text{Re}\{\epsilon(\omega)\}$ in the spectral region of interest and thus, possesses only the material absorption centered at E_c .

As mentioned above and shown by the red curve in Figure 36(a), the TDBC core sustains a strong LSE mode (E_c) at 2.15 eV in addition to a relatively weak material absorption (E_m) at 2.08 eV. The shell absorption (black curve) has a spectral match with the LSE mode at E_c . As we see in [PVII], LSE mode is analogous to the LSP mode in enhancing and confining light. Therefore, polaritons should emerge in the core-shell absorption due to a strong interaction between the LSE mode (core) and the dye molecules (shell) as it usually happens for a metallic core (LSP) [115]. Surprisingly, in Figure 36(a), we do not see any polariton formation. Instead, we see a mild broadening in the core-shell absorption at E_c with an increase in f_{dye} .

To understand such a perplexing finding, if we now carefully look at the core-shell absorption at E_c (2.15 eV) reported in Figure 36(b), we see a drop followed by a rise when f_{dye} is varied. Initially, an increase in f_{dye} engenders the energy-splitting induced transparency [115] causing such drop. However, for the large values of f_{dye} , the density of the nonhybridized molecular excitons increases incurring the observed rise [117]. Interestingly, in plasmon-molecule coupling, we see similar trend [PVIII, 115]. Therefore, the coupling between the LSE mode (core) and the dye molecules (shell) is indeed *strong*, although the polaritons are absent in the absorption spectra.

The absence of polaritons can be explained with the help of Figure 36(c)

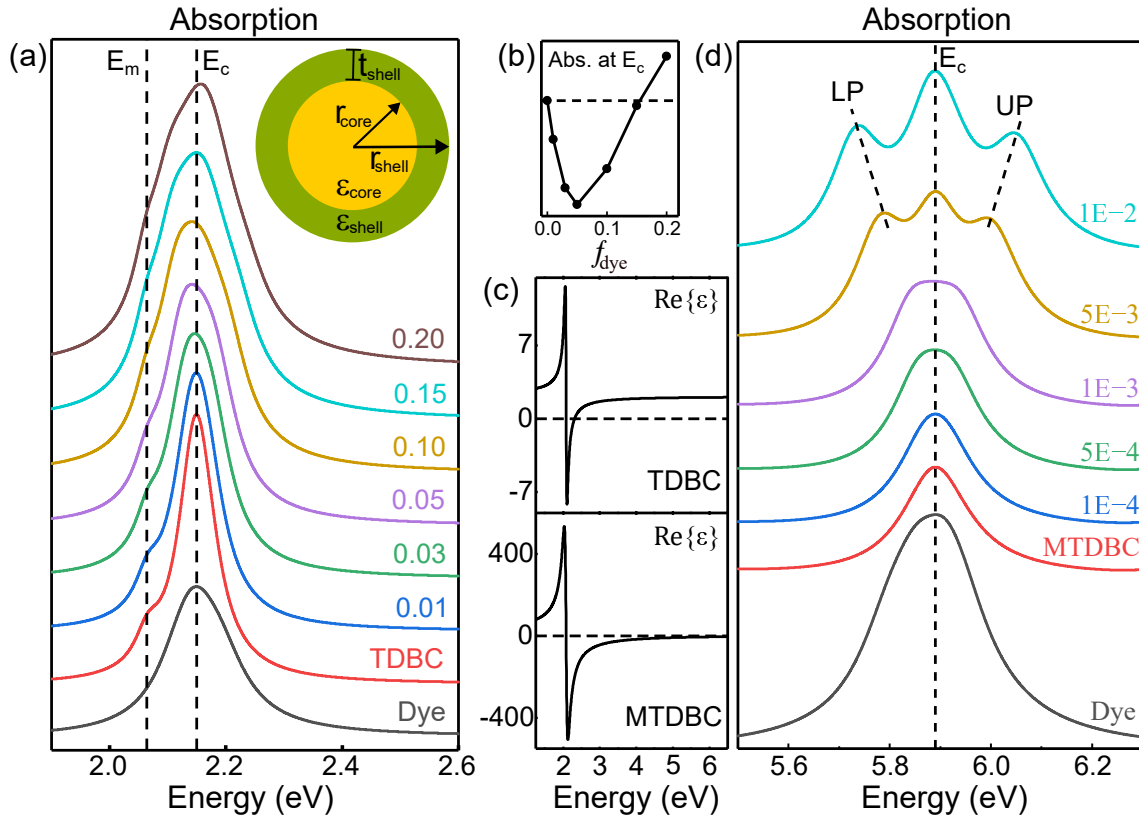


FIGURE 36 (a) Absorption of the dye shell (in black), TDBC core (in red), and TDBC core-dye shell NP having f_{dye} as 0.01, 0.03, 0.05, 0.10, 0.15, and 0.20 along with the NP schematic on top right corner. In the schematic, $r_{core} = 50$ nm, $t_{shell} = 25$ nm, and $r_{shell} = 75$ nm with ϵ_{core} and ϵ_{shell} as the core and shell permittivities. The vertical dashed black lines show the spectral positions of the LSE mode ($E_c = 2.15$ eV) and the material absorption ($E_m = 2.08$ eV) sustained by the core. (b) The f_{dye} -dependent profile of the absorption (Abs.) at $E_c = 2.15$ eV for the TDBC core-dye shell NP. The absorption of the core for $f_{dye} = 0$ is shown by the black horizontal dashed line, while the discrete data points are presented by the black squares. (c) Real component of the permittivity ($Re\{\epsilon\}$) of TDBC (MTDBC) in top (bottom) panel. (d) Absorption of the dye shell (in black), MTDBC core (in red), and MTDBC core-dye shell NP having f_{dye} as 0.0001, 0.0005, 0.001, 0.005, and 0.01. The vertical dashed black line shows the spectral position of the LSE mode ($E_c = 5.9$ eV) sustained by the core, while the tilted black dashed lines illustrate the polariton branches (lower: LP and upper: UP). In (a) and (d), all the curves are in same linear scale, except they are shifted vertically for clarity. Adapted from [PVIII] under the license CC BY NC ND 4.0.

where the top panel reports the values of $\text{Re}\{\epsilon\}$ for TDBC. As we see in the figure, $\text{Re}\{\epsilon\}$ of TDBC is negative only in a very narrow spectral region and polaritons residing outside of that region are absent in the absorption spectra. This hypothesis can easily be tested by modelling a modified TDBC (MTDBC) material having negative values of $\text{Re}\{\epsilon\}$ over a spectral window large enough to include the polaritons. In Figure 36(c), the bottom panel reports the values of $\text{Re}\{\epsilon\}$ for MTDBC obtained from Eq. (74) with ϵ_∞ as 1.45^2 , γ as 0.10 eV, f as 50, and E_0 as 2.08 eV. As we see in the figure, $\text{Re}\{\epsilon\}$ of MTDBC is negative over a broad spectral range.

Let us consider again the same core-shell geometry, i.e., the schematic in Figure 36(a), where a MTDBC core is now surrounded by a dye shell. The shell permittivity is calculated using Eq. (74) with ϵ_∞ as 1.45^2 , γ as 0.10 eV, and E_0 as 5.9 eV for a varying f , i.e., f_{dye} as 0.0001, 0.0005, 0.001, 0.005, and 0.01, to render the variation in the shell concentration. The red curve in Figure 36(d) shows the core absorption where the LSE mode (E_c) is now at 5.9 eV. The shell absorption (black curve) has a spectral match with the LSE mode at E_c . As one can see in Figure 36(d), the polaritons are now clearly visible in the core-shell absorption for large f_{dye} (0.005 and 0.01) in addition to a middle peak at E_c resulting from the nonhybridized molecular excitons [117]. Such outcome validates that strong coupling between the LSE mode (core) and the dye molecules (shell) is attainable. Although, the resulting polaritons might reside outside of the narrow spectral region where $\text{Re}\{\epsilon\}$ is negative and thus, might be absent in the absorption profile.

Another topic worth exploring is the strong coupling between two resonator modes. For example, cases of strong coupling between a cavity mode and surface plasmons [118], and between two types of plasmonic modes [119] have already been reported. In line with that, coupling between LSE and LSP modes is also investigated in [PVIII]. The same core-shell NP, i.e., the schematic in Figure 36(a), is considered where a Au core (LSP) is surrounded by a TDBC shell (LSE). The TDBC shell (ϵ_{shell}) has the permittivity similar to the TDBC core of the previous case, while Au permittivity (ϵ_{core}) is taken from the literature [31].

The green curve in Figure 37(a) shows the absorption of a TDBC shell when the core is inert (dielectric). The shell supports two LSE modes, E_{L1} and E_{L2} , originated from Fano-type hybridization of LSE modes at inner and outer shell surfaces, in addition to the material absorption (E_m) [112]. When an absorbing core is considered like the blue curve in Figure 37(a), only a single LSE mode remains, i.e., E_{L1} and E_{L2} merge as one can see in the red curve in Figure 37(a). In Au core-TDBC shell NP, the Au core is the absorbing core with a LSP mode (E_c) at 2.28 eV.

To explore what happens when E_c is spectrally tuned with E_{L1} , E_{L2} , or E_m , the parameter $E_m = E_0$ of the TDBC shell is treated as a variable in Eq. (74) ranging from 1.9 eV to 2.3 eV. On an energy difference scale ($E - E_m$ with the center at E_m), the positions of E_{L1} , E_{L2} , and E_m are shown by the black curve in Figure 37(b). In the same figure, the absorption spectra of Au core-TDBC shell NP are depicted (in other colors) on the energy difference ($E - E_m$) scale with E_m as 1.9 eV, 2 eV, 2.1 eV, 2.2 eV, and 2.3 eV. The LSP mode (E_c) of Au core at 2.28 eV is shown in $E - E_m$ scale by the thick black vertical lines on each curve (except on

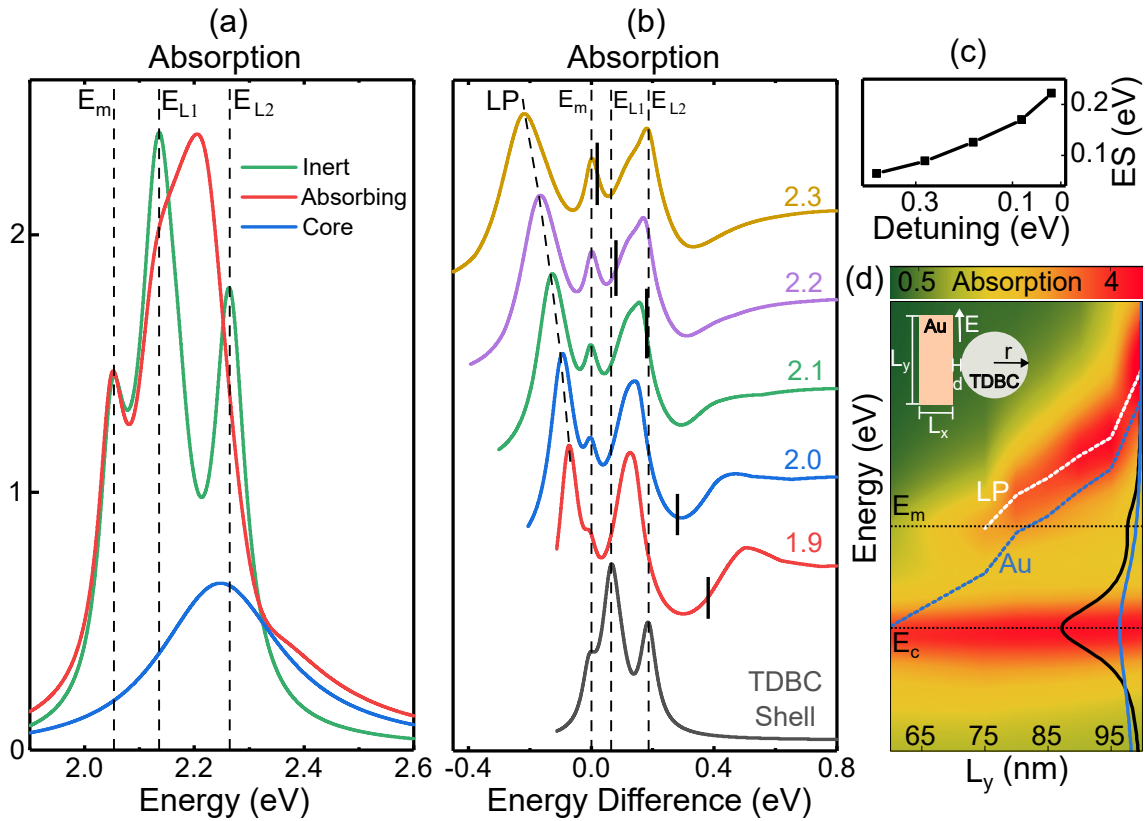


FIGURE 37 (a) TDBC shell absorption when the core is inert (in green) or absorbing (in red) with an absorption profile shown in blue. (b) Absorption of the TDBC shell (in black) and Au core-TDBC shell NP (in all colors) over the energy difference ($E - E_m$) scale with E_m as 1.9 eV, 2 eV, 2.1 eV, 2.2 eV, and 2.3 eV. All the curves are in same linear scale, except they are shifted vertically for clarity. The LSP mode (E_c) of Au core is at 2.28 eV and its position in $E - E_m$ scale is shown by the thick black vertical lines on each curve (except on black). In figures (a) and (b), the vertical dashed black lines show the spectral positions of the LSE modes (E_{L1} and E_{L2}) and the material absorption (E_m) sustained by the TDBC shell. The tilted black dashed line in (b) depict the lower (LP) polariton branch. (c) Energy splitting (ES) calculated as $E_m - E_{LP}$ on the detuning ($E_c - E_m$) scale. The discrete data points are marked by the black squares. (d) Contour plot of the dimer absorption. In the top left corner, a schematic of the dimer is given where $L_x = 30$ nm, $r = 50$ nm, and $d = 10$ nm. The L_y is treated as a variable ranging from 60 nm to 100 nm in 5 nm step. The excitation is polarized in y -direction (white arrow), i.e., the electric-field vector \mathbf{E} is parallel with L_y . In the right side of the contour plot, absorption of the TDBC nanosphere (in black) and Au nanobar (in blue) are shown for $L_y = 60$ nm. The horizontal black lines show the spectral positions of the LSE mode (E_c) and the material absorption (E_m) sustained by the TDBC nanosphere. The dispersion of the LSP mode in Au nanobar and the lower polariton (LP) branch are illustrated by the blue and white dashed lines. Adapted from [PVIII] under the license CC BY NC ND 4.0.

black). It is apparent from Figure 37(b) that when E_m is 2.1 eV (green), E_c and E_{L2} are in tune, when E_m is 2.2 eV (violet), E_c and E_{L1} are in tune, and when E_m is 2.3 eV (yellow), E_c and E_m are in tune.

As we see in Figure 37(b), for all E_m (1.9 eV to 2.3 eV), E_{L1} and E_{L2} merge since the Au core is absorbing. In addition to that, all the core-shell absorption spectra contain a peak at the energies lower than E_m . This is the lower polariton (LP) peak originated from the strong coupling between the LSP mode (E_c) of the Au core and the material absorption (E_m) of the TDBC shell. That is because the separation between this LP peak and E_m , i.e., the energy split (ES), drops with an increase in detuning ($E_c - E_m$) as one can see in Figure 37(c). In core-shell absorption, the upper polariton (UP) is masked by the Au absorption and the LSE mode, and hence, not resolvable. The results reported in Figure 37(b) strongly suggest that the coupling between the LSE modes (E_{L1} and E_{L2}) and the LSP mode (E_c) is weak, while only the coupling between the material absorption (E_m) and the LSP mode (E_c) is strong.

To further confirm the aforementioned finding, a dimer system is considered where a Au nanobar (LSP) is interacting with a TDBC nanosphere (LSE). Figure 37(d) shows the schematic of such dimer (top left corner) where the dimensions are $L_x = 30$ nm, $L_z = 50$ nm, $r = 50$ nm, and $d = 10$ nm. The nanobar length (L_y) is treated as a variable ranging from 60 nm to 100 nm, while the FDTD method (see Section 2.1.4) is used to compute the optical responses of the dimer.

In Figure 37(d), the black curve on the right shows the nanosphere absorption having a strong LSE mode (E_c) in addition to the material absorption (E_m). The LSP mode of the nanobar (blue curve on the right) is in tune with the LSE mode (E_c) when L_y is 60 nm. To explore what happens when the LSP mode overlaps with E_c or E_m , the LSP mode is shifted from E_c to E_m by increasing L_y (60 nm to 100 nm). The blue dashed line in Figure 37(d) shows the resulting dispersion of the LSP mode.

The contour plot of the dimer absorption is presented in Figure 37(d) and we can infer from the figure that no polaritons form when the LSP mode overlaps with the LSE mode at E_c . A LP branch (white dashed line) forms through an energy splitting only when the LSP mode overlaps with the material absorption (E_m). No upper polariton branch is observed since the upper polaritons overlap with the LSE mode (E_c). Clearly, Figures 37(b) and 37(d) report the same finding and thereby, confirm that the coupling between the LSE and LSP modes is weak, while only the coupling between the material absorption and the LSP mode is strong.

Chapter summary

In summary, from [PV] we learned that effect of molecular concentration can be modelled by varying f and γ leading to the generation of SE modes in excitonic nanostructures. We can conclude from [PVII, PVIII] that optical properties of SE modes supported by such excitonic nanostructures can be efficiently tuned via molecular concentration. In weak coupling regime, excitonic nanostructures are a potential alternative for plasmonics since the supported SE modes can provide equivalent or even better confinement of light compared to metals. However, in strong coupling regime, excitonic nanostructures fail to sustain polaritons since the spectral region supporting the SE modes is usually very narrow. Moreover, coupling between the SE modes and the other resonator modes is weak, while coupling between the material absorption of the excitonic materials and the surface plasmons is strong.

6 CONCLUSION

This dissertation is a synthesis of eight publications on weak and strong coupling between organic molecules and confined light achieved via optical nanostructures. To develop a foundation for this topic, the dissertation started by explaining the idea of weak and strong light-matter coupling (Chapter 1), how different kinds of nanostructures can be used to confine light to attain such coupling (Chapter 1), and how those nanostructures can be implemented in practice (Chapter 2). Considering the importance of organic molecules in photovoltaics, material science, and resonant nanophotonics, the dissertation summarized studies on three kinds of optical nanostructures, i.e., plasmonic (Chapter 3), photonic (Chapter 4), and excitonic (Chapter 5) nanostructures when weakly and/or strongly coupled to the molecules. Hopefully, the aforementioned Chapters provided the prerequisite for the included publications appended after the list of cited references. This chapter concludes the overall findings and presents an essence of the whole study.

Let us first consider *weak coupling* between organic molecules and confined light. In weak coupling regime, plasmonic nanostructures like Fano-resonant metallic oligomers [PI, PII] and metallic gratings [PIII] can be used to enhance the Raman response of the molecules via *surface enhancement*, while photonic nanostructures such as planar metallic Fabry-Pérot cavities [PIV] can be employed to enhance the molecular spontaneous emission rate through *Purcell enhancement*. In both cases, the coupling is *weak* since the confined light (plasmonic and cavity modes) acts as a small perturbation only to boost the molecular responses (Raman and fluorescence) without affecting the molecular energy states. For optimal surface enhancement, the subradiant part of a plasmonic mode should have a large near-field enhancement at the Raman excitation, while the superradiant part should have a strong far-field scattering nature at the Raman fingerprint regions [PI, PIII]. Such mode can be engineered with a high number of spatially localized hotspots by optimizing the nanostructure geometry [PII]. For optimal Purcell enhancement and for efficient collection of the enhanced emission, the planar metallic Fabry-Pérot cavity should have a leaky top mirror for emission collection and a non-transparent bottom mirror, i.e., a reflective geometry [PIV].

In *weak coupling* regime, whether it is a plasmonic [PI, PII, PIII] or photonic [PIV] nanostructure, the idea is to optimize its geometry in order to optimize its optical properties and thereby, the associated Raman or fluorescence enhancement. However, if a nanostructure is fully organic and made of polymer doped with excitonic molecules [PV], then its optical properties and the corresponding enhancements (surface or Purcell) can also be optimized by varying the molecular concentration of the dopant [PVII]. Very high dopant concentration induces a negative real part in the permittivity of the excitonic material [PV]. Consequently, the excitonic nanostructure shows plasmon-like behaviour by sustaining surface exciton modes analogous to the surface plasmon modes in metals. Such surface exciton modes, if optimized properly via molecular concentration, can outperform the plasmonic modes by providing equivalent or even better confinement of light [PVII].

Confined light, provided by various optical (plasmonic, photonic, or excitonic) nanostructures and optimized via geometry or molecular concentration, can merely influence (e.g., enhance) the molecular responses (Raman or fluorescence) in the weak coupling regime. To actually change the energy landscape of a molecule and potentially modify its chemical properties, the coupling needs to be strong. In the case of *strong coupling* between organic molecules and confined light, photonic nanostructures like planar metallic Fabry-Pérot cavities can be utilized to engineer the photochemical properties of molecules via *cavity polaritons* [PVI], while plasmonic nanostructures such as metal nanoparticles can be used to generate *exciton-plasmon polaritons* [PVIII]. However, unlike their plasmonic analog, excitonic nanostructures such as organic nanoparticles fail to sustain such hybrid *polaritonic* states [PVIII].

In *strong coupling* regime, formation of hybrid light-matter states (polaritons) induces drastic changes in the molecular energy landscape. The cavity polaritons, originated from the strong cavity-molecule coupling, can modify the emission yield of a photochemical reaction if the reaction timescale is comparable to the cavity photon lifetime. In such strongly-coupled systems, the bright polaritonic states act as an efficient pathway to access the reactive molecular dark states. This is the most significant and novel finding in this dissertation since it shows that unlike the theoretical predictions, cavity polaritons are only able to significantly modify the excitation spectrum of the molecules, but the reaction itself as well as the potential energy surfaces remain unperturbed [PVI].

The *strong coupling* between the material absorption of the excitonic materials and the surface plasmons forms new energy states, exciton-plasmon polaritons, which can absorb and emit light [PVIII]. In this regard, the surface exciton mode, unlike its plasmonic counterpart, can only support the strong coupling induced transparency and not the hybrid polaritonic states due to its narrowband existence. In addition, it can only weakly couple to the other optical modes such as surface plasmons [PVIII].

Hopefully, this dissertation along with the appended publications will provide insights on how optical nanostructures should be developed to attain better confinement of light leading to an effective light-matter coupling and how such

coupling can be utilized to influence molecular properties. The latter is crucial to achieve a leap in organic photovoltaics and modern organic nanophotonics. Considering the rapid progress in computational methods, nanofabrication techniques, *ab initio* theories, and artificial intelligence driven material science, development of novel excitonic, polaritonic, and meta devices is not far-fetched. The field of altering material properties by hybridizing light and matter will thrive, and optical nanostructures could soon take the role of *photonic catalysts* employed to achieve the *alchemy of vacuum*. This dissertation may have touched the topic only *on a surface level*.

REFERENCES

- [1] J. Weiner and F. Nunes, *Light-matter interaction*. Oxford University Press, 2017.
- [2] J. G. Pascual, *Polaritonic chemistry*. Springer, 2020.
- [3] M. S. Rider and W. L. Barnes, "Something from nothing: linking molecules with virtual light," *Contemporary Physics*, vol. 62, pp. 217–232, 2021.
- [4] J. Langer *et al.*, "Present and future of surface-enhanced Raman scattering," *ACS Nano*, vol. 14, p. 28–117, 2020.
- [5] S. M. Fothergill, C. Joyce, and F. Xie, "Metal enhanced fluorescence biosensing: from ultra-violet towards second near-infrared window," *Nanoscale*, vol. 10, pp. 20914–20929, 2018.
- [6] R. F. Ribeiro, L. A. Martínez-Martínez, M. Du, J. Campos-Gonzalez-Angulo, and J. Yuen-Zhou, "Polariton chemistry: controlling molecular dynamics with optical cavities," *Chemical Science*, vol. 9, pp. 6325–6339, 2018.
- [7] D. S. Dovzhenko, S. V. Ryabchuk, Y. P. Rakovich, and I. R. Nabiev, "Light-matter interaction in the strong coupling regime: configurations, conditions, and applications," *Nanoscale*, vol. 10, pp. 3589–3605, 2018.
- [8] J. A. Hutchison, T. Schwartz, C. Genet, E. Devaux, and T. W. Ebbesen, "Modifying chemical landscapes by coupling to vacuum fields," *Angewandte Chemie International Edition*, vol. 51, pp. 1592–1596, 2012.
- [9] B. Munkhbat, M. Wersäll, D. G. Baranov, T. J. Antosiewicz, and T. Shegai, "Suppression of photo-oxidation of organic chromophores by strong coupling to plasmonic nanoantennas," *Science Advances*, vol. 4, p. eaas9552, 2018.
- [10] B. Kolaric, B. Maes, K. Clays, T. Durt, and Y. Caudano, "Strong light-matter coupling as a new tool for molecular and material engineering: quantum approach," *Advanced Quantum Technologies*, vol. 1, p. 1800001, 2018.
- [11] Y. Chen, Y. Cheng, and M. Sun, "Physical mechanisms on plasmon-enhanced organic solar cells," *Journal of Physical Chemistry C*, vol. 125, pp. 21301–21309, 2021.
- [12] L. Feng, M. Niu, Z. Wen, and X. Hao, "Recent advances of plasmonic organic solar cells: photophysical investigations," *Polymers*, vol. 10, p. 123, 2018.
- [13] V. C. Nikolis *et al.*, "Strong light-matter coupling for reduced photon energy losses in organic photovoltaics," *Nature Communications*, vol. 10, p. 3706, 2019.

- [14] C. Bujalance, V. Estesó, L. Calió, G. Lavarda, T. Torres, J. Feist, F. J. García-Vidal, G. Bottari, and H. Míguez, "Ultrastrong exciton-photon coupling in broadband solar absorbers," *Journal of Physical Chemistry Letters*, vol. 12, pp. 10706–10712, 2021.
- [15] K. S. Daskalakis, F. Freire-Fernández, A. J. Moilanen, S. v. Dijken, and P. Törmä, "Converting an organic light-emitting diode from blue to white with Bragg modes," *ACS Photonics*, vol. 6, pp. 2655–2662, 2019.
- [16] K. S. Daskalakis, A. I. Väkeväinen, J.-P. Martikainen, T. K. Hakala, and P. Törmä, "Ultrafast pulse generation in an organic nanoparticle-array laser," *Nano Letters*, vol. 18, pp. 2658–2665, 2018.
- [17] A. Mischok, S. Hillebrandt, S. Kwon, and M. C. Gather, "Highly efficient polaritonic light-emitting diodes with angle-independent narrow-band emission," *Nature Photonics*, vol. 17, p. 393–400, 2023.
- [18] M. Wei, A. Ruseckas, V. T. N. Mai, A. Shukla, I. Allison, S.-C. Lo, E. B. Nandas, G. A. Turnbull, and I. D. W. Samuel, "Low threshold room temperature polariton lasing from fluorene-based oligomers," *Laser & Photonics Reviews*, vol. 15, p. 2100028, 2021.
- [19] M. Hertzog, M. Wang, J. Mony, and K. Börjesson, "Strong light–matter interactions: a new direction within chemistry," *Chemical Society Reviews*, vol. 48, pp. 937–961, 2019.
- [20] A. V. Kavokin *et al.*, *Microcavities*. Oxford University Press, 2017.
- [21] S. Hu, M. Khater, R. Salas-Montiel, E. Kratschmer, S. Engelmann, W. M. J. Green, and S. M. Weiss, "Experimental realization of deep-subwavelength confinement in dielectric optical resonators," *Science Advances*, vol. 4, p. eaat2355, 2018.
- [22] M. H. Bitarafan and R. G. DeCorby, "On-chip high-finesse Fabry-Perot microcavities for optical sensing and quantum information," *Sensors*, vol. 17, p. 1748, 2017.
- [23] K. Vahala, "Optical microcavities," *Nature*, vol. 424, p. 839–846, 2003.
- [24] S. A. Maier, *Plasmonics: fundamentals and applications*. Springer, 2007.
- [25] V. G. Kravets, A. V. Kabashin, W. L. Barnes, and A. N. Grigorenko, "Plasmonic surface lattice resonances: a review of properties and applications," *Chemical Reviews*, vol. 118, p. 5912–5951, 2018.
- [26] J. Homola, *Surface plasmon resonance based sensors*. Springer, 2006.
- [27] B. Špačková and J. Homola, "Sensing properties of lattice resonances of 2D metal nanoparticle arrays: an analytical model," *Optics Express*, vol. 21, p. 27490–27502, 2013.

- [28] L. Gu, J. Livenere, G. Zhu, E. E. Narimanov, and M. A. Noginov, "Quest for organic plasmonics," *Applied Physics Letters*, vol. 103, p. 021104, 2013.
- [29] M. J. Gentile, S. Núñez-Sánchez, and W. L. Barnes, "Optical field-enhancement and subwavelength field-confinement using excitonic nanostructures," *Nano Letters*, vol. 14, p. 2339–2344, 2014.
- [30] A. D. Humphrey, M. J. Gentile, and W. L. Barnes, "Excitonic surface lattice resonances," *Journal of Optics*, vol. 18, p. 085004, 2016.
- [31] P. B. Johnson and R. W. Christy, "Optical constants of the noble metals," *Physical Review B*, vol. 6, p. 4370–4379, 1972.
- [32] A. Sarangan, *Optical thin film design*. CRC Press, 2020.
- [33] T. G. Mackay and A. Lakhtakia, *The transfer-matrix method in electromagnetics and optics*. Morgan and Claypool, 2020.
- [34] K. J. Pascoe, *Reflectivity and transmissivity through layered, lossy media: a user-friendly approach*. Wright Patterson Air Force Base, 2001.
- [35] G. Mie, "Beiträge zur optik trüber medien, speziell kolloidaler metallösungen," *Annalen der Physik*, vol. 330, pp. 377–445, 1908.
- [36] C. F. Bohren and D. R. Huffman, *Absorption and scattering of light by small particles*. Wiley-VCH, 1998.
- [37] G. Baffou, *Thermoplasmonics: heating metal nanoparticles using light*. Cambridge University Press, 2017.
- [38] B. Gallinet, J. Butet, and O. J. F. Martin, "Numerical methods for nanophotonics: standard problems and future challenges," *Laser & Photonics Reviews*, vol. 9, pp. 577–603, 2015.
- [39] S. D. Gedney, *Introduction to the finite-difference time-domain (FDTD) method for electromagnetics*. Morgan and Claypool, 2011.
- [40] Z. Li, Z. Qiao, and T. Tang, *Numerical solution of differential equations: introduction to finite difference and finite element methods*. Cambridge University Press, 2017.
- [41] A. C. Polycarpou, *Introduction to the finite element method in electromagnetics*. Morgan and Claypool, 2006.
- [42] <https://www.mathworks.com/products/matlab.html>.
- [43] D. Khlopin, F. Laux, W. P. Wardley, J. Martin, G. A. Wurtz, J. Plain, N. Bonod, A. V. Zayats, W. Dickson, and D. Gérard, "Lattice modes and plasmonic linewidth engineering in gold and aluminum nanoparticle arrays," *Journal of the Optical Society of America B*, vol. 34, pp. 691–700, 2017.

- [44] <https://www.ansys.com/products/photonics/fdtd>.
- [45] <https://optics.ansys.com/hc/en-us/articles/360033154434>.
- [46] <https://www.comsol.com/comsol-multiphysics>.
- [47] A. Sarangan, *Nanofabrication: principles to laboratory practice*. CRC Press, 2017.
- [48] M. Altissimo, "E-beam lithography for micro-/nanofabrication," *Biomicrofluidics*, vol. 4, p. 026503, 2010.
- [49] R. F. Peters, L. Gutierrez-Rivera, S. K. Dew, and M. Stepanova, "Surface enhanced Raman spectroscopy detection of biomolecules using EBL fabricated nanostructured substrates," *Journal of Visualized Experiments*, vol. 97, p. e52712, 2015.
- [50] A. Behnam, Y. Choi, L. Noriega, Z. Wu, I. Kravchenko, A. G. Rinzler, and A. Ural, "Nanolithographic patterning of transparent, conductive single-walled carbon nanotube films by inductively coupled plasma reactive ion etching," *Journal of Vacuum Science & Technology B*, vol. 25, pp. 348–354, 2007.
- [51] M. Tosa, "Surface profilometer," in *Compendium of surface and interface analysis* (The Surface Science Society of Japan, ed.), ch. 110, pp. 679–682, Springer, 2018.
- [52] Y. Okano, "Scanning electron microscopy," in *Compendium of surface and interface analysis* (The Surface Science Society of Japan, ed.), ch. 91, pp. 563–569, Springer, 2018.
- [53] T. Dieing, O. Hollricher, and J. Toporski, *Confocal Raman microscopy*. Springer, 2011.
- [54] C. Banwell, *Fundamentals of molecular spectroscopy*. McGraw-Hill, 1972.
- [55] K. Kneipp, H. Kneipp, I. Itzkan, R. R. Dasari, and M. S. Feld, "Surface-enhanced Raman scattering and biophysics," *Journal of Physics: Condensed Matter*, vol. 14, p. R597–R624, 2002.
- [56] E. L. Ru and P. Etchegoin, *Principles of surface-enhanced Raman spectroscopy and related plasmonic effects*. Elsevier, 2008.
- [57] A. Volkmer, "Coherent Raman scattering microscopy," in *Emerging Raman applications and techniques in biomedical and pharmaceutical fields* (P. Matousek and M. D. Morris, eds.), ch. 6, p. 111–152, Springer, 2010.
- [58] A. Volkmer, "Vibrational imaging and microspectroscopies based on coherent anti-Stokes Raman scattering microscopy," *Journal of Physics D: Applied Physics*, vol. 38, p. R59–R81, 2005.

- [59] J.-X. Cheng and X. S. Xie, "Coherent anti-Stokes Raman scattering microscopy: instrumentation, theory, and applications," *Journal of Physical Chemistry B*, vol. 108, p. 827–840, 2004.
- [60] S.-Y. Ding, E.-M. You, Z.-Q. Tian, and M. Moskovits, "Electromagnetic theories of surface-enhanced Raman spectroscopy," *Chemical Society Reviews*, vol. 46, pp. 4042–4076, 2017.
- [61] Y. Zhang, Y.-R. Zhen, O. Neumann, J. K. Day, P. Nordlander, and N. J. Halas, "Coherent anti-Stokes Raman scattering with single-molecule sensitivity using a plasmonic Fano resonance," *Nature Communications*, vol. 5, p. 4424, 2014.
- [62] A. E. Miroshnichenko, S. Flach, and Y. S. Kivshar, "Fano resonances in nanoscale structures," *Reviews of Modern Physics*, vol. 82, pp. 2257–2298, 2010.
- [63] J. Ye, F. Wen, H. Sobhani, J. B. Lassiter, P. V. Dorpe, P. Nordlander, and N. J. Halas, "Plasmonic nanoclusters: near field properties of the Fano resonance interrogated with SERS," *Nano Letters*, vol. 12, pp. 1660–1667, 2012.
- [64] M. Hentschel, D. Dregely, R. Vogelgesang, H. Giessen, and N. Liu, "Plasmonic oligomers: the role of individual particles in collective behavior," *ACS Nano*, vol. 5, pp. 2042–2050, 2011.
- [65] M. Hentschel, M. Saliba, R. Vogelgesang, H. Giessen, A. P. Alivisatos, and N. Liu, "Transition from isolated to collective modes in plasmonic oligomers," *Nano Letters*, vol. 10, pp. 2721–2726, 2010.
- [66] J. A. Fan, K. Bao, C. Wu, J. Bao, R. Bardhan, N. J. Halas, V. N. Manoharan, G. Shvets, P. Nordlander, and F. Capasso, "Fano-like interference in self-assembled plasmonic quadrumer clusters," *Nano Letters*, vol. 10, pp. 4680–4685, 2010.
- [67] J. B. Lassiter, H. Sobhani, M. W. Knight, W. S. Mielczarek, P. Nordlander, and N. J. Halas, "Designing and deconstructing the Fano lineshape in plasmonic nanoclusters," *Nano Letters*, vol. 12, pp. 1058–1062, 2012.
- [68] J. B. Lassiter, H. Sobhani, J. A. Fan, J. Kundu, F. Capasso, P. Nordlander, and N. J. Halas, "Fano resonances in plasmonic nanoclusters: geometrical and chemical tunability," *Nano Letters*, vol. 10, pp. 3184–3189, 2010.
- [69] M. Rahmani, B. Lukiyanchuk, T. Tahmasebi, Y. Lin, T. Y. F. Liew, and M. H. Hong, "Polarization-controlled spatial localization of near-field energy in planar symmetric coupled oligomers," *Applied Physics A*, vol. 107, pp. 23–30, 2012.
- [70] B. Gallinet and O. J. F. Martin, "Relation between near-field and far-field properties of plasmonic Fano resonances," *Optics Express*, vol. 19, pp. 22167–22175, 2011.

- [71] S. Zhang, D. A. Genov, Y. Wang, M. Liu, and X. Zhang, "Plasmon-induced transparency in metamaterials," *Physical Review Letters*, vol. 101, p. 047401, 2008.
- [72] F. Madzharova, Z. Heiner, M. Gühlke, and J. Kneipp, "Surface-enhanced hyper-Raman spectra of adenine, guanine, cytosine, thymine, and uracil," *Journal of Physical Chemistry C*, vol. 120, pp. 15415–15423, 2016.
- [73] C. Wu, E. Chen, and J. Wei, "Surface enhanced Raman spectroscopy of rhodamine 6G on agglomerates of different-sized silver truncated nano-triangles," *Colloids and Surfaces A: Physicochemical and Engineering Aspects*, vol. 506, pp. 450–456, 2016.
- [74] Y. Kalachyova, D. Mares, O. Lyutakov, M. Kostejn, L. Lapcak, and V. Švorčík, "Surface plasmon polaritons on silver gratings for optimal SERS response," *Journal of Physical Chemistry C*, vol. 119, pp. 9506–9512, 2015.
- [75] M. Kahl and E. Voges, "Analysis of plasmon resonance and surface-enhanced Raman scattering on periodic silver structures," *Physical Review B*, vol. 61, pp. 14078–14088, 2000.
- [76] H. Raether, *Surface plasmons on smooth and rough surfaces and on gratings*. Springer, 1988.
- [77] I. Baltog, N. Primeau, R. Reinisch, and J. L. Coutaz, "Surface enhanced Raman scattering on silver grating: optimized antennalike gain of the Stokes signal of 10^4 ," *Applied Physics Letters*, vol. 66, pp. 1187–1189, 1995.
- [78] X. Deng, G. B. Braun, S. Liu, P. F. Sciortino, B. Koefer, T. Tombler, and M. Moskovits, "Single-order subwavelength resonant nanograting as a uniformly hot substrate for surface-enhanced Raman spectroscopy," *Nano Letters*, vol. 10, pp. 1780–1786, 2010.
- [79] A. I. Radu, M. Kuellmer, B. Giese, U. Huebner, K. Weber, D. Cialla-May, and J. Popp, "Surface-enhanced Raman spectroscopy (SERS) in food analytics: detection of vitamins B₂ and B₁₂ in cereals," *Talanta*, vol. 160, pp. 289–297, 2016.
- [80] Q. Zhou, J. Zhu, J. Yuan, and X. Fang, "Numerical simulation of surface-enhanced coherent anti-Stokes Raman scattering on gold nanoparticle substrate," *Journal of Nanoscience and Nanotechnology*, vol. 17, pp. 2152–2156, 2017.
- [81] J. He, C. Fan, P. Ding, S. Zhu, and E. Liang, "Near-field engineering of Fano resonances in a plasmonic assembly for maximizing CARS enhancements," *Scientific Reports*, vol. 6, p. 20777, 2016.
- [82] K. Hashimoto, J. Omachi, and T. Ideguchi, "Ultra-broadband rapid-scan Fourier-transform CARS spectroscopy with sub-10-fs optical pulses," *Optics Express*, vol. 26, pp. 14307–14314, 2018.

- [83] M. Nyman, A. Shevchenko, I. Shavrin, Y. Ando, K. Lindfors, and M. Kaivola, "Large-area enhancement of far-field fluorescence intensity using planar nanostructures," *APL Photonics*, vol. 4, p. 076101, 2019.
- [84] P. A. Hobson, W. L. Barnes, D. G. Lidzey, G. A. Gehring, D. M. Whittaker, M. S. Skolnick, and S. Walker, "Strong exciton–photon coupling in a low-Q all-metal mirror microcavity," *Applied Physics Letters*, vol. 81, pp. 3519–3521, 2002.
- [85] A. V. Kavokin, A. S. Sheremet, I. A. Shelykh, P. G. Lagoudakis, and Y. G. Rubo, "Exciton-photon correlations in bosonic condensates of exciton-polaritons," *Scientific Reports*, vol. 5, p. 12020, 2015.
- [86] J. J. Hopfield, "Theory of the contribution of excitons to the complex dielectric constant of crystals," *Physical Review*, vol. 112, pp. 1555–1567, 1958.
- [87] T. W. Ebbesen, "Hybrid light–matter states in a molecular and material science perspective," *Accounts of Chemical Research*, vol. 49, pp. 2403–2412, 2016.
- [88] J. Fregoni, G. Granucci, E. Coccia, M. Persico, and S. Corni, "Manipulating azobenzene photoisomerization through strong light–molecule coupling," *Nature Communications*, vol. 9, p. 4688, 2018.
- [89] J. Galego, F. J. Garcia-Vidal, and J. Feist, "Suppressing photochemical reactions with quantized light fields," *Nature Communications*, vol. 7, p. 13841, 2016.
- [90] D. M. Coles, N. Somaschi, P. Michetti, C. Clark, P. G. Lagoudakis, P. G. Savvidis, and D. G. Lidzey, "Polariton-mediated energy transfer between organic dyes in a strongly coupled optical microcavity," *Nature Materials*, vol. 13, p. 712–719, 2014.
- [91] K. Georgiou, P. Michetti, L. Gai, M. Cavazzini, Z. Shen, and D. G. Lidzey, "Control over energy transfer between fluorescent BODIPY dyes in a strongly coupled microcavity," *ACS Photonics*, vol. 5, pp. 258–266, 2018.
- [92] X. Zhong, T. Chervy, L. Zhang, A. Thomas, J. George, C. Genet, J. A. Hutchison, and T. W. Ebbesen, "Energy transfer between spatially separated entangled molecules," *Angewandte Chemie International Edition*, vol. 56, pp. 9034–9038, 2017.
- [93] K. Stranius, M. Hertzog, and K. Börjesson, "Selective manipulation of electronically excited states through strong light–matter interactions," *Nature Communications*, vol. 9, p. 2273, 2018.
- [94] E. Eizner, L. A. Martínez-Martínez, J. Yuen-Zhou, and S. Kéna-Cohen, "Inverting singlet and triplet excited states using strong light-matter coupling," *Science Advances*, vol. 5, p. eaax4482, 2019.

- [95] A. M. Berghuis, A. Halpin, Q. Le-Van, M. Ramezani, S. Wang, S. Murai, and J. G. Rivas, "Enhanced delayed fluorescence in tetracene crystals by strong light-matter coupling," *Advanced Functional Materials*, vol. 29, p. 1901317, 2019.
- [96] J. Fregoni, F. J. Garcia-Vidal, and J. Feist, "Theoretical challenges in polaritonic chemistry," *ACS Photonics*, vol. 9, pp. 1096–1107, 2022.
- [97] V. M. Agranovich, M. Litinskaia, and D. G. Lidzey, "Cavity polaritons in microcavities containing disordered organic semiconductors," *Physical Review B*, vol. 67, p. 085311, 2003.
- [98] G. Groenhof, C. Climent, J. Feist, D. Morozov, and J. J. Toppari, "Tracking polariton relaxation with multiscale molecular dynamics simulations," *Journal of Physical Chemistry Letters*, vol. 10, pp. 5476–5483, 2019.
- [99] D. LeGourri rec, V. Kharlanov, R. G. Brown, and W. Rettig, "Excited-state intramolecular proton transfer (ESIPT) in 2-(2'-hydroxyphenyl)pyridine and some carbon-bridged derivatives," *Journal of Photochemistry and Photobiology A: Chemistry*, vol. 117, pp. 209–216, 1998.
- [100] H. Marciniak, S. Hristova, V. Deneva, F. S. Kamounah, P. E. Hansen, S. Lochbrunner, and L. Antonov, "Dynamics of excited state proton transfer in nitro substituted 10-hydroxybenzo[h]quinolines," *Physical Chemistry Chemical Physics*, vol. 19, pp. 26621–26629, 2017.
- [101] G. Groenhof and J. J. Toppari, "Coherent light harvesting through strong coupling to confined light," *Journal of Physical Chemistry Letters*, vol. 9, pp. 4848–4851, 2018.
- [102] J. E. Kwon and S. Y. Park, "Advanced organic optoelectronic materials: harnessing excited-state intramolecular proton transfer (ESIPT) process," *Advanced Materials*, vol. 23, pp. 3615–3642, 2011.
- [103] S. K. Saikin, A. Eisfeld, S. Valleau, and A. Aspuru-Guzik, "Photonics meets excitonics: natural and artificial molecular aggregates," *Nanophotonics*, vol. 2, pp. 21–38, 2013.
- [104] D. Poelman and P. F. Smet, "Methods for the determination of the optical constants of thin films from single transmission measurements: a critical review," *Journal of Physics D: Applied Physics*, vol. 36, pp. 1850–1857, 2003.
- [105] A. B. Djuri i c, T. Fritz, and K. Leo, "Modelling the optical constants of organic thin films: impact of the choice of objective function," *Journal of Optics A: Pure and Applied Optics*, vol. 2, pp. 458–464, 2000.
- [106] S. S. Falahatgar and F. E. Ghodsi, "A developed model for the determination of the dielectric function for some absorbing thin films using pseudo-Urbach tail," *Physica B: Condensed Matter*, vol. 412, pp. 4–11, 2013.

- [107] C. C. Kim, J. W. Garland, H. Abad, and P. M. Raccah, "Modeling the optical dielectric function of semiconductors: extension of the critical-point parabolic-band approximation," *Physical Review B*, vol. 45, pp. 11749–11767, 1992.
- [108] A. B. Djurišić, T. Fritz, and K. Leo, "Modeling the optical constants of organic thin films: application to 3,4,9,10-perylenetetracarboxylic dianhydride (PTCDA)," *Optics Communications*, vol. 183, pp. 123–132, 2000.
- [109] K. Takatori, T. Okamoto, K. Ishibashi, and R. Micheletto, "Surface exciton polaritons supported by a J-aggregate-dye/air interface at room temperature," *Optics Letters*, vol. 42, pp. 3876–3879, 2017.
- [110] Y. Xu, L. Wu, and L. K. Ang, "Surface exciton polaritons: a promising mechanism for refractive-index sensing," *Physical Review Applied*, vol. 12, p. 024029, 2019.
- [111] M. J. Gentile, S. A. R. Horsley, and W. L. Barnes, "Localized exciton–polariton modes in dye-doped nanospheres: a quantum approach," *Journal of Optics*, vol. 18, p. 015001, 2016.
- [112] M. J. Gentile and W. L. Barnes, "Hybridised exciton–polariton resonances in core–shell nanoparticles," *Journal of Optics*, vol. 19, p. 035003, 2017.
- [113] A. Cacciola, C. Triolo, O. D. Stefano, A. Genco, M. Mazzeo, R. Saija, S. Patanè, and S. Savasta, "Subdiffraction light concentration by J-aggregate nanostructures," *ACS Photonics*, vol. 2, pp. 971–979, 2015.
- [114] S. T. Holder, C. Estévez-Varela, I. Pastoriza-Santos, M. Lopez-Garcia, R. Oulton, and S. Núñez-Sánchez, "Bio-inspired building blocks for all-organic metamaterials from visible to near-infrared," *Nanophotonics*, vol. 12, pp. 307–318, 2023.
- [115] G. Zengin, G. Johansson, P. Johansson, T. J. Antosiewicz, M. Käll, and T. Shegai, "Approaching the strong coupling limit in single plasmonic nanorods interacting with J-aggregates," *Scientific Reports*, vol. 3, p. 3074, 2013.
- [116] W. J. Tan, P. A. Thomas, I. J. Luxmoore, and W. L. Barnes, "Single vs double anti-crossing in the strong coupling between surface plasmons and molecular excitons," *Journal of Chemical Physics*, vol. 154, p. 024704, 2021.
- [117] W. Li, R. Liu, and X. Wang, "Anomalous spectral response of plasmon-exciton strong coupling beyond J-C model," *Results in Physics*, vol. 31, p. 105064, 2021.
- [118] D. G. Baranov, B. Munkhbat, E. Zhukova, A. Bisht, A. Canales, B. Rousseaux, G. Johansson, T. J. Antosiewicz, and T. Shegai, "Ultrastrong coupling between nanoparticle plasmons and cavity photons at ambient conditions," *Nature Communications*, vol. 11, p. 2715, 2020.

- [119] B. C. Yildiz, M. Habib, A. R. Rashed, and H. Caglayan, "Hybridized plasmon modes in a system of metal thin film–nanodisk array," *Journal of Applied Physics*, vol. 126, p. 113104, 2019.

ORIGINAL PAPERS

PI

INFLUENCE OF FANO RESONANCE ON SERS ENHANCEMENT IN FANO-PLASMONIC OLIGOMERS

by

A. Dutta, K. Alam, T. Nuutinen, E. Hulkko, P. Karvinen, M. Kuittinen, J. J.
Toppari, and E. M. Vartiainen,

Optics Express, **27**, 30031 (2019).

Reproduced with kind permission of Optica Publishing Group.



Influence of Fano resonance on SERS enhancement in Fano-plasmonic oligomers

ARPAN DUTTA,^{1,6} KHAIRUL ALAM,^{2,8} TARMO NUUTINEN,^{2,3,8} EERO HULKKO,^{1,4} PETRI KARVINEN,² MARKKU KUITTINEN,² J. JUSSI TOPPARI,^{1,7} AND ERIK M. VARTIAINEN⁵

¹Nanoscience Center and Department of Physics, University of Jyväskylä, FI-40014 University of Jyväskylä, Finland

²Institute of Photonics, University of Eastern Finland (UEF), FI-80101 Joensuu, Finland

³Department of Environmental and Biological Sciences, UEF, FI-80101 Joensuu, Finland

⁴Department of Electronics and Nanoengineering, Aalto University, FI-02150 Espoo, Finland

⁵School of Engineering Science, LUT University, FI-53851 Lappeenranta, Finland

⁶arpan.a.dutta@jyu.fi

⁷j.jussi.toppari@jyu.fi

⁸These authors contributed equally

Abstract: Plasmonic oligomers can provide profound Fano resonance in their scattering responses. The sub-radiant mode of Fano resonance can result in significant near-field enhancement due to its light trapping capability into the so-called hotspots. Appearance of these highly localized hotspots at the excitation and/or Stokes wavelengths of the analytes makes such oligomers promising SERS active substrates. In this work, we numerically and experimentally investigate optical properties of two disk-type gold oligomers, which have different strength and origin of Fano resonance. Raman analysis of rhodamine 6G and adenine with the presence of the fabricated oligomers clearly indicates that an increment in the strength of Fano resonance can improve the Raman enhancement of an oligomer significantly. Therefore, by suitable engineering of Fano lineshape, one can achieve efficient SERS active substrates with spatially localized hotspots.

© 2018 Optical Society of America under the terms of the [OSA Open Access Publishing Agreement](#)

1. Introduction

Raman spectroscopy is nowadays a standard method for investigating the structural information of the materials [1,2]. Raman spectrum contains information about the vibrational and the rotational states in the molecular system of a probed material [3]. Extraction of such a chemical ‘fingerprint’ enables the use of Raman spectroscopy in different scientific and industrial applications ranging from ultra-violet (UV) to near-infrared (NIR) region [4,5]. Despite all acclaimed advantages of Raman spectroscopy, its real-life implementation is somewhat limited due to its low efficiency and sensitivity when compared, e.g., to fluorescence spectroscopy [6].

The observation of an intense Raman response at the presence of a silver electrode by Fleischmann and co-workers in 1974 [7], and the theoretical explanation of the phenomenon by Van Duyne et al. in 1977 [6], opened an efficient way to enhance the Raman signal with the help of subwavelength metallic structures [8-11]. That is, the presence of a plasmonic substrate leads to vastly enhanced Raman signal, i.e., Surface-Enhanced Raman Scattering (SERS) [12-14]. Advancement in nanofabrication technologies, specifically in electron-beam and focused-ion beam lithography, makes the realization of SERS active substrates with predefined sizes, shapes, and the material properties so accurate that SERS has become a popular method in bio-sensing [15-17], and in single molecule detection [18-21].

Suitable engineering of plasmonic resonances in complex photonic structures can optimize the enhancement of Raman response of a material. Generation of Fano resonance (FR) in a coupled plasmonic system is one way to do it [22]. Fano resonance is an asymmetric non-

Lorentzian resonance formed as an interference between a broad continuum state and a narrow discrete state [23-28]. It was first reported in 1935 when found in the absorption spectra of noble gases [23-27]. Even though FR had its implementation mainly in quantum systems in the past decades, it can also be generated profoundly in plasmonic oligomers [29-31].

Plasmonic oligomers are clusters of metallic nanoparticles (NP) where size, shape, and interparticle distance are specially arranged to obtain the desired optical response. Presence of multiple nanoparticles very close to each other induces interference and coupling between the localized surface plasmon resonances (LSPR) of individual NPs. Such hybridization of particle plasmon modes opens the possibility of having profound FR in the scattering or extinction profile of the system [30,31]. In a plasmonic oligomer, when the plasmon oscillations of all particles are in phase, they interfere constructively and the net dipole moment of the structure increases. Such collective mode provides a broad peak in the scattering spectrum that is often called as the super-radiant mode or bright mode. The dark mode or the sub-radiant mode is found as a dip in the scattering profile and is generated due to the destructive interference between the LSPR modes of individual particles when the plasmon oscillations are not in phase and the net dipole moment decreases [32-35]. The depth of the Fano dip indicates the strength of the coupling between LSPR modes of the nanoparticles and can be modulated by varying the gap between the particles [31]. When the gaps between the particles widen, the coupling between the plasmon modes of each particle reduces and the Fano dip starts to disappear. If the gap becomes very small, the coupling greatly enhances and the depth of the Fano dip almost reaches to the zero level, which is referred as the plasmon-induced transparency [36]. The spectral position of FR can be tuned by controlling the structural and chemical properties of the oligomer such as size, shape, thickness and material of the particles present in the oligomer while the gap between the particles defines the strength of the coupling [31,37].

The sub-radiant (or dark) mode in a Fano resonant plasmonic system can significantly enhance the near-field intensity within the nanostructure due to its non-radiative nature and capability to trap energy at the gaps between the particles [38]. The highest near-field intensity is always obtained near the Fano dip or Fano window [39], and consequently, Fano-plasmonic structures can provide large Raman enhancements when the FR is tuned with the excitation frequency and the targeted Stokes frequencies of the analytes [22]. Origin of FR in a plasmonic oligomer can be explained theoretically with the help of multiple approaches such as the coupled oscillator model [40-42], the subgroup decomposition of plasmonic resonances [35,43], the circuit model of Fano resonance [44], and the rigorous quantum electrodynamic formulation [45].

In this article, we report on the SERS activity of two disk-type gold oligomers, a trimer and a pentamer, which have profound FR in their scattering profile but with different origin and strength. The origin of FR in the pentamer is purely electric in nature [38,42,46-48], while FR in the trimer is generated due to the interaction between the electric and the magnetic plasmon modes [49-52]. The strength of FR, which can be identified by the depth of the Fano dip, is higher in the pentamer than in the trimer. The oligomers were numerically modelled using the finite element method (FEM) to tune their FR into the targeted Raman signals of two Raman active analytes, 1360 cm^{-1} for rhodamine 6G [53], and 734 cm^{-1} for adenine [54]. Optical characterization of the fabricated oligomers showed agreement with the simulated responses and ensured deeper Fano dip in the pentamer than in the trimer. Raman spectroscopy of rhodamine 6G and adenine with the presence of the oligomers showed higher SERS intensity in the case of the pentamer than with the trimer for both analytes. Our experimental findings show how the strength of FR, in terms of the depth of the Fano dip, directly influences the SERS activity of the oligomer when it is tuned with the targeted Raman region of the analytes. Such investigation on the dependence of SERS enhancement on the strength of FR in plasmonic oligomers having different Fano origin is not reported earlier for our knowledge.

2. Methods

2.1 Numerical simulations

Optical responses of the plasmonic oligomers were calculated and optimized numerically with FEM-based commercial software package (COMSOL Multiphysics version 5.1). In the computation, a single oligomer was placed on top of a glass substrate, and it was surrounded by air. The perfectly matched layers were used at all the boundaries of the $2\ \mu\text{m} \times 2\ \mu\text{m} \times 2\ \mu\text{m}$ simulation space to prevent any reflections. The optical response of the oligomer, at the near- and far-field, for the normal incidence of light with electric field along the oligomer's main axis as illustrated in Fig. 1, was computed using the scattered-field formulation module of COMSOL [55]. The material model for gold was extracted from the measured optical constants recorded by Johnson and Christy [56]. The nondispersive refractive indices of air and glass (SiO_2) were considered as 1.0000 and 1.4585, respectively.

2.2 Fabrication

The plasmonic oligomers were fabricated using electron beam lithography and lift-off process. A 0.5 mm thick silicon (Si) wafer, with a 100 nm thick 'thermally grown' silicon dioxide (SiO_2) layer on it, was used as a substrate. A standard positive e-beam resist (AR-P 6200) was initially spin-coated on the substrate. The resist was patterned in an e-beam lithography system (Raith EBPG 5000+) according to the optimized design parameters obtained from the numerical simulations. Thermal evaporation method was used to deposit a uniform gold layer with a thickness of 20 nm on the patterned substrate, after which the resist was removed in a solvent resulting in gold structures on SiO_2 . The schematics of the fabricated trimers and pentamers are shown in Fig. 1. The structures were organized as a square array on the substrate with a gap of $2\ \mu\text{m}$ between each oligomer both in x and y directions to ensure prevention of any kind of coupling between them. Scanning electron microscope (SEM) imaging was used (SEMleo1550Gemini operated at an accelerated voltage of 5 kV) to determine the structures of the fabricated samples.

2.3 Optical characterization

Fabricated oligomers were characterized with a custom build optical setup where a white light source (Oriel 66182) was used to illuminate the array of gold trimers and pentamers. The light coming from the lamp was pseudo-collimated at best and two irises were used to align it. Rotatable Glan-Taylor polarizer was used to select the polarization of the excitation light. The scattering profiles of the oligomers were recorded by tracing the peak intensities of the reflected first diffraction order of the oligomer array at different angular positions by using a full 360° rotatable detection arrangement (F220SMA-A/ThorLabs, $f = 10.9\ \text{mm}$, $\text{NA} = 0.25$). The angle-resolved scattering was collected with an optical fiber connected to a spectrometer (Jobin Yvon iHR320) equipped with a CCD camera (Jobin Yvon Symphony). More details about the optical setup can be found elsewhere [57-59].

2.4 Raman spectroscopy of analytes

Raman responses of rhodamine 6G and adenine for both kinds of oligomers were collected using a commercially available Raman setup (Renishaw inVia confocal Raman microscope) where a continuous-wave gas laser with an emission wavelength of 785 nm was used as an excitation source. A numerical objective (100X, $\text{NA} = 0.85$) was used to illuminate the sample for 30 s with 3.10 mW excitation power and to collect the Stokes-shifted signal. The correct polarization of the tightly focused excitation beam with $1\ \mu\text{m}$ (approximated) spot size was maintained by rotating the sample stage. The analytes were deposited on the substrates with fabricated trimers and pentamers within a $10\ \mu\text{L}$ water droplet and then incubated at room temperature under normal humidity for 5 minutes until the drop had dried. The initial

concentrations of the analytes in solution were 1 μM for rhodamine 6G (R6G) and 1 mM for adenine (Ade).

3. Results and discussion

Plasmonic oligomers were optimized using FEM-based simulations so that their FR would overlap with the targeted Raman signature zones of the analytes (1360 cm^{-1} for rhodamine 6G [53] and 734 cm^{-1} for adenine [54]) when excited with the wavelength of the Raman experiment (785 nm). The trimer, depicted in Fig. 1(a), contains a pair of identical disks having a radius of 50 nm along with a larger disk with a radius of 100 nm. The pentamer, presented in Fig. 1(b), contains a chain of three identical disks having a radius of 75 nm and two small identical disks with a radius of 62.5 nm on the top and the bottom of the central disk of the chain. The gap between the disks and the thickness (or height) of the disks are kept 20 nm in both oligomers to ensure that the difference between the strength of FR in those oligomers did not occur due to the difference in their interparticle distances and thicknesses. All geometric parameters related to the disks (i.e. interparticle gap, thickness and disk radius) had fabrication tolerances of $\pm 5\text{ nm}$ obtained from the numerical simulations.

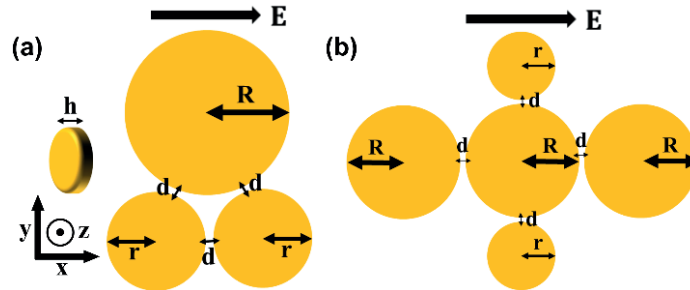


Fig. 1. (a) Optimized geometry for the trimer with $R = 100 \pm 5\text{ nm}$, $r = 50 \pm 5\text{ nm}$, $d = 20 \pm 5\text{ nm}$, $h = 20 \pm 5\text{ nm}$. (b) Optimized geometry for the pentamer with $R = 75 \pm 5\text{ nm}$, $r = 62.5 \pm 5\text{ nm}$, $d = 20 \pm 5\text{ nm}$, $h = 20 \pm 5\text{ nm}$. All geometric parameters related to the disks (i.e. interparticle gap, thickness and disk radius) had fabrication tolerances of $\pm 5\text{ nm}$ obtained from the numerical simulations. The arrows on top of the structures show the polarization of the excitation.

The existence of FR and its overlap with the intended spectral regimes are clearly seen in the simulated scattering cross-sections of the oligomers, presented in Fig. 2(a) after normalized by their geometrical cross-sections. The strength of FR, in terms of the depth of the Fano dip, can be quantified by a parameter k , which defines the ratio between the scattering cross-sections (or scattering intensities) at the Fano dip ($S_{\text{Fano dip}}$) and at the Fano peak ($S_{\text{Fano peak}}$), i.e. $k = S_{\text{Fano dip}}/S_{\text{Fano peak}}$. The pentamer shows a lower value of k ($k=0.21$) than the trimer ($k=0.43$) in the simulated spectra and hence, provides higher depth in FR and stronger FR than the trimer. The spectral profiles of the total near-field intensity enhancement (NFIE) for the oligomers were calculated as $|E_{\text{loc}}/E_0|^2$ integrated over the illuminated surfaces of the oligomers (i.e. the top and sides of the disks), where E_{loc} and E_0 are the local and incident electric field amplitudes, respectively. The NFIE profiles, normalized by the geometrical surface area of the corresponding illuminated surfaces, are depicted in Fig. 2(b). They yield higher enhancement in the case of the pentamer than in the case of the trimer. The spectral position of the highest enhancement was found close to the Fano dip in the scattering spectra for both oligomers. Such spectral correlation between the scattering minima and the NFIE maxima is a general property of systems having FR [39], and has been reported earlier also for different kind of structures [22].

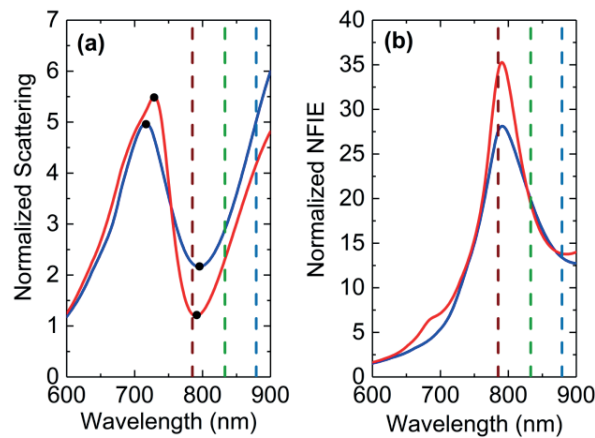


Fig. 2. (a) Simulated scattering cross-sections of the trimer (blue line) and the pentamer (red line). The black dots represent the position of the peak and the dip in the corresponding spectra used to calculate k . (b) Simulated NFIE of the trimer (blue line) and the pentamer (red line). The red, green and blue dashed lines in both diagrams represent, the excitation wavelength (785 nm), the targeted Raman line of adenine (734 cm^{-1} or 833 nm) and the targeted Raman line of rhodamine 6G (1360 cm^{-1} or 879 nm), respectively.

The near-field enhancement (NFE) maps $|E_{\text{loc}}/E_0|$ for the trimer and the pentamer, computed at a plane 1 nm above the top surfaces of the oligomers and presented in Fig. 3, show the spatial distribution of the NFE at the wavelengths of Fano dips and Fano peaks. The NFEs obtained at Fano dips (790 nm for the pentamer and 795 nm for the trimer) are higher than those of at Fano peaks (728 nm for the pentamer and 716 nm for the trimer) for both oligomers and their spatial distribution yields ‘hotspots’, i.e. confined regions with localized electromagnetic energy, at the gaps between the disks. In the trimer, the hotspots are found at the gap between the two small disks, showed in Fig. 3(a) and Fig. 3(b). In the pentamer, they situate at the gaps in the chain of the three identical disks, illustrated in Fig. 3(e) and Fig. 3(f), and they spatially overlap at both dip and peak wavelengths. The spatial locations of the hotspots at different wavelengths are not identical in general and are often distributed differently over the sample geometry [51]. Spatial overlap of the hotspots at multiple wavelengths is important for SERS applications since the electromagnetic enhancement factor (EEF) for SERS is defined as $\text{SERS EEF} = |E_{\text{loc}(\text{excitation})}/E_0|^2 \times |E_{\text{loc}(\text{Stokes})}/E_0|^2$ i.e. the product of the NFEs at the excitation and Stokes wavelengths [22]. Thus, spatially coinciding hotspots of these two wavelengths will yield the highest enhancement. The spatial distribution of the SERS EEFs (or SERS maps) for both oligomers at the targeted Raman signature zones of the analytes are reported in Fig. 3. From the figure we can see that the maximum SERS electromagnetic enhancement factors are about 3×10^6 for the trimer and 5×10^6 for the pentamer. Both of them are achieved for the 734 cm^{-1} Raman line of adenine.

Origin of FR in the trimer and the pentamer was investigated by computing the surface charge densities and the conduction current densities over the top surfaces of the disks. The surface charge density plots for the pentamer presented in Fig. 4 clearly show ‘in-phase’ plasmon oscillations in all disks at Fano peak (728 nm), shown in Fig. 4(a), but ‘out of phase’ oscillation in the central disk with respect to the other four disks at Fano dip (790 nm), shown in Fig. 4(b). This clearly explains generation of the broad super-radiant mode at 728 nm and the sub-radiant mode at 790 nm in the corresponding scattering profile. We can also infer that the nature of FR in the pentamer is purely electric since the interaction between the electric dipole moments causes the generation of FR [38,42,46-48].

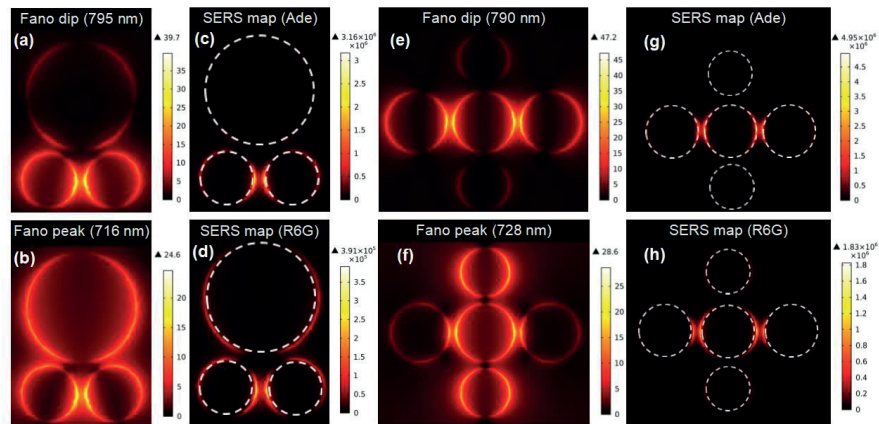


Fig. 3. Simulated NFE and SERS EEF maps calculated at a plane 1 nm above the top surface of the oligomers. (a-b) NFE plots for the trimer at Fano dip (795 nm) and Fano peak (716 nm). (c-d) SERS EEF maps of the trimer for the targeted Raman band of adenine (734 cm^{-1} or 833 nm) and rhodamine 6G (1360 cm^{-1} or 879 nm). (e-f) NFE plots for the pentamer at Fano dip (790 nm) and Fano peak (728 nm). (g-h) SERS EEF maps of the pentamer for the targeted Raman band of adenine (734 cm^{-1} or 833 nm) and rhodamine 6G (1360 cm^{-1} or 879 nm). In the plots (c-d) and (g-h), the white dashed lines represent the gold disks in the oligomer and for SERS EEF calculation, the excitation wavelength was considered as 785 nm . In (a-d) all the dimensions are along Fig. 1(a) and in (e-h) as illustrated in Fig. 1(b).

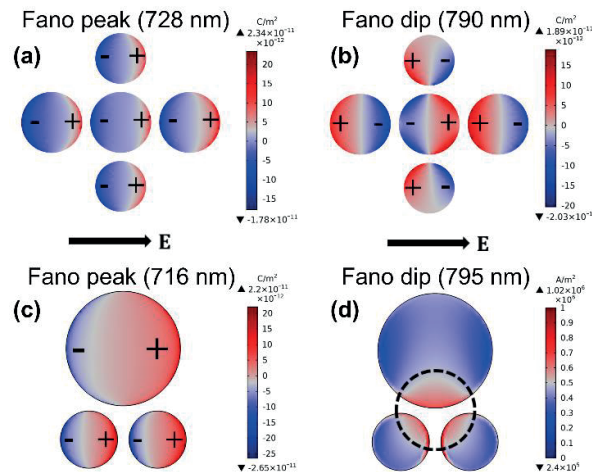


Fig. 4. Simulated surface charge densities and conduction current densities over the top surfaces of the disks present in the oligomers. (a-b) Surface charge density plots for the pentamer at Fano peak (728 nm) and Fano dip (790 nm). (c) Surface charge density plot for the trimer at Fano peak (716 nm). (d) Conduction current density plot for the trimer at Fano dip (795 nm). In the plots (a-d), the black arrows represent the polarization of the excitation electric field E .

The surface charge density plot for the trimer, depicted in Fig. 4(c), shows ‘in-phase’ plasmon oscillations in all disks at 716 nm and explains the creation of the broad super-radiant mode at that wavelength in corresponding scattering profile. The current density plot for the trimer at Fano dip (795 nm), illustrated in Fig. 4(d), reveals the presence of a ‘coil type’ magnetic resonant mode at 795 nm which has a sub-radiant nature in the scattering profile. Hence, the super-radiant mode in the trimer is electric in nature while the sub-radiant mode is magnetic (coil-type) and FR is originated from their hybridization [49-52].

The fabricated trimers and pentamers were arranged in a rectangular array with a gap of 2 μm between two adjacent oligomers to prevent direct crosstalk between them. The SEM images of the fabricated samples are presented in Fig. 5. Such oligomer arrays can be considered as periodic structures (reflective gratings) with a period of 2 μm and hence, they provide diffraction orders in their scattered light with scattering angle depending on wavelength. Of particular note is that in both fabricated structures, i.e. in the trimer and the pentamer (Fig. 5), the gaps between the bigger particles are slightly decreased due to the proximity effect in electron beam lithography. This effect was taken into account on the simulations also.

To determine the scattering intensity spectrum of the trimers and the pentamers, the first diffraction orders of the arrays were recorded at different angular positions, i.e., increment in the angle of detection redshifts the first diffraction order while its peak intensity follows the line shape of the scattering profile of an individual oligomer. To be specific, the intensity of the first diffraction order reached its minimum at an angle corresponding to the Fano dip, since, at that region, the nanostructures have a minimum in their scattering profile. Therefore, the peak intensities of the first diffraction order at different detection angles provide an intensity envelope from which the scattering profiles of the trimer and the pentamer can be extracted. The recorded peak intensities were normalized by dividing them with the lamp intensity at the corresponding spectral positions. The normalized intensities were further Lambertian corrected by dividing them with a cosine of the corresponding detection angle.

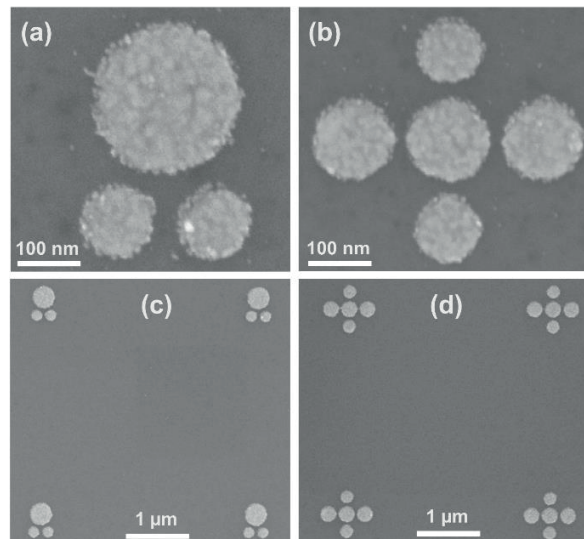


Fig. 5. SEM images of the fabricated oligomers. (a-b) SEM images of a single trimer and a single pentamer. (c-d) SEM images of the arrays of the trimer and the pentamer with 2 μm gap between two adjacent oligomers both in x and y direction.

Figure 6 shows the experimentally obtained scattering spectrum of the trimer and the pentamer along with their simulated estimations. The experimental spectra contain squares connected by dotted lines where the squares represent the measured peak intensities of the first diffraction order (normalized and Lambertian corrected) at different detection angles (and hence, at different spectral positions) thus forming the scattering intensity profiles of the oligomers. The experimental scattering profiles of the oligomers are in a good agreement with the simulated estimations and the pentamer shows stronger FR by yielding a lower value of k ($k=0.25$) than that of the trimer ($k=0.46$) in the experimental spectra.

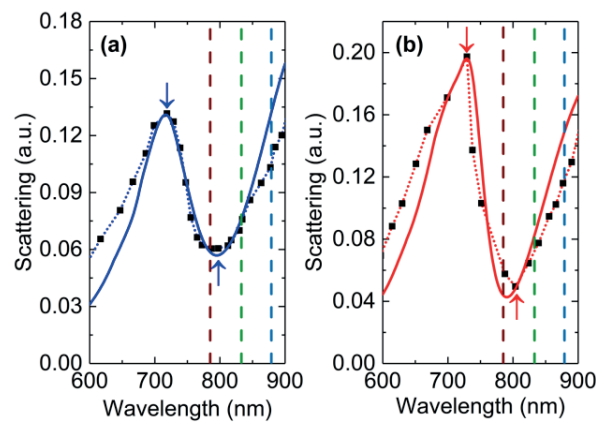


Fig. 6. (a) Simulated (solid blue line) scattering cross-section and experimental (dotted blue line) scattering intensity profiles of the trimer. (b) Simulated (solid red line) scattering cross-section and experimental (dotted red line) scattering intensity profiles of the pentamer. The simulated spectra are scaled with the experimental ones. The black squares in the experimental spectra represent the peak intensities of the first diffraction order (normalized and Lambertian corrected) collected at different detection angles. The red and blue arrows represent the position of the peak and the dip in the corresponding spectra used to calculate k . The red, green and blue (vertical) dashed lines in both diagrams represent, the excitation wavelength (785 nm), the targeted Raman line of adenine (734 cm^{-1} or 833 nm) and the targeted Raman line of rhodamine 6G (1360 cm^{-1} or 879 nm), respectively. For comparison between experimental scattering intensities of the trimer and the pentamer, please find Fig. 8 in Appendix.

To study the effect of FR on the SERS performance of the oligomers, we performed Raman spectroscopy of two Raman active analytes, adenine (Ade) and rhodamine 6G (R6G), on top of the trimers and the pentamers with an excitation at 785 nm. Our targeted Raman bands were the symmetric ring-breathing mode of adenine [54] around 734 cm^{-1} and C – C stretching mode (vibrational) of rhodamine 6G [53] around 1360 cm^{-1} . Collected SERS spectra were baseline-corrected using the asymmetric least squares algorithm for the baseline analysis [60] and smoothed using the Savitzky–Golay smoothing technique [61,62], both implemented by a commercially available data analysis software OriginPro 2017 [63]. The main areas of interest in Raman shifts were $1300 - 1400\text{ cm}^{-1}$ for R6G and $700 - 800\text{ cm}^{-1}$ for Ade during the collection. The resulting SERS spectra are presented in Fig. 7 and they are consistent with the existing literature [53,54,64-67]. The SERS spectrum of R6G shows also the N – H in-plane bend mode around 1312 cm^{-1} in addition to the targeted C – C vibrational stretching at 1363 cm^{-1} . No Raman signal was observed with the same amount of molecule, but without the oligomers.

Clearly, from Fig. 7, we can conclude that the pentamer, which has stronger FR in its simulated and experimental scattering profiles (in terms of the depth of the Fano dip, i.e., lower value of k) than the trimer, yielded stronger SERS signal than that of the trimer under the identical experimental conditions for both analytes. The obtained relative increases in the intensities of the targeted Raman lines were about 130% and even 330% for R6G and Ade, respectively. It should be noted that even the surface area of the pentamer is about 65% higher than that of the trimer, it would only account for a 65% increase in the SERS signal, when assuming constant surface concentration of the molecules, which is a reasonable assumption here. This is clearly not enough to explain the observed effect. In addition, the SERS signal of Ade is clearly higher than that of R6G, which could be due to the better matching of the FR to the targeted Raman line, but since the experimental conditions between different molecules differ, no proper conclusion can be drawn from that. Yet, the relative increase in the Raman line intensity when comparing the pentamer to the trimer is significantly higher for Ade, which can be addressed to the fact that the Raman line of Ade matches with the Fano-resonance, while

R6G Raman lines lie off from the resonance. The fact that the difference in SERS enhancement between the oligomers is higher for the Raman lines at FR than for the lines outside the resonance, implies that it is indeed the subradiant Fano mode that induces the highest SERS enhancement.

In this study, we did not focus to quantify explicitly any SERS enhancement factor for the trimer and the pentamer. However, since the detection sensitivity and number of molecules were same for one type of molecule and only the underlying nanostructure was changed, the induced increase in the SERS signal directly reflects the relative increase in the enhancement factor due to the oligomer properties. Thus, the above-mentioned experimental outcomes clearly present how the strength of FR directly influences the SERS activity of a plasmonic oligomer. Therefore, by engineering the strength of FR with a higher depth of Fano dip (or lower value of k) and by spectral tuning of FR at the targeted Raman region of the analytes as well as at the excitation wavelength, one can achieve higher SERS performance from a plasmonic oligomer.

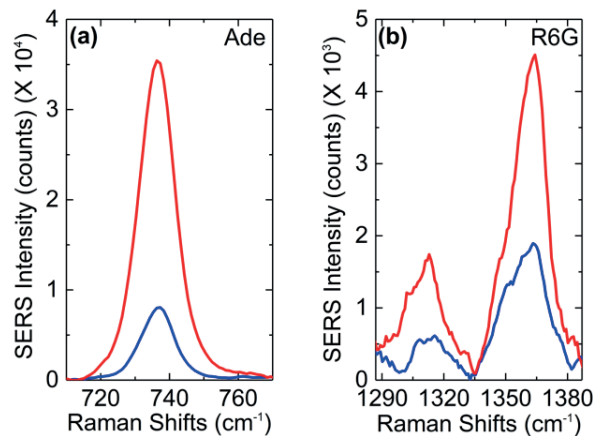


Fig. 7. (a) SERS intensity spectrum of the targeted Raman line of adenine (734 cm^{-1}) with the presence of the trimer (blue line) and the pentamer (red line). (b) SERS intensity spectrum of the targeted Raman lines of rhodamine 6G (1310 cm^{-1} and 1360 cm^{-1}) with the presence of the trimer (blue line) and the pentamer (red line). For complete spectra, please find Fig. 9 in Appendix.

4. Conclusions

Concisely, we designed and optimized two Fano-plasmonic disk-type gold oligomers using FEM-based simulations to ensure that their FR will overlap with our intended Raman lines of the analytes (1360 cm^{-1} for R6G and 734 cm^{-1} for adenine) recorded with the excitation wavelength of 785 nm . The simulated scattering profiles and the experimental scattering intensities of the fabricated oligomers clearly showed stronger FR (in terms of the depth of the Fano dip) in the pentamer than the trimer. The NFE plots and SERS maps of the oligomers also revealed that we achieved the spatial overlap of hotspots at the excitation and Raman wavelengths of the analytes. Our numerical analysis also explained that the origin of FR in the pentamer is electric in nature but in the trimer, FR originated from the interplay between the electric and the magnetic plasmon modes.

We then studied the SERS activity of the two oligomers having different strength and origin of FR. Our Raman analysis of the analytes resulted in higher enhancement of the Raman signal with the presence of the pentamer than that in the case of the trimer for both analytes. Consequently, from our experimental outcomes, we can conclude that the strength of FR in a Fano-plasmonic oligomer as well as its spectral overlap with the intended Raman lines significantly influences its SERS performance. Therefore, by suitable engineering of Fano lineshape, with stronger FR and spectral tuning with the intended Raman bands as well as with

the excitation frequency, one can achieve efficient SERS active substrates with spatially localized hotspots. We also got a hint that the optical properties and SERS activities of such oligomers may differ if their origin of FR differ but further studies required in this case to draw any concrete conclusions.

Appendix

Comparison between experimental scattering intensities of the trimer and the pentamer and complete SERS spectra of analytes.

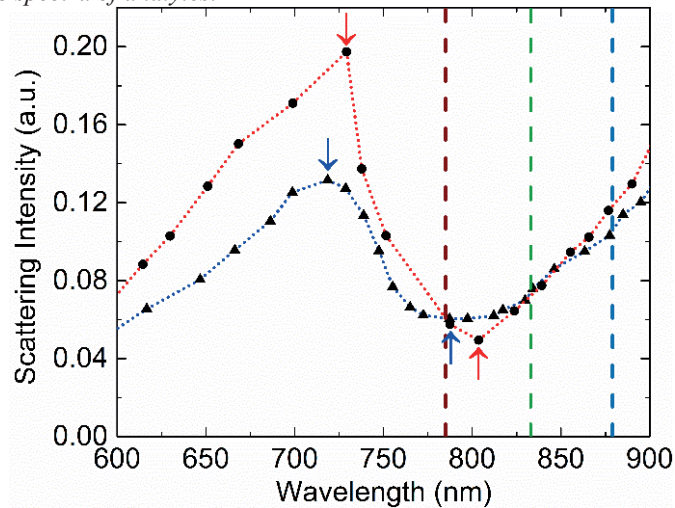


Fig. 8. Experimental scattering intensity profiles of the trimer (blue dotted line) and the pentamer (red dotted line). The black circles (in the red dotted line) and the black triangles (in the blue dotted line) represent the peak intensities of the first diffraction order (normalized and Lambertian corrected) collected at different detection angles. The red and blue arrows represent the position of the peak and the dip in the corresponding spectra used to calculate k . The red, green and blue (vertical) dashed lines represent, the excitation wavelength (785 nm), the targeted Raman line of adenine (734 cm^{-1} or 833 nm), and the targeted Raman line of rhodamine 6G (1360 cm^{-1} or 879 nm), respectively.

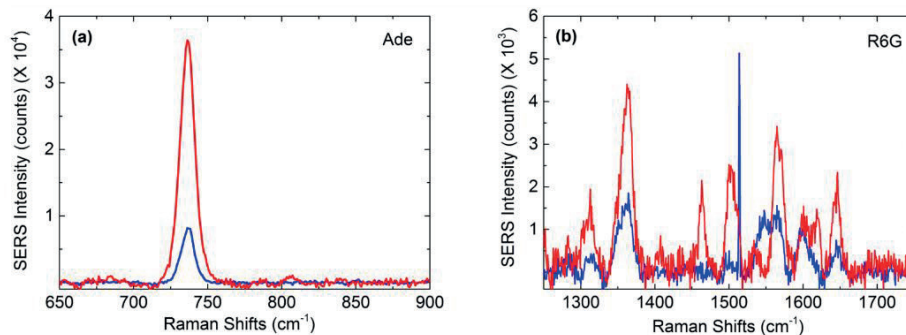


Fig. 9. (a) Complete SERS intensity spectrum of adenine (Ade) with the presence of the trimer (blue line) and the pentamer (red line). (b) Complete SERS intensity spectrum of rhodamine 6G (R6G) with the presence of the trimer (blue line) and the pentamer (red line). In (a-b), SERS spectra are reported without smoothing and baseline correction.

Funding

Academy of Finland (289947, 321066, 323995).

Acknowledgments

The authors gratefully acknowledge Prof. Kai-Erik Peiponen (University of Eastern Finland) and Prof. Mika Pettersson (University of Jyväskylä) for their valuable guidance during the research work, and Academy of Finland for funding.

Disclosures

The authors declare that there are no conflicts of interest related to this article.

References

1. D. Long, "Early history of the Raman effect," *Int. Rev. Phys. Chem.* **7** (4), 317-349 (1988).
2. C. Banwell, *Fundamentals of Molecular Spectroscopy* (McGraw-Hill, 1972), Chap. 4.
3. D. Long, *The Raman Effect: A Unified Treatment of The Theory of Raman Scattering by Molecules* (John Wiley & Sons, 2002).
4. D. Shipp, F. Sinjab, and I. Notinger, "Raman spectroscopy: techniques and applications in the life sciences," *Adv. Opt. Photonics* **9** (2), 315-428 (2017).
5. R. Das and Y. Agrawal, "Raman spectroscopy: recent advancements, techniques and applications," *Vib. Spectrosc.* **57**, 163-176 (2011).
6. C. Haynes, A. McFarland, and R. Van Duyne, "Surface-enhanced Raman spectroscopy," *Anal. Chem.* **77** (17), 338A-346A (2005).
7. M. Fleischmann, P. Hendra, and A. McQuillan, "Raman spectra of pyridine adsorbed at a silver electrode," *Chem. Phys. Lett.* **26**, 163-166 (1974).
8. S. Schlücker, "Surface-enhanced Raman spectroscopy: concepts and chemical applications," *Angew. Chem. Int. Ed.* **53**, 4756-4795 (2014).
9. B. Sharma, R. Frontiera, A. Henry, E. Ringe, and R. Van Duyne, "SERS: materials, applications, and the future," *Mater. Today* **15** (1-2), 16-25 (2012).
10. G. Schatz and R. Van Duyne, "Electromagnetic mechanism of surface-enhanced spectroscopy," in *Surface-Enhanced Vibrational Spectroscopy, Handbook of Vibrational Spectroscopy vol. 1*, J. Chalmers and P. Griffiths, eds. (John Wiley & Sons, 2002).
11. S. Ding, E. You, Z. Tian, and M. Moskovits, "Electromagnetic theories of surface-enhanced Raman spectroscopy," *Chem. Soc. Rev.* **46**, 4042-4076 (2017).
12. D. Cialla-May, X. Zheng, K. Weber, and J. Popp, "Recent progress in surface-enhanced Raman spectroscopy for biological and biomedical applications: from cells to clinics," *Chem. Soc. Rev.* **46**, 3945-3961 (2017).
13. C. Muehlethaler, M. Leona, and J. Lombardi, "Review of surface enhanced Raman scattering applications in forensic science," *Anal. Chem.* **88**, 152-169 (2016).
14. D. Chulhai, Z. Hu, J. Moore, X. Chen, and L. Jensen, "Theory of linear and nonlinear surface-enhanced vibrational spectroscopies," *Annu. Rev. Phys. Chem.* **67**, 541-564 (2016).
15. A. Henry, B. Sharma, M. Cardinal, D. Kuroski, and R. Van Duyne, "Surface-enhanced Raman spectroscopy biosensing: in vivo diagnostics and multimodal imaging," *Anal. Chem.* **88**, 6638-6647 (2016).
16. R. Tripp, R. Dluhy, and Y. Zhao, "Novel nanostructures for SERS biosensing," *Nano Today* **3** (3-4), 31-37 (2008).
17. K. Bantz, A. Meyer, N. Wittenberg, H. Im, Ö. Kurtulus, S. Lee, N. Lindquist, S-H. Oh, and C. Haynes, "Recent progress in SERS biosensing," *Phys. Chem. Chem. Phys.* **13**, 11551-11567 (2011).
18. E. Ru and P. Etchegoin, "Single-molecule surface-enhanced Raman spectroscopy," *Annu. Rev. Phys. Chem.* **63**, 65-87 (2012).
19. Y. Wang and J. Irudayaraj, "Surface-enhanced Raman spectroscopy at single-molecule scale and its implications in biology," *Phil. Trans. R Soc. B* **368**:20120026, 1-10 (2013).
20. H. Lee, S. Jin, H. Kim, and Y. Suh, "Single-molecule surface-enhanced Raman spectroscopy: a perspective on the current status," *Phys. Chem. Chem. Phys.* **15**, 5276-5287 (2013).
21. A. Zrimsek, N. Chiang, M. Mattei, S. Zaleski, M. McAnally, C. Chapman, A-I. Henry, G. Schatz, and R. Van Duyne, "Single-molecule chemistry with surface- and tip-enhanced Raman spectroscopy," *Chem. Rev.* **117**, 7583-7613 (2017).
22. J. Ye, F. Wen, H. Sobhani, J. Lassiter, P. Dorpe, P. Nordlander, and N. J. Halas, "Plasmonic nanoclusters: near-field properties of the Fano resonance interrogated with SERS," *Nano Lett.* **12** (3), 1660-1667 (2012).
23. M. Rahmani, B. Luk'yanchuk, and M. Hong, "Fano resonance in novel plasmonic nanostructures," *Laser Photonics Rev.* **7** (3), 329-349 (2013).
24. U. Fano, "On the absorption spectrum of noble gases at the arc spectrum limit," *Nuovo Cimento* **12**, 154-161 (1935).
25. B. Luk'yanchuk, N. Zheludev, S. Maier, N. J. Halas, P. Nordlander, H. Giessen, and C. Chong, "The Fano resonance in plasmonic nanostructures and metamaterials," *Nat. Mater.* **9**, 707-715 (2010).
26. A. Miroshnichenko, S. Flach, and Y. Kivshar, "Fano resonances in nanoscale structures," *Rev. Mod. Phys.* **82**, 2257-2298 (2010).

27. M. Limonov, M. Rybin, A. Poddubny, and Y. Kivshar, "Fano resonances in photonics," *Nat. Photon.* **11**, 543-554 (2017).
28. U. Fano, "Effects of configuration interaction on intensities and phase shifts," *Phys. Rev.* **124**, 1866-1878 (1961).
29. S. Emami, R. Penny, H. Rashid, W. Mohammed, and B. Rahman, "Fano resonance in plasmonic optical antennas," in *Reviews in Plasmonics 2015*, C. Geddes, ed. (Springer, 2016).
30. M. Hentschel, D. Dregely, R. Vogelgesang, H. Giessen, and N. Liu, "Plasmonic oligomers: the role of individual particles in collective behavior," *ACS Nano* **5** (3), 2042-2050 (2011).
31. M. Hentschel, M. Saliba, R. Vogelgesang, H. Giessen, P. Alivisatos, and N. Liu, "Transition from isolated to collective modes in plasmonic oligomers," *Nano Lett.* **10** (7), 2721-2726 (2010).
32. Y. Zhang, F. Wen, Y-R. Zhen, P. Nordlander, and N. J. Halas, "Coherent Fano resonances in a plasmonic nanocluster enhance optical four-wave mixing," *Proc. Natl. Acad. Sci. U.S.A.* **110** (23), 9215-9219 (2013).
33. J. Fan, K. Bao, C. Wu, J. Bao, R. Bardhan, N. J. Halas, V. Manoharan, G. Shvets, P. Nordlander, and F. Capasso, "Fano-like interference in self-assembled plasmonic quadrumer clusters," *Nano Lett.* **10** (11), 4680-4685 (2010).
34. B. Gallinet and O. Martin, "Influence of electromagnetic interactions on the line shape of plasmonic Fano resonances," *ACS Nano* **5** (11), 8999-9008 (2011).
35. B. Lassiter, H. Sobhani, M. Knight, W. Mielczarek, P. Nordlander, and N. J. Halas, "Designing and deconstructing the Fano lineshape in plasmonic nanoclusters," *Nano Lett.* **12**, 1058-1062 (2012).
36. S. Zhang, D. Genov, Y. Wang, M. Liu, and X. Zhang, "Plasmon-induced transparency in metamaterials," *Phys. Rev. Lett.* **101**, 0474011-0474014 (2008).
37. B. Lassiter, H. Sobhani, J. Fan, J. Kundu, F. Capasso, P. Nordlander, and N. J. Halas, "Fano resonances in plasmonic nanoclusters: geometrical and chemical tunability," *Nano Lett.* **10** (8), 3184-3189 (2010).
38. M. Rahmani, B. Lukiyanchuk, T. Tahmasebi, Y. Lin, T. Liew, and M. Hong, "Polarization-controlled spatial localization of near-field energy in planar symmetric coupled oligomers," *Appl. Phys. A* **107**, 23-30 (2012).
39. B. Gallinet and O. Martin, "Relation between near-field and far-field properties of plasmonic Fano resonances," *Opt. Express* **19** (22), 22167-22175 (2011).
40. Y. Joe, A. Satanin, and C. Kim, "Classical analogy of Fano resonances," *Phys. Scr.* **74**, 259-266 (2006).
41. A. Lovera, B. Gallinet, P. Nordlander, and O. Martin, "Mechanisms of Fano resonances in coupled plasmonic systems," *ACS Nano* **7** (5), 4527-4536 (2013).
42. M. Rahmani, T. Tahmasebi, Y. Lin, B. Lukiyanchuk, T. Liew, and M. Hong, "Influence of plasmon destructive interferences on optical properties of gold planar quadrumers," *Nanotechnology* **22**, 1-7 (2011).
43. M. Rahmani, D. Lei, V. Giannini, B. Lukiyanchuk, M. Ranjbar, T. Liew, M. Hong, and S. Maier, "Subgroup decomposition of plasmonic resonances in hybrid oligomers: modeling the resonance lineshape," *Nano Lett.* **12** (4), 2101-2106 (2012).
44. A. Attaran, S. Emami, M. Soltanian, R. Penny, F. Behbahani, S. Harun, H. Ahmad, H. Abdul-Rashid, and M. Moghavvemi, "Circuit model of Fano resonance on tetramers, pentamers and broken symmetry pentamers," *Plasmonics* **9**, 1303-1313 (2014).
45. B. Gallinet and O. Martin, "Ab-initio theory of Fano resonances in plasmonic nanostructures and metamaterials," *Phys. Rev. B* **83**, 2354271-2354276 (2011).
46. M. Rahmani, B. Lukiyanchuk, B. Ng, A. Tavakkoli, T. Liew, and M. Hong, "Generation of pronounced Fano resonances and tuning of subwavelength spatial light distribution in plasmonic pentamers," *Opt. Express* **19** (6), 4949-4956 (2011).
47. M. Rahmani, B. Lukiyanchuk, T. Nguyen, T. Tahmasebi, Y. Lin, T. Liew, and M. Hong, "Influence of symmetry breaking in pentamers on Fano resonance and near-field energy localization," *Opt. Mater. Express* **1** (8), 1409-1415 (2011).
48. Y. Zhang, Y. Zhen, O. Neumann, J. Day, P. Nordlander, and N. J. Halas, "Coherent anti-Stokes Raman scattering with single-molecule sensitivity using a plasmonic Fano resonance," *Nat. Commun.* **5**, 4424 (2014).
49. J. Wang, C. Fan, J. He, P. Ding, E. Liang, and Q. Xue, "Double Fano resonances due to interplay of electric and magnetic plasmon modes in planar plasmonic structure with high sensing sensitivity," *Opt. Express* **21** (2), 2236-2244 (2013).
50. S. Sheikholeslami, A. Etxarri, and J. Dionne, "Controlling the interplay of electric and magnetic modes via Fano-like plasmon resonances," *Nano Lett.* **11** (9), 3927-3934 (2011).
51. J. He, C. Fan, P. Ding, S. Zhu, and E. Liang, "Near-field engineering of Fano resonances in a plasmonic assembly for maximizing CARS enhancements," *Sci. Rep.* **6**, 20777 (2016).
52. A. Nazir, S. Panaro, R. Zaccaria, C. Liberale, F. Angelis, and A. Toma, "Fano coil-type resonance for magnetic hot-spot generation," *Nano Lett.* **14** (6), 3166-3171 (2014).
53. C. Wu, E. Chen, and J. Wei, "Surface enhanced Raman spectroscopy of rhodamine 6G on agglomerates of different-sized silver truncated nanotriangles," *Colloids Surf. A: Physicochem. Eng. Aspects* **506**, 450-456 (2016).
54. F. Madzharova, Z. Heiner, M. Gühlke, and J. Kneipp, "Surface-enhanced hyper-Raman spectra of adenine, guanine, cytosine, thymine and uracil," *J. Phys. Chem. C* **120**, 15415-15423 (2016).
55. COMSOL Multiphysics application gallery, "Scatterer on substrate" (COMSOL Multiphysics, 2019). https://www.comsol.fi/model/download/563151/models.woptics.scatterer_on_substrate.pdf
56. P. Johnson and R. Christy, "Optical constants of the noble metals," *Phys. Rev. B* **6**, 4370-4379 (1972).

57. S. Baieva, O. Hakamaa, G. Groenhof, T. Heikkilä, and J. J. Toppari, "Dynamics of strongly coupled modes between surface plasmon polaritons and photoactive molecules: the effect of the Stokes shift," *ACS Photonics* **4** (1), 28-37 (2017).
58. T. Hakala, J. J. Toppari, A. Kuzyk, M. Pettersson, H. Tikkanen, H. Kunttu, and P. Törmä, "Vacuum Rabi splitting and strong-coupling dynamics for surface-plasmon polaritons and rhodamine 6G molecules," *Phys. Rev. Lett.* **103**, 0536021-0536024 (2009).
59. M. Koponen, U. Hohenester, T. Hakala, and J. J. Toppari, "Absence of mutual polariton scattering for strongly coupled surface plasmon polaritons and dye molecules with a large Stokes shift," *Phys. Rev. B: Condens. Matter Mater. Phys.* **88**, 0854251-0854258 (2013).
60. S. He, W. Zhang, L. Liu, Y. Huang, J. He, W. Xie, P. Wu, and C. Du, "Baseline correction for Raman spectra using an improved asymmetric least squares method," *Anal. Methods* **6**, 4402-4407 (2014).
61. J. Luo, K. Ying, and J. Bai, "Savitzky–Golay smoothing and differentiation filter for even number data," *Signal Processing* **85**, 1429-1434 (2005).
62. M. Clupek, P. Matejka, and K. Volka, "Noise reduction in Raman spectra: finite impulse response filtration versus Savitzky–Golay smoothing," *J. Raman Spectrosc.* **38**, 1174-1179 (2007).
63. OriginLab documentation, "Origin user guide" (OriginLab, 2017).
https://www.originlab.com/pdfs/Origin2017_Documentation/English/Origin_User_Guide_2017_E.pdf
64. J. Kundu, O. Neumann, B. Janesko, D. Zhang, S. Lal, A. Barhoumi, G. Scuseria, and N. J. Halas, "Adenine- and adenosine monophosphate (AMP)-gold binding interactions studied by surface-enhanced Raman and infrared spectroscopies," *J. Phys. Chem. C* **113**, 14390-14397 (2009).
65. K. Kneipp, R. Dasari, and Y. Wang, "Near-infrared surface-enhanced Raman scattering (NIR SERS) on colloidal silver and gold," *Appl. Spectrosc.* **48** (8), 951-955 (1994).
66. E. Kohr, B. Karawdeniya, J. Dwyer, A. Gupta, and W. Euler, "A comparison of SERS and MEF of rhodamine 6G on a gold substrate," *Phys. Chem. Chem. Phys.* **19**, 27074-27080 (2017).
67. M. Suzuki, Y. Niidome, Y. Kuwahara, N. Terasaki, K. Inoue, and S. Yamada, "Surface-enhanced nonresonance Raman scattering from size- and morphology-controlled gold nanoparticle films," *J. Phys. Chem. B* **108**, 11660-11665 (2004).

PII

**SPATIAL LOCALIZATION OF HOTSPOTS IN
FANO-RESONANT PLASMONIC OLIGOMERS FOR
SURFACE-ENHANCED COHERENT ANTI-STOKES RAMAN
SCATTERING**

by

A. Dutta and E. M. Vartiainen,

Journal of the European Optical Society-Rapid Publications, **16**, 8 (2020).

Reproduced with kind permission of Springer Nature.

RESEARCH

Open Access

Spatial localization of hotspots in Fano-resonant plasmonic oligomers for surface-enhanced coherent anti-Stokes Raman scattering



Arpan Dutta^{1*} and Erik M. Vartiainen²

Abstract

Realization of Fano resonance in plasmonic oligomers is often exploited to design efficient plasmonic substrates for surface-enhanced coherent anti-Stokes Raman scattering. Disk-type Fano-resonant plasmonic oligomers are widely used to enhance the Raman signal of the probe material. Generally, hot spots are generated in those oligomers at different spatial locations at different wavelengths and only a few spatially overlapping hot spots at multiple wavelengths can be achieved with oblique incidence of excitation light. In this work, we proposed hexagonal gold nanoparticle based Fano-resonant plasmonic oligomers that can yield higher number of spatially overlapped hot spots compared to the disk type oligomers even with the normal incidence of excitation light. The oligomers were numerically modelled and optimized for surface-enhanced coherent anti-Stokes Raman scattering with 780 nm pumping and 500–1800 cm^{-1} Raman signature region. The Fano lineshape was engineered to ensure near-field energy coupling at pump while enhancing the coherent anti-Stokes Raman signal at the far field. Our computational studies explored the purely electric origin of Fano resonance in those oligomers and provided maximum Raman enhancements of 10^{12} – 10^{13} from them to enable single-molecular level applications. Our findings provide a way to realize fabrication-friendly nanostructures with higher number of spatially localized hotspots for improving the Raman detection sensitivity.

Keywords: Fano resonance, Plasmonic oligomers, Coherent anti-Stokes Raman scattering

Introduction

The ability of Raman spectroscopy (RS) to provide accurate chemical ‘fingerprint’ of probed material [1–3] enables its utilization as a powerful analytical tool in different scientific and industrial fields [4, 5]. Development of integrated optical technologies and ultrafast lasers made RS a unique diagnostic tool for non-destructive [6] and non-invasive analysis [7]. In spite of all acclaimed potentials of RS, its real-life implementations are often become challenging due to the inherited weakness of the

Raman response of the probe [8]. A linear approach to overcome the aforementioned limitation of RS is surface-enhanced Raman spectroscopy (SERS) where a plasmonic substrate is used to amplify the Raman signal of the probe material [8–12]. Biosensing at nanoscale [13–15] and single molecule detection [16–19] become realizable nowadays with the suitable application of SERS. Another approach of strengthening the Raman signal is coherent anti-Stokes Raman scattering (CARS) where the Raman response is amplified with the help of a nonlinear optical four-wave mixing (FWM) process, instead of a plasmonic substrate [20–27]. In CARS, two laser beams, the so-called pump (ω_p) and Stokes (ω_s), are focused into a sample and its molecular vibration

* Correspondence: arpan.a.dutta@jyu.fi

¹Department of Physics and Nanoscience Center, University of Jyväskylä, Jyväskylä, Finland

Full list of author information is available at the end of the article

modes are driven by the beat frequencies ($\omega_p - \omega_s$) of the laser beams and simultaneously probed by a third (probe, ω_{prb}) laser beam to produce an output signal at the blue-shifted anti-Stokes frequency ($\omega_p - \omega_s + \omega_{\text{prb}}$). In CARS micro-spectroscopy, the pump and probe beams are obtained from the same narrow-band pulsed laser and the Stokes from a broadband (femtosecond or supercontinuum) laser source [21–27]. CARS signal can further be enhanced by employing a plasmonic substrate along with the existing nonlinear process [12, 28–30]. Surface-enhanced CARS (SECARS) is such a method in which the Raman signal enhancement can attain a much higher level compared to the normal RS, SERS, or CARS alone [29, 30]. Achievement of single-molecular level sensitivity in molecular sensing become possible with SECARS [28].

Designing plasmonic substrates for multi-frequency based spectroscopic techniques such as SECARS is demanding since the optical properties of the substrate has to be engineered such a way that its plasmon resonances would overlap with all intended spectral regimes of the spectroscopic technique. Realization of Fano-resonant plasmonic (or Fano-plasmonic) oligomers is one option [28, 30]. In a plasmonic oligomer, metal nanoparticles (NPs) are clustered with optimal sizes, shapes and inter-particle distances to obtain desired optical responses from the oligomer. Hybridization between the localized surface plasmon resonances (LSPR) of the NPs engendered Fano resonance (FR) in the scattering (or extinction) profile of the oligomer, manifested as two peaks having one dip between them in the corresponding scattering (or extinction) lineshape [31, 32]. The scattering peaks, called as the super-radiant (or bright) mode of FR, are generated due to the constructive interference between the LSPR modes of the NPs when the plasmon oscillations in all NPs are ‘in phase’. The scattering dip, which is also known as the sub-radiant (or dark) mode of FR, is a result of the destructive interference between the LSPR modes of the NPs when the plasmon oscillations in all NPs are not ‘in phase’ [33–36]. Tuning of FR at the desired spectral regions can be obtained by optimizing the size, shape, thickness or height, and material of the NPs present in the oligomer while optimization of the interparticle gap provides a way to control the degree of the hybridization between the LSPR modes of the NPs [32, 37]. Theoretical explanation behind the origin of FR in plasmonic oligomers can be found elsewhere [36, 38–43].

Implementation of Fano-plasmonic oligomers in SECARS requires spectral overlap of the sub-radiant mode of FR (i.e. the scattering dip or Fano dip) with the pump frequency. The two super-radiant modes of FR (i.e. the scattering peaks or Fano peaks), situated in the red and blue side of the Fano dip, has to be tuned with the Stokes and the

CARS frequencies, respectively [28, 30]. Such strategy ensures an enhancement of the output light i.e. the CARS signal at the far field along with an optimized coupling between the excitation energy and the plasmonic substrate at the pump wavelength [28]. The achievable Raman signal enhancement in SECARS depends on the electric field enhancements at the pump, Stokes, and CARS frequencies as well as the spatial localization of the hot spots (i.e. confined regions with highly localized electromagnetic energy) at the same position at those three frequencies [30]. In general, hot spots are distributed at different positions over the substrate geometry at different wavelengths and spatial overlap of them can be achieved with the oblique incidence of excitation (i.e. pump) light as reported earlier [30]. In addition, higher number of hot spots is favorable for the optimal intensification of SECARS signal and in disk-type Fano-plasmonic oligomers, only a few hot spots are possible to achieve as shown in previous works [28, 30]. Eventually, realizing plasmonic substrates that can provide higher number of spatially localized hotspots is most desirable for improving the sensitivity of SECARS.

In this article, two Fano-plasmonic oligomers, a quadrumer and a heptamer, consisting of hexagonal-shaped gold NPs, are proposed as SECARS substrates. The oligomers are numerically modelled and optimized using the finite element method (FEM) for CARS applications where the pump wavelength is 780 nm. The targeted Raman signature zone is considered as the favorable ‘fingerprint region’ of analytes, i.e. 500–1800 cm^{-1} [44]. For the aforementioned Raman signature regime, the Stokes wavelengths cover approximately 810–908 nm and the corresponding CARS window becomes 683–753 nm. Unlike the existing literature [28, 30, 33, 34, 40, 45–47], the hexagonal shape is chosen for the nanoparticles present in the oligomers since the hexagonal geometry offers a higher number of nanogaps than that in the disk-type geometry. Our computational studies reveal that the hexagonal NP based Fano-resonant oligomers can yield higher number of spatially localized hot spots compared to the disk-type oligomers even with the normal incidence of the excitation light. Our numerical analysis also explores the origin of FR in the proposed oligomers in terms of the complex phase relations between the induced dipole moments of the hexagonal NPs. Such findings are important in the context of designing plasmonic substrates for SECARS and for multiphoton based spectroscopic techniques in general since they could provide a way to reach high sensitivity in Raman detection with fabrication-friendly nanostructures.

Methods

The oligomers were numerically modelled and optimized for CARS applications using a commercial FEM package (COMSOL Multiphysics version 5.4). In the

simulation environment, a single oligomer was kept on top of a glass (SiO_2) substrate and air was considered as the surrounding medium. The whole simulation space was $2\ \mu\text{m} \times 2\ \mu\text{m} \times 2\ \mu\text{m}$ and perfectly matched layers (PMLs) were used at all the boundaries of it to prevent spurious reflections. The near- and far-field (optical) properties of the oligomers were calculated for the normal incidence of light with electric field along the oligomer's main axis (as illustrated in Fig. 1) using the scattered-field formulation (wave optics module) of COMSOL [48]. The complex dielectric function of gold was collected from the experimental data reported by Johnson and Christy [49]. The nondispersive refractive indices of air and SiO_2 were taken as 1.00 and 1.45, respectively.

Results and discussion

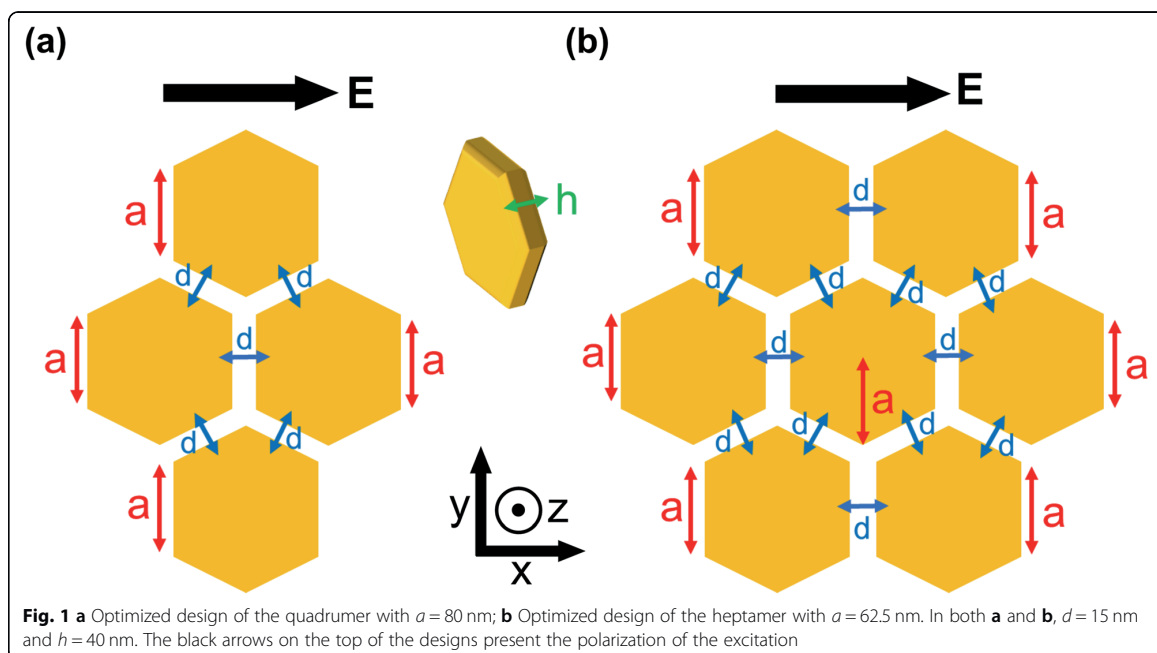
The oligomers were modelled and optimized using FEM so that their FR would spectrally overlap with the intended pump, Stokes and CARS regions. The schematic designs of the quadramer and the heptamer are presented in Fig. 1. The quadramer, depicted in Fig. 1a, contains four identical hexagonal NPs having same sizes (hexagon side length a) as well as equal thicknesses (h) and interparticle gaps (d). The heptamer, illustrated in Fig. 1b, contains seven identical hexagonal NPs of equal sizes (hexagon side length a) while the NP thicknesses (h) and the interparticle gaps (d) are similar with the quadramer.

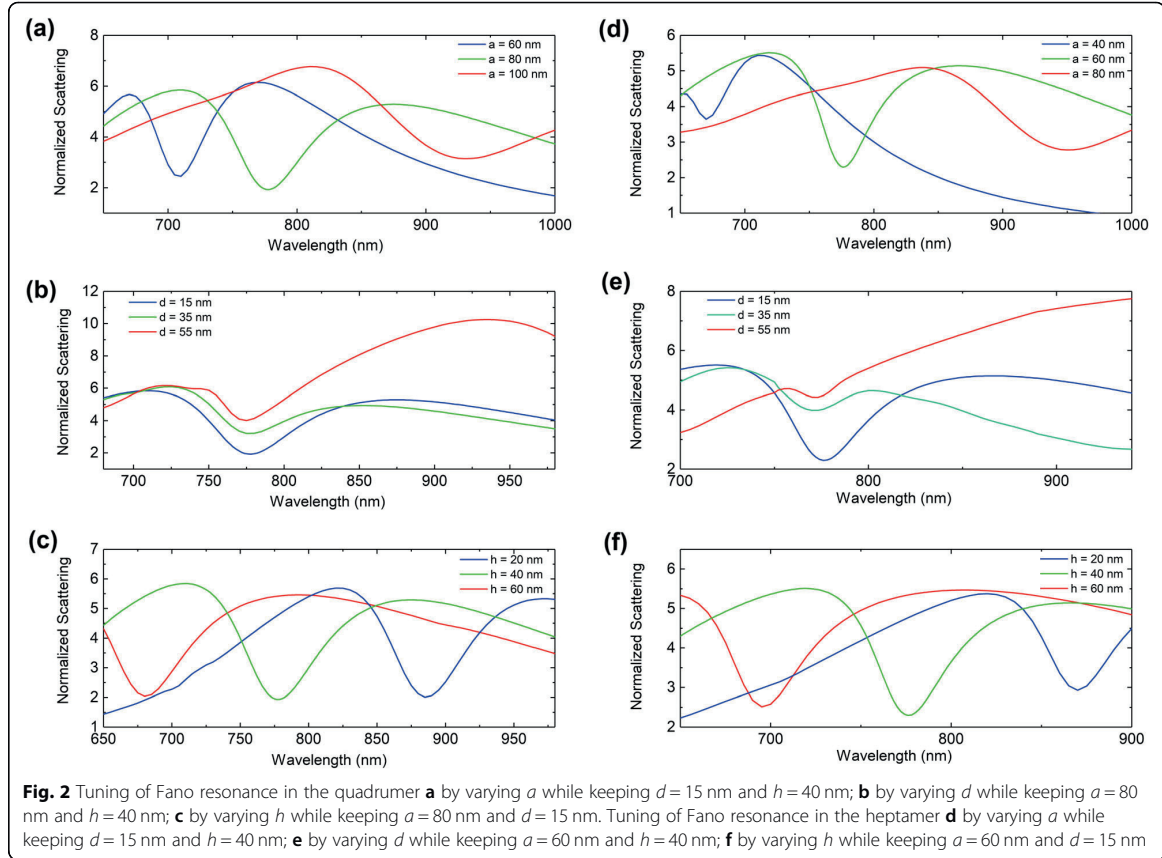
Tuning of FR at the intended spectral regimes was done by optimizing the geometrical parameters of the NPs (i.e. a , d and h). During optimization, effect of one parameter (a , d or h) on FR was studied while keeping all other parameters fixed. An increment in NP size (a) red shifts the Fano dip in both quadramer and heptamer, as depicted in Fig. 2a and d, respectively.

An increment in interparticle gap (d) slightly blue shifts the spectral position of the Fano dip but more importantly reduce the depth of the Fano dip significantly due to the lack of coupling between LSPRs of the NPs, as illustrated in Fig. 2b and e, in the case of the quadramer and the heptamer, respectively. An increment in NP thickness (h) also blue shifts the Fano dip in both quadramer and heptamer, as shown in Fig. 2c and f, respectively. The scattering cross-sections reported in Fig. 2 are normalized by the corresponding geometrical cross-sections.

The scattering profiles of the oligomers were also compared with the so-called Fano-formula [50], mathematically expressed as $\sigma = (\epsilon + q)^2 / (\epsilon^2 + 1)$, where σ is the scattering cross section, q is the asymmetry parameter and ϵ is a parameter related to the reduced energy [50]. Figure 3a depicts a (non-scaled) overlap between the Fano-formula (with $q = 1$) and the scattering lineshape of the oligomers.

As the Fano-formula contains only one maximum and minimum in its lineshape, we quantified the q -parameter in the case of the oligomers as the ratio between the scattering cross-section at the Fano dip (dotted magenta



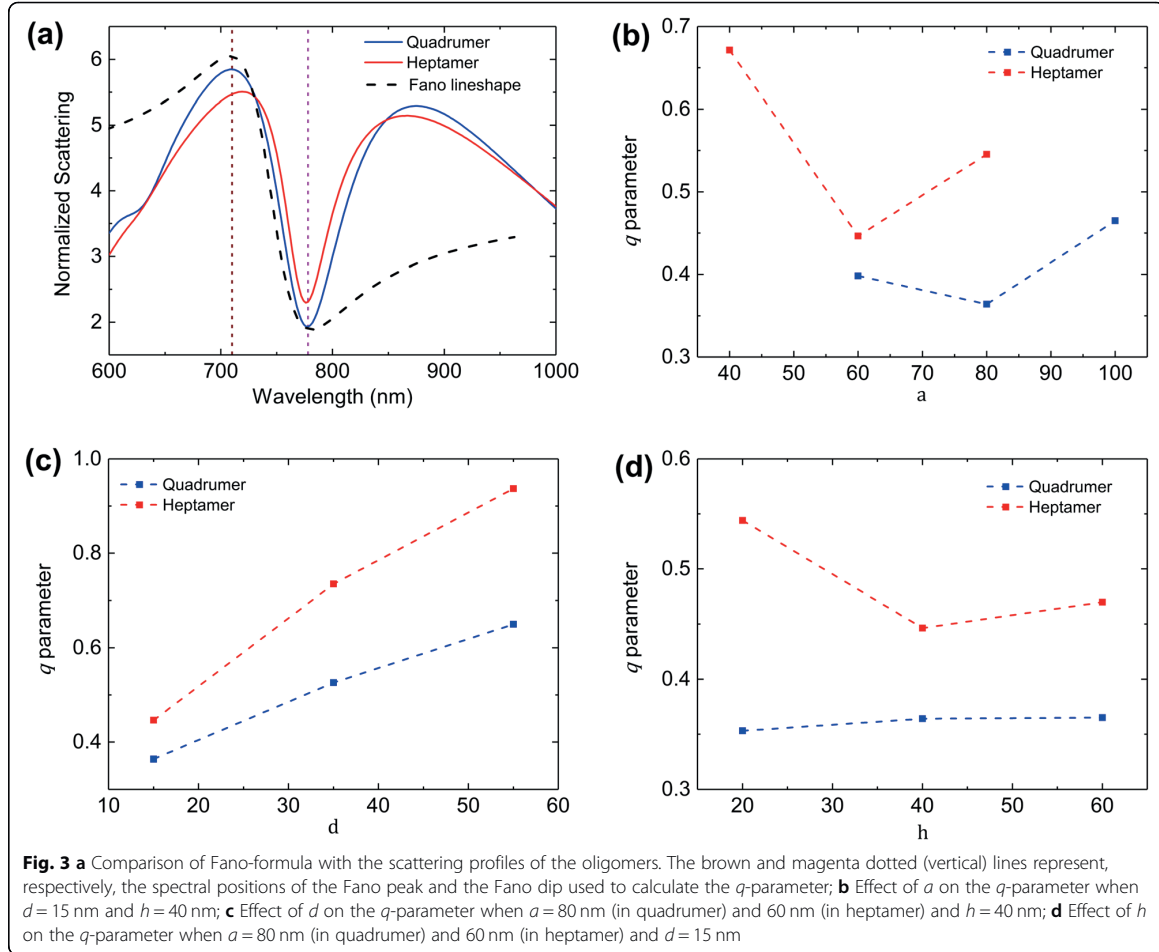


line) and the scattering cross-section at the Fano peak (dotted brown line) in the blue side. Figure 3b, c and d represent the effect of a , d and h on the q -parameter of the oligomers, respectively.

The q -parameter in the case of oligomers not only represents the degree of asymmetry in their corresponding scattering profiles but also quantifies the strength of FR in terms of the depth of the Fano dip (i.e. the strength of the coupling between the LSPR modes of the NPs). Lower the value of q -parameter, higher the depth of the Fano dip, stronger the FR. The strength of FR in a Fano-plasmonic oligomer can directly influence its Raman enhancement capability [45, 51]. Therefore, we optimized the geometrical parameters of the oligomers such a way that their FR spectrally overlapped with the pump, Stokes and CARS regions while maintaining the lowest q -parameter value to ensure the highest Raman enhancement. The optimized geometrical parameters for the quadrumer are $a = 80$ nm, $d = 15$ nm and $h = 40$ nm, providing a q -parameter value of 0.36. For the heptamer, the q -parameter value is 0.44 for $a = 62.5$ nm while d and h are similar with the quadrumer.

The optimized optical responses of the quadrumer and the heptamer are presented in Fig. 4a and b, respectively. In both panels of Fig. 4, the blue curves and the blue vertical axes (on the left side) present the simulated scattering cross-sections of the oligomers (normalized by the corresponding geometrical cross-sections) where the Fano lineshape is profoundly manifested. The Fano dips are clearly in overlap with the pump wavelength (green dashed vertical lines) while the Fano peaks are tune with the Stokes (red shaded rectangular regions) and the CARS (blue shaded rectangular regions) windows for both oligomers.

The red curves and the red vertical axes (on the right side) in both panels of Fig. 4 depict the total near-field intensity enhancement (NFIE) for the oligomers. The NFIE values are calculated as $|E_{loc}/E_0|^2$ integrated over the illuminated surfaces of the hexagonal NPs (i.e. the top and sides walls), where E_{loc} and E_0 are the local and the incident electric field amplitudes, respectively. The NFIE spectra are also normalized by the geometrical surface area of the corresponding illuminated surfaces. From Fig. 4 we can clearly find a spectral correlation between the far-field scattering minima and the NFIE



maxima for both oligomers. In other words, the spectral position of the highest NFIE is very close to the Fano dip in the scattering profile. Such correlation is a general property of Fano-resonant systems, reported earlier in theoretical [52] and experimental studies [45, 51].

The spatial localization of hot spots in such hexagonal NP based oligomers was studied in terms of the near-field enhancement (NFE) maps, computed as $|E_{loc}/E_0|$ at a plane 1 nm above the top surfaces of the oligomers.

To compare the hot spot localization in hexagon-based oligomers with that of the disk-type oligomers, similar NFE maps were computed for a disk-type quadramer and a disk-type heptamer having similar thicknesses, interparticle gaps and geometrical surface areas corresponds to their hexagonal versions. The NFE maps for the quadramer and the heptamer, calculated at the pump, Stokes and CARS frequencies for the 740 cm^{-1} Raman band of adenine [28], are reported in Figs. 5 and 6, respectively.

To study the localization of hot spots and its effect on SECARS enhancement, we plotted the spatial distribution (or map) of the SECARS (electromagnetic) enhancement factor G in Figs. 5d and 6d for the hexagon-based quadramer and heptamer, respectively. Figures 5h and 6h report the same for the disk-type quadramer and heptamer, respectively. The SECARS electromagnetic enhancement factor is calculated as $G = |E_{loc(pump)}/E_0|^4 \times |E_{loc(Stokes)}/E_0|^2 \times |E_{loc(CARS)}/E_0|^2$ for the 740 cm^{-1} Raman line of adenine [28]. We also assign five hot spot positions in Fig. 5 over the quadramer geometry and six hot spot positions in Fig. 6 over the heptamer geometry, labelled as 'i' to 'vi'.

From Fig. 5 we can clearly see that in the case of hexagon-based quadramer, the hot spots generated at position 'i', 'ii', 'iv', and 'v' spatially overlap at the pump and CARS wavelengths while the hot spot at position 'iii' spatially overlaps at the pump and Stokes wavelengths. Eventually, we achieved all the five hot spots in SECARS

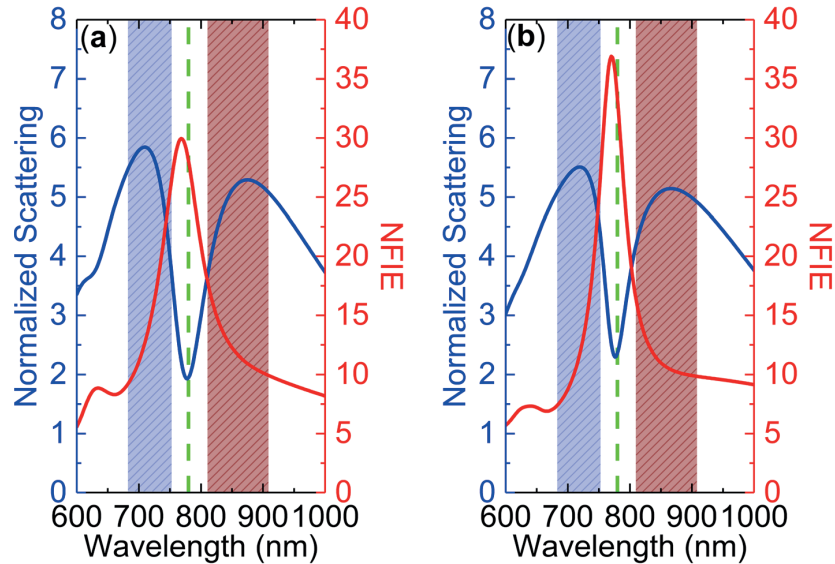


Fig. 4 **a** Simulated normalized scattering (blue curve) and NFIE (red curve) of the quadrumer; **b** Simulated normalized scattering (blue curve) and NFIE (red curve) of the heptamer. The blue and red vertical axes in both diagrams are corresponded to the blue and red curves present in those diagrams. The green dashed (vertical) lines and the red (blue) shaded rectangular regions in both diagrams depict the pump wavelength (780 nm) and the Stokes (CARS) window for the fingerprint region, respectively

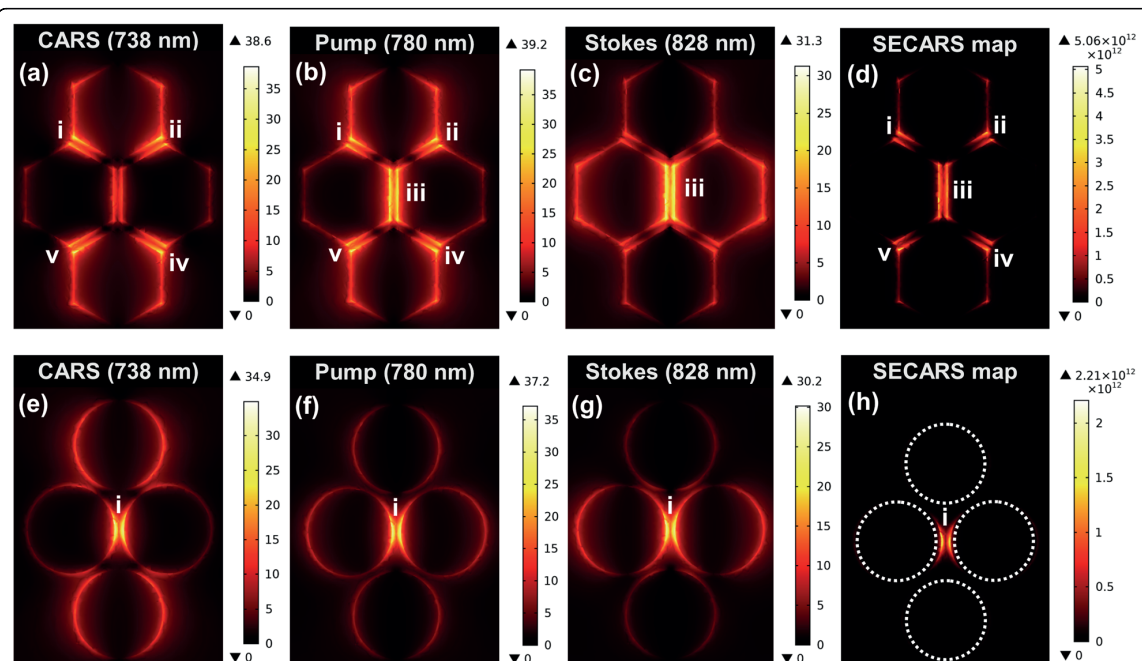


Fig. 5 Simulated NFE and SECARS maps computed at a plane 1 nm above the top surface of the quadrumer for the Raman band of adenine (740 cm^{-1}). **a-c** and **e-g** NFE plots at CARS (738 nm), pump (780 nm) and Stokes (828 nm) wavelengths; **d** and **h** the corresponding SECARS maps; In the plots **(a)-(d)**, all the dimensions are along Fig. 1a. In **h** the white dotted circles show the nano disks

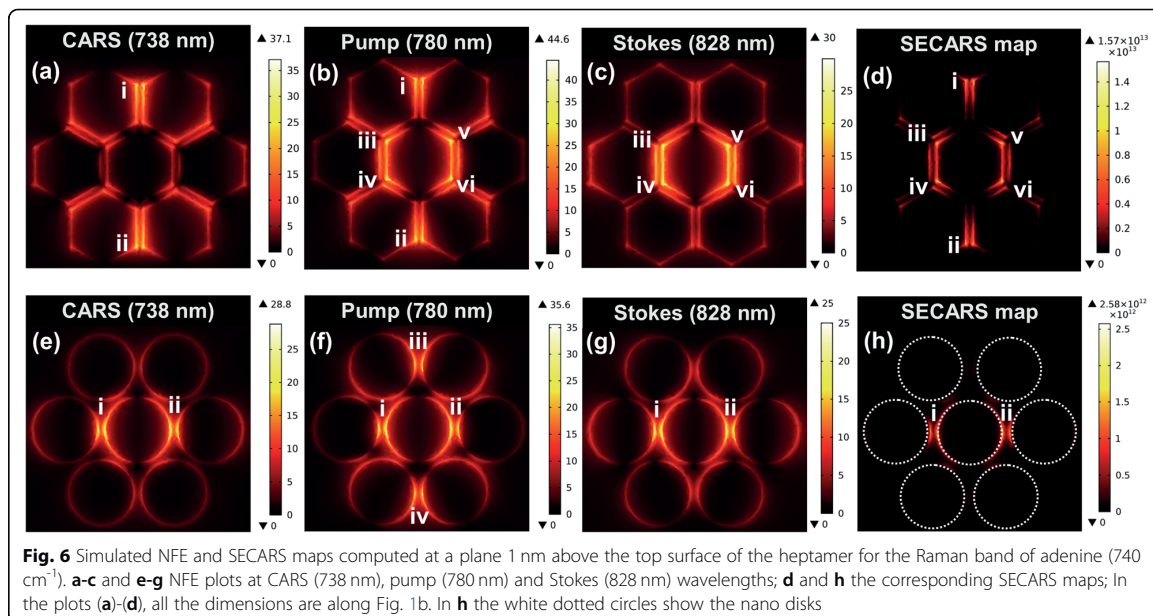


Fig. 6 Simulated NFE and SECARS maps computed at a plane 1 nm above the top surface of the heptamer for the Raman band of adenine (740 cm^{-1}). **a-c** and **e-g** NFE plots at CARS (738 nm), pump (780 nm) and Stokes (828 nm) wavelengths; **d** and **h** the corresponding SECARS maps; In the plots (**a-d**), all the dimensions are along Fig. 1b. In **h** the white dotted circles show the nano disks

map with an estimated enhancement factor G of 10^{12} at maximum. In the case of disk-type quadrumer, as depicted in Fig. 5e to h, only one hotspot, labelled as 'i', coincides at all three wavelengths and hence, only a single hotspot is obtained in SECARS map with an enhancement factor G of 10^{12} at maximum. For the hexagon-based heptamer, as shown in Fig. 6a to d, the hot spots at positions 'i' and 'ii' spatially overlap at the pump and CARS wavelengths whereas the hot spots at positions 'iii', 'iv', 'v', and 'vi' spatially overlap at the pump and Stokes wavelengths. Consequently, we obtained all the six hot spots in SECARS map with an estimated enhancement factor G of 10^{13} at maximum. However, in the disk-type heptamer, as reported in Fig. 6e to h, the hot spots at positions 'i' and 'ii' spatially overlap at all three wavelengths whereas the hot spots at positions 'iii' and 'iv' are only obtained at the pump wavelength. As a result, only two hotspots, at positions 'i' and 'ii', are obtained in SECARS map with an enhancement factor G of 10^{12} at maximum. The aforementioned findings clearly indicate that we achieved higher number of spatially overlapped hot spots in the hexagon-based oligomers compared to the disk-type oligomers with the normal incidence of excitation light. The predicted enhancement factors (G) for the hexagon-based oligomers are in the order of 10^{12} – 10^{13} , which meet the requirement of single molecular level sensitivity [28]. However, no hot spot is overlapped at all three frequencies (i.e. pump, Stokes and CARS) in the hexagon-based oligomers. Of particular note is that, in the hexagon-based oligomers, the hotspots yielded

higher spatial length compared to the corresponding disk-type versions due to the hexagonal symmetry but without losing the intensity of the field localization.

Achieving higher number of spatially overlapped hot spots with the normal incidence of light is beneficial in the context of hot spot engineering. Generally, hot spots are generated in the oligomers at different spatial locations at different wavelengths and only a few spatially overlapping hot spots at multiple wavelengths can be achieved with the normal incidence of excitation light. Existing literature [30] showed that by applying oblique incidence of excitation light instead of normal incidence, one could increase the number of hot spots over the oligomer geometry because of the spatial redistribution of the localized fields. However, such approach has two limitations. Firstly, the number of hot spots might increase in such approach but in expense of the intensity of the field localization and thereby weakening the total Raman enhancement [30]. Secondly, experimental realization of such approach could become more challenging due to the requirement of precise control on the excitation angle.

Our proposed hexagon-based oligomers provide a way to overcome the aforementioned limitations, by providing higher number of hot spots even with the normal incidence of excitation light and hence, neither losing the intensity of the field localization due to the oblique incidence nor bringing extra constraints in the experimental realization.

The underlying reason behind the generation of FR in those hexagon-based oligomers can be explained in terms of the complex phase relations between the

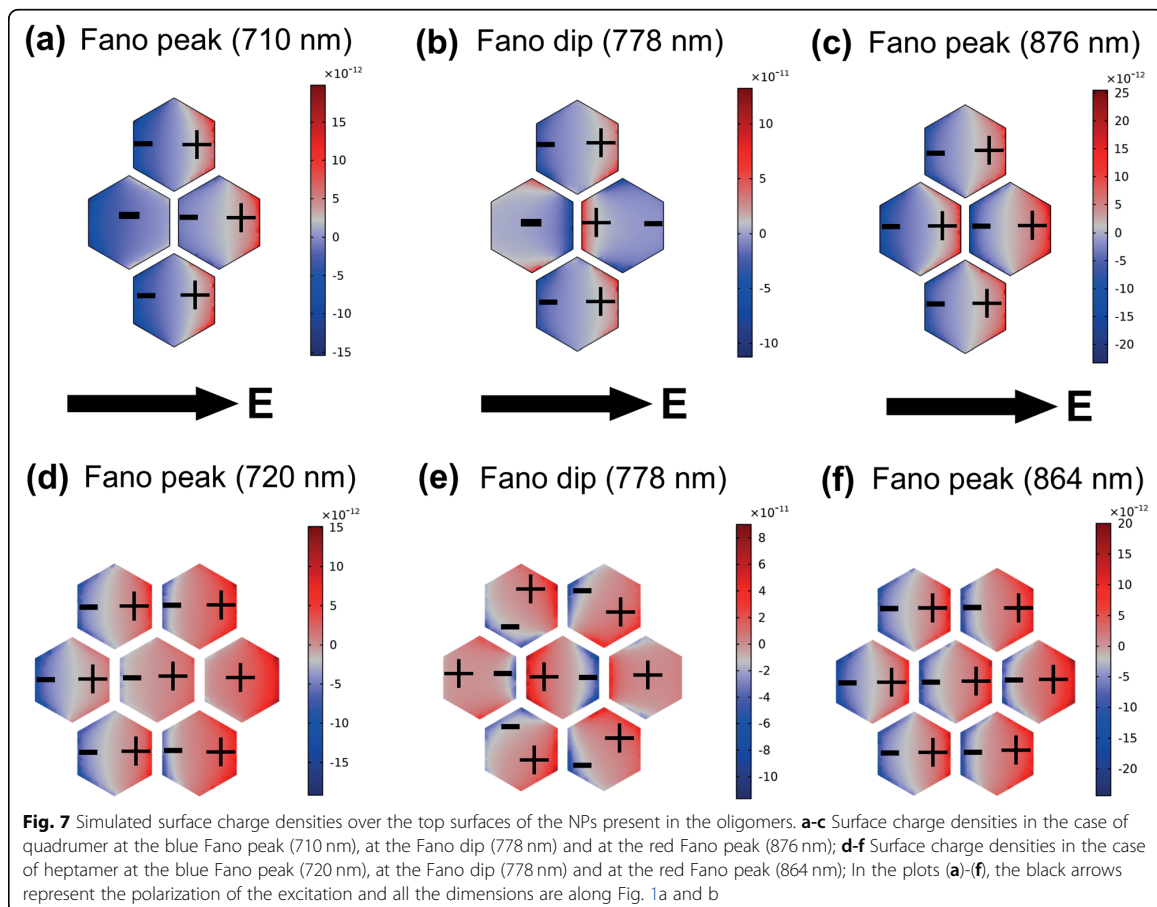
induced dipole moments of the hexagonal NPs. To investigate that, the surface charge densities are calculated over the top surfaces of the NPs present in the hexagon-based oligomers at the Fano peaks and the Fano dips of their corresponding scattering profiles. The surface charge density plots for the hexagon-based quadrumer and heptamer are shown in Fig. 7.

Polarized electromagnetic excitation induces dipole moments on the top surfaces of the NPs present in the oligomers [28, 47]. In the case of hexagon-based quadrumer (Fig. 7a to c), plasmon oscillations (and also the induced dipole moments) in all NPs are ‘in phase’ at the Fano peaks (710 nm and 876 nm) which eventually explains the origin of the broad super-radiant modes of FR as far-field scattering peaks at those wavelengths due to the constructive interference between those dipole moments. At the Fano dip (778 nm), NPs present in the hexagon-based quadrumer maintain an ‘anti-phase’ relation between them. The top and bottom NPs are in phase while the right middle NP is anti-phase with others, as shown in Fig. 7b, and hence, due to the destructive interference between those

dipole moments, a sub-radiant mode is generated at that wavelength in the scattering profile as a dip. In the hexagon-based heptamer (Fig. 7d to f), plasmon oscillations in all NPs are ‘in phase’ at the Fano peaks (720 nm and 864 nm) and like in quadrumer, constructive interference between them explains the generation of the broad super-radiant modes of FR as scattering peaks at the corresponding wavelengths. At the Fano dip (778 nm), NPs in the hexagon-based heptamer manifest a complex phase relation between them, as depicted in Fig. 7e, which is neither ‘anti-phase’ nor ‘in phase’ rather something in between. Consequently, like in quadrumer, the far-field scattering dip or sub-radiant mode of FR is generated due to the destructive interference between the plasmon oscillations in those NPs.

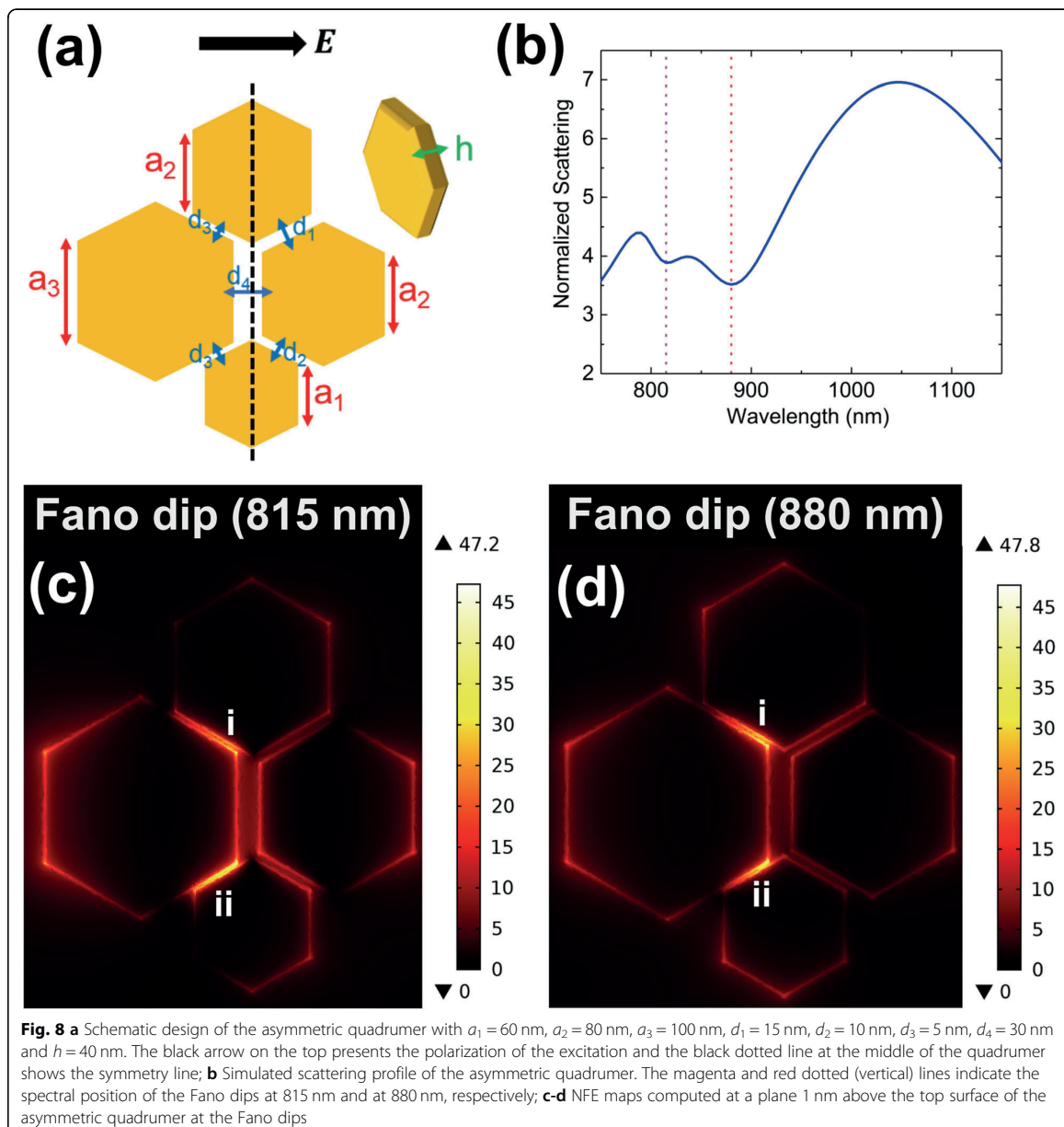
Certainly, we can infer from Fig. 7 that the origin of FR in those hexagon-based oligomers are purely electric in nature since FR originated due to the interaction between the electrical dipole moments of the NPs [28, 40, 46, 47, 53].

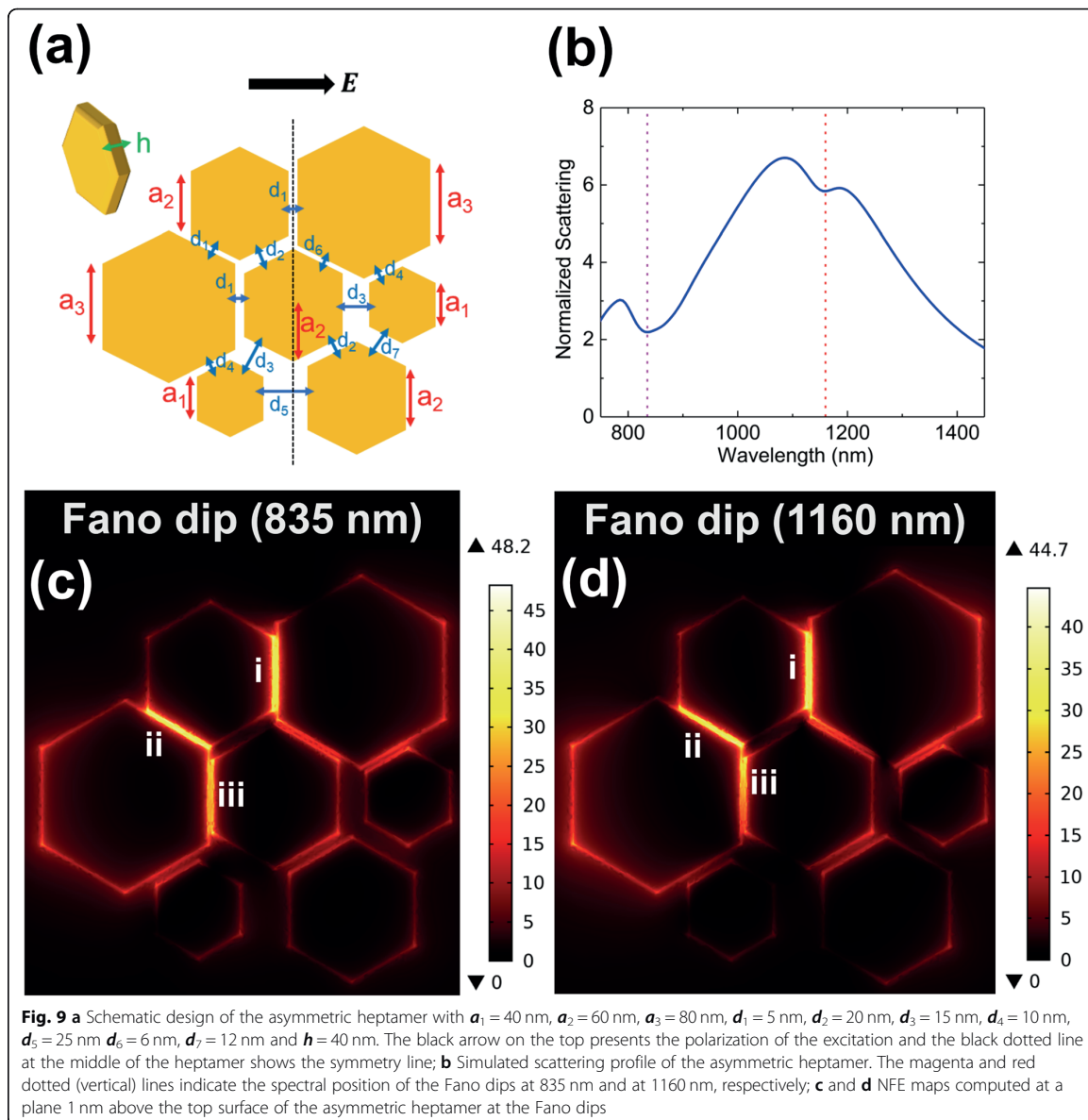
We also investigated the role of the symmetry breaking in the hexagon-based oligomers in terms of the asymmetry



in NP sizes and interparticle gaps with respect to a symmetry line correlated with the polarization of the excitation. Figures 8a and 9a represent the symmetry breaking schematically. In the asymmetric quadrumer, as illustrated in Fig. 8a, the sizes of two NPs were made unequal ($a_1 = 60$ nm, $a_3 = 100$ nm) while keeping the sizes of the rest two NPs equal ($a_2 = 80$ nm). The thicknesses of all four NPs were equal ($h = 40$ nm) but the interparticle gaps were different over the oligomer geometry with $d_1 = 15$ nm, $d_2 = 10$ nm, $d_3 = 5$ nm and $d_4 = 30$ nm. In Fig. 8a, the black

arrow shows the polarization of the excitation light and the black dotted line at the middle of the quadrumer represents the symmetry line. Clearly, the light, polarized along the direction shown in Fig. 8a, will face different NP sizes and interparticle gaps on the two sides of the symmetry line and hence, the symmetry of the oligomer is broken in terms of the polarization of light. Such symmetry breaking in the quadrumer geometry yielded double FR in its scattering profile (Fig. 8b), manifested as two Fano dips at 815 nm (dotted magenta line) and at 880 nm (dotted red line). The





NFE maps at the two Fano dips (Fig. 8c and d) show that we again achieved two hot spots spatially overlapped at both wavelengths.

In the asymmetric heptamer, as illustrated in Fig. 9a, the sizes of four NPs were made unequal ($a_1 = 40$ nm, $a_3 = 80$ nm) while keeping the sizes of the rest three NPs equal ($a_2 = 60$ nm). The thicknesses of all NPs were equal ($h = 40$ nm) but the interparticle gaps were different over the oligomer geometry with $d_1 = 5$ nm, $d_2 = 20$ nm, $d_3 = 15$ nm, $d_4 = 10$ nm, $d_5 = 25$ nm, $d_6 = 6$ nm and $d_7 = 12$ nm. According to Fig. 9a, like in the case of

quadrumer, the light, polarized along the direction shown by the black arrow, will face different NP sizes and interparticle gaps on the two sides of the symmetry line (the black dotted line at the middle of the heptamer) and hence, the symmetry of the oligomer is broken for the polarized light. Here also, profound signature of the double FR was obtained in the scattering profile of the asymmetric heptamer (Fig. 9b) with three hot spots spatially overlapped at both Fano dips (835 nm, dotted magenta line and 1160 nm, dotted red line), as reported in Fig. 9c and d. It is worth to mention here that in the

scattering spectra of asymmetric oligomers (Figs. 8b and 9b), neither any sign of quadrupolar peak was found at the lower wavelengths nor the peaks obtained at higher wavelengths match with the LSPR modes of the individual NPs (i.e. monomer peaks) present in the oligomer. Consequently, we can conclude that the scattering lineshapes are clearly a manifestation of the double FR, generated due to the complex hybridization between the LSPRs of the NPs.

Existence of double FR can also be exploited for SECARS enhancements by tuning the two Fano dips at the pump and Stokes wavelengths while the Fano peak (at the blue side of the both Fano dips) at the CARS wavelength. Such strategy will ensure minimization of scattering losses and efficient energy coupling between the oligomer and the excitation light at both excitation wavelengths (i.e. pump and Stokes) as well as an enhanced far-field propagation of CARS signal [30].

Generation of double FR in the optical responses of those hexagon-based oligomers is not a general effect of symmetry breaking and since, symmetry can be broken in different possible ways, it can also affect the optical response of the oligomers differently. Further studies required to draw any concrete conclusion on the role of symmetry breaking in such hexagon-based oligomers.

Conclusions

Succinctly, we designed hexagonal NP based Fano-resonant oligomers, a gold quadrumer and a gold heptamer, using FEM simulations for optimal performance in CARS applications at 780 nm pumping. The targeted Raman signature zone was the 'fingerprint region' ($500\text{--}1800\text{ cm}^{-1}$) of the analytes. Our proposed designs provide fabrication possible geometries for the oligomers. We achieved to engineer the lineshape of the FR in those oligomers so that the sub-radiant mode of FR would spectrally overlap with the pump to ensure energy coupling between the excitation light and the nanostructures while the super-radiant modes of FR would tune with the Stokes and CARS regimes to enhance far-field propagation of the output light. Our computational studies revealed that the hexagonal NP based oligomers yielded higher number of spatially overlapped hot spots compared to the disk-type oligomers even in the case of normal incidence of excitation light. Our estimated SECARS enhancements from the proposed oligomers were in the order of $10^{12}\text{--}10^{13}$, which meet the requirement of single molecular level applications. We also explored the origin of the FR in those oligomers, which is purely electric in nature. Our studies on the role of symmetry breaking in the proposed oligomers provided a way to implement double FR in such structures and enabled its exploitation for SECARS by yielding spatially overlapped hot spots at multiple Fano dips. Such

numerical findings are important in the context of designing plasmonic substrates with fabrication-friendly nanostructures for SECARS and for multi-photon based spectroscopic techniques in general to realize higher number of spatially localized hotspots for improving the detection sensitivity.

Abbreviations

CARS: Coherent anti-Stokes Raman scattering; FEM: Finite element method; FR: Fano resonance; FWM: Four-wave mixing; LSPR: Localized surface plasmon resonances; NFE: Near-field enhancement; NFIE: Near-field intensity enhancement; NPs: Nanoparticles; PMLs: Perfectly matched layers; RS: Raman spectroscopy; SECARS: Surface-enhanced coherent anti-Stokes Raman scattering; SERS: Surface-enhanced Raman spectroscopy

Acknowledgements

The authors gratefully acknowledge Prof. Kai-Erik Peiponen (University of Eastern Finland), Prof. Mika Pettersson (University of Jyväskylä), and Assoc. Prof. J. Jussi Toppari (University of Jyväskylä) for their valuable guidance during the research work.

Authors' contributions

A. Dutta proposed the original idea and implemented the simulations. E. M. Vartiainen guided the research. A. Dutta drafted and wrote the manuscript. Both authors read, revised and approved the final manuscript.

Funding

The work is part of the Academy of Finland Flagship Program, Photonics Research and Innovation (PREIN), decision 321066.

Availability of data and materials

Information about data was detailed in the article.

Ethics approval and consent to participate

Not applicable.

Consent for publication

Not applicable.

Competing interests

The authors declare that they have no competing interests.

Author details

¹Department of Physics and Nanoscience Center, University of Jyväskylä, Jyväskylä, Finland. ²School of Engineering Science, LUT University, Lappeenranta, Finland.

Received: 1 December 2019 Accepted: 24 February 2020

Published online: 09 April 2020

References

1. Long, D.: Early history of the Raman effect. *Int. Rev. Phys. Chem.* **7**(4), 317–349 (1988)
2. Banwell, C.: Raman spectroscopy. In: Banwell, C. (ed.) *Fundamentals of Molecular Spectroscopy*, pp. 124–154. McGraw-Hill, New York (1972)
3. Long, D.: *The Raman Effect: a Unified Treatment of the Theory of Raman Scattering by Molecules*. Wiley, New Jersey (2002)
4. Shipp, D., Sinjab, F., Nottingher, I.: Raman spectroscopy: techniques and applications in the life sciences. *Adv. Opt. Photonics.* **9**(2), 315–428 (2017)
5. Das, R., Agrawal, Y.: Raman spectroscopy: recent advancements, techniques and applications. *Vib. Spectrosc.* **57**, 163–176 (2011)
6. Vandenabeele, P., Tate, J., Moens, L.: Non-destructive analysis of museum objects by fiber-optic Raman spectroscopy. *Anal. Bioanal. Chem.* **387**(3), 813–819 (2007)
7. Meksiarun, P., Andriana, B., Matsuyoshi, H., Sato, H.: Non-invasive quantitative analysis of specific fat accumulation in subcutaneous adipose tissues using Raman spectroscopy. *Sci. Rep.* **6**, 37068 (2016)
8. Haynes, C., McFarland, A., Van Duyne, R.: Surface-enhanced Raman spectroscopy. *Anal. Chem.* **77**(17), 338A–346A (2005)

9. Schlücker, S.: Surface-enhanced Raman spectroscopy: concepts and chemical applications. *Angew. Chem. Int. Ed.* **53**, 4756–4795 (2014)
10. Sharma, B., Frontiera, R., Henry, A., Ringe, E., Van Duyne, R.: SERS: materials, applications, and the future. *Mater. Today*. **15**(1–2), 16–25 (2012)
11. Ding, S., You, E., Tian, Z., Moskovits, M.: Electromagnetic theories of surface-enhanced Raman spectroscopy. *Chem. Soc. Rev.* **46**, 4042–4076 (2017)
12. Chulhai, D., Hu, Z., Moore, J., Chen, X., Jensen, L.: Theory of linear and nonlinear surface-enhanced vibrational spectroscopies. *Annu. Rev. Phys. Chem.* **67**, 541–564 (2016)
13. Henry, A., Sharma, B., Cardinal, M., Kurouski, D., Van Duyne, R.: Surface-enhanced Raman spectroscopy biosensing: in vivo diagnostics and multimodal imaging. *Anal. Chem.* **88**, 6638–6647 (2016)
14. Tripp, R., Dluhy, R., Zhao, Y.: Novel nanostructures for SERS biosensing. *Nano Today*. **3**(3–4), 31–37 (2008)
15. Bantz, K., Meyer, A., Wittenberg, N., Im, H., Kurtulus, Ö., Lee, S., Lindquist, N., Oh, S.H., Haynes, C.: Recent progress in SERS biosensing. *Phys. Chem. Chem. Phys.* **13**, 11551–11567 (2011)
16. Ru, E., Etchegoin, P.: Single-molecule surface-enhanced Raman spectroscopy. *Annu. Rev. Phys. Chem.* **63**, 65–87 (2012)
17. Wang, Y., Irudayaraj, J.: Surface-enhanced Raman spectroscopy at single-molecule scale and its implications in biology. *Phil. Trans. R Soc. B.* **368**, 20120026 (2013)
18. Lee, H., Jin, S., Kim, H., Suh, Y.: Single-molecule surface-enhanced Raman spectroscopy: a perspective on the current status. *Phys. Chem. Chem. Phys.* **15**, 5276–5287 (2013)
19. Zrimsek, A., Chiang, N., Mattei, M., Zaleski, S., McAnally, M., Chapman, C., Henry, A.I., Schatz, G., Van Duyne, R.: Single-molecule chemistry with surface- and tip-enhanced Raman spectroscopy. *Chem. Rev.* **117**, 7583–7613 (2017)
20. Eesley, G.: *Coherent Raman Spectroscopy*. Pergamon Press, Oxford (1981)
21. Cheng, J.X., Xie, X.S. (eds.): *Coherent Raman Scattering Microscopy*. CRC Press, Boca Raton (2013)
22. Evans, C.L., Xie, X.S.: Coherent anti-Stokes Raman scattering microscopy: chemical imaging for biology and medicine. *Annu. Rev. Anal. Chem.* **1**, 883–909 (2008)
23. Cheng, J.X., Xie, X.S.: Coherent anti-Stokes Raman scattering microscopy: instrumentation, theory, and applications. *J. Phys. Chem. B.* **108**(3), 827–840 (2004)
24. Volkmer, A.: Vibrational imaging and microspectroscopies based on coherent anti-Stokes Raman scattering microscopy. *J. Phys. D: Appl. Phys.* **38**, R59–R81 (2005)
25. Krafft, C., Dietzek, B., Schmitt, M., Popp, J.: Raman and coherent anti-Stokes Raman scattering microspectroscopy for biomedical applications. *J. Biomed. Opt.* **17**(4), 0408011–04080115 (2012)
26. Volkmer, A.: Coherent Raman scattering microscopy. In: Matousek, P., Morris, M. (eds.) *Emerging Raman Applications and Techniques in Biomedical and Pharmaceutical Fields*, pp. 111–152. Springer – Verlag, Berlin (2010)
27. Xie, X.S., Cheng, J., Potma, E.: Coherent anti-Stokes Raman scattering microscopy. In: Pawley, J.B. (ed.) *Handbook of Biological Confocal Microscopy*, pp. 595–606. Springer – Verlag US, Boston (2006)
28. Zhang, Y., Zhen, Y., Neumann, O., Day, J., Nordlander, P., Halas, N.: Coherent anti-Stokes Raman scattering with single-molecule sensitivity using a plasmonic Fano resonance. *Nat. Commun.* **5**, 4424 (2014)
29. Zhou, Q., Zhu, J., Yuan, J., Fang, X.: Numerical simulation of surface-enhanced coherent anti-Stokes Raman scattering on gold nanoparticle substrate. *J. Nanosci. Nanotechnol.* **17**(3), 2152–2156 (2017)
30. He, J., Fan, C., Ding, P., Zhu, S., Liang, E.: Near-field engineering of Fano resonances in a plasmonic assembly for maximizing CARS enhancements. *Sci. Rep.* **6**, 20777 (2016)
31. Hentschel, M., Dregely, D., Vogelgesang, R., Giessen, H., Liu, N.: Plasmonic oligomers: the role of individual particles in collective behavior. *ACS Nano.* **5**(3), 2042–2050 (2011)
32. Hentschel, M., Saliba, M., Vogelgesang, R., Giessen, H., Alivisatos, P., Liu, N.: Transition from isolated to collective modes in plasmonic oligomers. *Nano Lett.* **10**(7), 2721–2726 (2010)
33. Zhang, Y., Wen, F., Zhen, Y.R., Nordlander, P., Halas, N.: Coherent Fano resonances in a plasmonic nanocluster enhance optical four-wave mixing. *Proc. Natl. Acad. Sci. U. S. A.* **110**(23), 9215–9219 (2013)
34. Fan, J., Bao, K., Wu, C., Bao, J., Bardhan, R., Halas, N., Manoharan, V., Shvets, G., Nordlander, P., Capasso, F.: Fano-like interference in self-assembled plasmonic quadrumer clusters. *Nano Lett.* **10**(11), 4680–4685 (2010)
35. Gallinet, B., Martin, O.: Influence of electromagnetic interactions on the line shape of plasmonic Fano resonances. *ACS Nano.* **5**(11), 8999–9008 (2011)
36. Lassiter, B., Sobhani, H., Knight, M., Mielczarek, W., Nordlander, P., Halas, N.: Designing and deconstructing the Fano lineshape in plasmonic nanoclusters. *Nano Lett.* **12**, 1058–1062 (2012)
37. Lassiter, B., Sobhani, H., Fan, J., Kundu, J., Capasso, F., Nordlander, P., Halas, N.: Fano resonances in plasmonic nanoclusters: geometrical and chemical tunability. *Nano Lett.* **10**(8), 3184–3189 (2010)
38. Joe, Y., Satanin, A., Kim, C.: Classical analogy of Fano resonances. *Phys. Scr.* **74**, 259–266 (2006)
39. Lovera, A., Gallinet, B., Nordlander, P., Martin, O.: Mechanisms of Fano resonances in coupled plasmonic systems. *ACS Nano.* **7**(5), 4527–4536 (2013)
40. Rahmani, M., Tahmasebi, T., Lin, Y., Lukiyanchuk, B., Liew, T., Hong, M.: Influence of plasmon destructive interferences on optical properties of gold planar quadrumers. *Nanotechnology.* **22**, 245204 (2011)
41. Rahmani, M., Lei, D., Giannini, V., Lukiyanchuk, B., Ranjbar, M., Liew, T., Hong, M., Maier, S.: Subgroup decomposition of plasmonic resonances in hybrid oligomers: modeling the resonance lineshape. *Nano Lett.* **12**(4), 2101–2106 (2012)
42. Attaran, A., Emami, S., Soltanian, M., Penny, R., Behbahani, F., Harun, S., Ahmad, H., Abdul-Rashid, H., Moghavvemi, M.: Circuit model of Fano resonance on tetramers, pentamers and broken symmetry pentamers. *Plasmonics.* **9**, 1303–1313 (2014)
43. Gallinet, B., Martin, O.: Ab-initio theory of Fano resonances in plasmonic nanostructures and metamaterials. *Phys. Rev. B.* **83**, 2354271–2354276 (2011)
44. Hashimoto, K., Omachi, J., Ideguchi, T.: Ultra-broadband rapid-scan Fourier-transform CARS spectroscopy with sub-10-fs optical pulses. *Opt. Express.* **26**, 14307–14314 (2018)
45. Ye, J., Wen, F., Sobhani, H., Lassiter, J., Dorpe, P., Nordlander, P., Halas, N.: Plasmonic nanoclusters: near-field properties of the Fano resonance interrogated with SERS. *Nano Lett.* **12**(3), 1660–1667 (2012)
46. Rahmani, M., Lukiyanchuk, B., Ng, B., Tavakkoli, A., Liew, T., Hong, M.: Generation of pronounced Fano resonances and tuning of subwavelength spatial light distribution in plasmonic pentamers. *Opt. Express.* **19**(6), 4949–4956 (2011)
47. Rahmani, M., Lukiyanchuk, B., Nguyen, T., Tahmasebi, T., Lin, Y., Liew, T., Hong, M.: Influence of symmetry breaking in pentamers on Fano resonance and near-field energy localization. *Opt. Mater. Express.* **1**(8), 1409–1415 (2011)
48. COMSOL Multiphysics v. 5.4. Application: Scatterer on Substrate. COMSOL AB, Stockholm. https://www.comsol.fi/model/download/563151/models_woptics.scatterer_on_substrate.pdf. Accessed 1 Dec 2019 (2019)
49. Johnson, P., Christy, R.: Optical constants of the noble metals. *Phys. Rev. B.* **6**, 4370–4379 (1972)
50. Miroshnichenko, A., Flach, S., Kivshar, Y.: Fano resonances in nanoscale structures. *Rev. Mod. Phys.* **82**, 2257–2298 (2010)
51. Dutta, A., Alam, K., Nuutinen, T., Hulkko, E., Karvinen, P., Kuittinen, M., Toppari, J.J., Vartiainen, E.: Influence of Fano resonance on SERS enhancement in Fano-plasmonic oligomers. *Opt. Express.* **27**(21), 30031–30043 (2019)
52. Gallinet, B., Martin, O.: Relation between near-field and far-field properties of plasmonic Fano resonances. *Opt. Express.* **19**(22), 22167–22175 (2011)
53. Rahmani, M., Lukiyanchuk, B., Tahmasebi, T., Lin, Y., Liew, T., Hong, M.: Polarization-controlled spatial localization of near-field energy in planar symmetric coupled oligomers. *Appl. Phys. A Mater. Sci. Process.* **107**, 23–30 (2012)

Publisher's Note

Springer Nature remains neutral with regard to jurisdictional claims in published maps and institutional affiliations.

PIII

**FABRICATION-FRIENDLY POLARIZATION-SENSITIVE
PLASMONIC GRATING FOR OPTIMAL SURFACE-ENHANCED
RAMAN SPECTROSCOPY**

by

A. Dutta, T. Nuutinen, K. Alam, A. Matikainen, P. Li, E. Hulkko, J. J. Toppari, H.
Lipsanen, and G. Kang,

Journal of the European Optical Society-Rapid Publications, **16**, 022 (2020).

Reproduced with kind permission of Springer Nature.

RESEARCH

Open Access

Fabrication-friendly polarization-sensitive plasmonic grating for optimal surface-enhanced Raman spectroscopy



Arpan Dutta^{1*†} , Tarmo Nuutinen^{2,3†}, Khairul Alam², Antti Matikainen⁴, Peng Li⁵, Eero Hulkko^{1,4}, J. Jussi Toppari^{1*}, Harri Lipsanen⁴ and Guoguo Kang⁵

Abstract

Plasmonic nanostructures are widely utilized in surface-enhanced Raman spectroscopy (SERS) from ultraviolet to near-infrared applications. Periodic nanoplasmonic systems such as plasmonic gratings are of great interest as SERS-active substrates due to their strong polarization dependence and ease of fabrication. In this work, we modelled a silver grating that manifests a subradiant plasmonic resonance as a dip in its reflectivity with significant near-field enhancement only for transverse-magnetic (TM) polarization of light. We investigated the role of its fill factor, commonly defined as a ratio between the width of the grating groove and the grating period, on the SERS enhancement. We designed multiple gratings having different fill factors using finite-difference time-domain (FDTD) simulations to incorporate different degrees of spectral detunings in their reflection dips from our Raman excitation (488 nm). Our numerical studies suggested that by tuning the spectral position of the optical resonance of the grating, via modifying their fill factor, we could optimize the achievable SERS enhancement. Moreover, by changing the polarization of the excitation light from transverse-magnetic to transverse-electric, we can disable the optical resonance of the gratings resulting in negligible SERS performance. To verify this, we fabricated and optically characterized the modelled gratings and ensured the presence of the desired detunings in their optical responses. Our Raman analysis on riboflavin confirmed that the higher overlap between the grating resonance and the intended Raman excitation yields stronger Raman enhancement only for TM polarized light. Our findings provide insight on the development of fabrication-friendly plasmonic gratings for optimal intensification of the Raman signal with an extra degree of control through the polarization of the excitation light. This feature enables studying Raman signal of exactly the same molecules with and without electromagnetic SERS enhancements, just by changing the polarization of the excitation, and thereby permits detailed studies on the selection rules and the chemical enhancements possibly involved in SERS.

Keywords: Plasmonic grating, Surface-enhanced Raman scattering, Fill factor

* Correspondence: arpan.a.dutta@jyu.fi; jjussi.toppari@jyu.fi

† Arpan Dutta and Tarmo Nuutinen contributed equally to this work.

¹Department of Physics and Nanoscience Center, University of Jyväskylä, Jyväskylä, Finland

Full list of author information is available at the end of the article



© The Author(s). 2020 **Open Access** This article is licensed under a Creative Commons Attribution 4.0 International License, which permits use, sharing, adaptation, distribution and reproduction in any medium or format, as long as you give appropriate credit to the original author(s) and the source, provide a link to the Creative Commons licence, and indicate if changes were made. The images or other third party material in this article are included in the article's Creative Commons licence, unless indicated otherwise in a credit line to the material. If material is not included in the article's Creative Commons licence and your intended use is not permitted by statutory regulation or exceeds the permitted use, you will need to obtain permission directly from the copyright holder. To view a copy of this licence, visit <http://creativecommons.org/licenses/by/4.0/>.

Introduction

Raman spectroscopy (RS) is a powerful vibrational spectroscopic technique and widely used as an analytical method to reveal ‘chemical fingerprint’ of the probed materials [1–7]. Surface-enhanced Raman spectroscopy (SERS) is an improved version of RS with the presence of a ‘surface’ underneath the probed materials to ‘enhance’ the weak Raman response of the probe. The ‘surface’ usually consists of plasmonic nanostructures possessing plasmonic resonances with enhanced near-field localization suitably tuned to spectrally match with the laser excitation and the vibrational Stokes region [8–13]. In combination with simultaneous rapid developments in computational nanophotonics and nanofabrication processes, SERS has become an established tool for bio-sensing [14–16] and single-molecule studies [17–20].

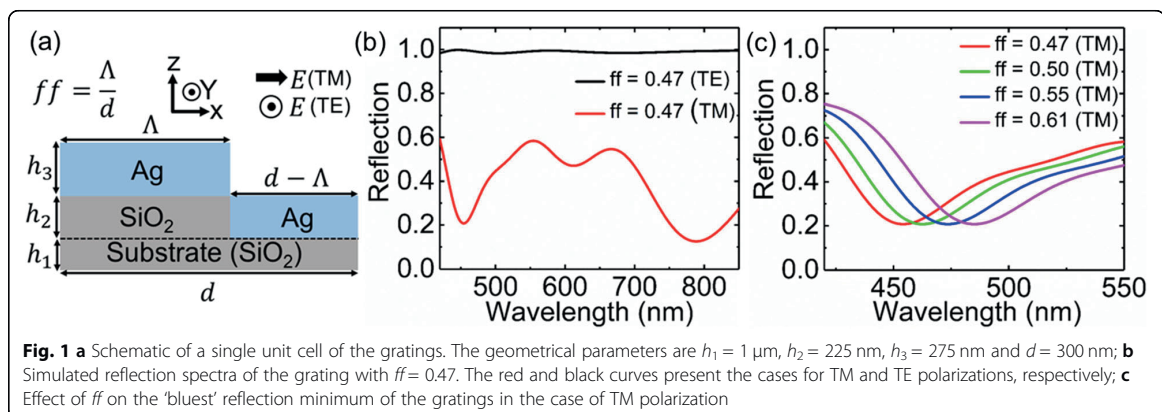
Plasmonic nanostructures for SERS typically include metallic nanoantennas with regular geometries such as nanospheres, nanocubes, nanotriangles, nanorods, nanotips [21–23], as well as irregular-shaped nanoparticles [24] and nanoparticle oligomers [25–27]. Periodic structures with lattice resonances, such as plasmonic gratings [28–34] and nanoparticle arrays [35], are also used as SERS substrates. In a plasmonic grating, excitations of surface plasmon polariton (SPP) modes are shown as reflectance dips at the resonance energies. The SPPs can provide local field enhancements up to the order of 10^3 . Unlike flat metal surfaces, excitation of SPP modes in metallic gratings with well-defined periodicity does not require special experimental arrangements and the resonance condition can be achieved with regular transverse-magnetic (TM) polarized light [36–41].

Resonant sub-wavelength plasmonic gratings [42] are important SERS substrates [43–45] due to their easy reproducibility and stability as SERS-active media [46]. Such gratings have a controllable preference to the polarization of the incident electromagnetic field [47]

and provide relatively high enhancement factors [48]. Thus, development of fabrication-friendly plasmonic gratings with favorable structure and surface topology as well as strong polarization sensitivity is essential for optimum Raman intensification.

In this article, we study a polarization-sensitive silver grating that manifests a subradiant plasmonic resonance as a dip in its reflectivity with significant near-field enhancement only for TM-polarized light. We investigate the role of its fill factor, commonly defined as a ratio between the width of the grating groove and the grating period (as illustrated in Fig. 1a), on the SERS enhancement. The grating is modelled and optimized for Raman applications using finite-difference time-domain (FDTD) method [49–51]. Riboflavin is used as a probe analyte, and the excitation wavelength is chosen to be 488 nm, since it yields a strong resonance Raman signal of the analyte. Riboflavin has prominent Raman lines [52] at 1321 cm^{-1} and 1345 cm^{-1} that are targeted in the grating design. Our FDTD simulations show that by varying the fill factor of the grating one can improve the SERS enhancement significantly by spectrally tuning the grating reflection dips to match energetically with the Raman excitation. The more the reflection minimum overlaps with the intended excitation, the higher the Raman enhancement one can obtain. Moreover, by changing the polarization of the excitation light from transverse-magnetic to transverse-electric, one can disable the SPP resonance of the gratings. These numerical predictions are confirmed by optical and SERS experiments on the fabricated gratings.

Overall, our reported results not just show a way to optimize fabrication-friendly nanostructures to reach high sensitivity in Raman detection, but also demonstrate an extra degree of control through the polarization of the excitation light. This feature enables studying Raman signal of exactly the same molecules with and



without electromagnetic SERS enhancements, just by changing the polarization of the excitation, and thereby permits detailed studies on the selection rules and the chemical enhancements possibly involved in SERS.

Materials and methods

FDTD simulations

Plasmonic gratings were modelled and optimized using the FDTD method [49–51] implemented by Lumerical FDTD Solutions [53]. The optical responses of the gratings were computed using the two-dimensional (2D-FDTD) simulations on XZ plane, as defined in Fig. 1a, by assuming that the grating volume extends uniformly in Y direction. In the simulation setup, a single unit cell of the grating (in air), as depicted in Fig. 1a, was considered with the geometrical parameters: $h_1 = 1 \mu\text{m}$, $h_2 = 225 \text{ nm}$, $h_3 = 275 \text{ nm}$ and $d = 300 \text{ nm}$. Four different fill factors (0.47, 0.50, 0.55 and 0.61) were considered where the fill factor is defined as $ff = \Lambda/d$ with Λ being the width of the silver layer on top and d as the period of the grating. Periodic boundary conditions (PBCs) and perfectly matched layers (PMLs) were used in the X- and Z-direction, respectively. Normal incidence of light (plane waves) with transverse-electric (TE) and transverse-magnetic (TM) polarizations, as defined in Fig. 1a, were considered as excitations. The dispersive dielectric function of silver (Ag) was extracted from the experimental data reported by Johnson and Christy [54]. The nondispersive refractive indices of air and glass (SiO_2) were considered as 1.00 and 1.45, respectively.

Fabrication

Fabrication of the designed gratings with four different fill factors was done using electron-beam lithography (EBL). Chromium was used as a hard mask and it was deposited on top of a glass (SiO_2) substrate by thermal evaporation technique. After the deposition, a standard e-beam resist was spin-coated on top of the chromium-masked substrate. The spin-coated resist was then patterned in an EBL system (Raith EBP 5000+) according to the optimized design parameters obtained from the FDTD simulations. After the resist-development, the patterns were transferred to the chromium layer by inductively coupled plasma reactive ion etching (ICP-RIE). A similar technique was used to transfer the patterns from chromium to the SiO_2 substrate. After that, chromium wet etching was performed to remove the remaining mask. Finally, silver was deposited on top of the patterned SiO_2 substrate by thermal evaporation technique. After the fabrication, scanning electron microscope (SEM) imaging has been carried out using LEO 1550 Gemini SEM (operated at the acceleration voltage of 5 kV) to determine the structural parameters of the fabricated gratings.

Optical characterization

Fabricated gratings were optically characterized using a microscopy (Olympus BX51) setup with a 5X objective (Olympus MPLN5x-BD, NA = 0.15) used for the excitation and the collection. The reflection spectra of the fabricated gratings were collected in a regular bright-field configuration with linearly polarized light. The desired excitation polarization was set by rotating the sample. The polarization at the detector end was tuned separately using an analyzer-polarizer filter. Collected light was focused into a fiber and guided to a spectrometer (Acton Spectrograph SP2150i with Andor iVAC CCD). The recorded reflectance spectra from the gratings were normalized by the instrument response spectrum obtained as a reflectance from a highly reflective silver mirror. The excitation light was incident on the gratings from all directions up to the angles of 23.6° . More details on the experimental setup can be found elsewhere [55].

SERS measurements

Raman response of riboflavin on top of the fabricated gratings was recorded using a commercially available Raman setup (WITec alpha300 confocal Raman microscope) where the wavelength of the excitation light was 488 nm. A 20X objective (NA = 0.40) was used to illuminate the sample for 5 s with $150 \mu\text{W}$ excitation power while collecting the Stokes-side Raman spectrum through the same objective. The correct polarization of the focused excitation beam was maintained by rotating the sample stage. Ten microliters aqueous solution of riboflavin ($1.0 \mu\text{M}$ concentration) was deposited on top of the fabricated gratings and incubated for 10 min under normal humidity. After incubation, the riboflavin solution was blown away with compressed nitrogen flow to avoid the coffee-ring effect resulting in an uneven coverage of the riboflavin molecules on the gratings. Raman spectra were collected from four different positions on each grating as an average of a 5×5 array of single shots (i.e. 25 shots) on each position. The collected spectra were further averaged over those four positions for each grating. Averaged spectra were baseline-corrected with the help of a commercially available data analysis software OriginPro 2017 [56].

Results and discussion

We carried out 2D-FDTD simulations to optimize the geometrical parameters of the gratings. Figure 1a schematically represents a single unit cell of the gratings with pictorial definitions of the fill factor (ff), TE/TM polarizations, and the simulation plane (XZ). During the optimization process, we varied the ff of the gratings as a key parameter while keeping all other parameters fixed (i.e. $h_1 = 1 \mu\text{m}$, $h_2 = 225 \text{ nm}$, $h_3 = 275 \text{ nm}$ and $d = 300 \text{ nm}$). Four different fill factors ($ff = 0.47, 0.50, 0.55$ and

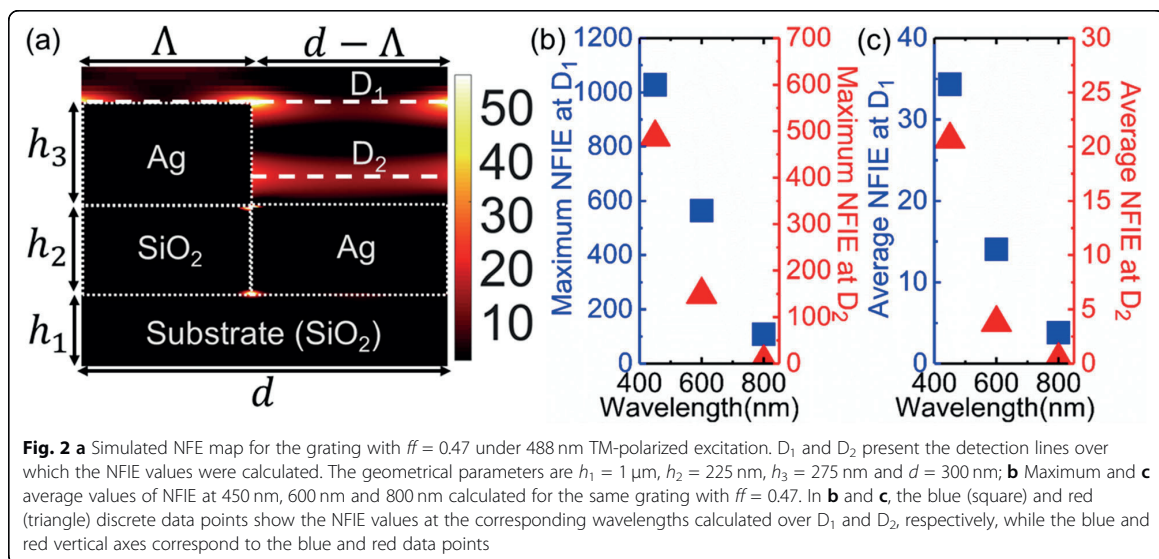
0.61) were chosen for the fabrication. The broad-range reflection spectra of a grating with $ff = 0.47$ are presented in Fig. 1b for TE and TM polarizations. From the figure, we can see that in the case of TE polarization (black curve), the grating act as a highly reflecting surface since only TM polarization of light can excite the SPP modes [36]. For TM-polarized light (red curve), the excitation of SPP modes is clearly manifested as the reflection dips close to 450 nm, 600 nm and 800 nm. The effect of ff on the bluest reflection minimum i.e. around 450–500 nm, is reported in Fig. 1c showing a clear red shift with increasing ff . Therefore, by choosing four different ff values in an increasing order, we set different amounts of spectral detuning in the ‘bluest’ reflection minima of the gratings from our Raman excitation (488 nm). The grating with $ff = 0.61$ has the lowest detuning since its ‘bluest’ reflection minimum is closest to the excitation (488 nm). Similarly, the grating with $ff = 0.47$ has the highest detuning while the other two gratings are in between.

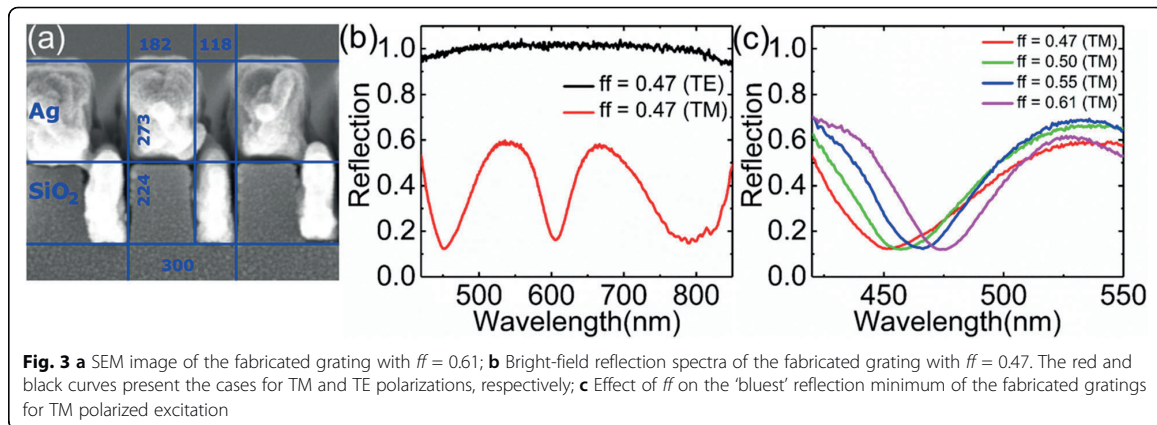
The reason behind our choice towards the ‘bluest’ reflection minima (~ 450 nm) of the gratings for this study, instead of the other two reflection minima at higher wavelengths, can be explained with the help of Fig. 2. Figure 2a shows the near-field enhancement (NFE) map for the grating with $ff = 0.47$ while illuminated with 488 nm TM-polarized excitation light. The NFE was calculated as $|E_{loc}/E_0|$ where E_{loc} is the electric-field amplitude of the local field and E_0 is the same for the incident field. We chose two detection lines (they are lines since the simulations were in 2D) D_1 and D_2 on the NFE map, as illustrated in Fig. 2a, where the field localizations are maximum. Then, we calculated the average and

maximum values of the near-field intensity enhancement (NFIE), defined as $|E_{loc}/E_0|^2$, over the D_1 and D_2 lines with excitations at three reflection minima (i.e. at 450 nm, 600 nm and 800 nm). Figure 2b reports the maximum NFIE values at three reflection minima over the D_1 (blue) and D_2 (red) lines. Figure 2c depicts the same for the average NFIE values.

From Fig. 2b and c it is clear that both the maximum and average values of NFIE are highest at the ‘bluest’ reflection minimum for both detection lines. Similar trend was found in the case of other three gratings (not shown). Since the electromagnetic enhancement factor of SERS is a product of NFIE at the excitation and the Stokes wavelengths, i.e. $G_{SERS} = |E_{loc(excitation)}/E_0|^2 \times |E_{loc(Stokes)}/E_0|^2$ [25, 26], the ‘bluest’ reflection minimum will always provide the highest G_{SERS} among the three reflection minima. Therefore, we optimized the spectral position of the ‘bluest’ reflection minimum of the gratings with different detunings from the excitation line to systematically study their effect on SERS.

Four gratings with fill factors 0.47, 0.50, 0.55 and 0.61 were fabricated using EBL where all other geometric parameters were similar with the values used in the numerical simulations. The SEM image of a fabricated grating having a ff of 0.61 is shown in Fig. 3a. Reflection spectra of the fabricated gratings were measured by a microscope under the bright-field configuration. The experimental reflection profiles of the gratings, shown in Fig. 3b and c, are in good agreement with the simulated responses. However, the reflection minima were found to be a bit deeper in the experimental curves (Fig. 3b) compared to the simulated ones (Fig. 1b). In addition, the ‘bluest’ reflection minimum of the gratings for all fill factors were found slightly blue-shifted in the



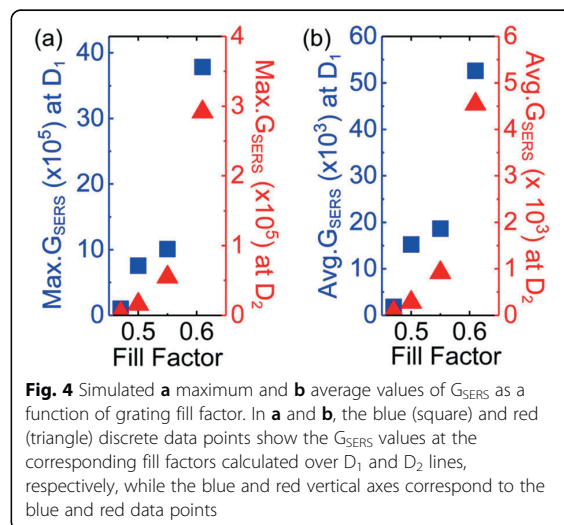


experimental spectra (Fig. 3c) compared to the simulated profiles (Fig. 1c). Such a small discrepancy between the experimental and 2D-FDTD results could be due to the effect of surface topology on the reflectance. In the 2D-FDTD simulations, all surfaces of the gratings were considered perfectly smooth while in the fabricated gratings, significant amount of surface corrugations were present as one can see in Fig. 3a. Taking into account that the surface corrugations with varying roughness can induce changes in the amplitude and spectral position of the reflection minima due to the changes in the dispersion relation of the SPP modes [37], our experimental findings showed relative minor deviation from the 2D-FDTD results. Nevertheless, like in our FDTD results, we achieved the desired detunings in the optical responses of the fabricated gratings, and their surface roughness neither affect the polarization sensitivity of the resonance, as shown in Fig. 3b, nor the NFE due to the SPP modes, as will be seen below.

We investigate the role of the fill factor on the SERS enhancement by computing G_{SERS} for the four simulated gratings over the D_1 and D_2 lines. In the computation, the TM polarized excitation wavelength was 488 nm while the Stokes wavelength was 522 nm for 1321 cm^{-1} and 1345 cm^{-1} Raman lines of riboflavin [52]. Figure 4a reports the maximum values of G_{SERS} with increasing fill factors over the D_1 (blue) and D_2 (red) lines. Figure 4b depicts the same for the average values of G_{SERS} . From Fig. 4a and b we can conclude that both the maximum and the average values of G_{SERS} are increasing with the increment in fill factor for both detection lines. The higher the fill factor, the lower the detuning, the stronger the Raman enhancement. Our simulated G_{SERS} values are in the order of 10^3 on average and in the order of 10^5 at maximum which are consistent with the existing literature [36, 37, 39, 48]. However, it is worth to mention here that further increment in the fill factor can red-shift the 'bluest' reflection minimum of the

grating so much that the detuning again tends to increase when the spectral position of the reflection minimum will reach longer wavelengths than the region of interest i.e. red side of 488 nm. Therefore, careful optimization of the fill factor is required to achieve the highest possible G_{SERS} .

To experimentally confirm the aforementioned findings, we performed Raman spectroscopy of riboflavin with an excitation at 488 nm where the molecule also has an electronic transition. Therefore, even without the plasmonic grating, we detect its resonance Raman signal. When the grating resonance also matched with 488 nm (or very close to it), the resonance Raman signal became 'surface-enhanced' by the SPPs. The Raman responses of riboflavin on top of the fabricated gratings are shown in Fig. 5a where our targeted Raman lines (around 1321 cm^{-1} and 1345 cm^{-1}) were profound for TM polarized excitation. For TE polarized excitation (black curve in



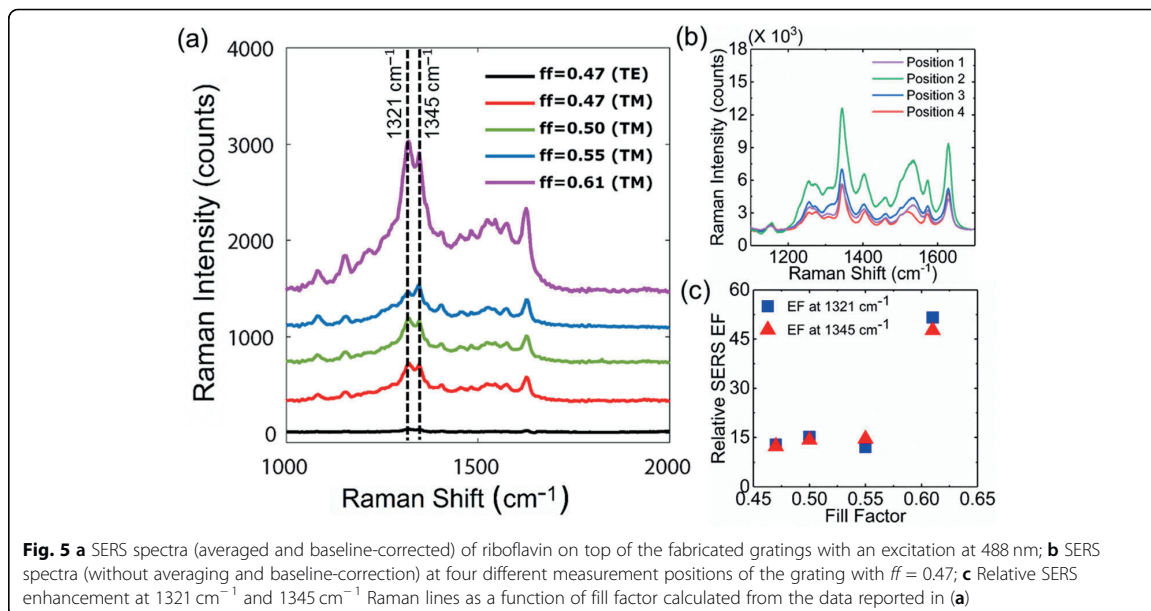


Fig. 5a) Raman signal intensities were insignificant for all gratings. The observed Raman peaks are consistent with the earlier reported works [52, 57, 58]. Of particular note is that our Raman measurements of the bare riboflavin molecules (i.e. without any gratings) with utilized concentrations yielded unreliable results due to the limited sensitivity of the experimental setup and the signal level was basically zero. Such limitation, however, does not affect our study because the detection sensitivity and the number of molecules were same during all the measurements and only the underlying gratings were changed in terms of fill factor while maintaining all other geometrical parameters identical. Moreover, in all gratings, the molecules were excited at 488 nm and hence, yielded similar resonance Raman signal. Therefore, the induced increase in the collected SERS signal directly reflects the relative increase in the enhancement factor due to the fill factor of the gratings, which was our interest. The quantitative values for the SERS enhancements are out of the scope of this article.

Even we minimized the coffee-ring effect on deposition by applying the high nitrogen flow after the incubation, we might not have avoided it completely, which can result in an uneven coverage of riboflavin. To address this reproducibility issue, Fig. 5b reports Raman spectra collected at four different measurement positions on one of the gratings ($ff = 0.47$). From the figure, we see that the Raman intensities vary between different measurement positions clearly implying uneven coverage of molecules. However, the intensities were not varied a lot (means the nitrogen flow was able to minimize the

coffee-ring effect) and no change in the spectral peak positions was found. We deduce that such intensity variations at different measurement positions is not due to any local plasmonic effect (such as surface roughness, wrinkles or holes) since then that would be polarization independent and should show the same variation for TE and TM polarized excitations. However, in our case, only TM polarized excitations resulted the intensity variation and thereby confirmed the uneven coverage of molecules. Such findings also confirmed that the grating SPP mode is the dominating factor for our obtained enhancements and the local plasmonic effects (if any) due to the corrugated surfaces, have negligible contribution. Since, the Raman intensities were not varied a lot at different measurement positions for each grating and maintained the spectral peak positions intact, a spectral averaging over the four positions was employed to compensate the local variations of molecular coverage.

An insight on the qualitative trend of SERS enhancement, with respect to the fill factor of the gratings, can be inferred from Fig. 5c. In the case of TE polarized excitation, the gratings have no SPP modes or optical resonances (i.e. reflection dips) and eventually, negligible SERS enhancement was obtained in this case. The gratings provide significant SERS enhancement only for TM polarized excitation, which also clearly implies the SPP mode being the main reason for the enhancement. Thus, we quantified 'relative' SERS enhancement at the targeted Raman lines as I_{TM}/I_{TE} where I_{TM} and I_{TE} are the Raman intensity counts collected from the corresponding gratings for TM and TE polarizations, respectively.

Such quantification is reasonable since I_{TE} values were almost equal for all four gratings (black curve in Fig. 5a). Figure 5c presents the relative SERS enhancement (SERS EF) at 1321 cm^{-1} and 1345 cm^{-1} Raman lines of riboflavin as a function of fill factor. Interestingly, Fig. 5c manifests very similar trend of Raman enhancement, which we already estimated from our FDTD calculations (Fig. 4a and b). However, the experimental SERS enhancement includes also the chemical enhancement factor [59, 60], so our simulated G_{SERS} values give only the minimum achieved enhancement. It is worth to highlight here that in the case of the grating with $ff = 0.61$, we are optimally enhancing the resonance Raman response of riboflavin. The same grating can provide the maximum Raman enhancement (among all other gratings) for any other molecule if using the same excitation wavelength matching the grating resonance (i.e. SPP as reflection dip). The grating efficiently improves the light-matter coupling at the excitation wavelength always when its SPP resonance is spectrally tuned with the excitation. Therefore, it does not matter if the molecule is non-resonant with the grating resonance as long as the grating resonance and the excitation wavelength are tuned. If this requirement is achieved, the same grating will provide an optimum Raman enhancement for any molecule even if the molecule is non-resonant with the substrate and the excitation wavelength. In this case, the grating will similarly enhance a normal Raman signal instead of resonant Raman signal as in our case.

Strong correlation between our numerical and experimental outcomes confirms that spectral tuning of the strongest reflection dip (i.e. the bluest one) of the grating with the Raman excitation can significantly improve the SERS enhancement. The more the reflection minimum overlaps with the intended excitation regime, the higher the Raman enhancement factor one can obtain. In addition, by changing the polarization of the excitation light from TM to TE, one can disable the SPP resonance of the gratings, i.e., their electromagnetic Raman enhancement capability and hence, study the molecular properties as well as the effect of bare chemical enhancement of SERS in the same experimental setup. Therefore, our reported findings are important in the context of designing fabrication-friendly polarization-sensitive SERS substrates to reach high sensitivity in Raman detection.

Conclusions

Concisely, we modelled and optimized optical responses of four gratings with different fill factors with the help of FDTD simulations such a way that they would have different amounts of detunings in their bluest reflection dip from the intended excitation regime of Raman spectroscopy. Our numerical studies revealed that the bluest reflection dip of the gratings has the highest NFIE among

all the reflection minima and the more it overlaps with the excitation region, the higher the Raman enhancement factor one can obtain. To experimentally verify our estimation, we fabricated the gratings by EBL. Our bright-field reflection measurements of the fabricated gratings showed good agreement with the simulated reflection spectra and thereby confirmed the presence of the desired detunings. Finally, by performing Raman analysis of riboflavin, we obtained very similar trend in the relative SERS enhancement of the gratings, which we already estimated from our FDTD calculations. Strong correlation between our computational and experimental results clearly indicates that one can achieve optimum SERS performance from a plasmonic grating by tuning its strongest optical resonance (via modifying its fill factor) with the Raman excitation. Our study on an easily fabricated plasmonic substrate provide a feasible way to realize optimal SERS with convenient polarization dependency to switch the SERS enhancement on or off.

Abbreviations

RS: Raman spectroscopy; SERS: Surface-enhanced Raman spectroscopy; SPP: Surface plasmon polariton; TM: Transverse-magnetic; TE: Transverse-electric; FDTD: Finite-difference time-domain; PBC: Periodic boundary condition; PML: Perfectly matched layer; EBL: Electron-beam lithography; ICP: Inductively coupled plasma; RIE: Reactive ion etching; SEM: Scanning electron microscope; NFE: Near-field enhancement; NFIE: Near-field intensity enhancement

Acknowledgements

The authors gratefully acknowledge Prof. Jari Turunen and Prof. Markku Kuittinen from Institute of Photonics, University of Eastern Finland, Joensuu, Finland for their valuable guidance during the research work.

Authors' contributions

T. Nuutinen and G. Kang proposed the original idea. A. Dutta, P. Li and G. Kang implemented the FDTD simulations. K. Alam fabricated the gratings. A. Dutta, E. Hulkko and J. J. Toppari optically characterized the fabricated gratings. A. Matikainen and T. Nuutinen carried out the Raman experiments. A. Dutta performed the experimental data analysis. H. Lipsanen, G. Kang and J. J. Toppari guided the research. A. Dutta drafted and wrote the manuscript. All the authors read, revised and approved the final manuscript.

Funding

The reported research work was supported by National Natural Science Foundation of China (NSFC) (No. 61675020), Academy of Finland (Nos. 298298, 289947, 323995, 320166 and 320167), NP-Nano FidiPro by the Finnish Funding Agency for Innovation (TEKES) and NATO project (No. G5250).

Availability of data and materials

Information about data was detailed in the article.

Ethics approval and consent to participate

Not applicable.

Consent for publication

Not applicable.

Competing interests

The author(s) declare(s) that they have no competing interests.

Author details

¹Department of Physics and Nanoscience Center, University of Jyväskylä, Jyväskylä, Finland. ²Institute of Photonics, University of Eastern Finland (UEF),

Joensuu, Finland. ³Department of Environmental and Biological Sciences, UEF, Joensuu, Finland. ⁴Department of Electronics and Nanoengineering, Aalto University, Espoo, Finland. ⁵School of Optoelectronics, Beijing Institute of Technology, Beijing, China.

Received: 17 July 2020 Accepted: 25 October 2020

Published online: 07 November 2020

References

1. Long, D.: Early history of the Raman effect. *Int. Rev. Phys. Chem.* **7**(4), 317–349 (1988)
2. Banwell, C.: Raman spectroscopy. In: Banwell, C. (ed.) *Fundamentals of Molecular Spectroscopy*, pp. 124–154. McGraw-Hill, New York (1972)
3. Long, D.: *The Raman Effect: a Unified Treatment of The Theory of Raman Scattering by Molecules*. Wiley, New Jersey (2002)
4. Mekiarun, P., Andriana, B., Matsuyoshi, H., Sato, H.: Non-invasive quantitative analysis of specific fat accumulation in subcutaneous adipose tissues using Raman spectroscopy. *Sci. Rep.* **6**, 37068 (2016)
5. Vandenabeele, P., Tate, J., Moens, L.: Non-destructive analysis of museum objects by fiber-optic Raman spectroscopy. *Anal. Bioanal. Chem.* **387**(3), 813–819 (2007)
6. Shipp, D., Sinjab, F., Notingher, I.: Raman spectroscopy: techniques and applications in the life sciences. *Adv. Opt. Photonics.* **9**(2), 315–428 (2017)
7. Das, R., Agrawal, Y.: Raman spectroscopy: recent advancements, techniques and applications. *Vib. Spectrosc.* **57**, 163–176 (2011)
8. Haynes, C., McFarland, A., Van Duyne, R.: Surface-enhanced Raman spectroscopy. *Anal. Chem.* **77**(17), 338A–346A (2005)
9. Schlücker, S.: Surface-enhanced Raman spectroscopy: concepts and chemical applications. *Angew. Chem. Int. Ed.* **53**, 4756–4795 (2014)
10. Sharma, B., Frontiera, R., Henry, A., Ringe, E., Van Duyne, R.: SERS: materials, applications, and the future. *Mater. Today.* **15**(1–2), 16–25 (2012)
11. Ding, S., You, E., Tian, Z., Moskovits, M.: Electromagnetic theories of surface-enhanced Raman spectroscopy. *Chem. Soc. Rev.* **46**, 4042–4076 (2017)
12. Kneipp, K., Moskovits, M., Kneipp, H.: *Surface-Enhanced Raman Scattering*. Springer-Verlag, Berlin (2006)
13. Le Ru, E., Etchegoin, P.: *Principles of Surface-Enhanced Raman Spectroscopy*. Elsevier Science, Amsterdam (2008)
14. Henry, A., Sharma, B., Cardinal, M., Kuroski, D., Van Duyne, R.: Surface-enhanced Raman spectroscopy biosensing: in vivo diagnostics and multimodal imaging. *Anal. Chem.* **88**, 6638–6647 (2016)
15. Tripp, R., Dluhy, R., Zhao, Y.: Novel nanostructures for SERS biosensing. *Nano Today.* **3**(3–4), 31–37 (2008)
16. Bantz, K., Meyer, A., Wittenberg, N., Im, H., Kurtulus, Ö., Lee, S., Lindquist, N., Oh, S.H., Haynes, C.: Recent progress in SERS biosensing. *Phys. Chem. Chem. Phys.* **13**, 11551–11567 (2011)
17. Le Ru, E., Etchegoin, P.: Single-molecule surface-enhanced Raman spectroscopy. *Annu. Rev. Phys. Chem.* **63**, 65–87 (2012)
18. Wang, Y., Irudayaraj, J.: Surface-enhanced Raman spectroscopy at single-molecule scale and its implications in biology. *Phil. Trans. R Soc. B.* **368**, 20120026 (2013)
19. Lee, H., Jin, S., Kim, H., Suh, Y.: Single-molecule surface-enhanced Raman spectroscopy: a perspective on the current status. *Phys. Chem. Chem. Phys.* **15**, 5276–5287 (2013)
20. Zrimsek, A., Chiang, N., Mattei, M., Zaleski, S., McAnally, M., Chapman, C., Henry, A.I., Schatz, G., Van Duyne, R.: Single-molecule chemistry with surface- and tip-enhanced Raman spectroscopy. *Chem. Rev.* **117**, 7583–7613 (2017)
21. Kumar, G.: Plasmonic nano-architectures for surface enhanced Raman scattering: a review. *J. Nanophotonics.* **6**(1), 064503 (2012)
22. Sharma, B., Cardinal, M., Kleinman, S., Greeneltch, N., Frontiera, R., Blaber, M., Schatz, G., Van Duyne, R.: High-performance SERS substrates: advances and challenges. *MRS Bull.* **38**(8), 615–624 (2013)
23. Kleinman, S., Frontiera, R., Henry, A.-I., Dieringer, J., Van Duyne, R.: Creating, characterizing, and controlling chemistry with SERS hot spots. *Phys. Chem. Chem. Phys.* **15**, 21–36 (2013)
24. Dutta, A., Matikainen, A., Andoh, S., Nuutinen, T.: SERS activity of photoreduced silver chloride crystals. *AIP Conf. Proc.* **2220**, 050004 (2020)
25. Ye, J., Wen, F., Sobhani, H., Lassiter, J., Dorpe, P., Nordlander, P., Halas, N.: Plasmonic nanoclusters: near field properties of the Fano resonance interrogated with SERS. *Nano Lett.* **12**(3), 1660–1667 (2012)
26. Dutta, A., Alam, K., Nuutinen, T., Hulkko, E., Karvinen, P., Kuittinen, M., Toppari, J.J., Vartiainen, E.: Influence of Fano resonance on SERS enhancement in Fano-plasmonic oligomers. *Opt. Express.* **27**(21), 30031–30043 (2019)
27. Dutta, A., Vartiainen, E.: Spatial localization of hotspots in Fano-resonant plasmonic oligomers for surface-enhanced coherent anti-stokes Raman scattering. *J. Eur. Opt. Soc.-Rapid Publ.* **16**, 8 (2020)
28. Romanato, F., Pilot, R., Massari, M., Ongarello, T., Pirruccio, G., Zilio, P., Ruffato, G., Carli, M., Sammito, D., Giorgis, V., Garoli, D., Signorini, R., Schiavuta, P., Bozio, R.: Design, fabrication and characterization of plasmonic gratings for SERS. *Microelectron. Eng.* **88**(8), 2717–2720 (2011)
29. Kalachyova, Y., Mares, D., Lyutakov, O., Kostejn, M., Lapcak, L., Svorcik, V.: Surface plasmon polaritons on silver gratings for optimal SERS response. *J. Phys. Chem. C.* **119**(17), 9506–9512 (2015)
30. Iqbal, T., Ashfaq, Z., Afsheen, S., Ijaz, M., Khan, M., Rafique, M., Nabi, G.: Surface-enhanced Raman scattering (SERS) on 1D nano-gratings. *Plasmonics.* **15**, 1053–1059 (2020)
31. Gillibert, R., Sarkar, M., Bryche, J., Yasukuni, R., Moreau, J., Besbes, M., Barbillon, G., Bartenlian, B., Canva, M., de la Chapelle, M.: Directional surface enhanced Raman scattering on gold nano-gratings. *Nanotechnology.* **27**, 115202 (2016)
32. Zanjani, N., Shayegannia, M., Prinja, R., Montazeri, A., Mohammadzadeh, A., Dixon, K., Zhu, S., Selvaganapathy, P., Zavodni, A., Matsuura, N., Kherani, N.: Multiwavelength surface-enhanced Raman spectroscopy using rainbow trapping in width-graded plasmonic gratings. *Adv. Opt. Mater.* **6**, 1701136 (2018)
33. Yaremchuk, I., Petrovska, H., Karelko, I., Fitiu, V., Bobitski, Y.: Optimization of the grating-based structures for the efficient SERS substrates. *Proc. IEEE ELNANO.* **37**, 119–123 (2017)
34. Xiao, C., Chen, Z., Qin, M., Zhang, D., Wu, H.: SERS polarization-independent performance of two-dimensional sinusoidal silver grating. *Appl. Phys. Lett.* **113**, 171604 (2018)
35. Ross, M., Mirkin, C., Schatz, G.: Optical properties of one-, two-, and three dimensional arrays of plasmonic nanostructures. *J. Phys. Chem. C.* **120**(2), 816–830 (2016)
36. Kahl, M., Voges, E.: Analysis of plasmon resonance and surface-enhanced Raman scattering on periodic silver structures. *Phys. Rev. B.* **61**(20), 14078 (2000)
37. Raether, H.: *Surface Plasmons on Smooth and Rough Surfaces and on Gratings*. Springer-Verlag, Berlin (1988)
38. Chan, C., Li, J., Ong, H., Xu, J., Wayne, M.: Angle-resolved surface-enhanced Raman scattering. In: Kumar, C. (ed.) *Raman Spectroscopy for Nanomaterials Characterization*, pp. 1–32. Springer-Verlag Berlin Heidelberg, Berlin (2012)
39. Baltog, I., Primeau, N., Reinisch, R., Coutaz, J.: Surface enhanced Raman scattering on silver grating: optimized antennalike gain of the stokes signal of 10^4 . *Appl. Phys. Lett.* **66**, 1187 (1995)
40. Baltog, I., Primeau, N., Reinisch, R., Coutaz, J.: Observation of stimulated surface-enhanced Raman scattering through grating excitation of surface plasmons. *J. Opt. Soc. Am. B.* **13**(4), 656–660 (1996)
41. Bog, U., Huska, K., Maerke, F., Nesterov-Mueller, A., Lemmer, U., Mappes, T.: Design of plasmonic grating structures towards optimum signal discrimination for biosensing applications. *Opt. Express.* **20**(10), 11357–11369 (2012)
42. Collin, S.: Nanostructure arrays in free-space: optical properties and applications. *Rep. Prog. Phys.* **77**, 126402 (2014)
43. Guselnikova, O., Svorcik, V., Lyutakov, O., Chehimi, M., Postnikov, P.: Preparation of selective and reproducible SERS sensors of Hg^{2+} ions via a sunlight-induced thiol-yne reaction on gold gratings. *Sensors.* **19**(9), 2110 (2019)
44. Guselnikova, O., Dvorankova, B., Kakisheva, K., Kalachyova, Y., Postnikov, P., Svorcik, V., Lyutakov, O.: Rapid SERS-based recognition of cell secretome on the folic acid-functionalized gold gratings. *Anal. Bioanal. Chem.* **411**, 3309–3319 (2019)
45. Dhawan, A., Du, Y., Batchelor, D., Wang, H., Leonard, D., Misra, V., Ozturk, M., Gerhold, M., Vo-Dinh, T.: Hybrid top-down and bottom-up fabrication approach for wafer-scale plasmonic nanoplatforms. *Small.* **7**, 727–731 (2011)
46. Kalachyova, Y., Mares, D., Jerabek, V., Elashnikov, R., Svorcik, V., Lyutakov, O.: Longtime stability of silver-based SERS substrate in the environment and (bio) environment with variable temperature and humidity. *Sens. Actuator A Phys.* **285**, 566–572 (2019)
47. Deng, X., Braun, G., Liu, S., Sciortino, P., Koefer, B., Tomblor, T., Moskovits, M.: Single-order, subwavelength resonant nanograting as a uniformly hot substrate for surface-enhanced Raman spectroscopy. *Nano Lett.* **10**(5), 1780–1786 (2010)
48. Kocabas, A., Ertas, G., Senlik, S., Aydinli, A.: Plasmonic band gap structures for surface-enhanced Raman scattering. *Opt. Express.* **16**(17), 12469–12477 (2008)

49. Yang, Z., Li, Q., Ruan, F., Li, Z., Ren, B., Xu, H., Tian, Z.: FDTD for plasmonics: applications in enhanced Raman spectroscopy. *Chin. Sci. Bull.* **55**, 2635–2642 (2010)
50. Taflove, A., Hagness, S.: *Computational Electrodynamics: the Finite-Difference Time-Domain Method*. Artech House, Boston (2005)
51. Johnson, S., Oskooi, A., Taflove, A.: *Advances in FDTD Computational Electrodynamics: Photonics and Nanotechnology*. Artech House, Boston (2013)
52. Radu, A., Kuellmer, M., Giese, B., Huebner, U., Weber, K., Cialla-May, D., Popp, J.: Surface-enhanced Raman spectroscopy (SERS) in food analytics: detection of vitamins B₂ and B₁₂ in cereals. *Talanta*. **160**, 289–297 (2016)
53. Lumerical FDTD Solutions 2019a. ANSYS Inc. (formerly acquired by Lumerical Inc.), Canonsburg. (2020). <https://www.lumerical.com/products/fdtd/>. Accessed 10 July 2020
54. Johnson, P., Christy, R.: Optical constants of the noble metals. *Phys. Rev. B*. **6**, 4370–4379 (1972)
55. Shen, B., Linko, V., Tapio, K., Pikker, S., Lemma, T., Gopinath, A., Gothelf, K., Kostainen, M., Toppari, J.J.: Plasmonic nanostructures through DNA-assisted lithography. *Sci. Adv.* **4**(2), eaap8978 (2018)
56. OriginPro 2017. OriginLab Corp., Northampton. (2020). <https://www.originlab.com/>. Accessed 10 July 2020
57. Dendisová-Vyškovská, M., Kokaislová, A., Oncák, M., Matejka, P.: SERS and in situ SERS spectroscopy of riboflavin adsorbed on silver, gold and copper substrates: elucidation of variability of surface orientation based on both experimental and theoretical approach. *J. Mol. Struct.* **1038**, 19–28 (2013)
58. Liu, F., Gu, H., Lin, Y., Qi, Y., Dong, X., Gao, J., Cai, T.: Surface-enhanced Raman scattering study of riboflavin on borohydride-reduced silver colloids: dependence of concentration, halide anions and pH values. *Spectrochim. Acta A*. **85**(1), 111–119 (2012)
59. Le Ru, E., Blackie, E., Meyer, M., Etchegoin, P.: Surface enhanced Raman scattering enhancement factors: a comprehensive study. *J. Phys. Chem. C*. **111**(37), 13794–13803 (2007)
60. Langer, J., et al.: Present and future of surface-enhanced Raman scattering. *ACS Nano*. **14**(1), 28–117 (2020)

Publisher's Note

Springer Nature remains neutral with regard to jurisdictional claims in published maps and institutional affiliations.

Submit your manuscript to a SpringerOpen[®] journal and benefit from:

- Convenient online submission
- Rigorous peer review
- Open access: articles freely available online
- High visibility within the field
- Retaining the copyright to your article

Submit your next manuscript at ► [springeropen.com](https://www.springeropen.com)

PIV

**OPTIMIZING GEOMETRY OF LOW-Q ALL-METAL
FABRY-PÉROT MICROCAVITY FOR FLUORESCENCE
SPECTROSCOPY**

by

A. Dutta, V. Tiainen, and J. J. Toppari,

IOPSciNotes, **2**, 015205 (2021).

Reproduced with kind permission of IOP Publishing.



ARTICLE

OPEN ACCESS

RECEIVED

22 December 2020

REVISED

2 March 2021

ACCEPTED FOR PUBLICATION

4 March 2021

PUBLISHED

15 March 2021

Original content from this work may be used under the terms of the [Creative Commons Attribution 4.0 licence](#).

Any further distribution of this work must maintain attribution to the author(s) and the title of the work, journal citation and DOI.



Optimizing geometry of low-Q all-metal Fabry-Pérot microcavity for fluorescence spectroscopy

Arpan Dutta^{*}, Ville Tiainen and Jussi Toppari^{*}

Nanoscience Center and Department of Physics, University of Jyväskylä, Jyväskylä, Finland

^{*} Authors to whom any correspondence should be addressed.E-mail: arpan.a.dutta@jyu.fi and j.jussi.toppari@jyu.fi

Keywords: Purcell factor, fluorescence, Fabry-Pérot microcavity

Abstract

Fluorescence spectroscopy is commonly employed to study the excited-state photophysics of organic molecules. Planar Fabry-Pérot microcavities play an essential role in such studies and a strategic cavity design is necessary to attain an enhanced light-matter interaction. In this work, we computationally study different geometries for a planar metallic Fabry-Pérot microcavity tuned for the absorption of Sulforhodamine 101, a typical dye for fluorescence spectroscopy. The cavity consists of a polymer layer enclosed between two silver mirrors, where the thicknesses of all the three layers are varied to optimize the cavity. Our transfer-matrix and finite-difference time-domain simulations suggest that a cavity with 30 nm thin top mirror and 200 nm fully reflective thick bottom mirror, thus having only reflection and absorption and no transmission, is an optimal design for maximizing the Purcell factor and spectral overlap between the cavity and molecule, while still sustaining an efficient measurability of the fluorescence.

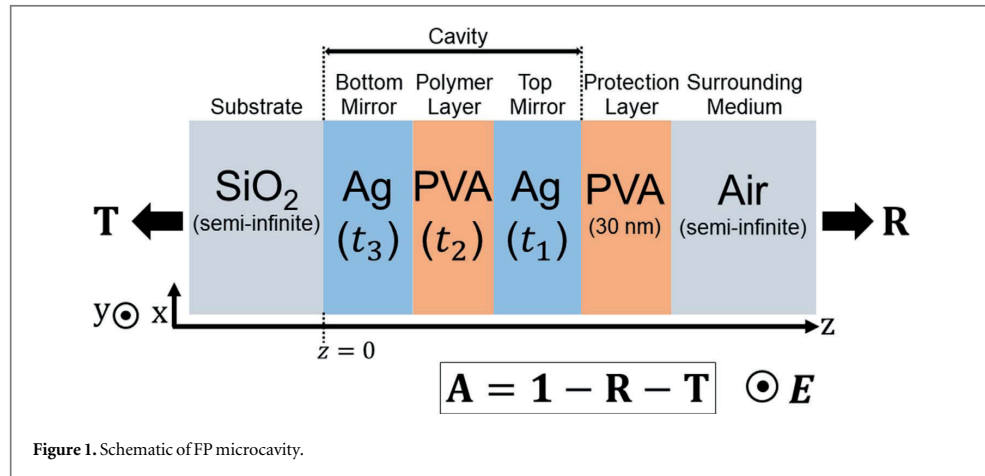
1. Introduction

Low-Q planar Fabry-Pérot (FP) microcavities, doped with photoactive organic molecules, are essential in exploring light-matter interactions under weak [1–4] and strong coupling limit [5, 6], and often employed in the studies of excited-state photochemistry [7, 8], photovoltaics [9], and cavity-quantum electrodynamics [10].

Planar metallic FP microcavities are popular in spectroscopy [3, 6] since they are simpler to fabricate and realize than dielectric cavities [11, 12]. However, implementing them in fluorescence spectroscopy is challenging, because usually one can tune the cavity resonance and thus the enhancement either for molecular absorption or emission, but not fully for both. The usual choice has been to do the excitation or detection via light leaking through a thin enough mirror, which, however, limits the quality factor (Q) of the microcavity to well below hundred. However, mode volumes (V_m) of the all-metallic microcavities are really small, which in the case of multimolecule coupling is enough to drive the system even to an ultrastrong coupling regime [13].

Performance of a FP cavity in fluorescence spectroscopy depends on its field-confinements in temporal (Q) and spatial (V_m) domains. Here $Q = \lambda_0 / \Delta\lambda$, where λ_0 is the wavelength of the cavity resonance and $\Delta\lambda$ is the full-width at half-maximum of the resonance peak [14]; and, $V_m = \left[\int \epsilon |E|^2 dV \right] / [\max(\epsilon |E|^2)]$, where ϵ is the dielectric function and E is the electric-field amplitude inside the interaction volume V [15]. Purcell factor determines the fluorescence enhancement inside the cavity and it is $F_p = (3/4\pi^2)(\lambda_0/n)^3(Q/V_m)$, where n is the refractive index in V [16]. Increasing Q and decreasing V_m readily improves F_p . However, increasing Q often requires highly reflective mirrors, incurring a reduced cavity transmission, which further reduces the measurability of the fluorescence. Thus, an optimized compromise is needed.

In addition, the aforementioned F_p is ‘ideal’, assuming—perfect spectral overlap of the cavity mode with the fluorescence spectrum, and emitter location at the antinode of the cavity mode with its transition dipole aligned with the local electric field [17]. In reality, matching of the cavity mode of doped microcavities, with the emission spectrum of an ensemble of emitters spatially distributed within the cavity field with randomly oriented dipoles,



can be challenging [18]. Hence, only a fraction of the emission couples to the cavity leading to an effective F_p much lower than the ideal [4].

Improving the effective F_p can be done by spectral tuning between the cavity mode and the emitter responses. Increasing the spectral overlap between the molecular emission $PL(\lambda)$ and the cavity absorption $A_c(\lambda)$, i.e. emission overlap $\Phi_E = \int A_c(\lambda) \cap PL(\lambda) d\lambda$, will increase the fraction of the emission coupled to the cavity, resulting in more efficient fluorescence enhancement [19]. Similarly, excitation efficiency of the fluorescent molecules inside the cavity depends on the spectral overlap between $A_c(\lambda)$ and the molecular absorption $A_m(\lambda)$, i.e. absorption overlap $\Phi_A = \int A_c(\lambda) \cap A_m(\lambda) d\lambda$, which has to be high for an efficient cavity-molecular coupling [20].

Taking into account the above excitation efficiency ($\propto \Phi_A$) and considering that—only a fraction of the molecular emission coupled with the cavity absorption ($\propto \Phi_E$) is enhanced by a factor of F_p and collected through a cavity mirror possessing an average transmissivity T_{avg} , the total integrated fluorescence intensity measurable outside of the microcavity can be formulated as $I_{FL} = F_p T_{avg} \Phi_E \Phi_A$. I_{FL} is an estimation of the measurability of fluorescence, which is not necessarily optimal at optimal F_p . Therefore, a strategic cavity design is needed to attain an optimal F_p , Φ_E , Φ_A and T_{avg} to obtain the best I_{FL} , which we use as our main criteria for the cavity here.

In this work, we computationally study different geometries for a planar metallic FP microcavity. To calculate I_{FL} we have chosen sulforhodamine 101 (SR101) dye as our model molecule and tuned the cavities for its absorption maximum (576 nm). The cavity consists of a polymer layer enclosed between two silver mirrors, and the thicknesses of all the three layers are varied to optimize the cavity properties. Our transfer-matrix method (TMM) and finite-difference time-domain (FDTD) based simulations suggest that a reflective (non-transmitting) cavity is an optimal choice in maximizing F_p , Φ_A , Φ_E and especially I_{FL} . Our findings provide insights on designing low-Q all-metal FP microcavities for fluorescence spectroscopy.

2. Materials and methods

Planar metallic FP microcavities with different geometries were studied using TMM [21, 22] and FDTD [23, 24] simulations. The two silver (Ag) mirrors with thicknesses t_1 and t_3 , and a layer (thickness t_2) of poly-vinyl alcohol (PVA) embedded in between, form the cavity (see figure 1). PVA was chosen since it is a suitable polymer matrix for SR101 molecules. The cavity mode was always tuned to the absorption maximum of SR101 (576 nm) by varying t_2 . A thin PVA layer (30 nm) was also considered on top of the top Ag mirror as a protection layer, which prevents the oxidation of Ag in ambient condition in the case of real cavities. The glass (SiO_2) substrate and the surrounding medium (air, refractive index is 1.0) were considered as semi-infinite. The material models for Ag, PVA and SiO_2 were extracted from [25–27], respectively. The absorption and emission spectra of SR101 were taken from [28].

Reflection, transmission and absorption (R, T, A) of the modelled microcavities were calculated using TMM where $A = 1 - R - T$. The Q values were calculated from the cavity absorption. Electric field distribution and mode volume in each cavity were computed using 3D-FDTD simulations where normal incidence of linearly polarized light with polarization defined in figure 1 was considered as an excitation. The entire radiation zone of the cavity mode, as illustrated by the white dotted boundary in the field-distribution plot

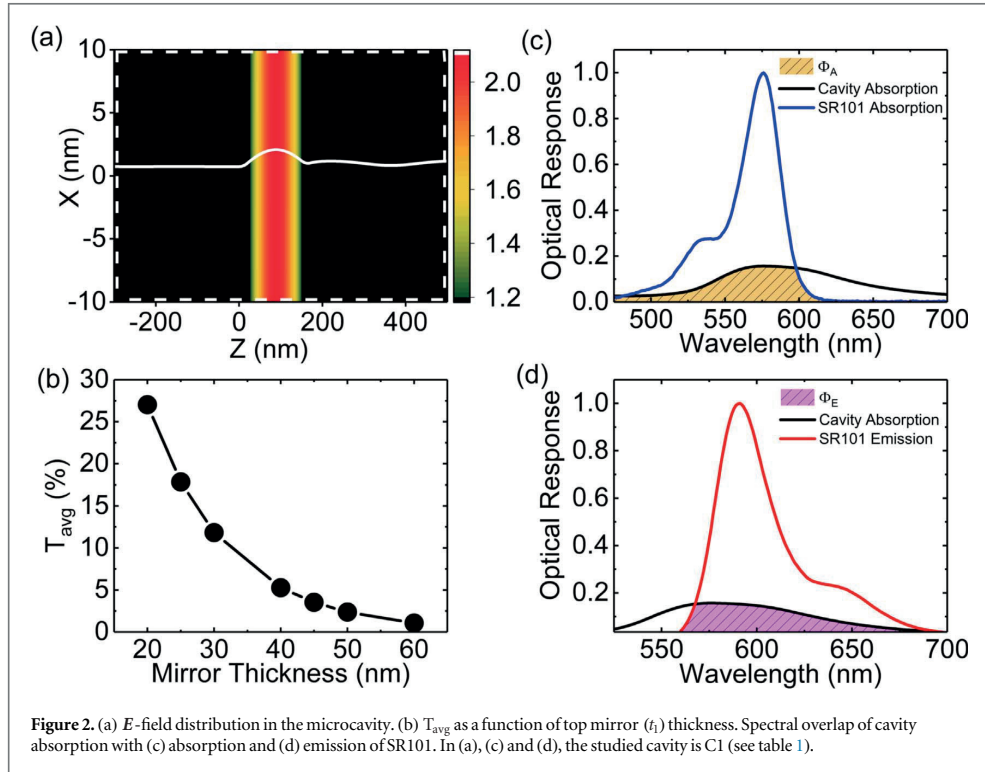


Table 1. Geometries for symmetric microcavities.

| Cavity | $t_1/t_2/t_3$ (nm) |
|--------|--------------------|
| C1 | 20/132/20 |
| C2 | 25/138/25 |
| C3 | 30/142/30 |
| C4 | 40/146/40 |
| C5 | 50/148/50 |

shown in figure 2(a), was considered as V in V_m calculation. T_{avg} were calculated as the average transmission of the top mirrors (t_1) within the SR101 emission (560–700 nm) as reported in figure 2(b). Spectral overlaps (Φ_A and Φ_E) were calculated as an integral of the common area (shaded yellow/magenta regions) under the cavity absorption (black) and the molecular absorption/emission (blue/red) curves for each cavity, as shown in figures 2(c), (d).

3. Results and discussions

In our first approach, we designed symmetric cavities where both mirrors had equal thicknesses. Five cavities (C1–C5) with increasing mirror thicknesses were considered with their geometrical parameters reported in table 1, while figures 3(a)–(c) show their R, T, A analysis. From figures 3(c), (d), it is clear that an increment in cavity mirror thickness makes the cavity absorption linewidth narrower, resulting a drastic fall in Φ_A and Φ_E . However, it simultaneously improves cavity Q, V_m and F_p as shown in figures 3(e), (f). The cavity C5 (50 nm mirrors) provides highest F_p but it yields poorest spectral overlaps and T_{avg} (see figure 2(b)). Consequently, I_{FL} drops at the highest F_p .

To overcome this limitation we designed asymmetric cavities where we made one mirror thin (leaky) for fluorescence collection while keeping the other mirror thick. Five cavities (C6–C10) were considered with increasing Δt ($\Delta t = t_3/t_1$) with their geometrical parameters reported in table 2 and their R, T, A analysis shown in figures 4(a)–(c).

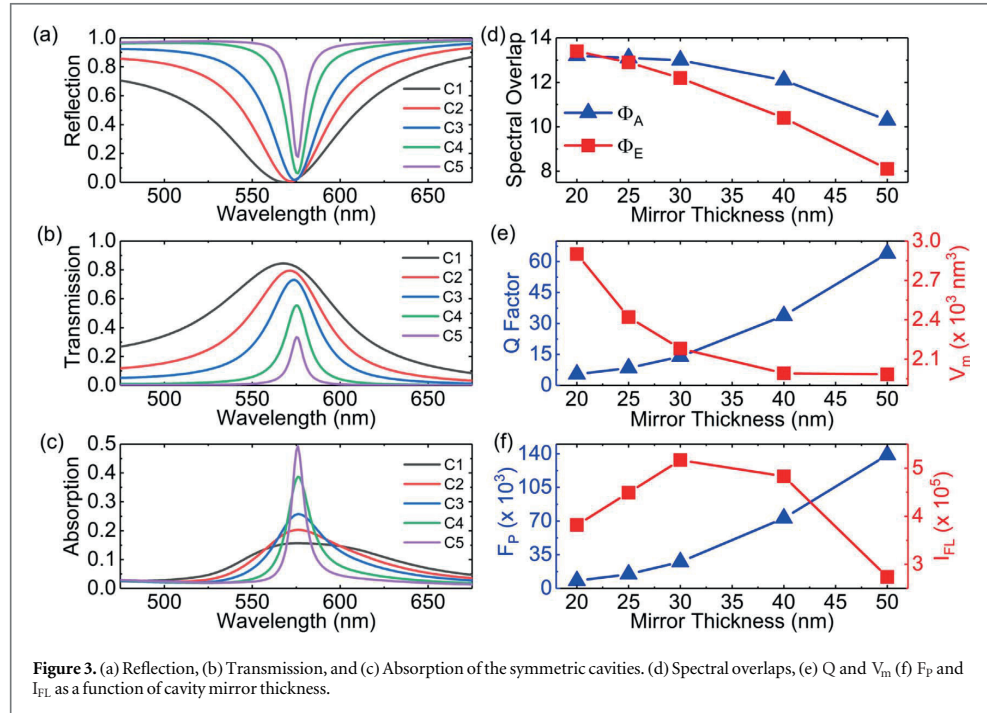


Table 2. Geometries for asymmetric microcavities.

| Cavity | $t_1/t_2/t_3$ (nm) |
|--------|--------------------|
| C6 | 60/146/30 |
| C7 | 45/145/30 |
| C8 | 30/145/45 |
| C9 | 30/145/60 |
| C10 | 30/145/90 |

Figures 4(c), (d) show that the cavities with thin top and thick bottom mirrors ($\Delta t > 1$: C8-C10) yield higher cavity absorption and spectral overlaps than the cavities with thick top and leaky bottom mirrors ($\Delta t < 1$: C6-C7). An increment in Δt improves cavity Q, V_m , F_P and I_{FL} as shown in figures 4(e), (f). The cavity C10 ($\Delta t = 3$) provides highest I_{FL} , F_P , Φ_A and Φ_E . Moreover, the change in the cavity geometry from symmetric to asymmetric yields 7.54% drop in F_P with 223.33% rise in I_{FL} on average. Therefore, by making a very thick bottom mirror with a thin top mirror, one can ensure a healthy trade-off between F_P and I_{FL} .

Such findings motivated us to design a reflective (non-transmitting) cavity having a very thick bottom mirror and thin top mirror so that the cavity transmission becomes zero ($T \approx 0$) and the absorption becomes $A = 1 - R$. Five reflective cavities (C11–C15) with increasing top mirror thickness were considered while the bottom mirror thickness was kept constant. Figures 5(a), (b) present their R, A analysis with their geometries specified in table 3. Figure 5(c) depicts the leaky transmissivity of the top mirrors used for all the cavities. It was computed by considering an Ag layer between semi-infinite PVA and air. From C11 to C15, as the top mirror thickness is increased, the cavity absorption, Φ_A and Φ_E are increased with a significant drop in the transmissivity of the top mirrors, as shown in figures 5(b)–(d). However, a simultaneous improvement in cavity Q, V_m and F_P is also observed as depicted in figures 5(e), (f).

In a reflective cavity, due to the non-transmitting bottom mirror, the omnidirectional fluorescence emission can only exit through the thin top mirror. Therefore, a fall in the leaky mirror transmissivity, as shown in figure 5(c), directly results a drop in I_{FL} at highest F_P as shown in figure 5(f). Nevertheless, the change in the cavity geometry from symmetric to reflective results 98.55% rise in F_P alongwith 386.56% rise in I_{FL} on average and clearly outperformed the asymmetric cavities. Therefore, we can conclude that of the cavities studied here,

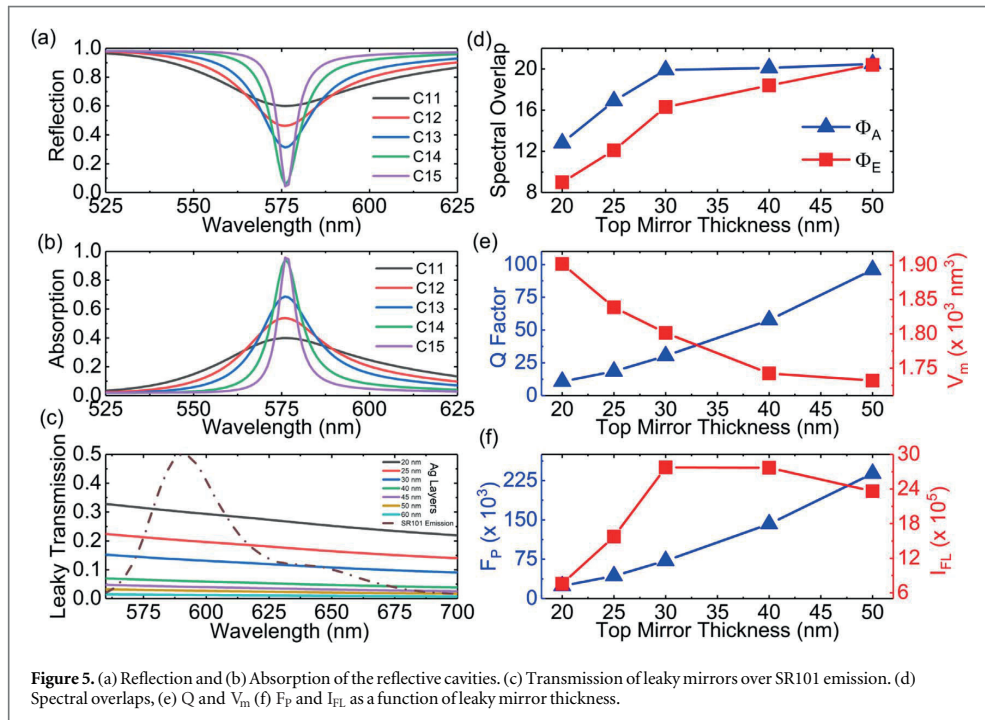
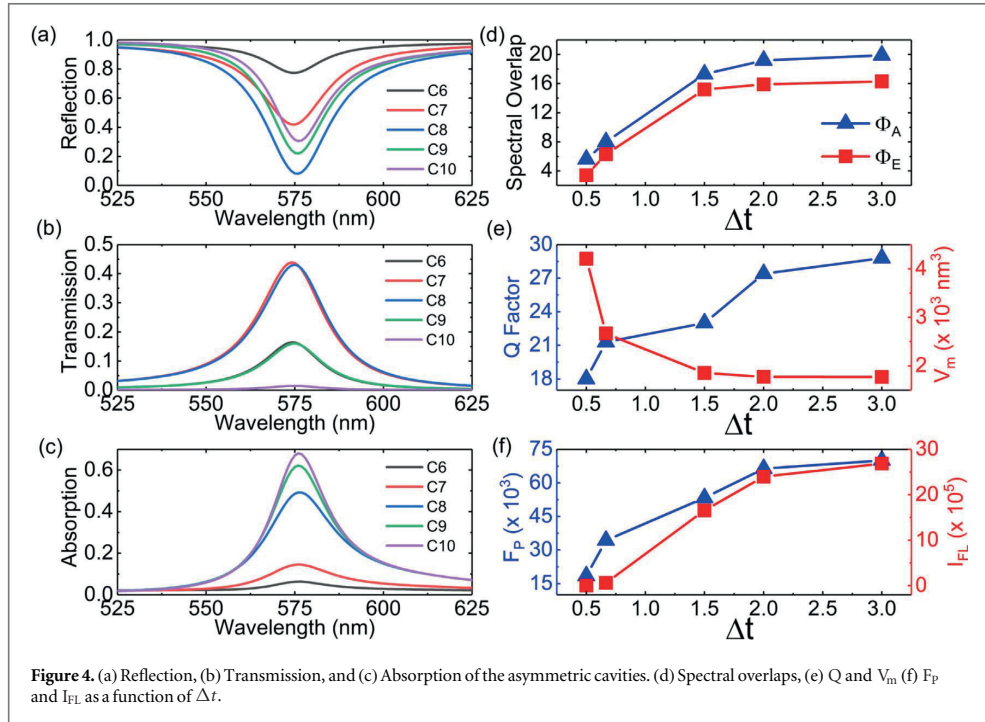


Table 3. Geometries for reflective microcavities.

| Cavity | $t_1/t_2/t_3$ (nm) |
|--------|--------------------|
| C11 | 20/140/200 |
| C12 | 25/143/200 |
| C13 | 30/145/200 |
| C14 | 40/148/200 |
| C15 | 50/149/200 |

the reflective cavities, and more precisely C13 is the optimal choice for fluorescence spectroscopy of SR101, providing the best possible I_{FL} .

4. Conclusions

We computationally investigated different geometries of a planar metallic FP microcavity tuned for the absorption of SR101. The cavities were modelled using TMM and FDTD simulations to optimize the Purcell factor, the spectral overlap between the cavity mode and the molecular responses, and the measurability of fluorescence. To quantify the total fluorescence measurability, we defined $I_{FL} = F_P T_{avg} \Phi_E \Phi_A$, which takes into account all the above properties. However, we also analyzed the different properties separately since they can be important for other studies.

Our findings revealed that the symmetric cavities are limited in providing high Purcell enhancement along with an acceptable measurability of fluorescence. Asymmetric cavities can provide more efficient light-matter interaction while maintaining a pathway to collect the fluorescence through the leaky top mirror. Finally, we achieved an optimal design, i.e. a reflective cavity (C13) with 30 nm thin/leaky top mirror and 200 nm thick/non-transmitting bottom mirror, which provides high Purcell factor and spectral overlaps, and most importantly, the best I_{FL} for fluorescence spectroscopy of SR101.

Acknowledgments

The authors gratefully acknowledge Academy of Finland (Projects: 323995, 289947) for the funding.

Data availability statement

The data that support the findings of this study are available upon reasonable request from the authors.

ORCID iDs

Arpan Dutta  <https://orcid.org/0000-0002-0139-2611>

Jussi Toppari  <https://orcid.org/0000-0002-1698-5591>

References

- [1] Deppe D G and Lei C 1992 *Appl. Phys. Lett.* **60** 527–9
- [2] Pokhriyal A, Lu M, Chaudhery V, George S and Cunningham B T 2013 *Appl. Phys. Lett.* **102** 221114
- [3] Nyman M, Shevchenko A, Shavrin I, Ando Y, Lindfors K and Kaivola M 2019 *APL Photonics* **4** 076101
- [4] Kaupp H, Deutsch C, Chang H-C, Reichel J, Hänsch T W and Hunger D 2013 *Phys. Rev. A* **88** 053812
- [5] Agranovich V M and La Rocca G C 2005 *Solid State Commun.* **135** 544–53
- [6] Hobson P A, Barnes W L, Lidzey D G, Gehring G A, Whittaker D M, Skolnick M S and Walker S 2002 *Appl. Phys. Lett.* **81** 3519–21
- [7] Ribeiro R, Martínez-Martínez L, Du M, Campos-González-Angulo J and Yuen-Zhou J 2018 *Chem. Sci.* **9** 6325–39
- [8] Sanvitto D and Kéna-Cohen S 2016 *Nat. Mater.* **15** 1061–73
- [9] Wang Y, Shen P, Liu J, Xue Y, Wang Y, Yao M and Shen L 2019 *Sol. RRL* **3** 1900181
- [10] Flick J, Ruggenthaler M, Appel H and Rubio A 2017 *Proc. Natl. Acad. Sci. USA* **114** 3026–34
- [11] Connolly L G, Lidzey D G, Butté R, Adawi A M, Whittaker D M, Skolnick M S and Airey R 2003 *Appl. Phys. Lett.* **83** 5377–9
- [12] Wang Z, Gogna R and Deng H 2017 *Appl. Phys. Lett.* **111** 061102
- [13] Suzuki M, Nishiyama K, Kani N, Yu X, Uzumi K, Funahashi M, Shimokawa F, Nakanishi S and Tsurumachi N 2019 *Appl. Phys. Lett.* **114** 191108
- [14] Bitarafan M H and DeCorby R G 2017 *Sensors* **17** 1748
- [15] Hu S, Khater M, Salas-Montiel R, Kratschmer E, Engelmann S, Green W M J and Weiss S M 2018 *Sci. Adv.* **4** eaat2355
- [16] Vahala K 2003 *Nature* **424** 839–46

- [17] Gerard J-M and Gayral B 1999 *J. Light. Technol.* **17** 2089–95
- [18] Gu Q and Fainman Y 2017 *Semiconductor Nanolasers* (Cambridge: Cambridge University Press)
- [19] Herrera F and Spano F C 2017 *Phys. Rev. A* **95** 053867
- [20] Groenhof G, Climent C, Feist J, Morozov D and Toppari J J 2019 *J. Phys. Chem. Lett.* **10** 5476–83
- [21] Mackay T G and Lakhtakia A 2020 *The Transfer-Matrix Method in Electromagnetics and Optics* (San Rafael: Morgan & Claypool Publishers)
- [22] Pascoe K J 2001 *Reflectivity and Transmissivity through Layered, Lossy Media: A User-Friendly Approach* (Ohio: Wright Patterson Air Force Base)
- [23] Gedney S 2011 *Introduction to the Finite-Difference Time-Domain (FDTD) Method for Electromagnetics* (San Rafael: Morgan & Claypool Publishers)
- [24] ANSYS Lumerical FDTD Solutions R2.4 2020
- [25] Johnson P and Christy R 1972 *Phys. Rev. B* **6** 4370–9
- [26] Schnepf M J *et al* 2017 *Nanoscale* **9** 9376–85
- [27] Palik E D 1997 *Handbook of Optical Constants of Solids* (Burlington: Academic)
- [28] Birge R R and Duarte F J 1990 *Kodak Optical Products* (Rochester: Kodak Publication)

PV

**MODELING OPTICAL CONSTANTS FROM THE ABSORPTION
OF ORGANIC THIN FILMS USING A MODIFIED LORENTZ
OSCILLATOR MODEL**

by

A. Dutta, V. Tiainen, H. A. Qureshi, L. Duarte, and J. J. Toppari,

Optical Materials Express, **12**, 2855 (2022).

Reproduced with kind permission of Optica Publishing Group.



Modeling optical constants from the absorption of organic thin films using a modified Lorentz oscillator model

ARPAN DUTTA,^{1,4} VILLE TIAINEN,¹ HASSAN ALI QURESHI,^{1,2} LUÍS DUARTE,^{1,3} AND J. JUSSI TOPPARI^{1,5}

¹Nanoscience Center and Department of Physics, University of Jyväskylä, P.O. Box 35, FI-40014, Finland

²Currently with Department of Mechanical and Materials Engineering, University of Turku, FI-20014, Finland

³Currently with Department of Chemistry, University of Helsinki, P.O. Box 55, FI-00014, Finland

⁴arpan.a.dutta@jyu.fi

⁵j.jussi.toppari@jyu.fi

Abstract: Optical constants of organic thin films can be evaluated using the Lorentz oscillator model (LOM) which fails to fit inhomogeneously broadened absorption of highly concentrated molecular films. In modified LOM (MLOM), the inhomogeneous broadening is implemented through a frequency-dependent adjustable broadening function. In this work, we evaluate the optical constants of rhodamine 6G doped poly-vinyl alcohol thin films with varying doping concentration (including also extensively high concentrations) using MLOM, which outperforms LOM by showing a better agreement with the experimental results. Our proposed method provides a way to accurately determine optical constants of isotropic organic thin films only from their absorption spectra without spectroscopic ellipsometry.

© 2022 Optica Publishing Group under the terms of the [Optica Open Access Publishing Agreement](#)

1. Introduction

Organic thin films are popular in photovoltaics [1–3] and optoelectronics [4–6] due to their compatibility with cost-effective synthesis procedures and large-scale manufacturing techniques on flexible substrates [1,2]. Such thin films usually consist of a polymer matrix doped with photoactive organic molecules (e.g. dyes) acting as Frenkel excitons [7]. These dye-doped thin films have potential applications in resonant nanophotonics [8–10] and their excitonic properties [7,11] can be used for enhancing light-matter coupling within the optical devices [12,13] even to a limit of strong coupling [10,14–17].

Optimal design of novel excitonic devices based on dye-doped organic thin films requires precise modeling of the local excitonic absorption bands manifested in those thin films [5–13]. Such modeling, however, often becomes challenging due to a lack of accurate information on the optical constants of the thin solid films, i.e., their wavelength-dependent complex refractive index and complex dielectric function. Usually these optical constants can be evaluated over the spectral region of interest using a spectral fitting involving a suitable dispersion relation [18,19]. In such fitting method, the experimental reflection, transmission and absorption spectra of the films are fitted by the corresponding theoretically calculated ones using a least squares fitting procedure where the theoretical calculation uses the optical constants derived from the dispersion model [18]. Here, a pointwise optimization approach is employed, in which an objective function representing the degree of dissimilarity between the experimental and the theoretical spectra is minimized at all spectral points under reasonable physical constraints to attain proper accuracy in the optical constant values [18–21].

The choice of dispersion model plays a key role in the spectral fitting. The absorption of an organic solid, for example, the local excitonic absorption band of a dye-doped polymer

film *ideally* should follow a Lorentzian profile [19] and hence, the corresponding dielectric function can be modelled via Lorentz oscillator model (LOM) [22,23]. The LOM provides lowest number of fitting parameters and inherent consistency with the Kramers-Kronig relation. The damping factor in LOM is a measure of the linewidth of the Lorentzian shaped absorption band and considered as a constant resulting from both the homogeneous broadening intrinsic to any molecular system [18,19,23], as well as lifetime broadening.

However, in the case of a highly concentrated molecular film, the system is an ensemble of numerous molecules doped in a polymeric medium. Increasing the doping concentration of such dye-doped polymer films usually results in significant changes in their absorption spectra [14,24]. This is because the system shifts away from the above-mentioned *ideal* case resulting in an inhomogeneously broadened absorption profile which does not follow a true Lorentzian or pure Gaussian shape [19,24–27]. Several factors are responsible for this inhomogeneous broadening such as formation of molecular aggregates, vibrational transitions accompanied with the electronic transitions, polycrystallinity of the doped film, and interaction of dye molecules with their polymeric surrounding having impurities/defects to name few [19,25–29]. The situation is too complicated to be fully determined from an experimental absorption spectrum since exact contributions from the different factors of inhomogeneity are unknown. Hence, LOM fails to extract the accurate dielectric function from an inhomogeneously broadened absorption [19,25–27].

This issue can be addressed by incorporating modifications in LOM such as – either using a higher number of oscillators [25] or using Gaussian/Voigt profiles to fit the absorption lineshape via convolution/superposition of (one or more) Lorentzian and Gaussian functions [24,27]. However, neither of these approaches are numerically optimal. Use of a higher number of oscillators involves a higher number of fitting parameters which makes the spectral fitting more complex and less meaningful for interpretation. On the other hand, Gaussian/Voigt functions may provide better fit to the absorption profile, but they lack analytically closed form and unlike LOM, there is no simple straightforward way to calculate the dielectric function from them [19,25].

Kim *et al.* [26] proposed a clever modification in LOM to overcome these shortcomings by including a spectrally dependent damping term working as an adjustable broadening function (ABF) [19,25,26]. The ABF includes two constant key parameters – the Lorentzian damping factor (γ) and an adjustable broadening parameter (α), and it is generalized for any arbitrary lineshape. This modified Lorentz oscillator model (MLOM) maintains an analytically closed form and hence, provides a simple straightforward way to calculate the dielectric function like LOM while it allows to fit any arbitrary broadening beyond the Lorentzian shape. For certain values of α , one can mimic the conventional spectral profiles, i.e., Lorentzian ($\alpha = 0$), Gaussian ($\alpha = 0.3$), and Voigt ($0 < \alpha < 0.3$) as well as most asymmetric/inhomogeneous lineshapes ($\alpha > 0.3$) [19,25,26]. Since inhomogeneous broadening does not necessarily always result in Gaussian or Voigt profile but can take any arbitrary complex form [24,27–29], the incorporation of ABF in LOM is an efficient way to fit any arbitrary absorption lineshape and extract optical constants from it using minimal amount of fitting parameters. Consequently, MLOM provides better agreement with the experimental results compared to the conventional LOM [19,25].

Since the MLOM provides more realistic model, it can be used to calculate accurate absorption band which is then fitted with the measured one, by using the constants of the MLOM as the fitting parameters. This way MLOM enables accurate determination of optical constants of an organic thin film from its absorption band alone. By this method one can avoid the spectroscopic ellipsometry (SE) [30], which is usually needed for determination of the optical constants and often tricky to perform [18]. That is because SE is extremely sensitive to the quality of sample surface, type of substrate material, contamination [18,31], and because of this often requires assistance from other techniques such as surface plasmon spectroscopy to attain better accuracy [32].

In this work, we propose a straightforward method to determine the optical constants of the isotropic organic thin films only from their absorption spectra. We evaluate the optical constants of rhodamine 6G (R6G) doped poly-vinyl alcohol (PVA) thin films with varying doping concentration (including also extensively high concentrations) from their experimental absorption using MLOM. The transfer-matrix method (TMM) [33–36] implemented in MATLAB [37] is used to calculate the theoretical absorption of the R6G films, which is further used to fit the experimental data using a least squares fitting method along with a pointwise optimization technique. Our proposed method outperforms the conventional LOM by yielding a better agreement with the experimental results, and avoids the need of ellipsometry. Our findings provide a way to model the local excitonic absorption bands of the isotropic organic thin films, using their evaluated optical constants, which is crucial for designing novel excitonic nanodevices.

2. Theory

The dispersive and complex dielectric function (ϵ) of a material can be described as

$$\epsilon(E) = \epsilon_1(E) + i\epsilon_2(E), \quad (1)$$

where E is the energy [19,25]. In LOM, the real (ϵ_1) and imaginary (ϵ_2) parts of the dielectric function are expressed as

$$\epsilon_1(E) = \epsilon_\infty + \sum_j \frac{f_j E_j^2 (E_j^2 - E^2)}{(E_j^2 - E^2)^2 + E^2 \gamma_j^2}, \quad (2)$$

$$\epsilon_2(E) = \sum_j \frac{f_j E_j^2 E \gamma_j}{(E_j^2 - E^2)^2 + E^2 \gamma_j^2}, \quad (3)$$

where $j = 0, 1, 2, \dots$ is the number of material resonances (transitions) with the resonant energy E_j , oscillator strength f_j , and damping rate γ_j [8,19,25], while ϵ_∞ represents the background dielectric constant within the exciton-energy region [14,38].

The corresponding real (n) and imaginary (k) parts of the refractive index (N) are

$$n(E) = \sqrt{\frac{\sqrt{\epsilon_1^2(E) + \epsilon_2^2(E)} + \epsilon_1(E)}{2}}, \quad (4)$$

$$k(E) = \sqrt{\frac{\sqrt{\epsilon_1^2(E) + \epsilon_2^2(E)} - \epsilon_1(E)}{2}}, \quad (5)$$

and

$$N(E) = n(E) + ik(E), \quad (6)$$

in their dispersive and complex form [19,25].

The LOM, i.e., Eq. (2) and Eq. (3), considers an ideal case where the damping rate (γ_j) is constant and consequently, the material resonances show homogeneous (Lorentzian) broadening where the resonance linewidth symmetrically broadens on both sides of the resonance peak energy (E_j) [22,23]. In the case of inhomogeneous broadening, the resonance lineshape for most of the time inherits Gaussian broadening or Voigt lineshape when combined with the homogeneous Lorentzian broadening [24,27]. Even higher inhomogeneous broadening usually results in asymmetric lineshapes with respect to the resonance peak (E_j) [19,24–29]. Therefore, the damping term has to be adjustable, i.e., frequency-dependent, to become adaptive for such

arbitrary broadening [19,25,26]. To implement the inhomogeneity in the resonance linewidth Kim *et al.* [26] proposed an adjustable broadening function (γ'_j) considered as

$$\gamma'_j(E) = \gamma_j \exp \left[-\alpha_j \left(\frac{E - E_j}{\gamma_j} \right)^2 \right], \quad (7)$$

where α_j is the adjustable broadening parameter associated with the material resonance j . Replacement of the damping rate γ_j in Eq. (2) and Eq. (3) by the frequency-dependent adjustable broadening function γ'_j will form the MLOM, which reduces to LOM for $\alpha_j = 0$ and can mimic any arbitrary lineshapes for $\alpha_j > 0$ [19,25,26].

In the spectral fitting, the fitting parameters (f_j , E_j , γ_j and α_j) are optimized by minimizing an objective function (Θ) defined as

$$\Theta = \sum_E [A_{\text{exp}}(E) - A_{\text{TMM}}(E)]^2, \quad (8)$$

where A_{exp} and A_{TMM} are the experimental and the TMM simulated absorption, respectively [20,21], calculated from the reflection (R) and the transmission (T) as $A = 1 - R - T$.

3. Materials and methods

3.1. Sample fabrication

Four R6G doped PVA films were fabricated with increasing R6G concentration on top of high optical quality BK7 glass substrates (Präzisions Glas and Optik GmbH, dimension: $15 \times 15 \text{ mm}^2$, thickness: 1 mm, surface roughness: $\pm 0.10 \text{ mm}$). Also a bare PVA film without R6G doping was made as a reference sample. The substrates were cleaned by isopropanol and blown by nitrogen for drying. The R6G:PVA and bare PVA films were spin-coated on top of the clean substrates and hardened by baking for 3 min on a hot plate at 95°C . The PVA crystals (Sigma-Aldrich, Hydrolyzed: 89%, CAS Number: 9002-89-5, Molecular Weight: 186) were dissolved in Millipore water at 90°C to make a 10 wt% aqueous solution of PVA. The spin solutions were prepared by dissolving the required amount of solid R6G powder (ACROS Organics, Purity: 99%, CAS Number: 989-38-8, Molecular Weight: 479.017) in Millipore water and ethanol, and mixing that with 10 wt% aqueous solution of PVA to attain the target concentrations, i.e., 0.2 mol/L, 0.6 mol/L, 1.7 mol/L, and 5.2 mol/L. The KLA Tencor P-15 Profilometer was used for thickness characterization of the fabricated films and the recorded thicknesses were $\sim 125 \text{ nm}$ for all films. The profilometer data for one of our sample is reported in Appendix (Fig. 9).

3.2. Optical measurements

Steady-state reflection and transmission spectra of the fabricated films at a near-normal angle of incidence (10°) were measured in a custom-made optical setup where a white light source (Oriel 66182) was used for the excitation. The films were kept at the rotation axis of a goniometric stage facing the pseudo-collimated excitation light. The excitation was coming through a prism polarizer with the polarization axis perpendicular to the rotation plane. The excitation spot size on the sample surface was about 2 mm. The angle of incidence was adjusted manually by rotating the goniometric stage. The reflected and transmitted spectra of the films were collected using a fiber coupler assembly (ThorLabs F220SMA-A, $f = 10.90 \text{ mm}$, $\text{NA} = 0.25$) connected to a fiber optic bundle (ThorLabs, model: BFL200HS02, 250 to 1200 nm, round to linear bundle, $7 \times 200 \mu\text{m}$ core fibers, high-OH, SMA). The collected light was guided to a spectrometer consisting of a monochromator (Acton monochromator SP2150i, slit size: $100 \mu\text{m}$, grating: 150 grooves/mm blazed at 500 nm) and CCD (Andor IVAC CCD DR-324B-FI, pixel size: $16 \times 16 \mu\text{m}^2$), and the spectra were recorded in ASCII format.

3.3. TMM simulation and spectral fitting

The experimental absorption (A_{exp}) of the R6G films was background corrected by subtracting the absorption of the reference sample (bare PVA film on BK7 glass) and in accordance with that, the R6G layers were considered in semi-infinite air in TMM simulation. The spectral fitting allowed an initial guess and two physical constraints, i.e., an upper and a lower bound for each fitting parameter. The initial guesses were fed to the MLOM to generate the initial values of n and k , which were used afterwards in TMM to calculate A_{TMM} and thereby, Θ . An optimization algorithm for finding the minimum of a constrained nonlinear multivariable function [39], as implemented in MATLAB, was employed to minimize Θ while the fitting parameters were allowed to vary between the upper and the lower bounds. The initial guesses and the physical constraints were estimated from a standard Voigt fit [40] on A_{exp} so that the fitting parameters can vary within a physically meaningful range.

4. Results and discussions

As explained earlier, the inhomogeneous broadening in the absorption of organic thin films can have various reasons and exact contributions from those different factors of inhomogeneity are impossible to know beforehand [19,25,27,29]. Therefore, application of an ABF via MLOM is a convenient way to fit such broadened and asymmetric spectra. The MLOM not only offers a quick and simple evaluation of optical constants from an experimental absorption spectrum but also provides a generalized model for all kinds of broadenings (Lorentzian, Gaussian, Voigt, and beyond) through the variation of an adjustable broadening parameter (α_j) [19,25,26].

To develop an insight on this adjustable broadening mechanism, we consider a single-oscillator MLOM framework representing material model for an organic thin film in a generic way. All the common parameters between LOM and MLOM are kept as constant, i.e., $f_0 = 0.03$, $\gamma_0 = 0.15$ eV, $E_0 = 2.3$ eV, and $\epsilon_\infty = 2.25$ while the adjustable broadening parameter (α_0) is varied, i.e., $\alpha_0 = 0, 0.15, 0.3, 3$. The optical constants are calculated using Eqs. (1–7) and subsequently used in TMM to simulate the corresponding absorption profiles. The simulated spectra are plotted in Fig. 1 along with the associated ABF in inset.

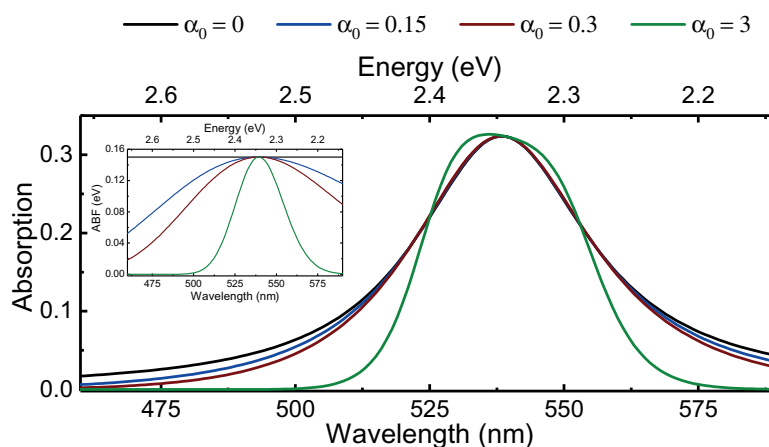


Fig. 1. MLOM/TMM simulated absorption spectra of a dye-doped polymer film for different values of adjustable broadening parameter (α_0). In the inset, spectral evolution of the corresponding adjustable broadening function is plotted. The other MLOM parameters are kept constant as $f_0 = 0.03$, $\gamma_0 = 0.15$ eV, $E_0 = 2.3$ eV, and $\epsilon_\infty = 2.25$.

In the figure, $\alpha_0 = 0$ represents the true Lorentzian broadening while $\alpha_0 = 0.15$ and $\alpha_0 = 0.3$ show the shift from that *ideal* case towards Gaussian profiles via Voigt. It is evident that using only one oscillator with such small values of α_0 (i.e. Lorentzian/Gaussian/Voigt) is often not sufficient to fit absorption of organic films where electronic transitions are accompanied by many vibrational responses and usually multi-oscillator approaches or convolution of non-Lorentzian functions are needed [24,25,27]. However, for larger values of α_0 , like $\alpha_0 = 3$, the absorption shows a flat and broad peak frequently observed in the absorption of highly concentrated molecular films as we will see in our experimental finding also. The associated changes in ABF (figure inset) clearly show the adaptive nature of the frequency-dependent damping since all the curves (except $\alpha_0 = 0$) show different degrees of spectral variation with varying α_0 . Such adaptive broadening is essential to fit absorption of organic films possessing unintuitive sharp and subtle changes in their spectra. Therefore, the MLOM provides a much quicker, simpler and straightforward pathway to fit absorption of organic films with any arbitrary lineshape compared to the numerically cumbersome conventional methods (multi-oscillator/convolution of non-Lorentzians).

Before presenting our findings it is important to discuss our MLOM/TMM fitting procedure depicted as a flowchart in Fig. 2. The spectral fitting starts with assigning four fitting parameters (f_j , E_j , γ_j and α_j) as initial guesses. The initial guesses are fed to the MLOM to generate the initial values of n and k , which are then used in TMM to calculate A_{TMM} . An objective function (Θ) is employed along with the experimental absorption (A_{exp}) to quantify the accuracy of the fit and hence, the goal is to minimize Θ . An optimization algorithm [39] is employed for that purpose and during the optimization, the values of each fitting parameter is allowed to vary only between its corresponding physical constraints, i.e., an upper and a lower bound. The initial guesses and the physical constraints are estimated from a standard Voigt fit [40] on A_{exp} so that the fitting parameters can vary within a feasible range compatible with the experimental reality. The exit condition of the optimization is met when the minimal value for Θ is achieved, which in practice means that the change of the value between the consecutive iterations is smaller than the predefined error tolerance. The associated optimal parameters, i.e., optimal values of f_j , E_j , γ_j and α_j are then used to calculate the optical constants using Eqs. (1–7).

It should be noted here that our choice for a Voigt fit to estimate the initial guesses and the physical constraints is merely our chosen approach and our MLOM fitting method is not limited to any specific method for evaluation of those initial starting values. However, proper choice of constraints, i.e., the upper and the lower bounds is very important for multiple reasons. First of all, without suitable constraints, the optimization algorithm can converge into a physically meaningless solution with unrealistic fitting parameter values. Moreover, poor choice of constraints can make MLOM even invalid since for very large values of α_j , MLOM shows limitations by being inconsistent with the Kramers-Kronig relation and by producing splitting of single peaks which are unrealistic in nature [25].

Next we apply the method to a real experimental data as an example. The absorption spectra of the R6G films covering the spectral range of the local excitonic band of interest (i.e. 460 nm - 590 nm) are depicted in Fig. 3. In the figure, the experimental spectra (A_{exp}) are very slightly smoothed just to remove the excess noise and clarify the figure. The simulated absorption profiles are computed by TMM using the optical constants calculated from LOM ($A_{\text{TMM(LOM)}}$) and MLOM ($A_{\text{TMM(MLOM)}}$) with identical initial guesses and physical constraints (except those absent in LOM) for each concentration.

Two Lorentz oscillators are employed in LOM and MLOM to implement the R6G absorption having a molecular resonance (~ 540 nm, $j = 1$) and a vibronic shoulder (~ 503 nm, $j = 2$) at the blue side [24,41]. The amplitudes, the full widths at half maxima (FWHM) and the peak positions of the absorption bands present in the Voigt fit are used as initial guesses for f_j , γ_j and E_j , respectively. The initial guesses for α_j are estimated from the ratio between the Gaussian widths and the Lorentzian widths used in the Voigt fit while the non-resonant background within

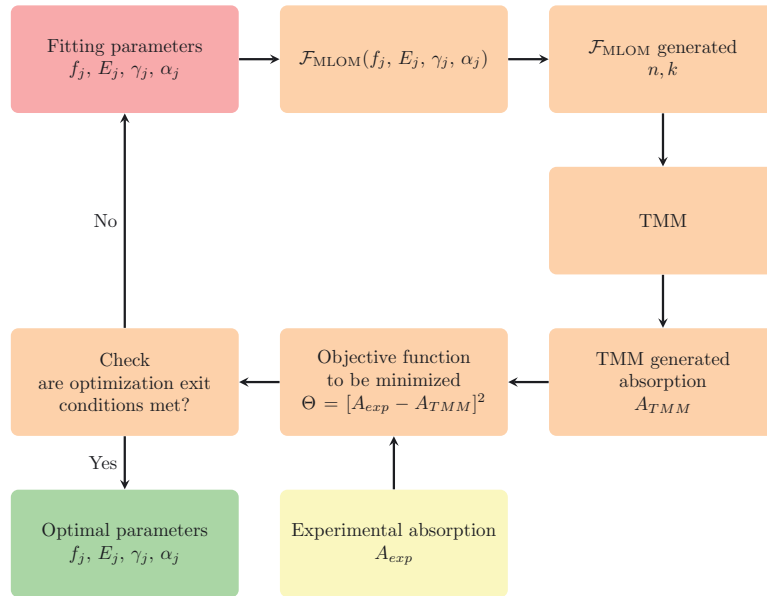


Fig. 2. Flowchart of the MLOM/TMM spectral fitting procedure.

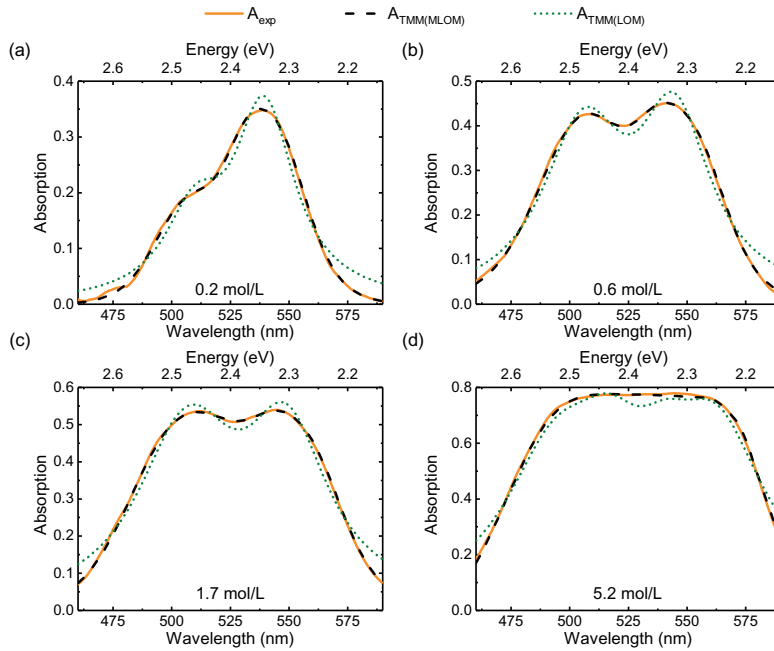


Fig. 3. Absorption profiles of the R6G films in the spectral range of the local excitonic band of interest for target concentrations: (a) 0.2 mol/L, (b) 0.6 mol/L, (c) 1.7 mol/L and (d) 5.2 mol/L. In the figure, $A_{TMM(LOM)}$ and $A_{TMM(MLOM)}$ represent the absorption profiles computed by TMM using the optical constants calculated from LOM and MLOM, respectively, while A_{exp} depicts the experimental (smoothed) absorption spectra.

the exciton-energy region is considered as the dielectric constant of PVA, i.e., $\epsilon_{\infty} = 2.25$ [38,42]. The initial guesses and the upper/lower bounds used for fitting the absorption of the four R6G films are listed in Table 1 (see Appendix).

From Fig. 3 one can clearly see that the spectral shape of film absorption changed significantly with increasing target concentration of R6G. For the lowest concentration (0.2 mol/L), the main peak (~ 540 nm) is showing higher absorption compared to the vibronic shoulder (~ 503 nm) as can be seen in Fig. 3(a). However, with increasing concentration, the vibronic shoulder gets more and more dominant in absorption and becoming a peak of its own as one can see in Figs. 3(b) and 3(c). The linewidths also broaden for both peaks (~ 540 nm and ~ 503 nm) with increasing concentration. Finally, for the highest concentration (5.2 mol/L), the absorption spectrum evolves into a flat top profile as shown in Fig. 3(d). That is because the rise in the absorption of the main peak is relatively less significant compared to that of the vibronic shoulder when concentration is increased. The broadening of both peaks further accelerates the merging of two separate peaks into a flat and wide spectral profile. Absorbance of dye molecules is linearly proportional with the molecular concentration and at high concentration, different intermolecular interactions (not limited to aggregation) can have different contributions leading to an inhomogeneous broadening of the absorption profile. Therefore, our observed changes (hike in absorbance and broadening) in the absorption due to the increase in concentration are consistent with the known effects of molecular systems reported earlier [14,24].

Considering the fact that spectral evolution of the two peaks is different when concentration is varied, we employed LOM and MLOM fitting (with identical initial guesses and physical constraints) on the experimental absorption spectra. It is evident from the figure that for all concentrations, $A_{TMM(MLOM)}$ outperforms $A_{TMM(LOM)}$ by providing a better agreement with A_{exp} . Such finding clearly indicates that an increase in the molecular concentration results in the excitonic absorption bands, which are neither a true Lorentzian nor a pure Gaussian [19], and therefore, utilizing the frequency-dependent inhomogeneous broadening function is the only way to fit such absorption profiles as shown by our MLOM fitting. A quantitative picture of our finding is depicted in Fig. 4 where the values of Θ for each cases are reported (in \log_{10} scale for better visualization) as a function of R6G concentration. It further confirms the superiority of MLOM over LOM in terms of minimal Θ . However, in both LOM and MLOM, the value of Θ is increasing with increasing concentration, indicating the challenge of maintaining accuracy of the methods for extremely high concentrated molecular films.

The effect of R6G concentration on the optimal fitting parameters of MLOM can be inferred from Fig. 5 with the optimal values reported in Table 1 (see Appendix). The optimal oscillator strengths (f_j) as a function of R6G concentration are depicted (in \log_{10} scale for better visualization) in Fig. 5(a). From the figure, we can see that the oscillator strength of the vibronic shoulder (f_2) is lower than that of the molecular resonance (f_1) for the lowest concentration. An increase in R6G concentration causes a significant rise in f_2 leading to a scenario where $f_2 > f_1$ manifested as a rise of the vibronic shoulder in the corresponding absorption profiles. In Fig. 5(b), one can see that with increasing concentration, the peak positions (E_j) of both the molecular resonance (E_1) and its vibronic shoulder (E_2) are shifting towards lower energy implying a spectral red shift in the wavelength scale. The separation between the peaks is also increasing with the concentration. At high concentration of dye molecules, the absorption bands experience spectral red shift due to various intermolecular dipolar interactions (e.g. formation of aggregates) leading to a reduction in the effective oscillation frequency of the molecular system (i.e. red shift in wavelength scale). The increasing separation between the main and shoulder peaks due to rise in concentration can be addressed with the help of quantum mechanics considering interactions between dye molecules as repulsive energy eigenstates in a perturbative scenario. Hence, all the observed trends are known spectroscopic features of dye molecules [14,24].

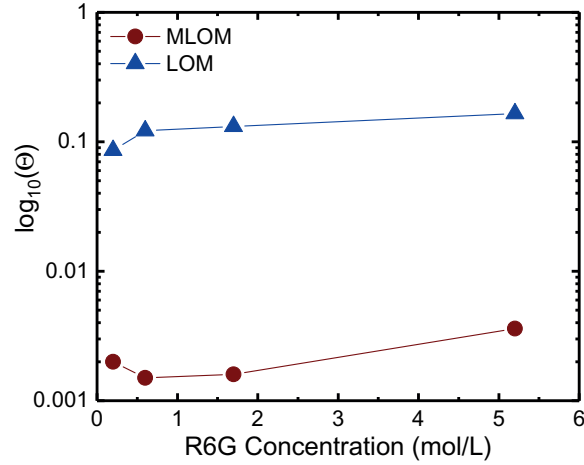


Fig. 4. Evolution of Θ (in \log_{10} scale) as a function of R6G concentration. The blue triangles and red circles connected by lines of corresponding color depict the discrete data points.

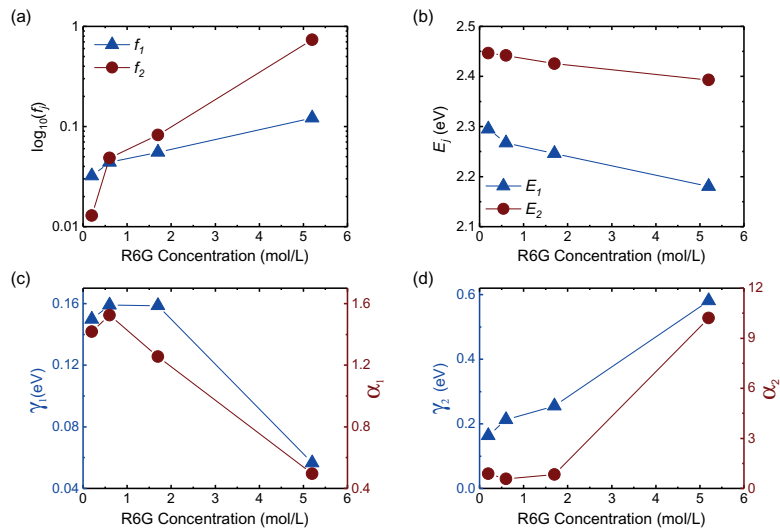


Fig. 5. Evolution of (a) f_j (in \log_{10} scale), (b) E_j , (c) γ_1 and α_1 , and (d) γ_2 and α_2 as a function of R6G concentration. In the figure, $j = 1$ and $j = 2$ represent the molecular resonance (~ 540 nm) and the vibronic shoulder (~ 503 nm) of R6G, respectively. The blue triangles and red circles connected by lines of corresponding color depict the discrete data points. In (c)-(d), the blue and red vertical axes correspond to the blue and red data points, respectively.

An insight on the role of the adjustable broadening function (γ'_j) can be developed from Figs. 5(c) and 5(d) where Fig. 5(c) depicts the evolution of the broadening parameters (γ_j and α_j) as a function of R6G concentration for the molecular resonance (γ_1 and α_1), while Fig. 5(d) shows the same for the vibronic shoulder (γ_2 and α_2). From Fig. 5(c) it is clear that both γ_1 and α_1 are initially increased as the concentration increases from 0.2 mol/L to 0.6 mol/L, but both drop unintuitively for the high concentrations (1.7 mol/L and 5.2 mol/L). On the other hand, Fig. 5(d) shows that the broadening parameters of the vibronic shoulder (γ_2 and α_2) are increasing with respect to the concentration validating its dominance at high concentrations. The aforementioned trend could, however, be exaggerated by the fitting, but it is also challenging to interpret spectroscopically since it requires further studies on the molecular aggregates formed at high concentrations, which is outside the scope of this article.

The optimal α_j values for both the molecular resonance (α_1) and the vibronic shoulder (α_2) are higher than 0.4 for all R6G films (see Table 1 in Appendix) indicating that the spectral nature of γ'_j is neither a true Lorentzian ($\alpha_j = 0$) nor a pure Gaussian ($\alpha_j \approx 0.3$) but an asymmetric lineshape instead [19].

It is worth to mention here that our MLOM approach is preferable not only over the use of convolution of different spectral functions (Gaussian/Voigt) which lacks analytically closed form but also over the use of higher number of oscillators in the conventional LOM since earlier studies have shown that the fit quality does not improve significantly with the increased number of oscillators compared to the use of a frequency-dependent adjustable broadening function [19,25].

The optical constants of the R6G films evaluated from the optimal MLOM show a similar trend to the one found for R6G molecules in solutions [43] and in dry solid film [44,45]. The dispersion of the complex dielectric function (ϵ) and the complex refractive index (N) for the four R6G films are reported in Fig. 6 and Fig. 7, respectively, while Fig. 8 reports the experimental optical constants of a R6G film reproduced from existing literature [45] for a better visual comparison.

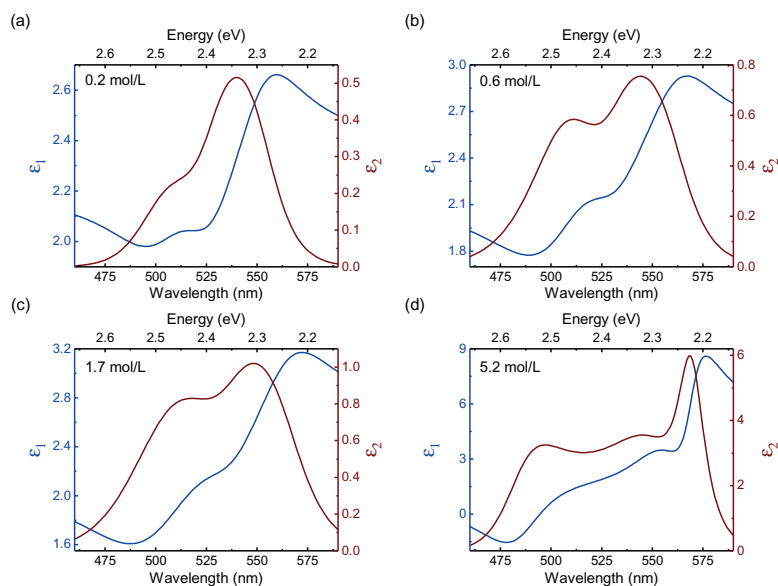


Fig. 6. Real (ϵ_1) and imaginary (ϵ_2) parts of the complex dielectric function (ϵ) of the R6G films in the spectral range of the local excitonic band of interest for target concentrations: (a) 0.2 mol/L, (b) 0.6 mol/L, (c) 1.7 mol/L and (d) 5.2 mol/L. The blue and red vertical axes correspond to the blue and red curves, respectively.

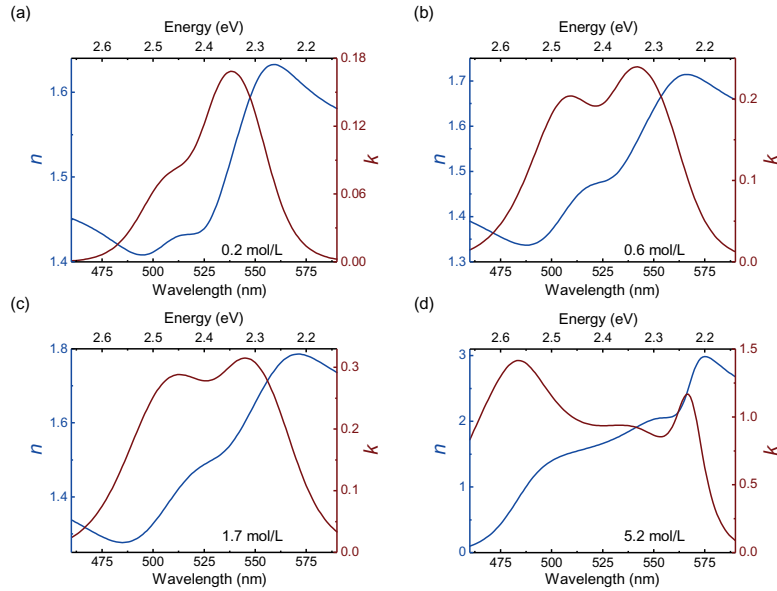


Fig. 7. Real (n) and imaginary (k) parts of the complex refractive index (N) of the R6G films in the spectral range of the local excitonic band of interest for target concentrations: (a) 0.2 mol/L, (b) 0.6 mol/L, (c) 1.7 mol/L and (d) 5.2 mol/L. The blue and red vertical axes correspond to the blue and red curves, respectively.

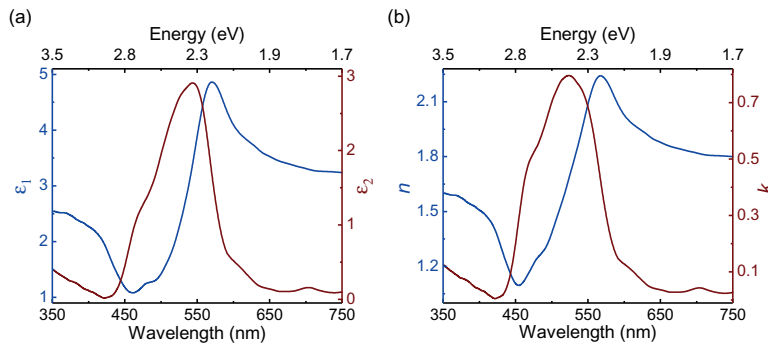


Fig. 8. Experimental complex (a) dielectric function ($\epsilon = \epsilon_1 + i\epsilon_2$) and (b) refractive index ($N = n + ik$) of R6G reproduced from Ref. [45]. The blue and red vertical axes correspond to the blue and red curves, respectively.

From Figs. 6 and 7 we can clearly see that the imaginary parts of ϵ and N , i.e., ϵ_2 and k , closely follow the absorption profiles of the films - except in the highest concentration where they show interesting profile with three peaks, which reveals that the exciton landscape is changing within these concentrations. However, in all samples the values of ϵ_2 and k are monotonically increasing with increasing concentration, in accordance with the absorption. The real parts of ϵ and N , i.e., ϵ_1 and n , show a similar trend in their values with respect to the concentration. In addition, the difference between the magnitudes of n in the blue and red regions of the spectrum is increasing with concentration. Similar nature is found in ϵ_1 which becomes negative, implying metallic like behavior [8,44], in the 460 nm - 500 nm region for the highest concentration sample as shown in Fig. 6(d). The dispersion of both the real and the imaginary components of N and ϵ , over the spectral region of interest, for all concentrations, show a similar qualitative nature to the one reported in the existing literature [45] as shown in Fig. 8 and to the one found in dye-doped excitonic films in general [8,25,44,46].

It is worth of noting that the exact values of the optical constants we report here for R6G cannot be generalized for arbitrary R6G doped films since depending on the molecular concentration, film thickness, type of the hosting polymer and any anisotropy in the film quality, the film absorption and consequently, the extracted optical constants can drastically differ from our case. Nevertheless, we have successfully demonstrated here a straightforward way to determine the optical constants of dye doped isotropic excitonic thin films directly from their absorption spectra without ellipsometry. Our method outperforms the conventional LOM in terms of fitting accuracy and can be easily generalized to many other isotropic excitonic thin films. Our findings are important in the context of designing photonic and optoelectronic devices based on organic materials where modeling of local excitonic absorption bands of organic thin films is crucial.

5. Conclusions

In this work, we reported a method to evaluate the complex-dispersive refractive index and dielectric function of isotropic organic thin films from their absorption spectra without ellipsometry. We used a spectral fitting approach which contains a MLOM and an optimization algorithm to minimize an objective function representing the degree of dissimilarity between the experimental and the fitted curve. The MLOM differs from the conventional LOM by employing a frequency-dependent adjustable broadening function in the damping rate term and hence, can fit any inhomogeneous spectral broadening other than Lorentzian, Gaussian or Voigt profiles. Our method was implemented via TMM to extract the optical constants of R6G:PVA films with varying R6G concentration.

Our findings quantitatively showed that MLOM can outperform LOM in terms of fitting accuracy, especially when the molecular concentration is very high. The effect of concentration on the MLOM parameters was also analyzed, and it validated the corresponding spectral changes in the experimental absorption. Our evaluated optical constants and their dispersion are in good agreement with the qualitative trend found in other excitonic thin films. Our findings provide a way to determine the optical constants of organic thin films and hence, to model their local excitonic absorption bands which is crucial in designing excitonic and polaritonic devices for organic nanophotonics.

Appendix

Table 1. Initial guesses and physical constraints of the fitting parameters, as well as the final fitted values, in MLOM and LOM (except α_j) for R6G films with different concentrations. Two-oscillator model was employed in the fitting to implement the R6G absorption having a molecular resonance at $E_1 = 2.30$ eV (540 nm) and a vibronic shoulder at $E_2 = 2.46$ eV (503 nm). Other parameters related to corresponding resonant energy E_j , are oscillator strength f_j , damping rate γ_j and adjustable broadening parameter α_j .

| Conc. (mol/L) | Parameters | Initial guess | Lower bound | Upper bound | Fitted value |
|---------------|-----------------|---------------|-------------|-------------|--------------|
| 0.20 | f_1 | 0.05 | 0.01 | 0.10 | 0.0320 |
| | f_2 | 0.05 | 0.01 | 0.10 | 0.0129 |
| | γ_1 (eV) | 0.30 | 0.10 | 0.50 | 0.1497 |
| | γ_2 (eV) | 0.30 | 0.10 | 0.50 | 0.1633 |
| | E_1 (eV) | 2.30 | 2.25 | 2.35 | 2.2946 |
| | E_2 (eV) | 2.45 | 2.40 | 2.50 | 2.4468 |
| | α_1 | 2.50 | 0.01 | 5.00 | 1.4171 |
| | α_2 | 2.50 | 0.01 | 5.00 | 0.8727 |
| 0.60 | f_1 | 0.05 | 0.01 | 0.10 | 0.0439 |
| | f_2 | 0.05 | 0.01 | 0.10 | 0.0486 |
| | γ_1 (eV) | 0.30 | 0.10 | 0.50 | 0.1590 |
| | γ_2 (eV) | 0.30 | 0.10 | 0.50 | 0.2129 |
| | E_1 (eV) | 2.26 | 2.24 | 2.28 | 2.2670 |
| | E_2 (eV) | 2.45 | 2.40 | 2.50 | 2.4419 |
| | α_1 | 2.50 | 0.01 | 5.00 | 1.5246 |
| | α_2 | 2.50 | 0.01 | 5.00 | 0.5771 |
| 1.70 | f_1 | 0.05 | 0.01 | 0.10 | 0.0554 |
| | f_2 | 0.05 | 0.01 | 0.10 | 0.0824 |
| | γ_1 (eV) | 0.30 | 0.10 | 0.50 | 0.1586 |
| | γ_2 (eV) | 0.30 | 0.10 | 0.50 | 0.2548 |
| | E_1 (eV) | 2.24 | 2.20 | 2.28 | 2.2459 |
| | E_2 (eV) | 2.45 | 2.40 | 2.50 | 2.4252 |
| | α_1 | 2.50 | 0.01 | 5.00 | 1.2550 |
| | α_2 | 2.50 | 0.01 | 5.00 | 0.8362 |
| 5.20 | f_1 | 0.25 | 0.01 | 1.00 | 0.1216 |
| | f_2 | 0.25 | 0.01 | 1.00 | 0.7330 |
| | γ_1 (eV) | 0.25 | 0.01 | 1.00 | 0.0565 |
| | γ_2 (eV) | 0.25 | 0.01 | 1.00 | 0.5807 |
| | E_1 (eV) | 2.20 | 2.00 | 2.40 | 2.1802 |
| | E_2 (eV) | 2.46 | 2.26 | 2.66 | 2.3931 |
| | α_1 | 7.50 | 0.01 | 15.00 | 0.4954 |
| | α_2 | 7.50 | 0.01 | 15.00 | 10.2070 |

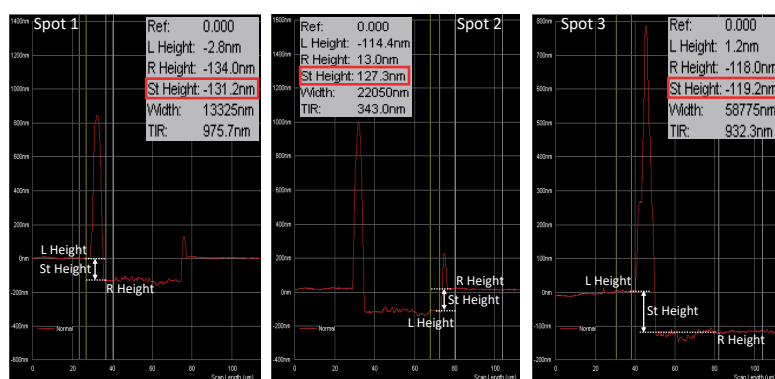


Fig. 9. Profilometer data for R6G:PVA film with target concentration 0.2 mol/L. The film thickness was measured by creating a score on the film and was estimated as the height difference (St height) between the right (R height) and left (L height) sides of the score edge. Thickness was measured at three different spots (131.2 nm, 127.3 nm, and 119.2 nm) along the score edge and the average value (125.9 nm, i.e., ~ 125 nm) was considered in TMM calculation.

Funding. Academy of Finland (289947, 323995).

Acknowledgments. The authors thank Dr. Henry A. Fernandez (Department of Electronics and Nanoengineering, Aalto University, Finland) for his helpful suggestions during the research work.

Disclosures. The authors declare no conflicts of interest.

Data availability. Data underlying the results presented in this paper are not publicly available at this time but may be obtained from the authors upon reasonable request.

References

- O. Inganäs, "Organic photovoltaics over three decades," *Adv. Mater.* **30**(35), 1800388 (2018).
- Z. Li, X. Zhao, X. Lu, Z. Gao, B. Mi, and W. Huang, "Organic thin-film solar cells: devices and materials," *Sci. China Chem.* **55**(4), 553–578 (2012).
- Y. Cui, H. Yao, L. Hong, T. Zhang, Y. Tang, B. Lin, K. Xian, B. Gao, C. An, P. Bi, W. Ma, and J. Hou, "Organic photovoltaic cell with 17% efficiency and superior processability," *Natl. Sci. Rev.* **7**(7), 1239–1246 (2020).
- O. Ostroverkhova, "Organic optoelectronic materials: mechanisms and applications," *Chem. Rev.* **116**(22), 13279–13412 (2016).
- I. D. W. Samuel and G. A. Turnbull, "Organic semiconductor lasers," *Chem. Rev.* **107**(4), 1272–1295 (2007).
- S. Tanida, K. Noda, H. Kawabata, and K. Matsushige, "N-channel thin-film transistors based on 1, 4, 5, 8-naphthalene tetracarboxylic dianhydride with ultrathin polymer gate buffer layer," *Thin Solid Films* **518**(2), 571–574 (2009).
- S. K. Saikin, A. Eisfeld, S. Valleau, and A. Aspuru-Guzik, "Photonics meets excitonics: natural and artificial molecular aggregates," *Nanophotonics* **2**(1), 21–38 (2013).
- M. J. Gentile, S. Núñez-Sánchez, and W. L. Barnes, "Optical field-enhancement and subwavelength field-confinement using excitonic nanostructures," *Nano Lett.* **14**(5), 2339–2344 (2014).
- M. J. Gentile, S. A. R. Horsley, and W. L. Barnes, "Localized exciton-polariton modes in dye-doped nanospheres: a quantum approach," *J. Opt.* **18**(1), 015001 (2016).
- A. Canales, D. G. Baranov, T. J. Antosiewicz, and T. Shegai, "Abundance of cavity-free polaritonic states in resonant materials and nanostructures," *J. Chem. Phys.* **154**(2), 024701 (2021).
- C. J. Bardeen, "The structure and dynamics of molecular excitons," *Annu. Rev. Phys. Chem.* **65**(1), 127–148 (2014).
- M. Nyman, A. Shevchenko, I. Shavrin, Y. Ando, K. Lindfors, and M. Kaivola, "Large-area enhancement of far-field fluorescence intensity using planar nanostructures," *APL Photonics* **4**(7), 076101 (2019).
- A. Dutta, V. Tiainen, and J. J. Toppari, "Optimizing geometry of low-Q all-metal Fabry-Pérot microcavity for fluorescence spectroscopy," *IOP SciNotes* **2**(1), 015205 (2021).
- S. V. Baieva, T. K. Hakala, and J. J. Toppari, "Strong coupling between surface plasmon polaritons and sulforhodamine 101 dye," *Nanoscale Res. Lett.* **7**(1), 191 (2012).
- P. A. Hobson, W. L. Barnes, D. G. Lidzey, G. A. Gehring, D. M. Whittaker, M. S. Skolnick, and S. Walker, "Strong exciton-photon coupling in a low-Q all-metal mirror microcavity," *Appl. Phys. Lett.* **81**(19), 3519–3521 (2002).
- E. Hülkkö, S. Pikker, V. Tiainen, R. H. Tichauer, G. Groenhof, and J. J. Toppari, "Effect of molecular Stokes shift on polariton dynamics," *J. Chem. Phys.* **154**(15), 154303 (2021).

17. D. S. Dovzhenko, S. V. Ryabchuk, Y. P. Rakovich, and I. R. Nabiev, "Light-matter interaction in the strong coupling regime: configurations, conditions, and applications," *Nanoscale* **10**(8), 3589–3605 (2018).
18. D. Poelman and P. F. Smet, "Methods for the determination of the optical constants of thin films from single transmission measurements: a critical review," *J. Phys. D: Appl. Phys.* **36**(15), 1850–1857 (2003).
19. A. B. Djurišić, T. Fritz, and K. Leo, "Modelling the optical constants of organic thin films: impact of the choice of objective function," *J. Opt. A: Pure Appl. Opt.* **2**(5), 458–464 (2000).
20. S. S. Falahatgar and F. E. Ghodsi, "A developed model for the determination of the dielectric function for some absorbing thin films using pseudo-Urbach tail," *Phys. B* **412**, 4–11 (2013).
21. I. Chambouleyron and J. M. Martínez, "Optical properties of dielectric and semiconductor thin films, in *Handbook of Thin Films: Volume 3*, H. S. Nalwa, ed. (Academic Press, 2002).
22. H. Fujiwara, *Spectroscopic Ellipsometry: Principles and Applications* (Wiley, 2007).
23. H. G. Tompkins and J. N. Hilfiker, *Spectroscopic Ellipsometry: Practical Application to Thin Film Characterization* (Momentum Press, 2015).
24. C. On, E. K. Tanyi, E. Harrison, and M. A. Noginov, "Effect of molecular concentration on spectroscopic properties of poly(methyl methacrylate) thin films doped with rhodamine 6G dye," *Opt. Mater. Express* **7**(12), 4286–4295 (2017).
25. A. B. Djurišić, T. Fritz, and K. Leo, "Modeling the optical constants of organic thin films: application to 3, 4, 9, 10-perylenetetracarboxylic dianhydride (PTCDA)," *Opt. Commun.* **183**(1-4), 123–132 (2000).
26. C. C. Kim, J. W. Garland, H. Abad, and P. M. Raccach, "Modeling the optical dielectric function of semiconductors: extension of the critical-point parabolic-band approximation," *Phys. Rev. B* **45**(20), 11749–11767 (1992).
27. A. Franke, A. Stendal, O. Stenzel, and C. von Borczyskowski, "Gaussian quadrature approach to the calculation of the optical constants in the vicinity of inhomogeneously broadened absorption lines," *Pure Appl. Opt.* **5**(6), 845–853 (1996).
28. M. V. Bondar, O. V. Przhonska, and Y. A. Tikhonov, "Inhomogeneous broadening of organic dyes in polymeric media: nonlinear transmission spectra and photochemical kinetics," *J. Phys. Chem.* **96**(26), 10831–10837 (1992).
29. S. T. Hoffmann, H. Bässler, and A. Köhler, "What determines inhomogeneous broadening of electronic transitions in conjugated polymers?" *J. Phys. Chem. B* **114**(51), 17037–17048 (2010).
30. D. Gonçalves and E. A. Irene, "Fundamentals and applications of spectroscopic ellipsometry," *Quím. Nova* **25**(5), 794–800 (2002).
31. G. Jungk, "Possibilities and limitations of ellipsometry," *Thin Solid Films* **234**(1-2), 428–431 (1993).
32. J. S. Schildkraut, "Limitations to the determination of the optical properties of a thin film by combined ellipsometric and surface plasmon resonance measurements," *Appl. Opt.* **27**(16), 3329–3333 (1988).
33. P. Markoš and C. M. Soukoulis, *Wave Propagation: From Electrons to Photonic Crystals and Left-Handed Materials* (Princeton University Press, 2008).
34. T. G. Mackay and A. Lakhtakia, *The Transfer-Matrix Method in Electromagnetics and Optics* (Morgan and Claypool, 2020).
35. R. B. Balili, "Transfer matrix method in nanophotonics," *Int. J. Mod. Phys. Conf. Ser.* **17**, 159–168 (2012).
36. K. J. Pascoe, "Reflectivity and transmissivity through layered, lossy media: a user-friendly approach," Tech. rep., Air Force Institute of Technology, Wright-Patterson Air Force Base (2001).
37. <https://www.mathworks.com/products/matlab.html>.
38. H. Sumi and Y. Kayanuma, "Is the Lorentz model applicable to optical absorption by excitons?" *Solid State Commun.* **85**(1), 1–4 (1993).
39. <https://www.mathworks.com/help/optim/ug/fmincon.html>.
40. S. M. Abrarov and B. M. Quine, "A rational approximation for efficient computation of the Voigt function in quantitative spectroscopy," *J. Math. Res.* **7**(2), 163–174 (2015).
41. B. L. Darby, B. Auguie, M. Meyer, A. E. Pantoja, and E. C. Le Ru, "Modified optical absorption of molecules on metallic nanoparticles at sub-monolayer coverage," *Nat. Photonics* **10**(1), 40–45 (2016).
42. M. J. Schnepf, M. Mayer, C. Kuttner, M. Tebbe, D. Wolf, M. Dulle, T. Altantzis, P. Formanek, S. Förster, S. Bals, T. A. F. König, and A. Fery, "Nanorattles with tailored electric field enhancement," *Nanoscale* **9**(27), 9376–9385 (2017).
43. W. Leupacher and A. Penzkofer, "Refractive-index measurement of absorbing condensed media," *Appl. Opt.* **23**(10), 1554–1558 (1984).
44. L. Gu, J. Livenere, G. Zhu, E. E. Narimanov, and M. A. Noginov, "Quest for organic plasmonics," *Appl. Phys. Lett.* **103**(2), 021104 (2013).
45. T. Itoh, Y. S. Yamamoto, and T. Okamoto, "Anti-crossing property of strong coupling system of silver nanoparticle dimers coated with thin dye molecular films analyzed by electromagnetism," *J. Chem. Phys.* **152**(5), 054710 (2020).
46. E. G. Bortchagovsky and U. C. Fischer, "Method for determination of the dielectric function of a thin absorbing film on variable substrates from transmission spectra," *Appl. Opt.* **42**(34), 6915–6918 (2003).

PVI

**ULTRA-FAST PHOTOCHEMISTRY IN THE STRONG
LIGHT-MATTER COUPLING REGIME**

by

A. Dutta, V. Tiainen, L. Duarte, N. Markešević, D. Morozov, H. A. Qureshi, G.
Groenhof, and J. J. Toppari,

Research Square, **Preprint**, 10.21203/rs.3.rs-3237899/v1 (2023).

Reproduced with kind permission of all the authors.

Ultra-fast photochemistry in the strong light-matter coupling regime

Arpan Dutta^{1,4}, Ville Tiainen¹, Luís Duarte^{1,3}, Nemanja Markešević¹, Dmitry Morozov², Hassan A. Qureshi^{1,4}, Gerrit Groenhof^{2*} and J. Jussi Toppari^{1*}

¹Nanoscience Center and Department of Physics, University of Jyväskylä, P.O. Box 35, Jyväskylä, 40014, Finland.

²Nanoscience Center and Department of Chemistry, University of Jyväskylä, P.O. Box 35, Jyväskylä, 40014, Finland.

³Present address: Department of Chemistry, University of Helsinki, P.O. Box 55, Helsinki, 00014, Finland.

⁴Present address: Department of Mechanical and Materials Engineering, University of Turku, Turku, 20014, Finland.

*Corresponding author(s). E-mail(s): gerrit.x.groenhof@jyu.fi; j.jussi.toppari@jyu.fi;
Contributing authors: arpan.dutta@utu.fi; vijutiai@jyu.fi; luis.duarte@helsinki.fi;
nemanja.markesevic@gmail.com; dmitry.morozov@jyu.fi; hassan.queshi@utu.fi;

Abstract

Strong coupling between molecules and confined light modes of optical cavities to form polaritons can alter photochemistry, but the origin of this effect remains largely unknown. While theoretical models suggest a suppression of photochemistry due to the formation of new polaritonic potential energy surfaces, many of these models do not account for the energetic disorder among the molecules, which is unavoidable at ambient conditions. Here, we combine experiments and simulations to show that for an ultra-fast photochemical reaction such thermal disorder prevents the modification of the potential energy surface and that suppression is due to radiative decay of the lossy cavity modes. We demonstrate that by increasing the coupling strength we can reduce such losses and enhance reactivity of the strongly coupled system, in contrast to the theoretical paradigm, which would predict stronger suppression. We also show that the excitation spectrum under strong coupling is a product of the excitation spectrum of the "bare" molecules and the absorption spectrum of the molecule-cavity system, suggesting that polaritons can act as gateways for channeling an excitation into a molecule, which then reacts "normally". Our results therefore imply that strong coupling provides a means to tune the action spectrum of a molecule, rather than to change the reaction.

Keywords: Polaritonic chemistry, strong coupling, excited-state intra-molecular proton transfer, optical micro-cavity, molecular dynamics simulations.

Introduction

Placing molecules between the mirrors of a Fabry-Pérot micro-cavity that is resonant with their excitation frequency, has been shown to alter their chemistry in both ground and excited states [1–9], but the origin of these effects are hitherto unknown. Inside the cavity, the rate of energy exchange between excitations of the molecules and confined light modes of the cavity can exceed the intrinsic decay rates of both the molecular excitations and the photonic modes [10]. Under these conditions, the system enters the strong light-matter coupling regime, in which the excitations of the molecules hybridize with the confined light modes of the cavity to form new light-matter states, called polaritons [11–14].

Changes to photo-chemical reactivity have been rationalized on the basis of differences between the potential energy surfaces of the polariton and that of the bare molecule, as illustrated in Figure 1c [15]. The key to this hypothesis is that the lifetime of the polariton is sufficiently long for the reactants to evolve over the modified portions of the potential energy surface. Despite recent suggestions that the lowest-energy polariton state can be very long-lived [16], polariton lifetimes are generally considered to be limited by the lifetime of the cavity photon [17, 18], which is on the order of a few tens of femtoseconds in the metallic cavities that have been used in experiments. Because the polariton decay rate in these experiments was significantly higher than the rate of the photo-chemical reaction [1, 6, 7, 9], it remains difficult to understand whether the observed changes in reactivity are due to the polaritonic states providing (i) a competing radiative decay channel [8], (ii) a different potential energy surface [15], or (iii) a combination of both.

To disentangle these effects, and understand how strong coupling affects photo-reactivity, experiments should instead be performed on a photo-chemical reaction that happens at same timescale as polariton decay. In this work, we therefore investigated the influence of strong light-matter coupling on the ultra-fast photochemical reaction of 10-hydroxybenzo[h]quinoline (HBQ) in an optical cavity (Figure 1). The reaction in the electronic excited-state (S_1) of this molecule happens on a timescale of ~ 15 fs [19, 20], which is

comparable to the lifetime of a cavity photon in metallic micro-cavities.

Figure 1(b) shows the normalized absorption and emission spectra of HBQ in polymethyl methacrylate (PMMA), which we used as a polymer matrix for embedding the molecules within the cavity (Figure 1(a)). Photon absorption at 375 nm triggers an ultra-fast excited state intramolecular proton transfer (ESIPT) from the phenol oxygen to the nitrogen atom [19, 20], as shown in Figure 1(c). The reaction coordinate is defined as the difference between Oxygen-Hydrogen and Nitrogen-Hydrogen distances $d_{O-H} - d_{N-H}$. After proton transfer, the keto-form of HBQ decays back to the electronic ground state (S_0) through photon emission with a maximum around 620 nm.

Results from Density Functional Theory (DFT) calculations at the TDA-CAM-B3LYP/6-31G* level of theory [21–24] suggest that outside of the cavity, proton transfer is a barrier-less process in the first singlet electronic excited-state (S_1 , Figure 1(c)). When N molecules are placed inside the cavity, the $S_0 \rightarrow S_1$ excitations couple to the confined light modes that are resonant with the excitation energy (375 nm in experiment, 305 nm at the TDA-CAM-B3LYP/6-31G* level of theory, see below), to form the upper (UP) and lower (LP) polaritons, as well as $N - 1$ dark states. The Rabi splitting that separates the LP and UP states, creates a local minimum on the potential energy surface of the LP state [15]. As a consequence, the excited-state intra-molecular proton transfer in the lowest-energy excited state of the molecule-cavity system is no longer barrier-less (Figure 1(c)). Because the Rabi splitting depends on the molecular concentration, *i.e.*, $\hbar\Omega^{\text{Rabi}} \propto \sqrt{N/V_{\text{cav}}}$ [14], we can control the barrier separating the local minimum on the LP surface from the product minimum by varying the number of molecules in the cavity mode volume, as illustrated in Figure 1(c), and thus systematically reduce the proton transfer rate. This reduction, in combination with the low LP lifetime, should hence suppress the emission at 620 nm, which is sufficiently far off-resonance from the lowest-frequency cavity mode to be affected by strong coupling or Purcell enhancement. To test this hypothesis [15], we performed both molecular dynamics (MD) simulations and experiments.

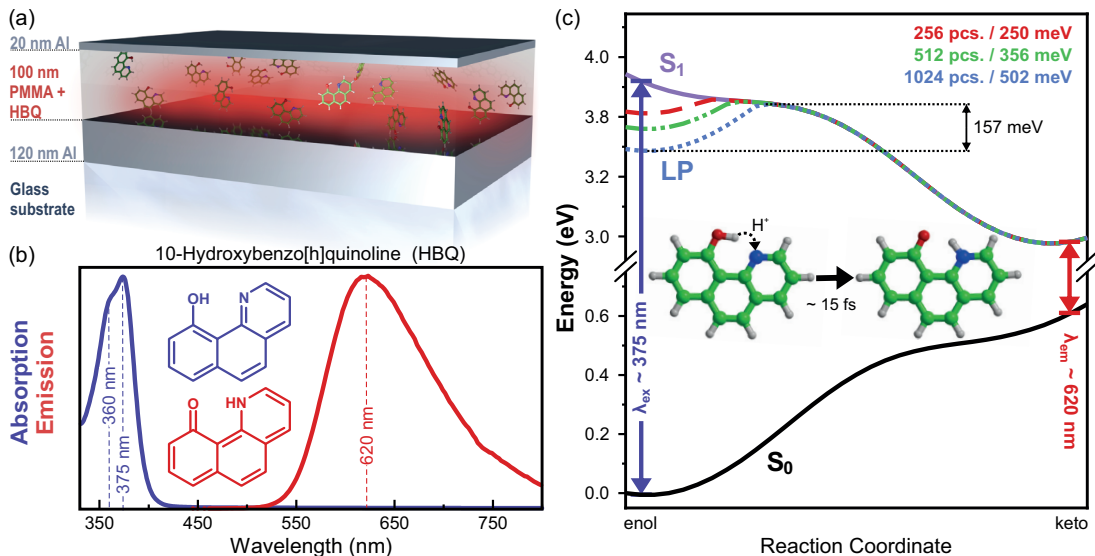


Fig. 1 (a) Schematic illustration of the cavity geometry (not to scale). (b) Normalized absorption and emission spectra of HBQ in PMMA films. (c) Potential energy profiles for intra-molecular proton transfer in the electronic ground state, (S_0 , black) first singlet electronic excited state (S_1 , purple), in the lower polariton (LP), when 256 (red dashed), 512 (green dashed-dotted) or 1024 (blue dotted) *identical* HBQ molecules are strongly coupled to a single confined light mode of an optical cavity that is resonant with the $S_0 \rightarrow S_1$ transition in HBQ. The Rabi splittings are listed in the upper right corner. The energy barrier for proton transfer in the LP state with highest Rabi split is indicated by the double-arrow.

Results & Discussion

In the simulations, the details of which can be found in the Supporting Information (SI, section 2), 512 HBQ molecules solvated in cyclohexane and equilibrated at 300 K, were placed inside a single-mode cavity with a photon energy of $\hbar\omega_{\text{cav}} = 4.02$ eV, selected to be in resonance with the absorption of our molecular model (see below), and a vacuum field strength of $\sqrt{\hbar\omega_{\text{cav}}/\epsilon_0 V_{\text{cav}}} = 0.00015$ au (0.77 MVcm $^{-1}$). The electronic ground (S_0) and excited (S_1) states of HBQ were modeled with Density Functional Theory (DFT) [25] and time-dependent density functional theory (TDDFT) [26] within the Tamm-Dancoff approximation (TDA) [21], respectively, using the CAM-B3LYP functional [22, 23] in combination with the 6-31G(d) basis set [27]. The cyclohexane solvent molecules were modelled with the GRO-MOS 2016H66 force field [28]. At this level of theory the vertical excitation energy of HBQ is $h\nu_{\text{mol}} = 4.06$ eV (305 nm), while the energy gap to the ground state is 2.58 eV (480 nm) in the S_1 minimum. Despite an overestimation of the S_1 - S_0 energy gap, which we compensated for by adding an offset to the cavity mode energy [29],

our model provides a description of the potential energy surfaces (see the computed potential energy profiles in Figure 1(c)) that is in qualitative agreement with the more accurate description at the TPSSh/cc-pVDZ level of theory (Figure S8 in Supporting Information (SI)) [30, 31].

As shown in Figure 2(a), the calculated QM/MM $S_0 \rightarrow S_1$ absorption spectrum of HBQ at 300 K (SI, subsection 2.5) splits inside the cavity, suggesting that the molecule-cavity system is in the strong coupling regime with a Rabi splitting of 240 meV. We performed 22 MD simulations, starting in various eigenstates of the molecule-cavity system, that are indicated by arrows in Figure 2(a). In all simulations, intra-molecular proton transfer occurs irrespective of the polaritonic eigenstate that was initially excited (Figure 2(d), Table S1, SI). Because the reaction rate in QM/MM simulations of HBQ *outside* of the cavity is very similar (Figure S7, SI), these results suggest that strong coupling does not have an appreciable effect on the reaction. Thus, even though the characteristic Rabi splitting implies strong coupling, the formation

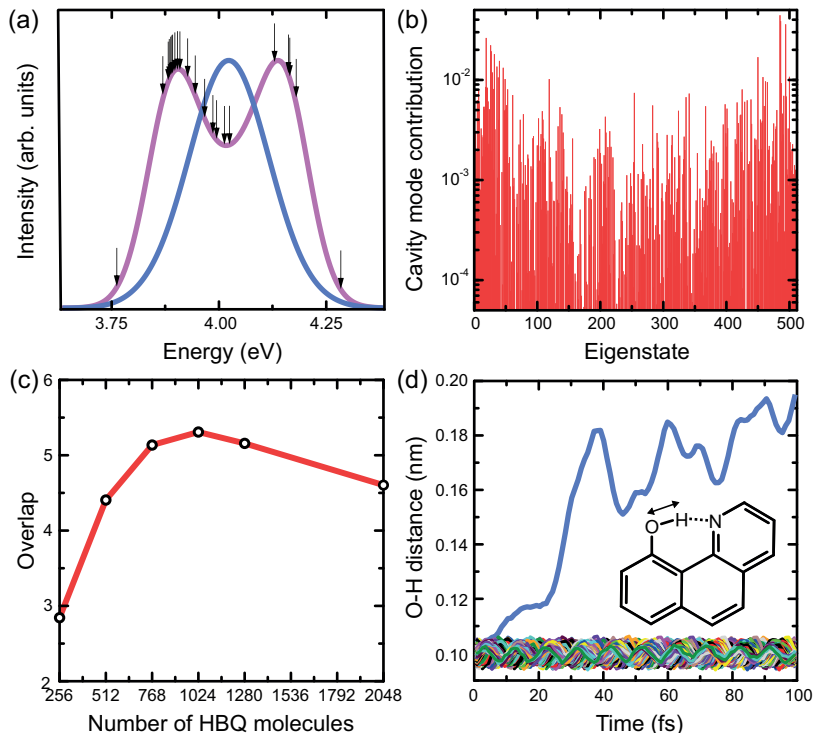


Fig. 2 (a) Absorption spectra of HBQ in cyclohexane at 300 K outside (blue) and inside (magenta) of a single-mode micro-cavity ($\hbar\omega_{\text{cav}} = 4.02$ eV, $\sqrt{\hbar\omega_{\text{cav}}/2\epsilon_0 V_{\text{cav}}} = 0.77$ MVcm $^{-1}$, $N = 512$ HBQ molecules) [32], computed at the CAM-B3LYP/6-31G(d)//Gromos96 level of QM/MM theory. Arrows indicate the eigenstates in which MD simulations were started. (b) Contribution of the cavity mode ($|\alpha_m|^2$, Equation S13, SI) to the eigenstates of the coupled HBQ-cavity system. (c) Overlap between the polaritonic absorption spectrum and the molecular density of states as a function of the number of strongly-coupled molecules. The overlap is proportional to the reaction yield [18]. (d) Time evolution of the distance between the oxygen atom and the proton in 512 HBQ molecules (all colors) after excitation into an optically bright polaritonic state. A distance of ~ 0.10 nm corresponds to the situation where proton is bonded to the phenol oxygen, whereas a distance around 0.19 nm means that proton is attached to the nitrogen.

of polaritonic states does not lead to a suppression of the photo-chemical reaction, in contrast to theoretical predictions [15].

To understand why excitation into a polaritonic eigenstate of the molecule-cavity system does not suppress the reactivity in our simulations, we inspected the composition of these states. As shown in Figure 2(b), the cavity mode is distributed over virtually *all* eigenstates of the molecule-cavity system. As pointed out by Houdré *et al.* [33] for atoms, and later by Mony *et al.* [9] for molecules, this is due to structural, and hence energetic disorder among the HBQ molecules at 300 K. Without disorder, only the optically accessible upper and lower polariton states include contribution of the cavity mode and thus have a different potential energy surface on which reactivity can be suppressed (Figure 1). The other

$N - 1$ eigenstates are "dark", *i.e.*, without contribution from the cavity mode, and have potential energy surfaces that are similar to the S_1 surface of the uncoupled molecule. In contrast, when there is disorder, which is unavoidable in experiments under ambient conditions, *all* states are optically accessible, but because molecular excitations dominate these states, rather than the cavity mode, the potential energy surfaces are hardly perturbed with respect to the bare molecules - not even for the brightest polaritonic states.

In our simulations a perfect cavity was assumed, without any losses. However, in reality photon leakage through the mirrors is unavoidable and hence provides an additional decay channel for the excited population that could reduce the quantum yield and hence suppress the reaction. Under the assumption that the rate of radiative

decay during an MD timestep Δt from a polaritonic state is proportional to its cavity mode contribution [18, 34, 35], we accounted for such reduction in the quantum yield *a posteriori* by recomputing the evolution of the polaritonic wave function under the influence of cavity losses along the MD trajectories (SI, section 2.5). In these calculations we assumed a cavity decay rate of $\gamma_{\text{cav}} = 250 \text{ ps}^{-1}$, which is typical for a low quality metallic cavity with $Q \sim 15$. The yields estimated under these assumptions are listed in Table S1 (SI), and suggest an average loss of only 5% for the 512 molecule-cavity system, which we consider negligible.

The extent of the radiative loss depends on how rapidly the population transfers from a bright polaritonic state with cavity mode contribution and hence susceptible to radiative decay, into a dark state that is localized on a single molecule and therefore lacks cavity mode contribution [36, 37]. Because the rate of this non-adiabatic population transfer process is inversely proportional to the energy difference between the states [38], the radiative loss depends on the overlap between the optically-bright states and the molecular dark states [18]. Because that overlap is determined by the Rabi splitting, the loss can be controlled by varying the HBQ concentration [18].

However, because adding more molecules inside the cavity mode volume not only increases the Rabi splitting, but also the number of dark states, the overlap between the polaritonic absorption spectrum (Figure 2(a)), which represents the distribution of the optically-bright states (Figure 2(b)), on the one hand, and the molecular absorption spectrum, which represents the distribution of the molecular dark states [18], on the other hand, has a maximum at a specific Rabi splitting, or equivalently a specific number of molecules, as shown in Figure 2(c). Therefore, also the suppression of the reaction due to radiative loss has a minimum at that Rabi splitting and increases again at higher concentrations. Losses estimated for simulations with a different number of molecules in the same cavity confirm this (SI, Table S3).

To remove the overlap and hence suppress photo-product emission in HBQ, the Rabi splitting must exceed 600 meV (SI, Figure S9a), placing the system firmly in the *ultra-strong* coupling regime. Such coupling strengths are not only

challenging to achieve experimentally due to the limited solubility of HBQ in PMMA, but also difficult to simulate, as the rotating wave approximation (RWA), on which our model is based [34], may lose its validity in this regime [39]. Notwithstanding the potential limitations of the RWA, we observed full suppression of the reaction in simulations at a Rabi splitting of 640 meV (Figure S9b).

Summarizing, the results of our calculations suggest that the main mechanism by which strong coupling can suppress the ultra-fast ESIP reaction in HBQ is to provide a competing radiative loss channel, rather than to change the potential energy surface. Our calculations furthermore suggest that the extent of such suppression can be tuned through the HBQ concentration (Figure 2(c)).

To verify the validity of these findings experimentally, we fabricated metallic Fabry-Pérot micro-cavities containing HBQ molecules and measured the photo-luminescence associated with the photo-product at 620 nm as a function of light-matter coupling strength, g , and the excitation wavelength. As shown schematically in Figure 1(a), a ~ 100 nm PMMA film doped with HBQ, was covered with a 20 nm thick semitransparent aluminum (Al) mirror on top and a 120 nm non-transparent Al mirror on the bottom [40]. The top mirror is sufficiently thin for the HBQ photo-product emission around 620 nm to leak through and be detected. The thickness of the cavities was tuned to match the first-order cavity mode with the HBQ absorption maximum at 375 nm. To control the collective light-matter coupling strength ($g \propto \sqrt{N}$), we varied the concentration of HBQ in the PMMA film. Because the first-order cavity mode is sufficiently higher in energy than the emission maximum of the HBQ photo-product, we can exclude fluorescence enhancement due to the Purcell effect [41]. Further details on the design, fabrication and characterization of the cavity systems are provided in SI (section 1).

Three micro-cavities were fabricated with HBQ/PMMA ratios of 0.5 (low), 1.0 (mid), and 1.6 (high concentration). In addition, three bare films were fabricated with the same HBQ/PMMA ratios as in the cavities. To provide a similar geometry for the reflection measurements, these

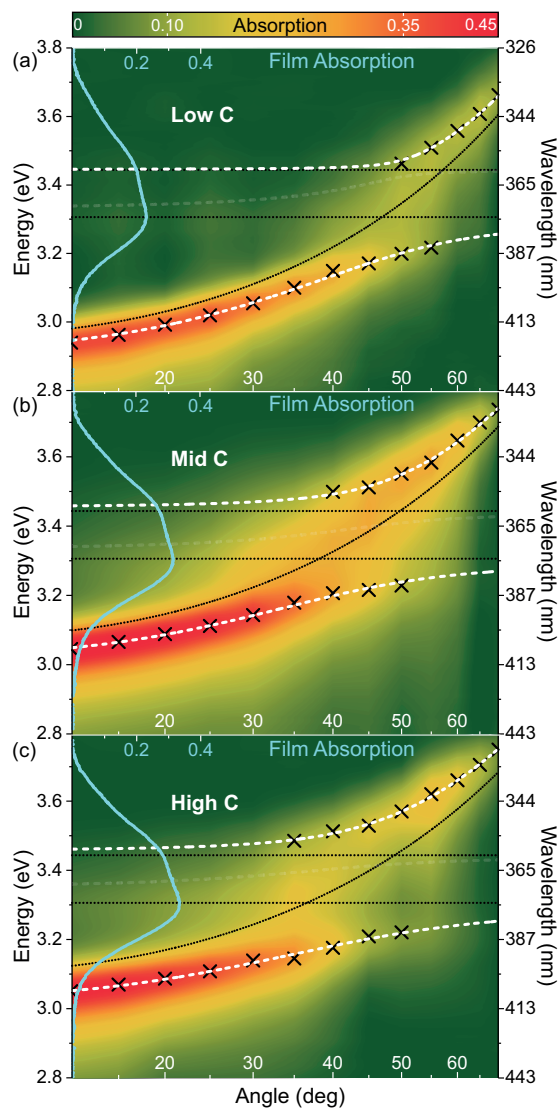


Fig. 3 Angle-resolved absorption (contour map) of cavities containing HBQ at (a) low, (b) mid, and (c) high concentration (C). The absorption spectra of the bare HBQ/PMMA films are shown in cyan on the left axis. The white dashed curves represent the upper, middle, and lower polariton branches obtained from fitting the coupled harmonic oscillator model (CHOM, SI, subsection 1.5) to the measured spectral positions (black crosses). The black dotted curves depict the dispersion of an undoped cavity (*i.e.*, containing only PMMA), while the horizontal black dotted lines show the molecular absorption peaks at 360 nm and 375 nm of HBQ.

films were also deposited on a 120 nm thick non-transparent Al mirror, *i.e.*, the structure was identical to the cavity geometry shown in Figure 1(a) except for the top mirror.

We measured angle-dependent steady-state absorption spectra of the cavities (SI, subsection 1.3), which are shown as contour maps in Figure 3. The anti-crossings between the bright polaritonic branches around $40^\circ - 50^\circ$ incident angle suggest that the cavities are in the strong coupling regime and that the first-order cavity mode is hybridized with the two lowest-energy electronic transitions in HBQ, namely the main peak at 375 nm and the (vibronic) shoulder at 360 nm (Figure 1(b)). These molecular transitions are shown as black dotted horizontal lines, together with the complete absorption spectrum of the HBQ/PMMA film in cyan. The energies of LP and UP, extracted from the angle-resolved experimental spectra, are shown as black crosses. By fitting the coupled harmonic oscillator model (CHOM, SI, subsection 1.5) to these data points, we obtain UP, LP and the middle polariton (MP) branches, shown as white dashed curves in Figure 3. The MP between the two molecular excitations was not used in the fitting, because it is weak and not well resolved in the measured spectra, and thus has a high uncertainty in its energy. In addition, the fit provides an estimate for the thickness of the cavities and thus their dispersion without molecules, which are plotted as dotted black curves.

From the CHOM fits we extracted the coupling strengths for both the main (g_1) and the shoulder (g_2) peaks, as well as the Hopfield coefficients for the polaritons, which are shown in Figure S6 (SI). Because of the uncertainty in the MP, we characterize the total coupling strength of the cavities as the sum of the two coupling strengths $g_{\text{tot}} = g_1 + g_2$. This sum depends only on the positions of the UP and LP, which are more clearly resolved, and is therefore free of possible errors due to the uncertainty in the MP position. The values of g_{tot} extracted from the CHOM fits, are listed in Table 1 for all cavities. The observed increase of the coupling with increasing molecular concentration and absorption is consistent with the theory and the existing literature [12–14].

To verify the main finding in our simulations that exciting any eigenstate of the molecule-cavity system leads to proton transfer and the formation of the photo-product, we recorded cavity

Table 1 Total coupling strengths (g_{tot}) for the HBQ cavities, as well as resonance angles (θ_{ex}) and wavelengths (λ_{ex}) used for the resonant excitation in Figure 5

| C | HBQ/PMMA | g_{tot} (meV) | θ_{ex} (deg) | λ_{ex} (nm) |
|------|----------|------------------------|----------------------------|----------------------------|
| Low | 0.5 | ~ 140 | 50 | 385 |
| Mid | 1 | ~ 170 | 40 | 386 |
| High | 1.6 | ~ 190 | 40 | 390 |

excitation spectra by measuring the intensity of the steady-state emission of the photo-product at 620 nm as a function of excitation wavelength and angle. The cavity system was excited with ~ 5 ns pulses at a 100 Hz repetition rate from a tunable laser source (SI, subsection 1.4). Because the fluorescence is emitted from uncoupled molecules without angular dependence, the emission was always collected at the sample surface normal (*i.e.*, at 0°).

The observation that the yield of the reaction in our simulations depends on the overlap between bright and dark states (Figure 2(c)) [18], suggests that the excitation spectra of the HBQ-cavity systems can be obtained by multiplying the probability to absorb a photon, determined by the absorption spectrum of the HBQ cavity, and the probability to undergo ES IPT, which is determined by the density of molecular states. Since the latter density of states can be directly obtained as the excitation spectrum of the bare molecules, we also measured the excitation spectra of the HBQ/PMMA films. Because in the films neither absorption nor fluorescence depend on angle, the films were excited at a fixed angle of 30° and probed at 0° .

In Figure 4 we show the absorption spectra (a,b) and excitation spectra (c,d) at various incident angles for the mid C (left column) and the high C (right column) HBQ/PMMA cavities, as well as the excitation spectra of films with the same HBQ/PMMA doping ratios as the cavities (c,d). The agreement between the measured cavity excitation spectra, on the one hand, and the spectra obtained by multiplying the cavity absorption spectra and film excitation spectra (Figure 4(e,f)), on the other hand, confirm the results from the simulations that the efficiency of the reaction is primarily controlled by the overlap between the bright polaritons and the molecular dark states. Likewise, dividing the excitation spectra of the HBQ/PMMA-cavity systems by the excitation spectra of the HBQ/PMMA films, yields

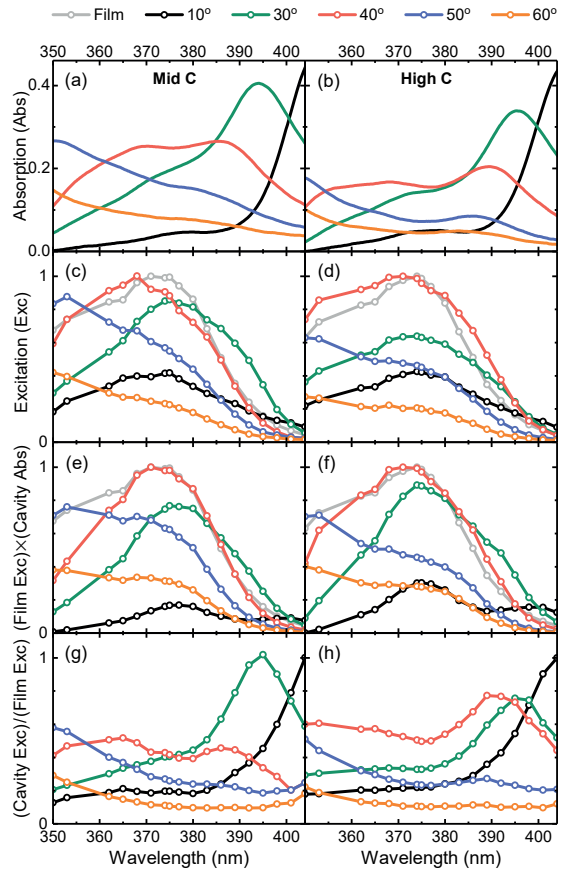


Fig. 4 Absorption spectra of (a) mid C and (b) high C HBQ/PMMA cavities at various excitation angles. Excitation spectra for emission at 620 nm of (c) mid C and (d) high C HBQ/PMMA cavities as a function of excitation angle. The excitation spectrum of the films are scaled down and shown in light grey. Scaling of the film excitation spectra was done to compensate for the absence of the top mirror and to facilitate comparison. The product of the cavity absorption spectrum and film excitation spectrum for (e) mid C and (f) high C cavities. The scaling of the film excitation spectra has no effect on the shape of these product spectra. Cavity excitation spectrum divided by the film excitation spectrum for (g) mid C and (h) high C HBQ/PMMA cavities. The curves are normalized so that the highest value within a group of spectra in each panel (c-h) is scaled to one, *i.e.*, the relative intensities of the curves are preserved to facilitate comparison.

the polaritonic absorption spectra (Figure 4(g,h)), affirming our conjecture.

Additional support is provided by the lower yield of the product emission at the largest angles where the overlap between the polaritonic absorption maxima and film excitation spectrum is smallest. Simulations, in which the cavity is

red-detuned to mimic excitation at such angles, confirm this (Table S2, SI). Thus, the results of both our MD simulations and excitation spectra measurements suggest that in the strong coupling regime the bright polaritonic states act as a gateway to access the reactive dark states and that the efficiency of this gateway, or "optical filter", depends on the overlap between the polaritonic absorption spectrum and the molecular density of states [18].

Our simulations furthermore suggest that within the strong coupling regime, increasing HBQ concentration enhances the overlap at the resonance angle (Figure 2(c)), and hence the efficiency of the ESIPT reaction. To verify also this finding, we measured the steady-state emission intensity at 620 nm from our HBQ cavities while exciting directly into the lower polariton at the resonance angle, *i.e.*, the angle at which the excitation energy of bare HBQ matches the dispersion of the cavity, and the energy gap between UP and LP is minimal. The excitation wavelength and angle are listed for each sample in Table 1. As reference, we also measured the emission from the HBQ/PMMA films with the excitation tuned to the absorption maximum ($\lambda_{ex} = 375$ nm). As in the measurements of the excitation spectra, the samples were excited with ~ 5 ns laser pulses at a 100 Hz repetition rate. Details of these experiments are provided as SI (section 1).

We quantify the emission yield (η) in these experiments as

$$\eta^{\text{exp.}} = I(\lambda_e)/A(\theta_{ex}, \lambda_{ex}) \quad (1)$$

with $I(\lambda_e)$ the intensity at the maximum of the emission band ($\lambda_e = 620$ nm) and $A(\theta_{ex}, \lambda_{ex})$ the absorption at the excitation wavelength λ_{ex} , and incident angle θ_{ex} . In Figure 5 we plot the yields as a function of the HBQ/PMMA doping ratio, which is correlated to both the number of HBQ molecules within the mode volume of the cavity and the coupling strength (Table 1). The films show almost constant emission yield with only a minor decrease at higher concentrations, presumably due to quenching [42]. Although the relative increase of the cavity emission yield is larger than in the simulations due to the overestimation of population transfer rates in small ensembles of molecules [38], the increase is in line with our calculations. Therefore, both simulations

and experiments suggest that increasing the coupling by adding more molecules, decreases the suppression by enhancing the rate at which population transfers from the lossy polariton modes into the reactive dark state manifold.

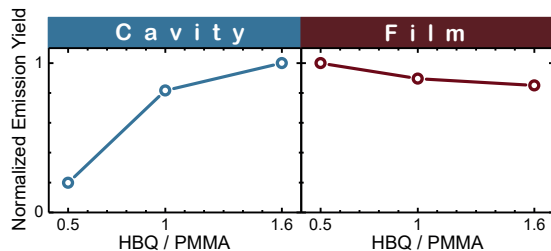


Fig. 5 Emission yield, $\eta^{\text{exp.}}$, in HBQ-cavity systems and films as a function of HBQ/PMMA doping ratio. The emission yield is normalized to the highest value.

Conclusion

In summary, we have investigated how strong light-matter coupling affects an ultra-fast photochemical reaction that occurs on the same timescale as the cavity lifetime. While the coupling leads to the characteristic Rabi splitting in the absorption spectra, the cavity mode excitations are smeared out over so many states that their contributions are too small to significantly perturb the potential energy surface of the electronic excited state and affect the reaction dynamics. While radiative decay from the polaritonic states in a lossy cavity can reduce the excited state population, the efficiency with which such losses suppress the reaction, depends on the competition with non-adiabatic population transfer into the molecular dark states. Since the rate of population transfer between bright and dark states is inversely proportional to the energy gap [38], the transfer is fastest when these states overlap, which for a Fabry-Pérot cavity depends on the number of molecules in the mode volume [18]. Thus, the extent of suppression can be controlled by tuning the cavity Q-factor and the concentration. Because the non-adiabatic population transfer between the dark and bright states is reversible [18], photo-chemical reactions with much slower rates than polariton emission, such as photo-oxidation [8], *cis-trans* photoisomerization [9], or intersystem crossing [7], can

be more easily suppressed via the radiative decay of the polaritonic states than the 15 fs ES IPT reaction in HBQ. In addition to providing additional non-reactive decay channels, cavities can also affect the excitation spectrum, and thereby selectively enhance excitation of states at the edges of the molecular excitation spectrum, where a system may be more reactive, as for example in Photoactive Yellow Protein [43]. We believe our findings, obtained by combining computations and experiments, provide important new insights into the possibilities of altering chemistry with strong coupling as well as the limitations.

Supplementary information. The Supporting Information contains: (i) Experimental methods with metallic Fabry-Pérot cavities containing HBQ molecules - Optical microcavity design; Sample fabrication; Steady-state reflection measurements; Steady-state fluorescence measurements; Coupled harmonic oscillator model fitting; (ii) Molecular Dynamics of HBQ in the collective strong coupling regime - Multi-scale Tavis-Cummings model; Non-adiabatic molecular dynamics simulations; Simulation details; Estimation of losses; Cavity absorption spectra; Overlap between molecular polaritonic states; Additional MD results; Reference Potential Energy Surfaces of HBQ molecule; and results of MD simulations in the ultra-strong coupling regime.

Acknowledgments. We thank Satu Mustalahti, Ossi Hakamaa, Mikael Kautto, Oskar Celik and Ruth Tichauer for their assistance in the initial stages of the project. We thank the Academy of Finland for funding, which made this work possible, and the Center for Scientific Computing (CSC-IT Center for Science) for generous computational resources.

Declarations

- Funding: This work was supported by the Academy of Finland via Research projects (Grants No. 323996 and 332743 to GG No. 323995, 289947 and 350797 to JJT) and University profiling funding (Profi4).
- Conflict of interest/Competing interests: The authors declare no competing financial interests.
- Consent for publication: All authors consent to publication

- Availability of data and materials: All simulation data, including simulations models, input files, trajectories and structures, analysis scripts and programs, including raw data, are available for download from Fairdata IDA. All experimental data is stored and packed up within University of Jyväskylä IT-services, and is available for anyone on reasonable request to the corresponding author.
- Code availability: The GROMACS-4.5.3 fork with the multi-scale Tavis-Cummings model is available for download from: <https://github.com/rhti/gromacs qed>
- Authors' contributions: GG and JJT conceptualized the project. LD and VT developed the optical measurement setup. AD, VT, LD, NM and HAQ carried out all the measurements. AD, VT and HAQ fabricated the samples. DM and GG performed the simulations. All authors contributed to the interpretation of the data. The manuscript was written by GG, JJT and AD with input from all authors. All authors reviewed, commented on the manuscript and accepted the final version.

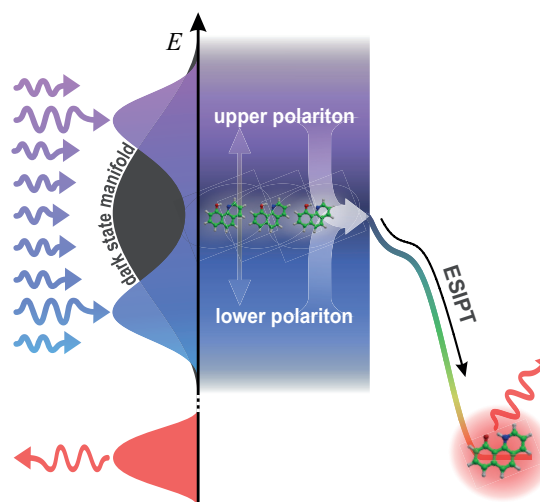


TABLE OF CONTENT (TOC) GRAPHICS

References

- [1] Hutchison, J. A., Schwartz, T., Genet, C., Devaux, E. & Ebbesen, T. W. Modifying chemical landscapes by coupling to vacuum

- fields. *Angew. Chem. Int. Ed.* **51**, 1592–1596 (2012) .
- [2] Thomas, A. *et al.* Ground-state chemical reactivity under vibrational coupling to the vacuum electromagnetic field. *Angew. Chem. Int. Ed.* **55**, 11462–11466 (2016) .
- [3] Thomas, A. *et al.* Tilting a ground-state reactivity landscape by vibrational strong coupling. *Science* **363**, 615–619 (2019) .
- [4] Vergauwe, R. M. A. *et al.* Modification of enzyme activity by vibrational strong coupling of water. *Angew. Chem. Int. Ed.* **58**, 15324–15328 (2019) .
- [5] Lather, J., Bhatt, P., Thomas, A., Ebbesen, T. W. & George, J. Cavity catalysis by cooperative vibrational strong coupling of reactant and solvent molecules. *Angew. Chem. Int. Ed.* **58**, 10635–10638 (2019) .
- [6] Yu, Y., Mallick, S., Wang, M. & Börjesson, K. Barrier-free reverse-intersystem crossing in organic molecules by strong light-matter coupling. *Nat Commun* **12**, 3255 (2021) .
- [7] Stranius, K., Herzog, M. & Börjesson, K. Selective manipulation of electronically excited states through strong light-matter interactions. *Nat. Comm.* **9**, 2273 (2018) .
- [8] Munkhbat, B., Wersäll, M., Baranov, D. G., Antosiewicz, T. J. & Shegai, T. Suppression of photo-oxidation of organic chromophores by strong coupling to plasmonic nanoantennas. *Sci. Adv.* **4**, eaas9552 (2018) .
- [9] Mony, J., Climent, C., Anne Ugleholdt Petersen, J. F., Kasper Moth-Poulsen & Börjesson, K. Photoisomerization efficiency of a solar thermal fuel in the strong coupling regime. *Adv. Funct. Mater.* **31**, 2010737 (2021) .
- [10] Tropf, L. *et al.* Influence of optical material properties on strong coupling in organic semiconductor based microcavities. *Appl. Phys. Lett.* **110**, 153302 (2017) .
- [11] Agranovich, V., Benisty, H. & Weisbuch, C. Organic and inorganic quantum wells in a microcavity: Frenkel-wannier-mott excitons hybridization and energy transformation. *Solid State Communications* **102**, 631–636 (1997) .
- [12] Lidzey, D. G. *et al.* Strong exciton-photon coupling in an organic semiconductor microcavity. *Nature* **395**, 53–55 (1998) .
- [13] Törmä, P. & Barnes, W. L. Strong coupling between surface plasmon polaritons and emitters: a review. *Rep. Prog. Phys.* **78**, 013901 (2015) .
- [14] Rider, M. S. & Barnes, W. L. Something from nothing: linking molecules with virtual light. *Contemporary Physics* **62** (4), 217–232 (2022) .
- [15] Galego, J., Garcia-Vidal, F. J. & Feist, J. Suppressing photochemical reactions with quantized light fields. *Nat. Comm.* **7**, 13841 (2016) .
- [16] Garcia-Vidal, F. J., Ciuti, C. & Ebbesen, T. W. Manipulating matter by strong coupling to vacuum fields. *Science* **373**, eabd0336 (2021) .
- [17] Agranovich, V. M., Litinskaia, M. & Lidzey, D. G. Cavity polaritons in microcavities containing disordered organic semiconductors. *Phys. Rev. B* **67**, 085311 (2003) .
- [18] Groenhof, G., Climent, C., Feist, J., Morozov, D. & Toppari, J. J. Tracking polariton relaxation with multiscale molecular dynamics simulations. *J. Chem. Phys. Lett.* **10**, 5476–5483 (2019) .
- [19] Kim, C. H. & Joo, T. Coherent excited state intramolecular proton transfer probed by time-resolved fluorescence. *Phys. Chem. Chem. Phys.* **11**, 10266–10269 (2009) .
- [20] Lee, J., Kim, C. H. & Joo, T. Active role of proton in excited state intramolecular proton transfer reaction. *J. Phys. Chem. A* **117**, 1400–1405 (2013) .

- [21] Hirata, S. & Head-Gordon, M. Time-dependent density functional theory within the tamm-dancoff approximation. *Chem. Phys. Lett.* **314**, 291–299 (1999) .
- [22] Yanai, T., Tew, D. P. & Handy, N. C. A new hybrid exchange-correlation functional using the coulomb-attenuating method (cam-b3lyp). *Chem. Phys. Lett.* **393**, 51–57 (2004) .
- [23] Becke, A. D. A new mixing of Hartree-Fock and local density-functional theories. *J. Chem. Phys.* **98**, 1372 (1993) .
- [24] Dunning, T. H. Basis functions for use in molecular calculations. i. contractions of (9s5p) atomic basis sets for the first-row atoms. *J. Chem. Phys.* **53**, 2823–2833 (1970) .
- [25] Hohenberg, P. & Kohn, W. Inhomogeneous electron gas. *Phys. Rev.* **136**, 864–871 (1964) .
- [26] Runge, E. & Gross, E. K. U. Density-functional theory for time-dependent systems. *Phys. Rev. Lett.* **52**, 997–1000 (1984) .
- [27] Ditchfield, R., Hehre, W. J. & Pople, J. A. Self-consistent molecular-orbital methods. ix. an extended gaussian-type basis for molecular-orbital studies of organic molecules. *J. Chem. Phys.* **54**, 724–728 (1971) .
- [28] Horta, B. A. C. *et al.* A gromos-compatible force field for small organic molecules in the condensed phase: The 2016h66 parameter set. *J. Chem. Theory. Comput.* **12**, 3825–3850 (2016) .
- [29] Sokolovskii, I., Tichauer, R. H., Morozov, D., Feist, J. & Groenhof, G. Enhanced excitation energy transfer under strong light-matter coupling: Insights from multi-scale molecular dynamics simulations. *arXiv* 2209.07309 (2022) .
- [30] Staroverov, V. N., Scuseria, G. E., Tao, J. & Perdew, J. P. Comparative assessment of a new nonempirical density functional: Molecules and hydrogen-bonded complexes. *The Journal of chemical physics* **119** (23), 12129–12137 (2003) .
- [31] Picconi, D. Nonadiabatic quantum dynamics of the coherent excited state intramolecular proton transfer of 10-hydroxybenzo [h] quinoline. *Photochemical & Photobiological Sciences* **20**, 1455–1473 (2021) .
- [32] Lidzey, D., Bradley, D., Armitage, A., Walker, S. & Skolnick, M. Photon-mediated hybridization of frenkel excitons in organic semiconductor microcavities. *Science* **288**, 1620–1623 (2000) .
- [33] Houdré, R., Stanley, R. P. & Ilegems, M. Vacuum-field rabi splitting in the presence of inhomogeneous broadening: Resolution of a homogeneous linewidth in an inhomogeneously broadened system. *Phys. Rev. A* **53**, 2711–2715 (1996) .
- [34] Luk, H.-L., Feist, J., Toppari, J. J. & Groenhof, G. Multiscale molecular dynamics simulations of polaritonic chemistry. *J. Chem. Theory Comput.* **13**, 4324–4335 (2017) .
- [35] Tichauer, R. H., Feist, J. & Groenhof, G. Multiscale simulations of molecular polaritons: the effect of multiple cavity modes on polariton relaxation. *J. Chem. Phys.* **154**, 104112 (2021) .
- [36] Vendrell, O. Collective jahn-teller interactions through light-matter coupling in a cavity. *Phys. Rev. Lett.* **121**, 253001 (2018) .
- [37] Ulusoy, I. S., Gomez, J. A. & Vendrell, O. Modifying the nonradiative decay dynamics through conical intersections via collective coupling to a cavity mode. *J. Phys. Chem. A* **123**, 8832–8844 (2019) .
- [38] Tichauer, R. H., Morozov, D., Sokolovskii, I., Toppari, J. J. & Groenhof, G. Identifying vibrations that control non-adiabatic relaxation of polaritons in strongly coupled molecule-cavity systems. *J. Phys. Chem. Lett.* **13**, 6259 (2022) .

- [39] Flick, J., Ruggenthaler, M., Appel, H. & Rubio, A. Atoms and molecules in cavities: From weak to strong coupling in qed chemistry. *Proc. Natl. Acad. Sci. USA* **114**, 3026–3034 (2017) .
- [40] Dutta, A., Tiainen, V. & Toppari, J. J. Optimizing geometry of low-q all-metal fabry-pérot microcavity for fluorescence spectroscopy. *IOP SciNotes* **2**, 015205 (2021) .
- [41] Purcell, E. M. Spontaneous emission probabilities at radio frequencies. *Phys. Rev.* **69**, 681 (1946) .
- [42] Kwon, J. E. & Park, S. Y. Advanced organic optoelectronic materials: Harnessing excited-state intramolecular proton transfer (esipt) process. *Advanced Materials* **23** (32), 3615–3642 (2011) .
- [43] Mix, L. T. *et al.* Excitation-wavelength-dependent photocycle initiation dynamics resolve heterogeneity in the photoactive yellow protein from halorhodospira halophila. *Biochemistry* **57**, 1733–1747 (2017) .

Supplementary information for ultra-fast photochemistry in the strong light-matter coupling regime

Arpan Dutta^{1,4}, Ville Tiainen¹, Luís Duarte^{1,3}, Nemanja Markešević¹, Dmitry Morozov², Hassan A. Qureshi^{1,4}, Gerrit Groenhof^{2,*}, and J. Jussi Toppari^{1,*}

¹*Nanoscience Center and Department of Physics, University of Jyväskylä, P.O. Box 35, FI-40014, Finland*

²*Nanoscience Center and Department of Chemistry, University of Jyväskylä, P.O. Box 35, FI-40014, Finland*

³*Present address: Department of Chemistry, University of Helsinki, P.O. Box 55, FI-00014, Finland*

⁴*Present address: Department of Mechanical and Materials Engineering, University of Turku, FI-20014, Finland*

**Correspondence: j.jussi.toppari@jyu.fi gerrit.x.groenhof@jyu.fi*

Contents

| | | |
|----------|--|-----------|
| 1 | Experiments with metallic Fabry-Pérot cavities containing HBQ molecules | 2 |
| 1.1 | Optical microcavity design | 2 |
| 1.2 | Sample fabrication | 3 |
| 1.3 | Steady-state reflection measurements | 4 |
| 1.4 | Steady-state fluorescence measurements | 6 |
| 1.5 | Coupled harmonic oscillator model fitting | 7 |
| 2 | Molecular Dynamics of HBQ in the collective strong coupling regime | 9 |
| 2.1 | Multi-scale Tavis-Cummings model | 9 |
| 2.2 | Non-adiabatic molecular dynamics simulations | 11 |
| 2.3 | Simulation details | 12 |
| 2.4 | Estimation of radiative losses | 13 |
| 2.5 | Cavity absorption spectra | 13 |
| 2.6 | Overlap between molecular polaritonic states | 14 |
| 2.7 | Additional MD results | 15 |
| 2.7.1 | ESIPT in "bare" HBQ | 15 |
| 2.7.2 | ESIPT in HBQ under strong light-matter coupling | 15 |
| 2.8 | Reference Potential Energy Surfaces of HBQ molecule | 18 |
| 2.9 | Simulations in Ultra-Strong Coupling Regime | 18 |
| | References | 19 |

1 Experiments with metallic Fabry-Pérot cavities containing HBQ molecules

1.1 Optical microcavity design

Our molecular films used as a reference consist of a 100 nm thick polymer layer on top of a 120 nm thick aluminum (Al) mirror on a glass substrate. The polymer layer is a polymethyl methacrylate (PMMA) matrix doped with 10-hydroxybenzo[h]quinoline (HBQ) molecules, purchased from TCI Europe N.V. (Belgium, CAS Number: 33155-90-7, Molecular Weight: 195.22 g/mol) and used as received. In the case of cavities, we added a 20 nm Al mirror on top of the film. This yields a low-Q ($Q \approx 17$) all-metal Fabry-Pérot microcavity with an asymmetric geometry having a thin/leaky mirror (20 nm Al) on top and a thick/non-transparent (120 nm Al) mirror at the bottom. The structures of the HBQ film and cavity are schematically shown in Fig. S1.

We optimized our cavity geometry using transfer-matrix method (TMM) [S1, S2] and finite-difference time-domain (FDTD) [S3, S4] simulations. In TMM calculations, the glass substrate (SiO_2) and the surrounding medium (air, refractive index 1.00) were considered as semi-infinite. The excitation light was s-polarized and the refractive index of PMMA was 1.50. The material models for Al and SiO_2 were taken from the existing literature [S5]. In 2D-FDTD computations, the simulations were carried out on xz -plane considering the cavity and the film thickness extending in z -direction while in x - and y -directions, the structures are uniform. Perfectly matched layers (PML) were used in all boundaries and the material models were the same that were used for the TMM. The normal incidence of light, *i.e.*, a plane wave linearly polarized in x/y direction was used as the excitation in the simulations.

We chose a reflective (non-transmissive) cavity since that can provide an efficient light confinement combined with a quality detection of molecular fluorescence [S6]. The cavity thickness was set to 100 nm to tune the first order cavity mode with the HBQ absorption (375 nm) at 0° excitation. However, considering the fabrication tolerance, the actual cavity thickness was $\sim 100 - 120$ nm resulting in the resonant tuning around 40° due to the cavity dispersion.

The TMM calculated absorption of the undoped cavity and film with pure PMMA as a polymer layer, are reported in Fig. S2(a) for 40° excitation angle. The TMM computed dispersion of the undoped cavity is depicted in Fig. S2(b). The 2D-FDTD simulated spatial distribution of the electric-field inside the undoped cavity and film are depicted in Fig. S2(c) and Fig. S2(d), respectively, at resonance (375 nm) for the normal incidence of light. Unlike for the cavity, no field-confinement was found in the film.



Fig. S1. Schematics of HBQ film and cavity.

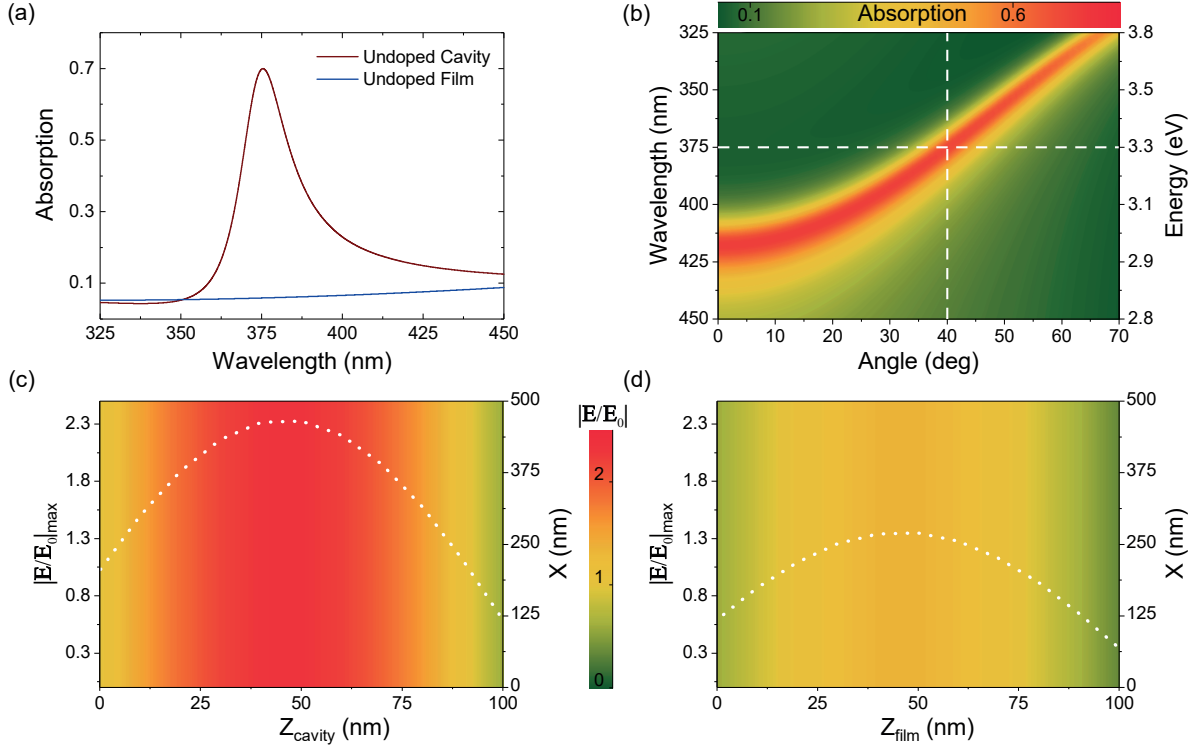


Fig. S2. (a) Absorption of the undoped cavity and film at 40° excitation angle. (b) Dispersion of the undoped cavity where the horizontal and vertical white dashed lines show the HBQ absorption (375 nm) and the resonant angle at which the first order cavity mode is at 375 nm, respectively. Spatial distribution of the electric field at 375 nm inside the undoped (c) cavity and (d) film shown as a color contour plot. Since the field is homogeneous in x -direction, the white dotted curves with their scale at left axis show the spatial profile of the electric field inside the corresponding structures.

1.2 Sample fabrication

HBQ films and cavities were fabricated on top of BK7 glass substrates (Präzisions Glas and Optik GmbH, dimension: $15 \times 15 \text{ mm}^2$, thickness: 1 mm). The substrates were cleaned with heated acetone and sonication in isopropanol followed by drying by nitrogen flow. The bottom mirrors for the films and cavities were made by evaporating 120 nm of Al on top of the cleaned substrates in ultra high vacuum (e-beam evaporation with deposition rate 0.1 nm/s under $10^{-8} - 10^{-9}$ mbar pressure). The yellow crystalline HBQ powder (TCI Europe N.V.) was dissolved in chlorobenzene at room temperature to make a 8 wt% stock solution of HBQ. The spin solutions were prepared by mixing the required amount of 2 wt% solution of PMMA in chlorobenzene (950PMMA C2, Microchem) with the 8 wt% stock solution of HBQ to attain the target concentrations, i.e., HBQ:PMMA ratios 0.5 (low), 1 (mid), and 1.6 (high). The HBQ:PMMA thin films were made by spin-coating the bottom mirrors with the spin solution at an optimal spin speed to achieve $\sim 100 - 120$ nm film thickness. The obtained films were baked for 15 min on a hot plate at 65°C . The temperature was lowered from the common PMMA baking temperature to avoid excess evaporation of HBQ. The

thickness characterization was performed using the KLA Tencor P-15 profilometer. For each concentration, two identical HBQ:PMMA films were prepared - one for cavity and one for corresponding film. For cavities, the top mirrors were made by evaporating 20 nm of Al on top of the HBQ:PMMA films under the same evaporation conditions as for the bottom mirrors. The undoped cavity was made using the similar procedure except the HBQ doping.

1.3 Steady-state reflection measurements

The reflection measurements on the fabricated samples were carried out using a custom made optical setup shown schematically in Fig. S3. The samples were illuminated by a deuterium lamp (Cathodeon, model C710). The pseudo-collimated excitation light passed two pinholes P_1 and P_2 having diameters of ~ 6 mm and ~ 3 mm, respectively, before hitting the sample. The samples were placed at the rotation axis of a goniometric sample stage facing the excitation light with the axis of the prism polarizer along with the rotation axis, i.e., vertical or s-polarization. The excitation (θ) and detection (ϕ) angles were adjusted manually by rotating the goniometric stage and the rotational arm, respectively. For reflection measurements eventually $\theta = \phi$ and θ ranges from 10° to 70° with an increment of 5° . The reflection spectra of the samples were collected using a fiber coupler (ThorLabs F220SMA-A, $f = 10.90$ mm, $NA = 0.25$) connected to an optical fiber (ThorLabs, model: M112L02, 2 m, $200 \mu\text{m}$ core, $NA = 0.22$, SMA). The collected light was guided to a spectrometer consisting of a monochromator (Acton monochromator SP2150i, slit size: $100 \mu\text{m}$, grating: 600 grooves/mm blazed at 500 nm) and CCD (Andor InstaSpec IV CCD DU420-OE, pixel size: $16 \times 16 \mu\text{m}^2$). The obtained spectra were recorded in ASCII format.

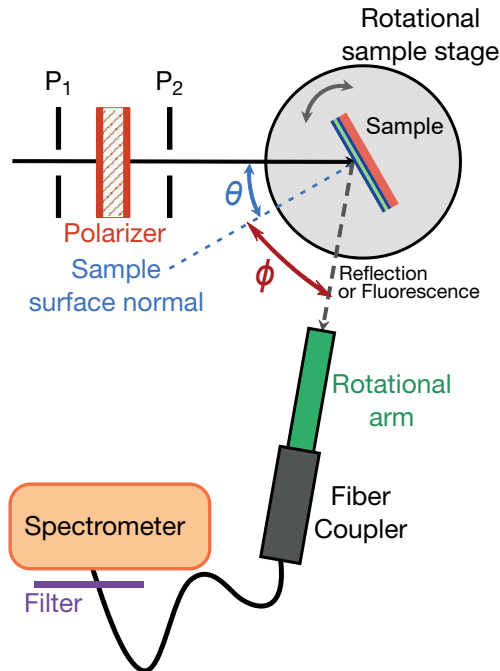


Fig. S3. Schematic of the experimental set-up.

The angle-resolved reflection spectra $R(\theta, \lambda)$ were calculated as $R(\theta, \lambda) = I(\theta, \lambda)/I_0(\lambda)$, where $I(\theta, \lambda)$ is the collected signal (in counts) reflected from the sample while $I_0(\lambda)$ is the lamp spectrum. Since our samples are non-transmissive, *i.e.*, $T(\theta, \lambda) = 0$, the absorption can be calculated simply as $1 - R(\theta, \lambda)$. First, we estimated the scattered part of the excitation light that never reached to the HBQ molecules embedded in our samples due to scattering from polymer/top mirror using a baseline correction. The baseline-correction is done by interpolating the baseline in between the known baseline points in MATLAB [S7]. The interpolation was done by using a MATLAB function *interp1* [S8] along with the piecewise cubic Hermite polynomial method implemented through the MATLAB function *pchip* [S9]. The trend in baseline was similar in almost all cases, *i.e.*, raising baseline towards blue. This is exactly something one would expect from a nonspecular Rayleigh scattering from a rough sample surface, which is the main reason for the non-zero baseline. It should be noted that many interpolation methods as well as parameters were tested, and all of them yielded the same trend as reported in the main text.

Finally, the angle-dependent absorption spectra $A(\theta, \lambda)$ were considered as

$$A(\theta, \lambda) = 1 - \frac{I(\theta, \lambda)}{I_0(\lambda) - [I_0(\lambda) \times BL(\lambda)]}$$

where $BL(\lambda)$ is the estimated baseline.

The measured dispersion of a fabricated undoped cavity is reported in Fig. S4 which is consistent with our simulated dispersion shown in Fig. S2(b) except for the fact that the fabricated cavity thickness is ~ 118 nm resulting in the resonant tuning of the first order cavity mode with 375 nm at 50° , *i.e.*, 10° detuning from the simulated case due to a higher thickness.

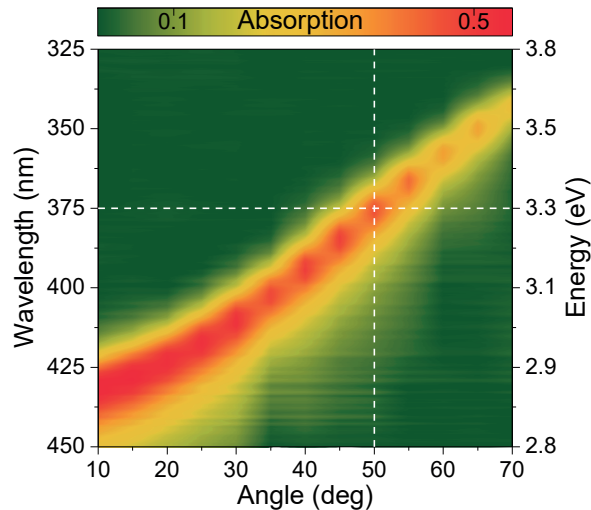


Fig. S4. Measured dispersion of a fabricated undoped cavity where the horizontal and vertical white dashed lines show the HBQ absorption (375 nm) and the resonant angle at which the first order cavity mode is at 375 nm, respectively.

The angle-dependent absorption spectra after baseline correction for low, mid, and high concentration (C) cavities are illustrated in Figs. S5(a), S5(c), and Fig. S5(e), respectively. The same without baseline correction for low, mid, and high C cavities are presented in Figs. S5(b), S5(d), and Fig. S5(f), respectively. From Fig. S5 it is clear that the resonant condition in all cavities appears close to 40° angle.

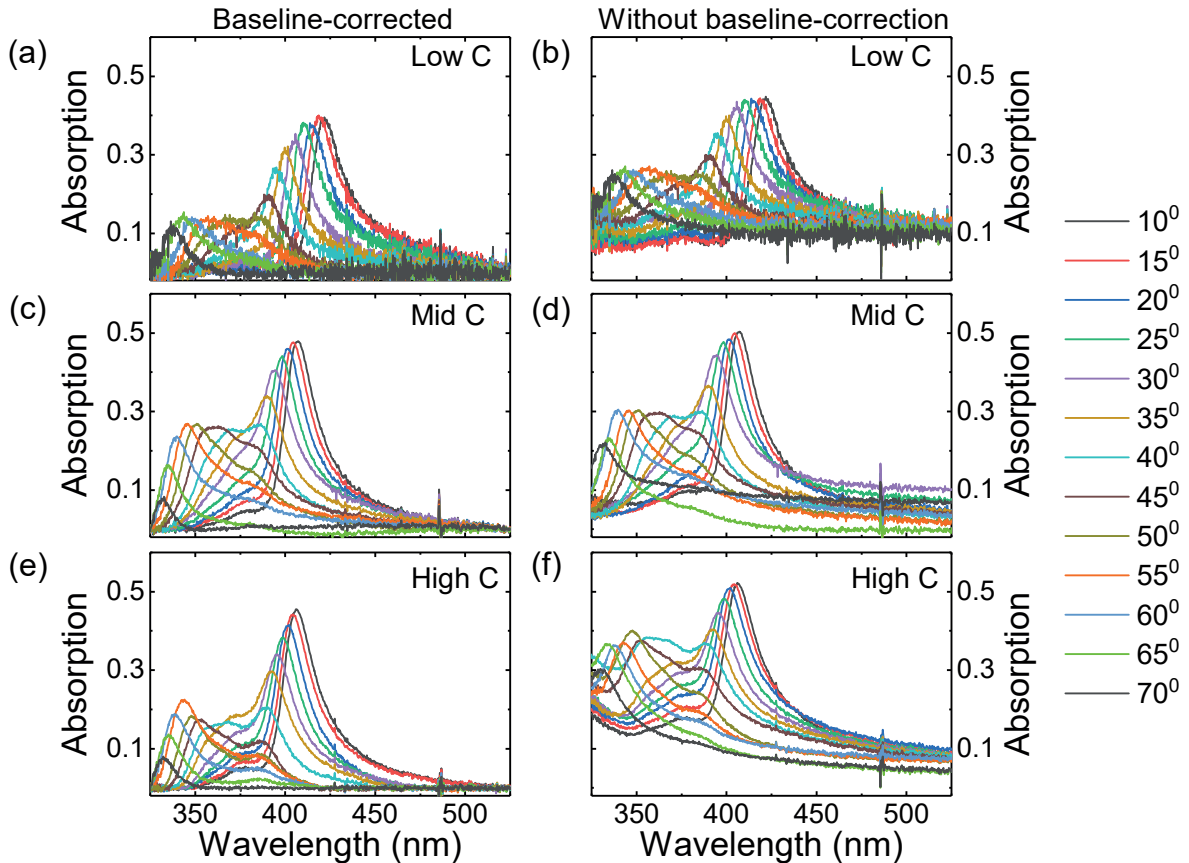


Fig. S5. Angle-dependent absorption spectra for (a) low, (c) mid, and (e) high C cavities after baseline correction. The same for (b) low, (d) mid, and (f) high C cavities without baseline correction.

1.4 Steady-state fluorescence measurements

In fluorescence studies, the fabricated samples were excited by a tunable diode pumped pulse laser (EKSPLA OPO NT230 series, model: NT231-100-SH/FH-OPO-SH, pulse width: 3 - 6 ns, repetition rate: 100 Hz) where the excitation beam was pseudo-collimated before reaching the samples. The sample positioning on the rotational stage, the polarization axis, the adjustment of the excitation/detection angles, and the pinhole sizes were identical with the reflection measurements. For cavities, five excitation angles were considered, *i.e.*, θ as 10° , 30° , 40° , 50° and 60° . The detection angle ϕ was set to 0° for all θ except for $\theta = 10^\circ$ where ϕ was set to 30° to avoid the reflection of the incident laser light at the detector. For

films, θ was 30° with ϕ as 0° since there is no dispersion. The sample emission was collected using the same fiber coupler used in the reflectivity measurements connected to a fiber optic bundle (ThorLabs, model: BFL200HS02, 250 to 1200 nm, $7 \times 200 \mu\text{m}$ core fibers, high-OH, SMA). The collected light was guided to a monochromator (Acton monochromator SP2150i, slit size: $750 \mu\text{m}$, grating: 300 grooves/mm blazed at 750 nm) – CCD (Andor IVAC CCD DR-324B-FI, pixel size: $16 \times 16 \mu\text{m}^2$) combination and recorded in ASCII format. The filter before the spectrometer shown in Fig. S3 (Semrock EdgeBasic, BLP01-488R-25 long pass filter, transparency: $\geq 488 \text{ nm}$) was only used in the fluorescence measurements to block the excitation light during emission collection. To take into account the typical fluctuations in the pulse energy of our excitation laser, we recorded the energy of each excitation pulse using a sensor (Ophir PD10-C) and used the sum of energies of all excitation pulses to correct the collected emission intensity (in counts).

The energy-corrected emission spectra $I_E(\lambda)$ in counts/mJ were calculated as $I_E(\lambda) = I_C(\lambda) / \sum E_P$ where $I_C(\lambda)$ is the collected emission in counts and $\sum E_P$ represents the sum of energies of all excitation pulses in mJ during the detection/integration time. The excitation spectra were constructed by extracting the energy-corrected emission intensities at 620 nm, i.e., $I_E(\lambda = 620 \text{ nm})$ as a function of excitation wavelengths (λ_{ex}) where λ_{ex} was varied from 350 - 400 nm with an increment of 3 nm.

1.5 Coupled harmonic oscillator model fitting

The probabilities of polariton formation in a strongly-coupled cavity-molecular system are given by the Hopfield coefficients [S10]. In order to extract those coefficients from the experimental data, the coupled harmonic oscillator model (CHOM) [S11, S12] was fitted to the experimental polariton dispersions. In the case of two excitons the coupling is described by a 3×3 matrix of regular James-Cummings Hamiltonian

$$\begin{pmatrix} E_c(k_{\parallel}) & g_1 & g_2 \\ g_1 & E_1 & 0 \\ g_2 & 0 & E_2 \end{pmatrix} \begin{pmatrix} \alpha \\ \beta \\ \gamma \end{pmatrix} = E \begin{pmatrix} \alpha \\ \beta \\ \gamma \end{pmatrix}, \quad (\text{S.1})$$

where g_1 and g_2 are the coupling strengths related to the molecular excitation energies, the molecular exciton at $E_1 = 3.30 \text{ eV}$ (375 nm) and the vibronic shoulder at $E_2 = 3.44 \text{ eV}$ (360 nm), respectively. In Eq. (S.1), α , β , and γ are the Hopfield coefficients and $E_c(k_{\parallel})$ is the cavity energy given by

$$E_c(k_{\parallel}) = \frac{\hbar c}{n_c} \sqrt{\left(\frac{\pi}{L}\right)^2 + k_{\parallel}^2}, \quad (\text{S.2})$$

where n_c is the refractive index of the cavity medium and L is the cavity thickness. The in-plane wave vector k_{\parallel} is given by

$$k_{\parallel} = \frac{2\pi}{\lambda} \sin \theta, \quad (\text{S.3})$$

where λ is the wavelength and θ is the angle of incidence relative to the cavity surface normal [S11, S12].

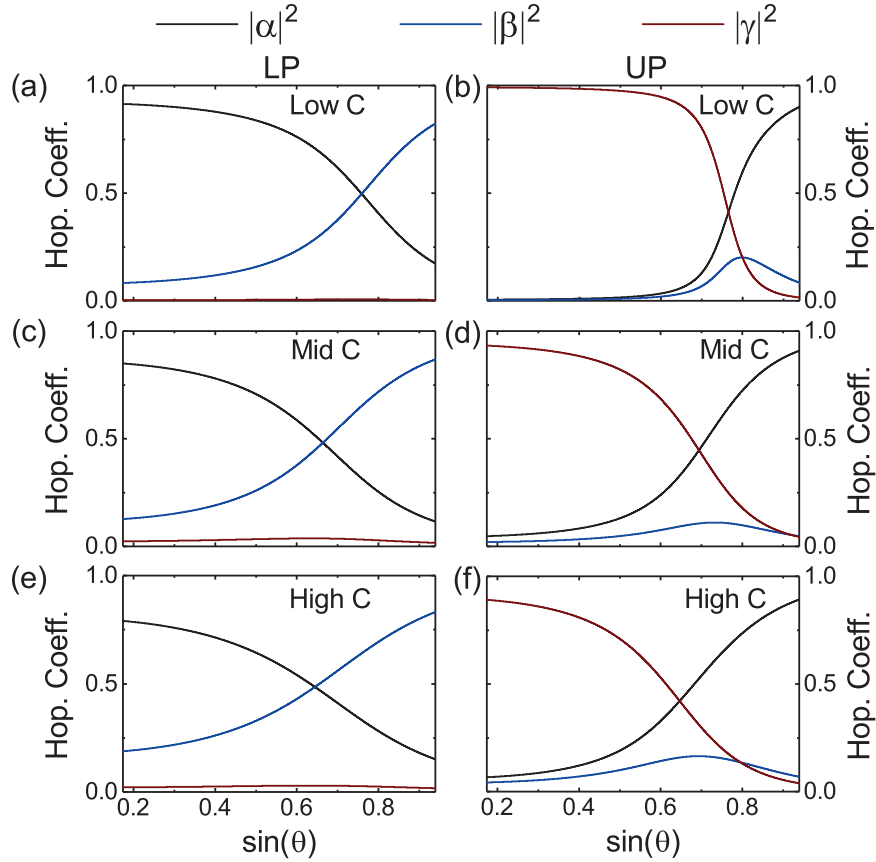


Fig. S6. Hopfield coefficients of the lower polariton (LP) branch for (a) low, (c) mid, and (e) high concentration (C) HBQ cavities. Hopfield coefficients of the upper polariton (UP) branch for (b) low, (d) mid, and (f) high C HBQ cavities. In (a)-(f), the relative coefficients are calculated from the CHOM fitting.

A custom made MATLAB script was used to fit Eq. (S.1) to the experimental data. To obtain the fit parameters g_1 , g_2 , n_c and L were varied until the difference between experimental polariton energies and the ones obtained from Eq. (S.1) was minimized. The method of least squares was used to define the minimum. Experimental polariton energies were extracted from the measured cavity absorption maxima, by fitting a suitable peak functions corresponding to the three polaritons, and the corresponding incident angles were converted to k_{\parallel} for the purposes of fitting. The fitted dispersion curves for all samples are shown together with the measured data in Fig. 2 of the main article, and the corresponding Hopfield coefficients are presented in Fig. S6.

2 Molecular Dynamics of HBQ in the collective strong coupling regime

2.1 Multi-scale Tavis-Cummings model

To model the dynamics of N HBQ molecules strongly coupled to the confined light mode of a single-mode cavity, we extended the Tavis-Cummings model [S13, S14] to account for the molecular degrees of freedom [S15]:

$$\begin{aligned} \hat{H}^{\text{TC}} = & \sum_j^N h\nu_j(\mathbf{R}_j) \hat{\sigma}_j^+ \hat{\sigma}_j^- + \hbar\omega_{\text{cav}} \hat{a}^\dagger \hat{a} + \\ & \sum_j^N \hbar g_j (\hat{\sigma}_j^+ \hat{a} + \hat{\sigma}_j^- \hat{a}^\dagger) + \\ & \sum_i^N V_{S_0}^{\text{mol}}(\mathbf{R}_i) \end{aligned} \quad (\text{S.4})$$

Here, $\hat{\sigma}_j^+$ ($\hat{\sigma}_j^-$) is the operator that excites (de-excites) HBQ molecule j from the electronic ground (excited) state $|S_0^j(\mathbf{R}_j)\rangle$ ($|S_1^j(\mathbf{R}_j)\rangle$) into the electronic excited (ground) state $|S_1^j(\mathbf{R}_j)\rangle$ ($|S_0^j(\mathbf{R}_j)\rangle$); \mathbf{R}_j is the vector of the Cartesian coordinates of all atoms in HBQ molecule j ; \hat{a} (\hat{a}^\dagger) is the annihilation (creation) operator of an excitation in the cavity mode; $h\nu_j(\mathbf{R}_j)$ is the excitation energy of molecule j , defined as:

$$h\nu_j(\mathbf{R}_j) = V_{S_1}^{\text{mol}}(\mathbf{R}_j) - V_{S_0}^{\text{mol}}(\mathbf{R}_j) \quad (\text{S.5})$$

with $V_{S_0}^{\text{mol}}(\mathbf{R}_j)$ and $V_{S_1}^{\text{mol}}(\mathbf{R}_j)$ the adiabatic potential energy surfaces of molecule j in the electronic ground (S_0) and excited (S_1) state, respectively.

The last term in Equation S.4 is the total potential energy of the system in the absolute ground state (*i.e.*, with no excitations in neither the molecules nor the cavity modes), defined as the sum of the ground-state potential energies of all molecules in the cavity. The $V_{S_0}^{\text{mol}}(\mathbf{R}_j)$ and $V_{S_1}^{\text{mol}}(\mathbf{R}_j)$ adiabatic potential energy surfaces are modelled at the QM/MM level of theory [S16, S17].

The third term in Equation S.4 models the light-matter interaction within the dipolar approximation through g_j :

$$g_j = -\boldsymbol{\mu}_j^{\text{TDM}}(\mathbf{R}_j) \cdot \mathbf{u}_{\text{cav}} \sqrt{\frac{\hbar\omega_{\text{cav}}}{2\epsilon_0 V_{\text{cav}}}} \quad (\text{S.6})$$

where $\boldsymbol{\mu}_j^{\text{TDM}}(\mathbf{R}_j)$ is the transition dipole moment of HBQ molecule j that depends on the molecular geometry (\mathbf{R}_j); \mathbf{u}_{cav} the unit vector in the direction of the electric component of the cavity vacuum field (*i.e.*, $|\mathbf{E}| = \sqrt{\hbar\omega_{\text{cav}}(k_z)/2\epsilon_0 V_{\text{cav}}}$); ϵ_0 the vacuum permittivity; and V_{cav} the cavity mode volume.

The matrix elements of the multi-scale Tavis-Cummings Hamiltonian are evaluated in the product basis of adiabatic molecular states times cavity mode excitation:

$$\begin{aligned} |\phi_j\rangle &= \hat{\sigma}_j^+ |S_0^1 S_0^2 \dots S_0^{N-1} S_0^N\rangle \otimes |0\rangle \\ &= \hat{\sigma}_j^+ |\Pi_i^N S_0^i\rangle \otimes |0\rangle \\ &= \hat{\sigma}_j^+ |\phi_0\rangle \end{aligned} \quad (\text{S.7})$$

for $1 \leq j \leq N$, and

$$\begin{aligned}
|\phi_{N+1}\rangle &= \hat{a}^\dagger |S_0^1 S_0^2 \dots S_0^{N-1} S_0^N\rangle \otimes |0\rangle \\
&= \hat{a}^\dagger |\Pi_i^N S_0^i\rangle \otimes |0\rangle \\
&= \hat{a}^\dagger |\phi_0\rangle
\end{aligned} \tag{S.8}$$

In these expressions $|0\rangle$ indicates that the Fock state of the cavity mode is empty. The basis state $|\phi_0\rangle$ is the ground state of the molecule-cavity system with no excitations in neither the molecules nor the cavity mode:

$$|\phi_0\rangle = |S_0^1 S_0^2 \dots S_0^{N-1} S_0^N\rangle \otimes |0\rangle = |\Pi_i^N S_0^i\rangle \otimes |0\rangle \tag{S.9}$$

Within this basis, the Matrix representation of the Tavis-Cummings matrix becomes:

$$\mathbf{H}^{\text{TC}} = \begin{pmatrix} \mathbf{H}^{\text{mol}} & \mathbf{H}^{\text{int}} \\ \mathbf{H}^{\text{int}\dagger} & H^{\text{cav}} \end{pmatrix} \tag{S.10}$$

The upper left block, \mathbf{H}^{mol} , is an $N \times N$ matrix that contains the single-photon excitations of the molecules. Because we neglect direct excitonic interactions between molecules, this block is diagonal, with elements labeled by the molecule indices j :

$$H_{j,j}^{\text{mol}} = \langle \phi_0 | \hat{\sigma}_j \hat{H}^{\text{TC}} \hat{\sigma}_j^\dagger | \phi_0 \rangle \tag{S.11}$$

for $1 \leq j \leq N$. Each matrix element of \mathbf{H}^{mol} thus represents the potential energy of a HBQ molecule, j , in the electronic excited state $|S_1^j(\mathbf{R}_j)\rangle$ while all other molecules, $i \neq j$, are in the electronic ground state $|S_0^i(\mathbf{R}_i)\rangle$:

$$H_{j,j}^{\text{mol}} = V_{S_1}^{\text{mol}}(\mathbf{R}_j) + \sum_{i \neq j}^N V_{S_0}^{\text{mol}}(\mathbf{R}_i) \tag{S.12}$$

The lower right diagonal element in Equation S.10, \mathbf{H}^{cav} , represents the single-photon excitation of the cavity mode,:

$$H_{N+1,N+1}^{\text{cav}} = \langle \phi_0 | \hat{a} \hat{H}^{\text{TC}} \hat{a}^\dagger | \phi_0 \rangle \tag{S.13}$$

In these matrix elements, all HBQ molecules are in the electronic ground state (S_0). The energy is therefore the sum of the cavity energy at $k_{z,p}$, and the molecular ground state energies:

$$H_{N+1,N+1}^{\text{cav}} = \hbar\omega_{\text{cav}} + \sum_j^N V_{S_0}^{\text{mol}}(\mathbf{R}_j) \tag{S.14}$$

where ω_{cav} is the cavity frequency.

The two N dimensional off-diagonal vectors \mathbf{H}^{int} and $\mathbf{H}^{\text{int}\dagger}$ in the Tavis-Cummings Hamiltonian (Equation S.10) model the light-matter interactions between the HBQ molecules and

the cavity mode. The elements of these vectors are approximated as the inner product between the molecular transition dipole moments on the one hand, and the transverse electric field of the cavity mode at the center of the molecules, on the other hand:

$$\begin{aligned} H_{j,N+1}^{\text{int}} &= -\mu_j^{\text{TDM}}(\mathbf{R}_j) \cdot \mathbf{u}_{\text{cav}} \sqrt{\frac{\hbar\omega_{\text{cav}}}{2\epsilon_0 V_{\text{cav}}}} \langle \phi_0 | \hat{\sigma}_j (\hat{\sigma}_j^+ \hat{a}) \hat{a}^\dagger | \phi_0 \rangle \\ &= -\mu_j^{\text{TDM}}(\mathbf{R}_j) \cdot \mathbf{u}_{\text{cav}} \sqrt{\frac{\hbar\omega_{\text{cav}}}{2\epsilon_0 V_{\text{cav}}}} \end{aligned} \quad (\text{S.15})$$

Diagonalization of the multi-scale Tavis-Cummings Hamiltonian in Equation S.10 yields the $N + 1$ eigenstates $|\psi^m\rangle$:

$$|\psi^m\rangle = \left(\sum_j^N \beta_j^m \hat{\sigma}_j^+ + \alpha^m \hat{a}^\dagger \right) |\phi_0\rangle \quad (\text{S.16})$$

with eigenenergies E_m . Expansion coefficients β_j^m and α^m reflect the contribution of the molecular excitons ($|\text{S}_1^j(\mathbf{R}_j)\rangle$) and the cavity mode excitation ($|1\rangle$) to eigenstate $|\psi^m\rangle$, respectively.

2.2 Non-adiabatic molecular dynamics simulations

MD trajectories of all molecules (including environment) were computed by numerically integrating Newton's equations of motion. The multi-mode Tavis-Cummings Hamiltonian (Equation S.10) was diagonalized at each time-step of the simulation to obtain the $N + 1$ (adiabatic) eigenstates $|\psi^m\rangle$ and energies E^m . The trajectories were evolved on the PES of a *single* eigenstate, $|\psi^m\rangle$:

$$V({}_m\mathbf{R}) = \langle \psi^m | \hat{H}^{\text{TC}} | \psi^m \rangle \quad (\text{S.17})$$

Population transfers between states were modelled with a surface hopping method [S18].

The surface hopping algorithm used in this work [S19] is based on the Landau-Zener model [S20, S21], which relates the probability of a transition between two adiabatic states $|\psi_k\rangle$ and $|\psi_m\rangle$ to the non-adiabatic coupling, via:

$$P_{k \rightarrow m} = \exp\left[-\frac{1}{4}\pi\xi\right] \quad (\text{S.18})$$

with ξ the Massey parameter, defined as [S22]:

$$\xi = \frac{\Delta E_{km}}{\hbar \langle \psi^k | \frac{\partial}{\partial t} \psi^m \rangle} \quad (\text{S.19})$$

Following Hammes-Schiffer and Tully [S23] we approximate the non-adiabatic coupling $\langle \psi^k | \frac{\partial}{\partial t} \psi^m \rangle$ as $\langle \psi^k(t) | \psi^m(t + \Delta t) \rangle / \Delta t$, *i.e.*, the overlap between the state $|\psi^k\rangle$ at the current time step and the state $|\psi_m\rangle$ at the previous time step. Under the additional assumption that the uncoupled molecular wave functions vary slowly, we can further approximate this overlap as the inner product of the eigenvectors of the Tavis-Cummings matrix (Equation S.10):

$$\langle \psi^k(t) | \psi^m(t + \Delta t) \rangle = \sum_i^N \beta_i^k(t) \beta_i^m(t + \Delta t) + \alpha^k(t) \alpha^m(t + \Delta t) \quad (\text{S.20})$$

Calculating this overlap and the energy gap ΔE_{km} at every time step is straightforward and we can use the Landau-Zener formula to calculate the probability of a transition to the other surface (equation S.18). In principle, this transition probability could be used to spawn a new trajectory on the other polaritonic surface, but since this procedure would lead to multiple trajectories that have to be computed simultaneously, spawning will be too demanding in practice, in particular when there are many molecules. Instead, we restricted hopping to situations where the transition probability approaches unity. This happens when the states $|\psi^k\rangle$ and $|\psi^m\rangle$ are degenerate: $\Delta E_{km} \approx 0$ and $\langle \psi^k(t) | \psi^m(t + \Delta t) \rangle > \langle \psi^m(t) | \psi^k(t + \Delta t) \rangle$.

2.3 Simulation details

The Gromos-2016H66 force field was used to model the interactions, because it contains a validated cyclohexane model [S24], which was used as the solvent for HBQ in our simulations. In this united atom representation of cyclohexane, none of the atoms carries a partial charge. Because HBQ was kept frozen during the solvent equilibration and modeled at the QM level in all other simulations, there was no need to assign partial charges to the HBQ atoms. The Gromos96 atom-types used in the simulations are HC for all aromatic hydrogen atoms, C for all carbon atoms, NR for the aromatic nitrogen atom, OA for the hydroxyl oxygen atom and H for the hydroxyl proton.

One HBQ molecule was placed at the center of a rectangular box that was filled with 402 cyclohexane molecules. The simulation box, which thus contained 2436 atoms, was equilibrated for 100 ns. During equilibration, the coordinates of the HBQ atoms were kept fixed. The LINCS algorithm was used to constrain bond lengths in cyclohexane [S25] enabling a time step of 2 fs. Temperature and pressure were maintained at 300 K and 1 atmosphere by means of weak-coupling to an external bath ($\tau_T = 0.1$ ps, $\tau_P = 1$ ps) [S26]. The Lennard-Jones potential was truncated at 1.4 nm.

Snapshots were extracted from the equilibration trajectory and further equilibrated for 50 ps at the QM/MM level with a time step of 1 fs. HBQ was modeled with density functional theory (DFT), using the CAM-B3LYP functional [S27–S29] in combination with a 6-31G(d) basis set [S30]. The cyclohexane solvent was described with the 2016H66 parameter set of the Gromos96 force field [S24]. The QM subsystem was mechanically embedded and because cyclohexane atoms are uncharged, the interactions between the QM and MM regions were modeled with Lennard-Jones potentials only. We used time-dependent density functional theory [S31] within the Tamm-Dancoff approximation (TDA) [S32] in combination with the CAM-B3LYP functional and the 6-31G(d) basis set, to model the singlet excited electronic (S_1) state of HBQ in our simulations. All QM/MM simulations of HBQ outside of the cavity were performed with Gromacs 4.5.3 [S33] using the QM/MM interface to TeraChem [S34, S35].

A hundred snapshots were extracted from the 50 ps ground-state trajectories and the simulations were continued in the excited state to get an estimate for the proton transfer rate outside of the cavity. For the simulations in the cavity configurations were extracted from the QM/MM ground-state trajectory and coupled to a single confined light mode with an infinite lifetime and a vacuum field strength of 0.77 MVcm^{-1} (0.00015 au). To maximize the collective coupling strength, the transition dipole moments were aligned to the cavity field. MD trajectories of 100 fs were calculated with 256 and 512 molecules in the cavity. In

these simulations, the cavity energy $\hbar\omega_{\text{cav}}$ was tuned to be in resonance with the maximum of HBQ absorption, which is 4.02 eV at the TD-CAM-B3LYP/6-31G(d)//Gromos2016H66 level of QM/MM theory. In total 22 trajectories were computed, each starting in a different polaritonic eigenstate of the HBQ-cavity system. The simulations of 512 molecules were repeated with a cavity that was red-detuned from the HBQ absorption maximum by 123 meV. All simulations were performed with Gromacs 4.5.3 [S33], in which the Tavis-Cummings Hamiltonian (Equation S.10) was implemented [S15], using the QM/MM interface to Gaussian16 [S36].

2.4 Estimation of radiative losses

To estimate the radiative loss through the imperfect cavity mirrors *a posteriori*, we coherently propagated the *total* polaritonic wavefunction $|\Psi(t)\rangle$ along the classical trajectory of the N molecules as a time-dependent superposition of the $N + n_{\text{mode}}$ time-independent adiabatic polaritonic states:

$$|\Psi(t)\rangle = \sum_m^{N+n_{\text{mode}}} c_m(t)|\psi^m\rangle \quad (\text{S.21})$$

where $c_m(t)$ are the time-dependent expansion coefficients of the time-independent polaritonic basis functions $|\psi^m\rangle$ defined in Equation S.16. A unitary propagator in the *local* diabatic basis was used to integrate these coefficients [S37].

Radiative loss was modeled as a first-order decay process into the overall ground state of the system (*i.e.*, no excitation in neither the molecules nor the cavity mode) [S15]. Assuming an intrinsic decay rate of the cavity, γ_{cav} , the radiative loss rate was calculated as the product of γ_{cav} and the photonic weight, $|\alpha^m|^2$, of state $|\psi^m\rangle$ (Equation S.16). Thus, after an MD step Δt , the change in population of state $|\psi_m\rangle$, $\rho_m(t) = |c_m(t)|^2$, due to the loss is:

$$\rho_m(t + \Delta t) = \rho_m(t) \exp[-\gamma_{\text{cav}}|\alpha^m(t)|^2\Delta t] \quad (\text{S.22})$$

Since $\rho_m = (\Re[c_m])^2 + (\Im[c_m])^2$, changes in the real and imaginary parts of the (complex) expansion coefficients $c_m(t)$ due to spontaneous photonic loss through the mirrors of a low-Q cavity, are:

$$\begin{aligned} \Re[c_m(t + \Delta t)] &= \Re[c_m(t)] \exp\left[-\frac{1}{2}\gamma_{\text{cav}}|\alpha_p^m(t)|\Delta t\right] \\ \Im[c_m(t + \Delta t)] &= \Im[c_m(t)] \exp\left[-\frac{1}{2}\gamma_{\text{cav}}|\alpha^m(t)|^2\Delta t\right] \end{aligned}$$

In our simulations we assumed a decay rate of $\gamma_{\text{cav}} = 250 \text{ ps}^{-1}$.

2.5 Cavity absorption spectra

Following Lidzey and coworkers [S38], we define the "visibility", I^m , of polaritonic state $|\psi^m\rangle$ as the photonic contribution to that state (*i.e.*, $I^m \propto |\alpha^m|^2$). Thus, the one-photon absorption spectra of the HBQ cavity systems were computed from the QM/MM trajectory of the uncoupled HBQ as follows: For each frame of this trajectory, the polaritonic states were computed and the energy gaps of these states with respect to the overall ground state

(*i.e.*, E^0 , with all molecules in S_0 , no photon in the cavity: $|S_0^1 S_0^2 \dots S_0^N\rangle|0\rangle$) were extracted, multiplied by $|\alpha^m|^2$ and summed up into a superposition of Gaussian functions:

$$I^{\text{abs}}(E) \propto \sum_i^s \left[\sum_m^{N+n_{\text{max}}+1} |\alpha_i^m|^2 \exp\left[-\frac{(E - \Delta E_i^m)^2}{2\sigma^2}\right] \right] \quad (\text{S.23})$$

Here, $I^{\text{abs}}(E)$ is the absorption intensity as a function of excitation energy E , s the number of trajectory frames included in the analysis, ΔE_i^m the excitation energy of polaritonic state $|\psi^m\rangle$ in frame i ($\Delta E_i^m = E_i^m - E_i^0$) and α_i^m the expansion coefficient of the cavity mode in polaritonic state $|\psi^m\rangle$ in that frame (Equation S.16). A width of $\sigma = 0.05$ eV was chosen for all convolutions in this work.

2.6 Overlap between molecular polaritonic states

The density of states (DOS) of the bare HBQ in cyclohexane was determined by convoluting the distribution of the 2,048 QM/MM excitation energies with a Gaussian function:

$$p_{\text{mol}}^{\text{DOS}}(E) = \sum_i^s \Delta E_i \exp\left[-\frac{(E - \Delta E_i)^2}{2\sigma^2}\right] \quad (\text{S.24})$$

where E is the excitation energy, $s = 2048$ and we again use $\sigma = 0.05$ eV. Because polaritonic states are characterized by a non-zero photonic contribution (*i.e.* $|\alpha^k|^2 > 0$, Equation S.16) the DOS of these polaritonic states was calculated by weighing all polaritonic states by their photonic contribution:

$$p_{\text{pol}}^{\text{DOS}}(E) = \sum_i^S \left[\sum_k^{N+1} (E_i^k - E_i^0) \exp\left[-\frac{(E - (E_i^k - E_i^0))^2}{2\sigma^2}\right] |\alpha_i^k|^2 \right] \quad (\text{S.25})$$

where subscript i indicates the value of the parameter in snapshot i . To estimate the overlap between the DOS of the lower polariton and the DOS of the molecules, we fitted Gaussian functions to the DOS profiles of equations S.24 and S.25. A single Gaussian was used to fit $p_{\text{mol}}^{\text{DOS}}(E)$ while $p_{\text{pol}}^{\text{DOS}}(E)$ was fitted with a sum of two Gaussians. The overlap integral between the fits to the molecular and polaritonic DOS was then calculated analytically.

2.7 Additional MD results

2.7.1 ESIPT in "bare" HBQ

We performed 100 TDA-CAM-B3LYP/6-31G(d)//Gromos-2016H66 QM/MM MD simulations of HBQ in cyclohexane without a cavity, *i.e.*, *bare* HBQ. The starting structures were selected at 0.5 ps intervals from the ground-state CAM-B3LYP/6-31G(d)//Gromos-2016H66 equilibrium trajectory and instantaneously excited into the S_1 electronic state. In figure S7 we plot the distance between the hydroxyl oxygen and hydroxyl hydrogen as a function of time for all simulations. In all simulations, the intra-molecular proton transfer took place within 100 fs with an average reaction time, defined as the time at which the distance between the oxygen and hydrogen exceeds 0.125 nm, of 0.44 fs.

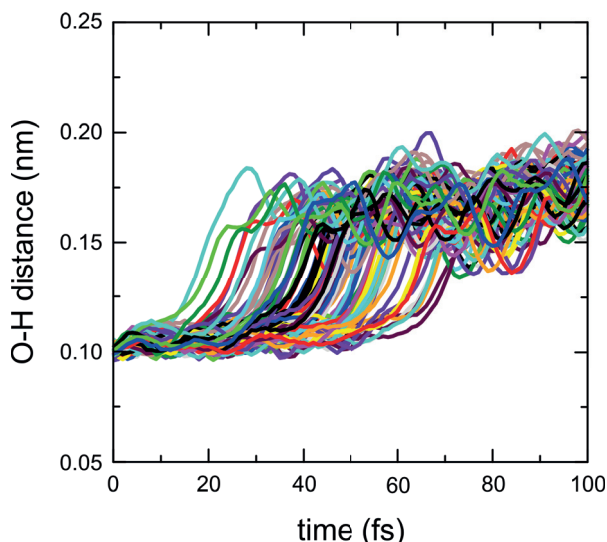


Fig. S7. Distance between the Oxygen and Hydrogen atoms for 100 QM/MM trajectories (all colours) of HBQ in cyclohexane as a function of time after instantaneous excitation into the S_1 electronic state.

2.7.2 ESIPT in HBQ under strong light-matter coupling

Tables 1-3 provide an overview of the results of MD simulations with 512 and 256 molecules in a single-mode cavity. In all simulations, proton transfer occurred, and the average quantum yields, η^{sim} , defined as the population in the product state at the end of the simulation (Equation S.22, last column in Tables 1-3), were 95% for 512 HBQ molecules in a tuned cavity, 86% for the 512 HBQ molecules in a red-detuned cavity, and 91% for 256 HBQ molecules in a tuned cavity.

Table 1: Simulation results for 512 HBQ molecules in a *tuned* single-mode cavity, with parameters: $\hbar\omega_{\text{cav}} = 4.01$ eV, $\sqrt{\hbar\omega_{\text{cav}}/2\epsilon_0 V_{\text{cav}}} = 0.77$ MVcm⁻¹, and $\gamma_{\text{cav}} = 250$ ps⁻¹

| $ \psi^m\rangle$ | $ \alpha^m ^2$ | t^{ESIPT} | molecule | $\eta^{\text{sim.}}$ |
|------------------|-------------------|--------------------|----------|----------------------|
| 0 | 0.0008 | 48 fs | 404 | 0.97 |
| 19 | 0.026 | 25 fs | 400 | 0.97 |
| 26 | 0.022 | 36 fs | 254 | 0.96 |
| 27 | 0.019 | 37 fs | 254 | 0.95 |
| 29 | 0.011 | 33 fs | 484 | 0.95 |
| 31 | 0.008 | 36 fs | 312 | 0.95 |
| 32 | 0.018 | 35 fs | 312 | 0.96 |
| 36 | 0.014 | 34 fs | 340 | 0.95 |
| 40 | 0.015 | 27 fs | 194 | 0.95 |
| 46 | 0.013 | 29 fs | 384 | 0.95 |
| 63 | 0.001 | 58 fs | 495 | 0.98 |
| 95 | 0.0001 | 60 fs | 173 | 0.96 |
| 127 | 0.0006 | 16 fs | 179 | 0.98 |
| 159 | $4 \cdot 10^{-5}$ | 27 fs | 138 | 0.95 |
| 191 | $3 \cdot 10^{-6}$ | 52 fs | 394 | 0.97 |
| 223 | 0.0002 | 56 fs | 306 | 0.94 |
| 255 | 0.0005 | 54 fs | 450 | 0.96 |
| 450 | 0.017 | 26 fs | 120 | 0.94 |
| 485 | 0.044 | 41 fs | 368 | 0.93 |
| 486 | 0.039 | 58 fs | 422 | 0.96 |
| 494 | 0.036 | 43 fs | 278 | 0.93 |
| 512 | 0.0006 | 56 fs | 131 | 0.94 |

Table 2: Simulation results for 512 HBQ molecules in a *detuned* single-mode cavity, with parameters: $\hbar\omega_{\text{cav}} = 3.90$ eV, $\sqrt{\hbar\omega_{\text{cav}}/2\epsilon_0 V_{\text{cav}}} = 0.77$ MVcm⁻¹, and $\gamma_{\text{cav}} = 250$ ps⁻¹

| $ \psi^m\rangle$ | $ \alpha^m ^2$ | t^{ESIPT} | molecule | $\eta^{\text{sim.}}$ |
|------------------|----------------|--------------------|----------|----------------------|
| 2 | 0.19 | 21 fs | 5 | 0.79 |
| 4 | 0.12 | 11 fs | 212 | 0.82 |
| 5 | 0.13 | 23 fs | 167 | 0.80 |
| 7 | 0.03 | 52 fs | 331 | 0.92 |
| 11 | 0.02 | 12 fs | 35 | 0.93 |
| 14 | 0.02 | 94 fs | 396 | 0.86 |
| 15 | 0.03 | 75 fs | 67 | 0.92 |

Table 3: Simulation results for 256 HBQ molecules in a *tuned* single-mode cavity, with parameters: $\hbar\omega_{\text{cav}} = 4.01$ eV, $\sqrt{\hbar\omega_{\text{cav}}/2\epsilon_0 V_{\text{cav}}} = 0.77$ MVcm⁻¹, and $\gamma_{\text{cav}} = 250$ ps⁻¹

| $ \psi^m\rangle$ | $ \alpha^m ^2$ | t^{ESIPT} | molecule | $\eta^{\text{sim.}}$ |
|------------------|----------------|--------------------|----------|----------------------|
| 17 | 0.027 | 53 fs | 209 | 0.95 |
| 27 | 0.033 | 85 fs | 110 | 0.90 |
| 36 | 0.022 | 26 fs | 200 | 0.89 |
| 51 | 0.017 | 49 fs | 102 | 0.93 |
| 55 | 0.022 | 59 fs | 191 | 0.92 |
| 66 | 0.011 | 25 fs | 77 | 0.90 |
| 69 | 0.015 | 12 fs | 137 | 0.89 |
| 132 | 0.016 | 25 fs | 77 | 0.90 |
| 146 | 0.018 | 33 fs | 118 | 0.91 |
| 165 | 0.037 | 51 fs | 29 | 0.90 |
| 167 | 0.038 | 77 fs | 249 | 0.90 |
| 170 | 0.014 | 30 fs | 235 | 0.94 |
| 183 | 0.0156 | 20 fs | 92 | 0.90 |
| 188 | 0.011 | 59 fs | 191 | 0.91 |
| 192 | 0.029 | 66 fs | 85 | 0.90 |
| 196 | 0.011 | 69 fs | 46 | 0.91 |
| 197 | 0.011 | 76 fs | 9 | 0.90 |
| 204 | 0.011 | 71 fs | 54 | 0.90 |
| 205 | 0.020 | 70 fs | 65 | 0.95 |
| 223 | 0.020 | 54 fs | 58 | 0.92 |
| 241 | 0.013 | 25 | 19 | 0.90 |

2.8 Reference Potential Energy Surfaces of HBQ molecule

First, we computed the potential energy surfaces (PES) of HBQ molecule on ground (S_0) and excited (S_1) states using TPSSh/cc-pVDZ level of theory. To reproduce the results of Picconi [S39], we performed relaxed surface scans on both states, while constraining the reaction coordinate, defined as $RC = d_{O-H} - d_{N-H}$ in Ångström (see Figure S8). Results of that scan are plotted as dashed lines with open circles in Figure S8. At this level of theory proton transfer is barrierless in the excited state. From the S_0 and S_1 minima excitation and fluorescence peaks have been calculated: 3.13 eV (396 nm) and 2.29 eV (541 nm), respectively.

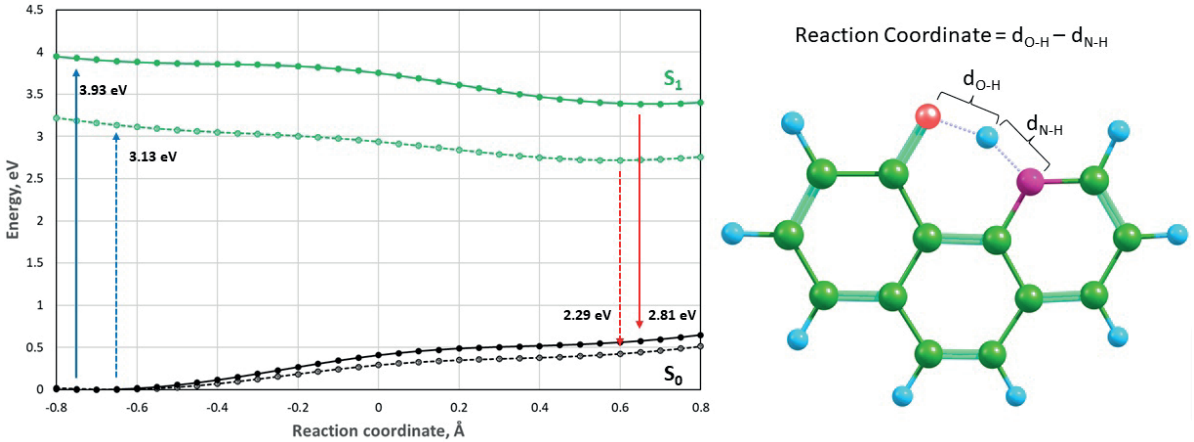


Fig. S8. Potential energy surface are shown on the left panel: solid lines for CAM-B3LYP/cc-pVDZ and dashed lines for TPSSh/cc-pVDZ levels of theory. Reaction coordinate used for relaxed scans are shown on the right panel.

While the TPSSh functional shows very good results for HBQ molecule, the lack of that functional in TeraChem quantum chemistry package [S34, S35] forced us to search for qualitatively similar functional that can reproduce the barrierless character of the intramolecular proton transfer reaction. We found that the CAM-B3LYP/cc-pVDZ level of theory (solid lines on Figure S8) suited our purposes, despite an overestimation of both the excitation and fluorescence energies: 3.93 eV (315 nm) and 2.81 eV (441 nm).

2.9 Simulations in Ultra-Strong Coupling Regime

In the ideal situation, in which all HBQ molecules are identical and the mirrors of the single-mode cavity are perfect, two bright polaritons and $N - 1$ degenerate states form, irrespective of the coupling strength (provided it is not zero) and the ratio $N_{\text{dark}}/N_{\text{pol}} = (N - 1)/2$ for all Rabi splittings. In contrast, when there is thermal disorder, the cavity modes are smeared-out over many eigenstates [S40–S42]. In this situation, there is no longer a clear distinction between dark and polaritonic states. Instead, we applied a numerical criterion and consider a state $|\psi^m\rangle$ polaritonic if the total cavity mode contribution to that state exceeds a threshold *i.e.*, $|\alpha^m|^2 \geq 0.01$.

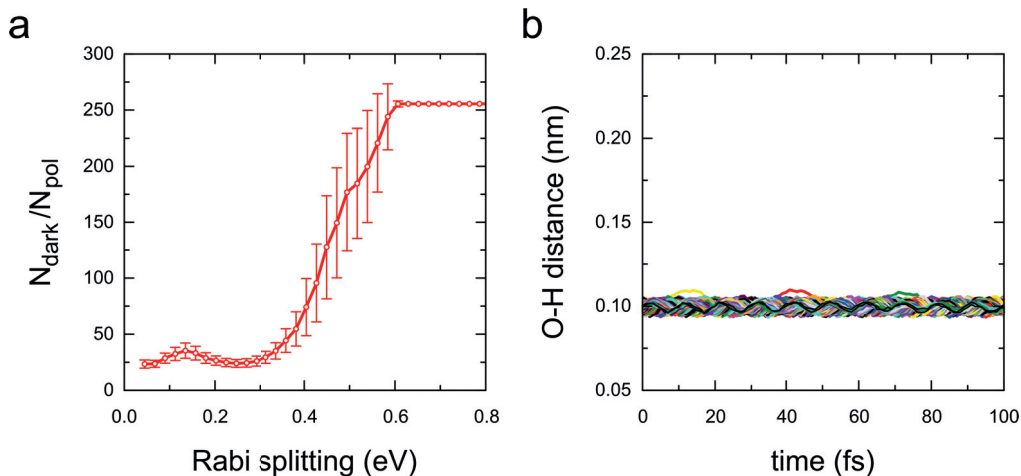


Fig. S9. Panel a shows the ratio between the dark and polaritonic states ($N_{\text{dark}}/N_{\text{pol}}$) as a function of Rabi splitting for a disordered ensemble of 512 molecules collectively coupled to a single cavity mode that is resonant with the molecular excitation energy (4.01 eV) and a threshold of $\epsilon = 0.01$. Panel b shows the distance between the hydroxyl oxygen atom and hydroxyl hydrogen atom in 512 HBQ molecules after excitation into the lower polariton with a cavity vacuum field strength of 1.92 MVcm^{-1} (0.000375 au), which yields a Rabi splitting of $\hbar\Omega^{\text{Rabi}} = 0.64 \text{ eV}$.

In Fig. S9a we plot the ratio between the dark and polaritonic states of 512 HQB molecules in the single-mode cavity as a function of the Rabi splitting, or equivalently the coupling strength. In these calculations, we controlled the coupling strength by varying the cavity mode volume (V_{cav} , Equation S.6). To account for the thermal disorder among the molecules, we randomly selected 1000 different sets of 512 energies plus transition dipole moments from the QM/MM equilibrium trajectory at 300 K for each coupling strength.

For Rabi splittings exceeding 0.6 eV, the ratio becomes "ideal" (*i.e.*, $N_{\text{dark}}/N_{\text{pol}} = (N - 1)/2 = 253.5$), and the UP and LP polaritons are coherent hybrids of *all* molecular excitations and the cavity mode excitation. Indeed, at a Rabi splitting of 0.64 eV, no proton transfer was observed in a simulation initiated in the LP state (Fig. S9b). However, because the Rabi splitting is larger than 10% of the excitation energy, the system is in the Ultra Strong Coupling regime [S43]. In this regime, the Rotating Wave Approximation (RWA), on which our simulation model is based, may no longer be strictly valid [S44, S45]. Nevertheless, the results of the analysis and simulations suggest that for typical organic molecules, ultra-strong coupling conditions is required to suppress photo-reactivity.

References

- S1. Mackay, T. G. & Lakhtakia, A. *The Transfer-Matrix Method in Electromagnetics and Optics* (Morgan and Claypool, San Rafael, 2020).
- S2. Pascoe, K. J. *Reflectivity and Transmissivity through Layered, Lossy Media: A User-Friendly Approach* (Wright Patterson Air Force Base, Ohio, 2001).

- S3. Gedney, S. *Introduction to the Finite-Difference Time-Domain (FDTD) Method for Electromagnetics* (Morgan and Claypool, San Rafael, 2011).
- S4. <https://www.ansys.com/products/photonics/fdtd>.
- S5. Palik, E. D. *Handbook of Optical Constants of Solids* (Academic, Burlington, 1997).
- S6. Dutta, A., Tiainen, V. & Toppari, J. J. Optimizing geometry of low-Q all-metal Fabry-Pérot microcavity for fluorescence spectroscopy. *IOP SciNotes* **2**, 015205 (2021).
- S7. <https://www.mathworks.com/products/matlab.html>.
- S8. <https://www.mathworks.com/help/matlab/ref/interp1.html>.
- S9. <https://www.mathworks.com/help/matlab/ref/pchip.html>.
- S10. Kavokin, A. V., Sheremet, A. S., Shelykh, I. A., Lagoudakis, P. G. & Rubo, Y. G. Exciton-photon correlations in bosonic condensates of exciton-polaritons. *Sci. Rep.* **5**, 12020 (2015).
- S11. Hertzog, M., Wang, M., Mony, J. & Börjesson, K. Strong light–matter interactions: a new direction within chemistry. *Chem. Soc. Rev.* **48**, 937–961 (2019).
- S12. Baieva, S. *Interaction between surface plasmon polaritons and molecules in strong coupling limit* (University of Jyväskylä, PhD Dissertation, 2016).
- S13. Jaynes, E. T. & Cummings, F. W. Comparison of quantum and semiclassical radiation theories with to the beam maser. *Proc. IEEE* **51**, 89–109 (1963).
- S14. Tavis, M. & Cummings, F. W. Approximate solutions for an N-molecule radiation-field Hamiltonian. *Phys. Rev.* **188**, 692–695 (1969).
- S15. Luk, H.-L., Feist, J., Toppari, J. J. & Groenhof, G. Multiscale Molecular Dynamics Simulations of Polaritonic Chemistry. *J. Chem. Theory Comput.* **13**, 4324–4335 (2017).
- S16. Warshel, A. & Levitt, M. Theoretical studies of enzymatic reactions: Dielectric, electrostatic and steric stabilization of carbonium ion in the reaction of lysozyme. *J. Mol. Biol.* **103**, 227–249 (1976).
- S17. Boggio-Pasqua, M., Burmeister, C. F., Robb, M. A. & Groenhof, G. Photochemical reactions in biological systems: probing the effect of the environment by means of hybrid quantum chemistry/molecular mechanics simulations. *Phys. Chem. Chem. Phys.* **14**, 7912–7928 (2012).
- S18. Crespo-Otero, R. & Barbatti, M. Recent Advances and Perspectives on Nonadiabatic Mixed Quantum-Classical Dynamics. *Chem. Rev.* **118**, 7026–7068 (2018).
- S19. Groenhof, G. *et al.* Photoactivation of the photoactive yellow protein: Why photon absorption triggers a trans-to-cis isomerization of the chromophore in the protein. *J. Am. Chem. Soc.* **124**, 4228–4232 (2004).
- S20. Landau, L. Zur theorie der energieübertragung. II. *Phys. Z. Sowjetunion* **2**, 1–13 (1932).
- S21. Zener, C. Non-adiabatic crossing of energy levels. *Proc. R. Soc. A* **137**, 696–702 (1932).

- S22. Desouter-Lecomte, M. & Lorquet, J. Nonadiabatic interactions in unimolecular decay. IV. Transition probability as a function of the Massey parameter. *J. Chem. Phys.* **71**, 4391–4403 (1979).
- S23. Hammes-Schiffer, S. & Tully, J. C. Proton transfer in solution: molecular dynamics with quantum transitions. *J. Chem. Phys.* **101**, 4657–4667 (1994).
- S24. Horta, B. A. C. *et al.* A GROMOS-Compatible Force Field for Small Organic Molecules in the Condensed Phase: The 2016H66 Parameter Set. *J. Chem. Theory. Comput.* **12**, 3825–3850 (2016).
- S25. Hess, B., Bekker, H., Berendsen, H. J. C. & Fraaije, J. G. E. M. LINCS: A linear constraint solver for molecular simulations. *J. Comput. Chem.* **18**, 1463–1472 (1997).
- S26. Berendsen, H., Postma, J., van Gunsteren, W., la, A. D. & Haak, J. Molecular dynamics with coupling to an external bath. *J. Chem. Phys.* **81**, 3684–3690 (1984).
- S27. Becke, A. D. A new mixing of Hartree-Fock and local density-functional theories. *J. Chem. Phys.* **98**, 1372 (1993).
- S28. Lee, C. T., Yang, W. T. & Parr, R. G. Development of the Colle-Salvetti correlation-energy formula into a functional of the electron density. *Phys. Rev. B* **37**, 785–789 (1988).
- S29. Yanai, T., Tew, D. P. & Handy, N. C. A new hybrid exchange-correlation functional using the Coulomb-attenuating method (CAM-B3LYP). *Chem. Phys. Lett.* **393**, 51–57 (2004).
- S30. Dunning, T. H. Basis Functions for Use in Molecular Calculations. I. Contractions of (9s5p) Atomic Basis Sets for the First-Row Atoms. *J. Chem. Phys.* **53**, 2823–2833 (1970).
- S31. Runge, E. & Gross, E. K. U. Density-Functional Theory for Time-Dependent Systems. *Phys. Rev. Lett* **52**, 997–1000 (1984).
- S32. Hirata, S. & Head-Gordon, M. Time-dependent density functional theory within the Tamm–Dancoff approximation. *Chem. Phys. Lett.* **314**, 291–299 (1999).
- S33. Hess, B., Kutzner, C., van der Spoel, D. & Lindahl, E. GROMACS 4: Algorithms for Highly Efficient, Load-Balanced, and Scalable Molecular Simulation. *J. Chem. Theory Comput.* **4**, 435–447 (2008).
- S34. Ufimtsev, I. & Martínez, T. J. Quantum Chemistry on Graphical Processing Units. 3. Analytical Energy Gradients and First Principles Molecular Dynamics. *J. Chem. Theory Comput.* **5**, 2619–2628 (2009).
- S35. Titov, A., Ufimtsev, I., Luehr, N. & Martínez, T. J. Generating Efficient Quantum Chemistry Codes for Novel Architectures. *J. Chem. Theory Comput.* **9**, 213–221 (2013).
- S36. Frisch, M. J. *et al.* *Gaussian~16 Revision C.01* Gaussian Inc. Wallingford CT. 2016.
- S37. Granucci, G., Persico, M. & Toniolo, A. Direct semiclassical simulation of photochemical processes with semiempirical wave functions. *J. Chem. Phys.* **114**, 10608–10615 (2001).

- S38. Lidzey, D., Bradley, D., Armitage, A., Walker, S. & Skolnick, M. Photon-Mediated Hybridization of Frenkel Excitons in Organic Semiconductor Microcavities. *Science* **288**, 1620–1623 (2000).
- S39. Picconi, D. Nonadiabatic quantum dynamics of the coherent excited state intramolecular proton transfer of 10-hydroxybenzo [h] quinoline. *Photochemical & Photobiological Sciences* **20**, 1455–1473 (2021).
- S40. Houdré, R., Stanley, R. P. & Ilegems, M. Vacuum-field Rabi splitting in the presence of inhomogeneous broadening: Resolution of a homogeneous linewidth in an inhomogeneously broadened system. *Phys. Rev. A* **53**, 2711–2715 (1996).
- S41. Groenhof, G., Climent, C., Feist, J., Morozov, D. & Toppari, J. J. Tracking Polariton Relaxation with Multiscale Molecular Dynamics Simulations. *J. Chem. Phys. Lett.* **10**, 5476–5483 (2019).
- S42. Mony, J., Climent, C., Anne Ugleholdt Petersen Kasper Moth-Poulsen, J. F. & Börjesson, K. Photoisomerization Efficiency of a Solar Thermal Fuel in the Strong Coupling Regime. *Adv. Funct. Mater.* **31**, 2010737 (2021).
- S43. Forn-Díaz, P., Lamata, L., Rico, E., Kono, J. & Solano, E. Ultrastrong coupling regimes of light-matter interaction. *Rev. Mod. Phys.* **91**, 025005 (2019).
- S44. Flick, J., Ruggenthaler, M., Appel, H. & Rubio, A. Cavity Born-Oppenheimer Approximation for correlated Electron-Nuclear-Photon Systems. *J. Chem. Theory Comput.* **13**, 1616–1625 (2017).
- S45. Flick, J., Ruggenthaler, M., Appel, H. & Rubio, A. Atoms and Molecules in Cavities: From Weak to Strong Coupling in QED Chemistry. *Proc. Natl. Acad. Sci. USA* **114**, 3026–3034 (2017).

PVII

**EFFECT OF MOLECULAR CONCENTRATION ON EXCITONIC
NANOSTRUCTURE BASED REFRACTIVE-INDEX SENSING
AND NEAR-FIELD ENHANCED SPECTROSCOPY**

by

A. Dutta and J. J. Toppari,

Optical Materials Express, **13**, 2426 (2023).

Reproduced with kind permission of Optica Publishing Group.



Effect of molecular concentration on excitonic nanostructure based refractive index sensing and near-field enhanced spectroscopy

ARPAN DUTTA^{1,2,3}  AND J. JUSSI TOPPARI^{1,4} 

¹Nanoscience Center and Department of Physics, University of Jyväskylä, P.O. Box 35, FI-40014, Finland

²Currently with Department of Mechanical and Materials Engineering, University of Turku, FI-20014, Finland

³arpan.dutta@utu.fi

⁴j.jussi.toppari@jyu.fi

Abstract: Organic thin film based excitonic nanostructures are of great interest in modern resonant nanophotonics as a promising alternative for plasmonic systems. Such nanostructures sustain propagating and localized surface exciton modes that can be exploited in refractive index sensing and near-field enhanced spectroscopy. To realize these surface excitonic modes and to enhance their optical performance, the concentration of the excitonic molecules present in the organic thin film has to be quite high so that a large oscillator strength can be achieved. Unfortunately, this often results in a broadening of the material response, which might prevent achieving the very goal. Therefore, systematic and in-depth studies are needed on the molecular concentration dependence of the surface excitonic modes to acquire optimal performance from them. Here, we study the effect of molecular concentration in terms of oscillator strength and Lorentzian broadening on various surface excitonic modes when employed in sensing and spectroscopy. The optical performance of the modes is evaluated in terms of sensing, like sensitivity and figure of merit, as well as near-field enhancement, like enhancement factor and field confinement. Our numerical investigation reveals that, in general, an increase in oscillator strength enhances the performance of the surface excitonic modes while a broadening degrades that as a counteracting effect. Most of all, this demonstrates that the optical performance of an excitonic system is tunable via molecular concentration unlike the plasmonic systems. Moreover, different surface excitonic modes show different degrees of tunability and equivalency in performance when compared to plasmons in metals (silver and gold). Our findings provide crucial information for developing and optimizing novel excitonic nanodevices for contemporary organic nanophotonics.

Published by Optica Publishing Group under the terms of the [Creative Commons Attribution 4.0 License](https://creativecommons.org/licenses/by/4.0/). Further distribution of this work must maintain attribution to the author(s) and the published article's title, journal citation, and DOI.

1. Introduction

Interaction of light with metallic nanostructures can excite a collective oscillation of the metal's conduction electrons, also known as plasmons. The excited plasmonic modes can be spectroscopically resolvable in the optical response of the metallic system and usually involve a strongly enhanced electromagnetic near-field around the structure [1–3]. Depending on the type of the nanostructure, different plasmonic modes can be excited such as surface plasmon polariton (SPP) at the interface of a flat metal film and a dielectric material [4], localized surface plasmon (LSP) in a metal nanoparticle (NP) [5], and plasmonic surface lattice resonance (PSLR) in a periodic structure, e.g., an array of metal NPs [6].

Plasmonic modes are extremely sensitive to the dielectric constant of their surrounding medium and even a slightest change in the refractive index (RI) of the host medium can significantly shift

the spectral position of the SPP [7], LSP [8], and PSLR [9] modes. Such feature enables the application of nanoplasmonic structures in the development of RI sensors [5,7–11].

Plasmonic modes (SPP, LSP, and PSLR) can also provide enhancement [12–15] and confinement [16–18] of light at the near-field close to the structure. Consequently, metallic nanostructures are widely exploited as resonant substrates for near-field enhanced spectroscopy ranging from weak [19–22] to strong [23–25] light-matter coupling.

The origin of the plasmonic properties in metals can be explained in terms of the real part of their complex and dispersive dielectric function ($Re\{\epsilon\}$) [1–3,26,27]. The SPP mode can be supported by a flat metal film in the spectral region where $Re\{\epsilon\} < -1$ while manifestation of LSP mode in a metal NP is only possible in the spectral regime where $Re\{\epsilon\} < -2$ [27]. In the case of noble metals like gold and silver, the negative $Re\{\epsilon\}$ regime, i.e., the spectral regime where $Re\{\epsilon\} < -1$ or -2 , covers a major part of the visible spectrum, making them a popular choice in nanoplasmonics [28,29].

Despite the fact that plasmonic materials show unique optical properties ranging from ultra-violet to infrared wavelengths, their performance is often hindered due to the absorption losses, and their fabrication might become complex and expensive. Consequently, a quest emerges for alternative materials which can provide a plasmon-like negative $Re\{\epsilon\}$ regime, especially in the visible range, while exhibiting less losses as well as being somewhat simpler and inexpensive to fabricate compared to the metallic nanostructures. One important class of such materials is highly concentrated organic thin films possessing Frenkel excitons which induce a negative $Re\{\epsilon\}$ regime spectrally located very close to their strong excitonic absorption band [26,27]. Such excitonic materials can support surface exciton polariton (SEP) at an interface of an excitonic film and a dielectric material [26,27,30,31], localized surface exciton (LSE) in an excitonic NP [27,32,33], and excitonic surface lattice resonance (ESLR) in a periodic array of excitonic NPs [34]. The SEP, LSE, and ESLR modes are analogous to the SPP, LSP, and PSLR modes, respectively. Eventually, like the plasmonic modes, these surface excitonic modes show sensitivity towards the surrounding dielectric environment [31] and provide enhancement as well as confinement of the near-field [35]. Hence, excitonic nanostructures possessing these modes can be a potential alternative for the plasmonic systems in RI sensing and in near-field enhanced spectroscopy.

The optical responses associated with the aforementioned plasmonic and excitonic modes might appear analogous but the underlying physical mechanism in those systems differs fundamentally. The plasmonic resonances originate from the presence of free conduction electrons in metals which in the simplest case can be described by the Drude model. Contrastingly, the excitonic modes in the organic thin films appear due to the Frenkel excitons which can be expressed by the Lorentz oscillator model [27]. Unlike Drude metals, the complex permittivity (ϵ) of an excitonic material is directly proportional to the Lorentz oscillator strength (f) and the Lorentz linewidth (γ) of the material absorption [36,37] which scales with the molecular concentration [27,32,33,38]. An increase in molecular concentration usually results in a rise in molecular absorption accompanied with a linewidth broadening, which accounts for a simultaneous rise in the magnitude of f and γ [36,37]. Such rise in f and γ can directly affect the magnitude of $Re\{\epsilon\}$ and thereby, the negative $Re\{\epsilon\}$ regime. As a consequence, the surface excitonic modes exhibit modification in their strength and light coupling efficiency [26,27,39,40]. Therefore, optical performance of the surface excitonic modes can be tuned by varying the concentration of the excitonic molecules.

In this work, we investigate the effect of the molecular concentration (in terms of f and γ) on the performance of excitonic nanostructures when used for RI sensing and near-field enhanced spectroscopy. The J-aggregate of cyanine dye (TDBC) is considered as the excitonic molecule doped in a polyvinyl alcohol (PVA) matrix. Three kinds of excitonic nanostructures are studied, as shown in Fig. 1 - (i) a TDBC-PVA thin film which supports SEP under excitation in the Kretschmann configuration (Fig. 1(a)), (ii) a TDBC-PVA nanosphere which possesses LSE

(Fig. 1(b)), and (iii) a square lattice of TDBC-PVA nanospheres manifesting ESLR (Fig. 1(c)). In all cases, the sensing performance is evaluated in terms of sensitivity and a commonly used figure of merit for RI sensing, i.e. the sensitivity divided by the width of the utilized spectral resonance, while the assessment in spectroscopy is based on the near-field intensity enhancement (NFIE), Purcell enhancement, and field-confinement. Our numerical findings show that the performance parameters (sensitivity, figure of merit, NFIE, Purcell enhancement, and field-confinement) of a surface excitonic mode can be tuned efficiently by varying the molecular concentration. Moreover, SEP, LSE, and ESLR based nanostructures provide different degrees of tunability when concentration is varied. Our comprehensive study on different types of surface excitonic modes with varying concentration provides key information for developing and optimizing novel organic material based excitonic nanodevices for sensing and spectroscopy.

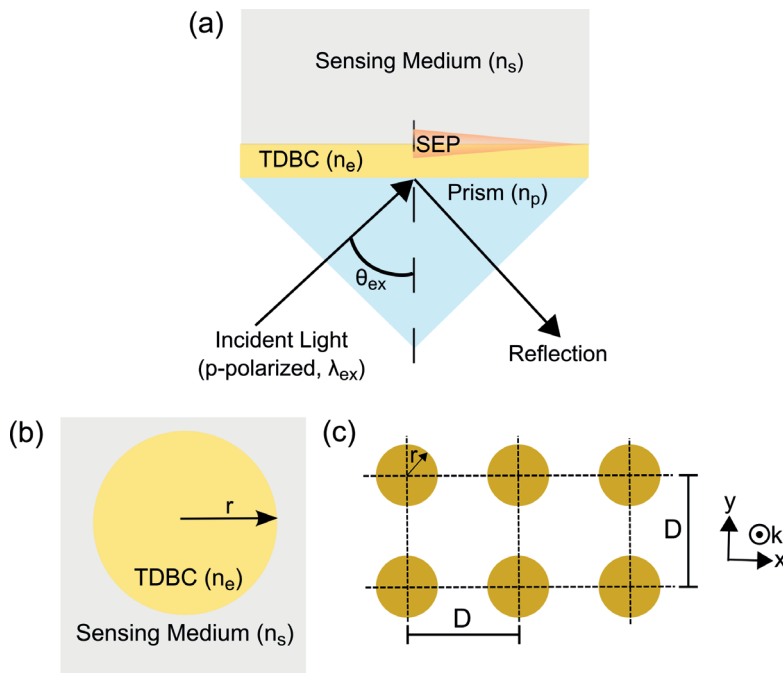


Fig. 1. (a) A TDBC-PVA thin film supporting SEP under excitation in the Kretschmann configuration. (b) A TDBC-PVA nanosphere possessing LSE. (c) A square lattice of TDBC-PVA nanospheres manifesting ESLR.

2. Negative $Re\{\epsilon\}$ regime

Before analyzing the performance of different excitonic systems it is important to determine their negative $Re\{\epsilon\}$ regime as a function of molecular concentration. To do so, we evaluate the spectral regime where $Re\{\epsilon\} < -1$ or -2 as a function of Lorentz oscillator strength (f) and Lorentz linewidth (γ). The complex and dispersive dielectric function (ϵ) of an excitonic material like our TDBC-PVA system can be estimated using the Lorentz oscillator model (LOM) [27,37,41] as

$$\epsilon(E) = \epsilon_{\infty} + \frac{fE_0^2}{(E_0^2 - E^2 - i\gamma E)}, \quad (1)$$

where E is the energy, ϵ_∞ is the dielectric constant of the host polymer (i.e. PVA), f is the oscillator strength of the excitonic absorption having E_0 as its spectral peak position and γ as its spectral linewidth [27,37,41]. To model TDBC, we choose realistic values for LOM parameters taken from the existing experimental studies [27,41–44]. In Eq. (1), we consider $\epsilon_\infty = 2.1025$ [41] and $E_0 = 2.08$ eV [41], while f and γ are treated as variables. In the Refs. [27,41–44], γ varies from 0.025 eV to 0.12 eV and f varies from 0.05 to 0.51. In line with this realistic parameter range, we vary γ from 0.05 eV to 0.15 eV while the range of f (0.05 to 0.9) is extended upwards to see whether a possible increase in the absorption beyond the already achieved values could bring extra improvements.

An increase in molecular concentration results in an increase in molecular absorption usually accompanied with a linewidth broadening accounting for a simultaneous rise in f and γ [36,37,44]. We used an experimental study on TDBC [44] to extract γ as a function of f . The γ values are directly from the study while the values for f were obtained by fitting the absorption data (see Fig. 7(a) in Appendix). The details of the fitting method can be found in our earlier work [37]. The correlation between f and γ is plotted in Appendix in Fig. 7(b) where all the values are within the realistic ranges discussed above. It should be noted here that this is a correlation extracted from a single study and thus, not the only possible relation. The aggregation of molecules and thus, the broadening (γ) depends on many different factors (e.g., fabrication process) and can vary a lot. Thus, we need to study wider range of parameter combinations and keep this as a guiding example of the interdependence of the parameters.

To model the above, we calculate real ($Re\{\epsilon\}$) and imaginary ($Im\{\epsilon\}$) parts of the dielectric function (ϵ) of a 60 nm thick TDBC-PVA layer using Eq. (1) with varying f and γ . The curves are shown in Fig. 2(a). The associated absorption is calculated using transfer-matrix method (TMM) [45,46] implemented in MATLAB [47,48], similarly as in our earlier studies [37].

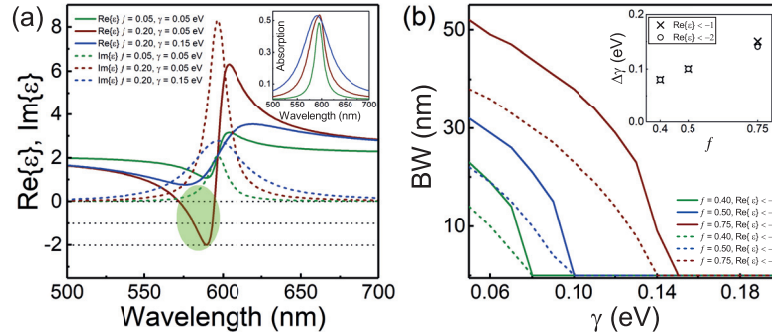


Fig. 2. (a) The real ($Re\{\epsilon\}$, solid curves) and imaginary ($Im\{\epsilon\}$, dashed curves) parts of the dielectric function (ϵ) of a 60 nm thick TDBC-PVA layer calculated using Eq. (1) for different values of Lorentz oscillator strength (f) and Lorentz linewidth (γ). Here, $\epsilon_\infty = 2.1025$ and $E_0 = 2.08$ eV as discussed in the text. The corresponding absorption spectra (in matching colors) computed by TMM are shown in the inset. The green spot on the figure depicts the region where $Re\{\epsilon\} < 0$ and $|Im\{\epsilon\}| < |Re\{\epsilon\}|$ for the red curves. (b) Bandwidth (BW) of surface excitonic modes for different values of f and γ . In the inset, the broadening tolerance ($\Delta\gamma$) is plotted as a function of f .

The green curves in Fig. 2(a) represent $Re\{\epsilon\}$ (solid) and $Im\{\epsilon\}$ (dashed) of our *pristine* TDBC-PVA film with $f = 0.05$ and $\gamma = 0.05$ eV. The corresponding absorption is shown in the inset of Fig. 2(a) (green curve). It is clear from the figure that our *pristine* layer is unable to support any surface excitonic mode since its $Re\{\epsilon\}$ is positive in the wavelength region of interest (500–700 nm). To address a rise in concentration, we first increase f to 0.20 while keeping γ at

0.05 eV. The red curves in Fig. 2(a) depict the case with the corresponding absorption with the same color in the inset. Clearly now $Re\{\epsilon\}$ becomes negative (almost -2) indicating that our TDBC layer can support the surface excitonic modes in a narrow spectral window ($\sim 575 - 595$ nm) at the blue side of the molecular absorption peak (~ 600 nm). However, to realize the actual effect of a rising concentration one should increase both f and γ simultaneously. The blue curves in Fig. 2(a) show the case (with the related absorption in the inset) where f is kept at 0.20 and γ rises from 0.05 eV to 0.15 eV. Clearly, the increase in γ counteracts the effect seen for the sole rise in only f by making $Re\{\epsilon\}$ positive again like in the *pristine* case, and eventually, no surface excitonic mode can be supported by the TDBC layer.

To develop more insight on this counteracting behaviour we calculate the spectral regions where $Re\{\epsilon\} < -1$ and $Re\{\epsilon\} < -2$, reported in Fig. 8 in Appendix, for different values of f and γ . To ensure minimal material loss, we also impose an additional condition, i.e., $|Im\{\epsilon\}| < |Re\{\epsilon\}|$ [40], for our reported spectral region. The bandwidth (BW) for the possible existence of the surface excitonic modes is evaluated as the difference between the upper and the lower boundaries of the aforementioned spectral regions (see Fig. 8 in Appendix). The solid curves in Fig. 2(b) report the BW of SEP mode ($Re\{\epsilon\} < -1$) while the dashed curves report the same for LSE and ESLR mode ($Re\{\epsilon\} < -2$).

In Fig. 2(b), the BW values at the vertical axis, i.e., at $\gamma = 0.05$ eV, present the scenario where the BW is increasing with increasing f , i.e., $f = 0.40$ (green) to $f = 0.75$ (red) via $f = 0.50$ (blue), considering a constant γ (no broadening). However, when the broadening is incorporated, i.e., γ increases from 0.05 eV to 0.20 eV for a constant value of f (0.40 or 0.50 or 0.75), in all cases, the BW drops drastically and vanishes after a certain value of γ as one can see in Fig. 2(b). This finding clearly indicates that when both f and γ increase, as usually happens when increasing the film concentration [36,37,44], they counteract each other's effects.

As seen from Fig. 2(b), for all f there always exists a maximum γ , after which the surface excitonic mode is no more possible, because there is no more spectral region with $Re\{\epsilon\} < -1$ or $Re\{\epsilon\} < -2$, i.e., BW = 0. For example, for $f = 0.5$ this value is $\gamma = 0.1$ eV (blue curve). This range (e.g., $\gamma \in [0, 0.1]$ eV for $f = 0.5$) can be considered as a broadening tolerance, $\Delta\gamma(f)$, of a surface excitonic mode since at any $\gamma < \Delta\gamma$ the mode is always allowed at some spectral region, but for $\gamma > \Delta\gamma$ it vanishes in all frequencies. The evolution of $\Delta\gamma(f)$ as a function of f is plotted in the inset of Fig. 2(b) and it is clear from the figure that the higher the f , the larger the $\Delta\gamma$. This is an important finding since it can provide a solution to mitigate the above-mentioned counteracting problem while increasing the molecular concentration. By increasing the molecular concentration one can increase f which will push the magnitude of $\Delta\gamma$ to better tolerate the inevitable linewidth broadening. However, care has to be taken in choosing the molecule, so that γ will not increase too much while increasing the concentration and f .

3. Surface exciton polariton

After establishing the initial conditions as well as the spectral range where TDBC-PVA system can support the surface excitonic modes, we first focus on SEP mode under the Kretschmann configuration [30,31]. The SEP mode can be excited in a multilayer system such as air/TDBC-PVA thin film/prism structure where the p -polarized incident light is coupled through the prism. The air can be replaced by the sensing medium for sensing application [31] and by the analyte for spectroscopy [23,36]. The schematic of such SEP based system is presented in Fig. 1(a). We use the Fresnel multilayer reflection theory [7,49,50] implemented in MATLAB for calculating the reflectivity (R) of the system since SEP mode is manifested as a dip in the attenuated total reflection (ATR) spectrum [50]. The RI of the prism (n_p) is considered as 1.50 which corresponds to the common BK7 glass in practice [7]. The RI of the sensing medium (n_s) is varied from 1 to 1.01 with a step size of 0.001 to evaluate the performance of the sensor. The RI of the TDBC-PVA film is obtained as $n_e = \sqrt{\epsilon}$ [51], where ϵ is calculated using Eq. (1).

We excite the SEP mode supported by a 60 nm thick TDBC-PVA film ($f = 0.5$ and $\gamma = 0.05$ eV) using the Kretschmann configuration in two ways. In the angular scheme we use the p -polarized monochromatic light of wavelength λ_{ex} to excite the system over a broad range of incident angles higher than the critical angle of total internal reflection ($\sim 42^\circ - 90^\circ$). The angle-dependent reflectivity is presented in Fig. 3(a) (blue curve) for $\lambda_{ex} = 569$ nm. The dip found in the reflection profile is the signature of the excited SEP mode. In the spectral scheme, we excite the system by a broadband source (p -polarized white light) at a fixed incident angle (θ_{ex}) and the reflectivity is computed over a wide spectral range. The wavelength-dependent reflectivity is depicted in Fig. 3(a) (red curve) for $\theta_{ex} = 54^\circ$. Similar to the angular case, profound presence of the SEP mode is found as a dip in the spectral reflectance.

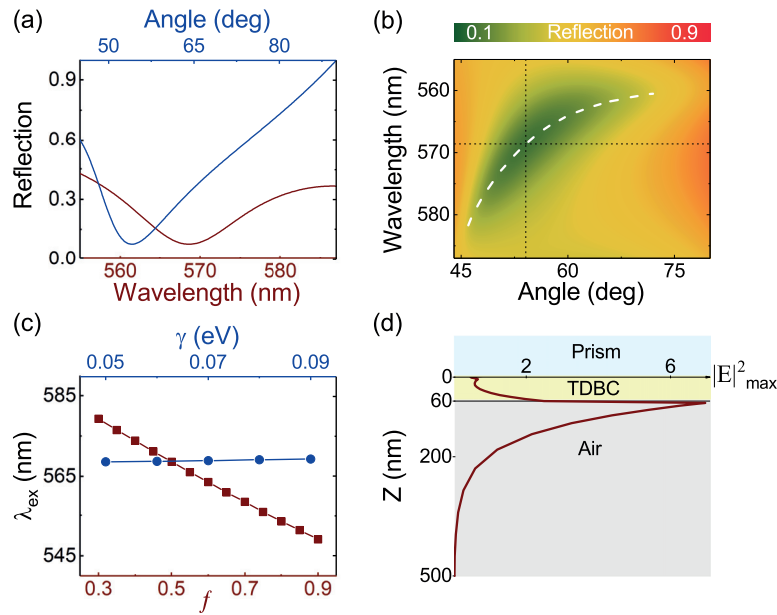


Fig. 3. (a) Angular (excited at $\lambda_{ex} = 569$ nm) and spectral (excited at $\theta_{ex} = 54^\circ$) reflectance of a 60 nm thick TDBC-PVA film ($f = 0.5$ and $\gamma = 0.05$ eV) under Kretschmann configuration. (b) Reflectance of the same film as a contour map where the white dashed curve shows the dispersion of the SEP mode and the black dotted lines show the optimal excitation conditions with minimal reflectance $R(\theta_{ex}, \lambda_{ex})$. (c) Evolution of the optimal excitation wavelength (λ_{ex}) as a function of f and γ . The value of f is varied when $\gamma = 0.05$ eV and the value of γ is varied when $f = 0.5$. (d) FDTD simulated near-field intensity profile of SEP mode. In (a) and (c), the blue and red horizontal axes correspond to the blue and red curves, respectively, while in (c), the blue circles and red squares on the curves of corresponding color depict the discrete data points.

To obtain the optimal excitation conditions (i.e. θ_{ex} and λ_{ex}) of the SEP mode, we compute the reflectance $R(\theta_{ex}, \lambda_{ex})$, with all the angles ($42^\circ - 90^\circ$) and wavelengths supporting the SEP, i.e., within the BW discussed in previous section. The results are reported as a contour map in Fig. 3(b). In the figure, the white dashed curve shows the dispersion of the SEP mode following the spectral and angular minima of the reflectance. The optimal excitation angle (θ_{ex}) and wavelength (λ_{ex}) for sensing are evaluated as the position where $R(\theta_{ex}, \lambda_{ex})$ is the minimum of the whole contour map as shown by the black dotted lines in Fig. 3(b).

The excitation conditions can also vary with respect to f and γ since the BW of the SEP mode is concentration-dependent. To address this, we compute the dispersion of the SEP mode for

different f and γ where the effect of one parameter is studied by keeping the other as constant. To study the effect of f , it is varied from 0.30 to 0.90, as discussed in the previous section (for $f < 0.3$ BW = 0) with a step size of 0.05 while keeping $\gamma = 0.05$ eV (no broadening). To study the effect of broadening, γ is varied from 0.05 eV to 0.09 eV (extent of $\Delta\gamma$) with a step size of 0.01 eV while keeping $f = 0.5$ constant. In both cases, we extract the excitation conditions (θ_{ex} and λ_{ex}) as $R(\theta_{ex}, \lambda_{ex}) = \text{Min}[R(\theta, \lambda)]$. The evolution of the excitation wavelength (λ_{ex}) as a function of f (when $\gamma = 0.05$ eV) and of γ (when $f = 0.5$) is illustrated in Fig. 3(c). From the figure it is clear that λ_{ex} is significantly blue-shifted with increasing f when no broadening is allowed (red curve in Fig. 3(c)). This is consistent with our finding in Fig. 8 (see Appendix) where the BW of SEP mode widens only in the blue-wavelength side with increasing f . However, when the broadening is introduced, λ_{ex} experiences a mild red-shift (blue curve in Fig. 3(c)) counteracting the effect of sole rise only in f without broadening. On the other hand, the angle of excitation (θ_{ex}) is almost unaffected ($\approx 54^\circ$) irrespective of whether f or γ is varied (not shown).

Therefore, for each f (when $\gamma = 0.05$ eV) or for each γ (when $f = 0.5$) there will be a corresponding λ_{ex} at which the SEP mode can be optimally excited over a broad range of incident angles in the angular scheme. On the other hand, at $\theta_{ex} \approx 54^\circ$ the SEP mode can be optimally excited over a wide range of wavelengths in the spectral scheme irrespective of the magnitude of f and γ . Furthermore, one can tune the spectral region of excitation (λ_{ex}) by varying f and γ .

The near-field intensity enhancement (NFIE) is a crucial parameter for surface-enhanced spectroscopy and can be calculated as $|E|^2$ where $E = E_{loc}/E_0$ represents the enhanced (electric) near-field (E_{loc}) normalized by the incident field (E_0) [13,18]. We perform finite-difference time-domain (FDTD) [52,53] simulation to calculate the spatial near-field intensity profile of $|E|^2$ for the SEP mode shown in Fig. 3(d). Like SPP, the evanescent nature of the SEP mode can be seen from the figure and it is consistent with the earlier findings [31,40].

The performance of a RI sensor can be quantified in terms of its sensitivity (S) and figure of merit (F). The sensitivity of a SEP sensor is defined in the angular (spectral) domain as the change in the dip angular (spectral) position $\theta_{dip}(\lambda_{dip})$ divided by the change in the refractive index of the sensing medium (Δn_s) causing the change, i.e., $S_{\theta/\lambda} = \Delta(\theta/\lambda)_{dip}/\Delta n_s$. The angular (spectral) figure of merit, F , commonly used in plasmonic sensing is expressed as the angular (spectral) sensitivity divided by the angular (spectral) full-width at half-maximum (FWHM) of the SEP resonance dip, $\Delta\theta(\Delta\lambda)$ in air ($n_s = 1$), i.e., $F_{\theta/\lambda} = S_{\theta/\lambda}/\Delta(\theta/\lambda)$ [7,9,31]. In practice, the sensitivities (S_θ and S_λ) are calculated as a slope of the calibration curve, i.e., a plot of the reflectance minimum (θ_{dip} in deg and λ_{dip} in nm) as a function of the RI of sensing medium (n_s in refractive index unit or RIU). The slope is extracted from a linear fit on the calibration curve (see Fig. 9(a) in Appendix).

The effect of f and γ on the sensing performance of a SEP-based system can be understood from Fig. 4. From Fig. 4(a) it is clear that both angular sensitivity (S_θ) and figure of merit (F_θ) increase with increasing f when no broadening is considered ($\gamma = 0.05$ eV). Similar trend is found in spectral sensitivity (S_λ) and figure of merit (F_λ) as one can see in Fig. 4(c). Along with a rise in both sensitivities (S_θ and S_λ), the FWHM of the SEP mode experiences a narrowing in both angular ($\Delta\theta$) and spectral ($\Delta\lambda$) domains due to a sole rise in f only (see Fig. 9(c) in Appendix) which results in a monotonic increase in the figure of merits (F_θ and F_λ).

Incorporation of broadening, i.e., increasing γ within $\Delta\gamma$ while keeping $f = 0.5$, results in a drastic drop in S_θ and a mild fall in S_λ as one can see in Figs. 4(b) and 4(d). Moreover, both $\Delta\theta$ and $\Delta\lambda$ increase when the broadening is considered (see Fig. 9(d) in Appendix). As a result, both F_θ and F_λ drop with a sole rise in γ only. Such outcome implies that the performance of a SEP sensor can be tuned by varying its molecular concentration and the broadening counteracts the positive effect of increasing f .

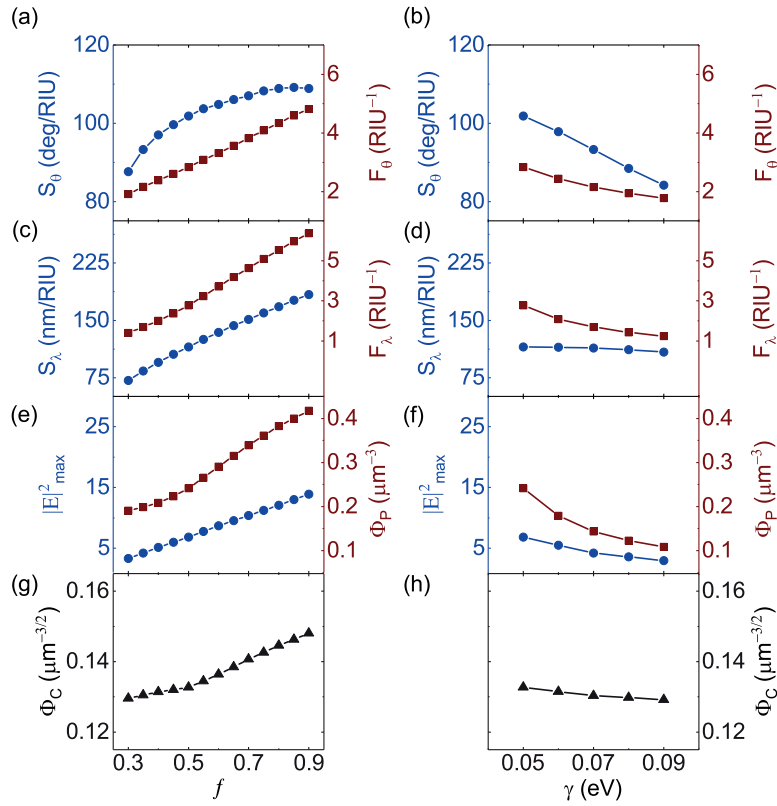


Fig. 4. Performance parameters of the SEP mode supported by a 60 nm thick TDBC-PVA film under the Kretschmann configuration - angular sensitivity (S_θ) and figure of merit (F_θ) as a function of (a) f and (b) γ ; spectral sensitivity (S_λ) and figure of merit (F_λ) as a function of (c) f and (d) γ ; NFIE maximum ($|E|^2_{max}$) and Purcell enhancement (Φ_P) as a function of (e) f and (f) γ ; field-confinement (Φ_C) as a function of (g) f and (h) γ . In the figures in left panel, f is varied when $\gamma = 0.05$ eV, while in right panel, γ is varied within $\Delta\gamma$ when $f = 0.5$. In (a)-(f), the blue and red vertical axes correspond to the blue and red curves, respectively. In all figures, the blue circles, red squares, and black triangles connected by the curves of corresponding color depict the discrete data points.

The performance of our SEP-based system as a resonant platform for near-field enhanced spectroscopy can be determined in terms of NFIE ($|E|^2$), Purcell enhancement, and field-confinement. The NFIE is directly proportional to the electromagnetic enhancement utilized in surface-enhanced spectroscopy [13,18]. The Purcell enhancement for a weak light-matter coupling is the amount of emission enhancement, which is determined by the ratio between the temporal and the spatial confinement of light field [54]. The temporal confinement is defined by the quality factor (Q) while the spatial confinement is determined by the mode volume (V_m), and thus the whole Purcell enhancement is $\Phi_P \propto Q/V_m$ [54,55]. The field-confinement is expressed as $\Phi_C = V_m^{-1/2}$, which is directly proportional to the coupling strength in a single-molecular picture, when the light-matter interaction is strong [17,56].

The effect of f and γ on $|E|^2$, Φ_P , and Φ_C can be seen in Figs. 4(e) to 4(h). We perform FDTD simulations to calculate the distribution of $|E|^2$ and the mode volume (V_m) [57] over a spatial region shown in Fig. 3(d) for different f and γ . In each case, we extract the maximum ($|E|^2_{max}$)

and the average ($|E|_{avg}^2$) of the NFIE distribution. From Figs. 4(e) and 4(f) it is evident that $|E|_{max}^2$ increases with a rise in f without broadening ($\gamma = 0.05$ eV) while drops when the broadening is considered (at $f = 0.5$). Similar trend is found for $|E|_{avg}^2$ (see Fig. 9(b) in Appendix).

The Purcell enhancement (Φ_P) and field-confinement (Φ_C) improve when Q increases along with a drop in V_m . That happens for increasing f when $\gamma = 0.05$ eV is constant (see Fig. 9(e) in Appendix). Consequently, Φ_P and Φ_C show a monotonic increase as a function of f as shown in Figs. 4(e) and 4(g). In the presence of broadening (at $f = 0.5$), however, Q decreases accompanied with a rise in V_m (see Fig. 9(f) in Appendix). Eventually, Φ_P and Φ_C drop with an increase in γ as depicted in Figs. 4(f) and 4(h). We can infer from such outcomes that efficiency of the SEP mode in confining and enhancing the near-field can be optimized by varying the molecular concentration and like sensing, here also the broadening acts against the positive effect of increasing f .

It is worth to mention here that excitonic thin films possessing SEP mode can be fabricated using solution-based techniques such as spin coating [27] and layer-by-layer deposition [44], which are relatively easy and inexpensive compared to the physical vapor deposition methods typically used to develop metal thin films supporting SPP modes [23,36].

4. Localized surface exciton

After showing that the SEP mode can be exploited for sensing and spectroscopy, and its efficiency can be tuned by the molecular concentration, we next investigate the localized surface exciton (LSE) based system, i.e., a TDBC-PVA nanosphere illustrated in Fig. 1(b). The radius (r) of the nanosphere is taken as 50 nm and the RI of the TDBC-PVA material (n_e) is obtained as $n_e = \sqrt{\epsilon}$ [51], where ϵ is calculated using Eq. (1). The RI of the sensing medium (n_s) is varied again from 1 to 1.01 with a step size of 0.001 to evaluate the performance of the sensor.

The LSE mode of an excitonic NP manifests as a broad peak in its extinction spectrum [27,32,33]. We employ Mie theory [58–62] implemented in MATLAB to compute the extinction efficiency, i.e., the extinction cross-section normalized by the geometrical cross-section, of the nanosphere since its size ($2r = 100$ nm) is beyond the quasi-static limit [63]. In our calculation, the NP is excited by normal incidence of light.

The simulated extinction efficiency (Q_{ext}) in air for the nanosphere with $f = 0.5$ and $\gamma = 0.05$ eV is reported in Fig. 5(a) where the LSE mode is profound as a broad peak around 569 nm. The spatial distribution of NFIE at that wavelength computed by the FDTD method is shown in Fig. 5(b) which resembles a dipolar resonance identical to the particle plasmon mode [64]. The spectral sensitivity (S_λ) and figure of merit (F_λ) of the excitonic nanosphere are calculated using the similar approach used for SEP where $\Delta\lambda$ is now the FWHM of the LSE mode at $n_s = 1$ (air) and λ_{dip} is replaced by the spectral peak position of the LSE mode (λ_{peak}). We track λ_{peak} (≈ 569 nm) as a function of n_s to construct the calibration curve. Then, S_λ is determined as the slope of that curve through a linear fit similar to the case of SEP.

The f -dependent profiles ($\gamma = 0.05$ eV) of the sensing parameters plotted in Fig. 5(c) depict that both S_λ and F_λ monotonically increase with a rise in f , similar to the trend found in the case of SEP. Incorporation of broadening, i.e., varying γ within $\Delta\gamma$ while $f = 0.5$, shows almost no effect on S_λ , however, F_λ drops significantly due to a rise in $\Delta\lambda$ (see Fig. 10 in Appendix), as one can see in Fig. 5(d).

The f - and γ -dependent profiles of $|E|^2$, Φ_P , and Φ_C for the LSE mode can be seen from Figs. 5(e) to 5(h). From the figures it is clear that similar to SEP, $|E|_{max}^2$ and Φ_C increase with rise in f only ($\gamma = 0.05$ eV) while drop when the broadening is incorporated (at $f = 0.5$). Identical trend is found for $|E|_{avg}^2$ while the trend is opposite for V_m (see Fig. 10 in Appendix) which explains the profile of Φ_C . Strikingly, the trend of Φ_P is monotonically decreasing irrespective of the broadening. That is because, unlike in SEP, $\Delta\lambda$ of the LSE mode increases and hence, Q drops regardless of whether f or γ is increasing (see Fig. 10 in Appendix). Based on these findings, we

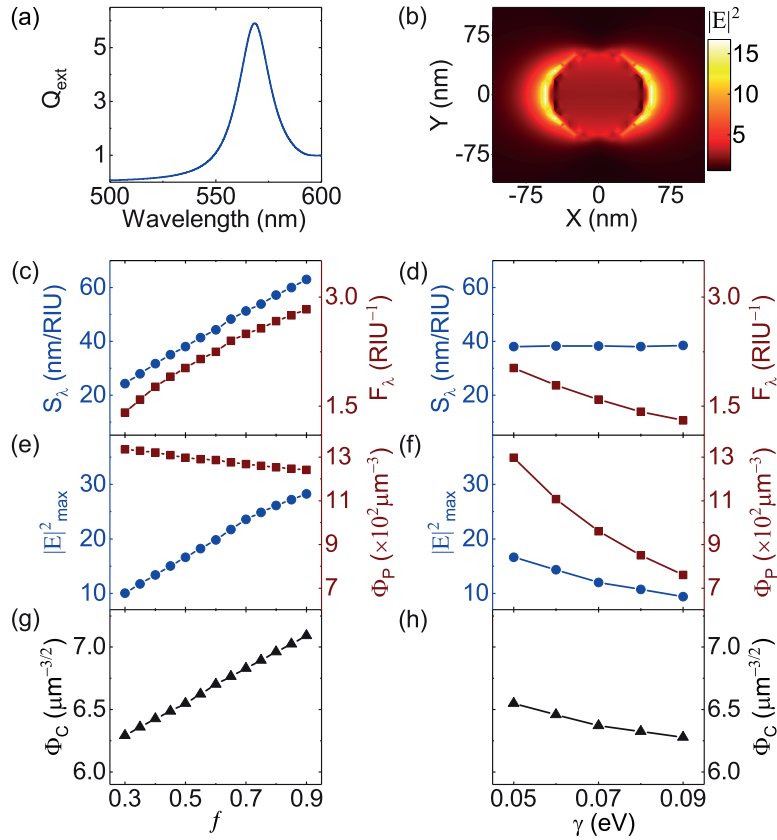


Fig. 5. (a) Extinction efficiency (Q_{ext}) of a TDBC-PVA nanosphere having a diameter of 100 nm, $f = 0.5$, and $\gamma = 0.05$ eV. (b) Spatial distribution of NFIE around the nanosphere in air at its LSE resonance wavelength 569 nm computed by FDTD method. Performance parameters of the LSE mode - spectral sensitivity (S_λ) and figure of merit (F_λ) as a function of (c) f and (d) γ ; NFIE maximum ($|E|^2_{max}$) and Purcell enhancement (Φ_P) as a function of (e) f and (f) γ ; field-confinement (Φ_C) as a function of (g) f and (h) γ . In the left panel of figures (c)-(h), f is varied when $\gamma = 0.05$ eV, while in the right panel, γ is varied within $\Delta\gamma$ when $f = 0.5$. The blue circles, red squares, and black triangles connected by the curves of corresponding color depict the calculated discrete data points. In (c)-(f), the blue and red vertical axes correspond to the blue and red curves, respectively.

can reckon that like SEP, the performance of the LSE mode in sensing and spectroscopy can also be modified via molecular concentration where the effects of f and γ are mostly counteracting.

It should be noted here that we choose excitonic nanospheres [27,32] as the LSE based system for simplicity and existence of an analytic solution. In practice, any arbitrary-shaped excitonic NP can support the LSE mode in the spectral regime where $Re\{\epsilon\} < -2$ [35,65]. Thus, an LSE based system can be fabricated either as a homogeneous system, e.g., a planar structure by lithographically patterning an excitonic thin film [66], or as a core-shell system, e.g., a dielectric

NP (core) coated with an excitonic material (shell) [33] using inexpensive chemical synthesis methods [41]. In both cases, one can avoid the expensive physical vapor deposition methods typically used to develop metal NPs supporting LSP modes [13].

5. Excitonic surface lattice resonance

After confirming that both the fundamental surface excitonic modes of the excitonic material are promising as a RI sensor and resonant substrate, we delve into a periodic array of previous NPs possessing excitonic surface lattice resonance (ESLR). The ESLR mode is usually much sharper/narrower and stronger than the dipolar LSE mode present in an isolated NP [9]. To advance this idea, we study a two-dimensional (2D) array (square lattice) of excitonic nanospheres having a well-defined lattice period (D) in both x and y directions as illustrated in Fig. 1(c).

The PSLR mode supported by a metal NP array performs optimally when the mediums above and below the array have identical RI, i.e., the difference between the refractive indices of the substrate and superstrate is very small [9,67,68]. For an excitonic NP array, the same index-matching condition applies and an asymmetric refractive-index environment (a large index mismatch between substrate and superstrate) results in a suppression of the ESLR mode. Keeping that in mind we consider that our designed array is in an index-matched environment having the same RI (n_s) everywhere. In practice, this can be implemented by having the array on a glass substrate with an index-matching oil on top [9,67]. The sensing performance of the array is evaluated by varying n_s similar to the case of SEP and LSE.

The ESLR mode of a NP array manifests as a sharp peak in the extinction spectrum of the array. Such mode can only be excited when the Rayleigh anomaly (or diffraction edge) of the array exists at a higher wavelength than the LSE mode of the individual NPs present in that array [9]. The lattice period (D) of our array is considered as $D = 400$ nm yielding the Rayleigh anomaly around 600 nm which is at a longer wavelength compared to the LSE mode of our individual nanosphere (569 nm). The number of nanospheres (N) included in the array is taken as $N = 400$ resulting in a square lattice of $N \times N$ nanospheres. The extinction profile of our NP array is computed using the coupled dipole (CD) method [34,69–76] implemented in MATLAB. In our computation, the array is excited by normal incidence of light and the nanospheres present in the array are identical with the one discussed in the previous section.

The simulated extinction efficiency (Q_{ext}) of the array is reported in Fig. 6(a) for $f = 0.5$ and $\gamma = 0.05$ eV. The sharp ESLR mode is profound at a wavelength of 606 nm, i.e., higher than the Rayleigh anomaly (600 nm) shown by the dashed vertical line. The spatial distribution of NFIE around each particle at the ESLR wavelength computed by the FDTD method is shown in Fig. 6(b). It clearly depicts a stronger dipole like resonance compared to that of the LSE mode.

The sensing behaviour of our NP array can be understood from Figs. 6(c) and 6(d) where the sensing parameters (S_λ and F_λ) are evaluated using the similar approach employed for the LSE mode. Interestingly, from the figures, one can see that unlike SEP and LSE, S_λ of the ESLR mode increases with both increasing f and γ . However, in both cases, F_λ drops noticeably. That is because, like in LSE, here also $\Delta\lambda$ of the ESLR mode increases along with a drop in Q regardless of whether f or γ is increasing (see Fig. 11 in Appendix).

The f - and γ -dependent profiles of $|E|_{max}^2$ reported in Figs. 6(e) and 6(f), respectively, show an increase in $|E|_{max}^2$ with a sole rise in f only ($\gamma = 0.05$ eV) while a drop when the broadening is incorporated (at $f = 0.5$). The trend is same for $|E|_{avg}^2$ (see Fig. 11 in Appendix) so as for Φ_C as shown in Figs. 6(g) and 6(h) due to a reciprocal trend in V_m (see Fig. 11 in Appendix). Despite that fact, Φ_P shows a decreasing nature due to the same trend in Q as mentioned before irrespective of the broadening. Such findings confirm the dependency of the ESLR mode on molecular concentration and thereby, its tunability considering the counteracting effects of f and γ .

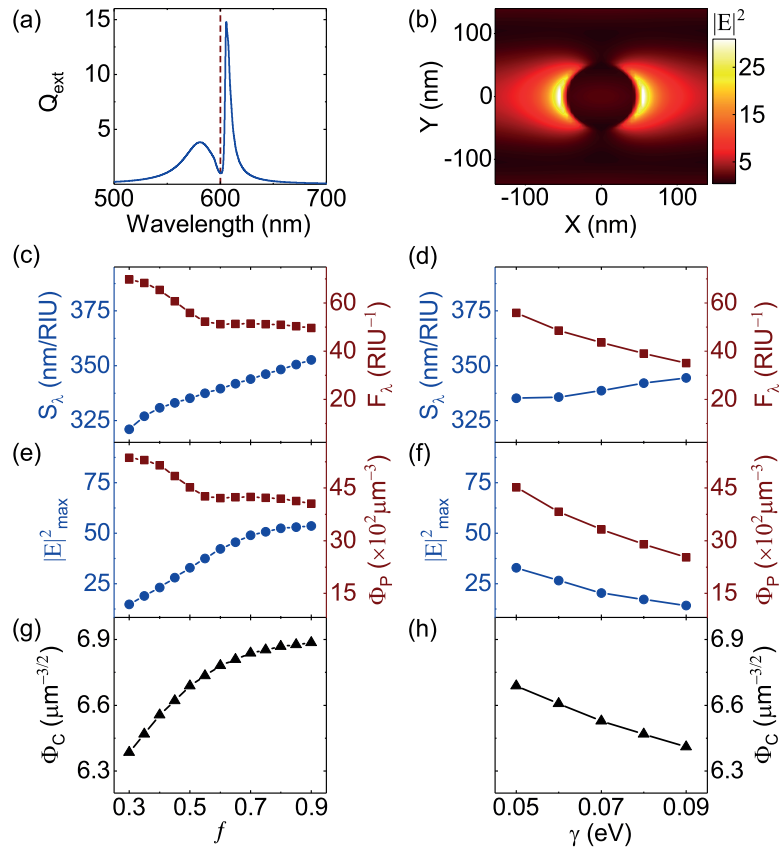


Fig. 6. (a) Extinction efficiency (Q_{ext}) of a 400×400 square lattice of TDBC-PVA nanospheres having a diameter of 100 nm and a lattice period of 400 nm with $f = 0.5$ and $\gamma = 0.05$ eV. The vertical dashed line represents the spectral position of the Rayleigh anomaly. (b) Spatial distribution of NFIE around a single particle computed by FDTD method at the wavelength of ESLR. Performance parameters of the ESLR - spectral sensitivity (S_λ) and figure of merit (F_λ) as a function of (c) f and (d) γ ; NFIE maximum ($|E|_{max}^2$) and Purcell enhancement (Φ_P) as a function of (e) f and (f) γ ; field-confinement (Φ_C) as a function of (g) f and (h) γ . In the left panel of figures (c)-(h), f is varied when $\gamma = 0.05$ eV while in the right panel, γ is varied within $\Delta\gamma$ when $f = 0.5$. The blue circles, red squares, and black triangles connected by the curves of corresponding color depict the calculated discrete data points. In (c)-(f), the blue and red vertical axes correspond to the blue and red curves, respectively.

It is worth to highlight here that like in LSE, we choose arrays of excitonic nanospheres [34] as the ESLR based system for simplicity. Considering the fact, that planar excitonic NPs can also support the surface excitonic modes [35,65], an ESLR based system can be fabricated as a planar NP array (or nano-hole array) by lithographically patterning an excitonic thin film [66]. Like in LSE, here also, one can avoid the expensive metal deposition methods typically used to develop metal NP arrays supporting ESLR modes [67,72].

6. Comparison with metals

To compare our excitonic systems with their plasmonic analogs, we study similar nanostructures (thin films, nanospheres, and their 2D arrays) made of silver (Ag) and gold (Au) in identical numerical environment. The material models for Ag and Au are taken from existing literature [77]. A detailed comparison in tabular form can be found in Table 1 (see Appendix).

Succinctly, we found that the SEP mode performs comparable or better in angular RI sensing compared to the SPP mode in Au which is consistent with the earlier finding [31]. The LSE mode provides comparable or better electromagnetic enhancement for surface-enhanced spectroscopy than that of the LSP mode in Au which is also inline with the existing literature [35]. Nevertheless, the most surprising and important finding is that all the surface excitonic modes (SEP, LSE, and ESLR) provide comparable (or even better) confinement of light in weak (Φ_P) and strong (Φ_C) coupling regimes compared to their plasmonic counterparts (Ag and Au). Such outcome strongly validates the fact that excitonic nanostructures are a potential alternative for plasmonic systems in RI sensing and enhanced spectroscopy. In our case, TDBC-PVA is a good replacement for Au, however, outperformed by Ag in the visible wavelengths.

7. Conclusion

Concisely, we investigated effect of molecular concentration on excitonic nanostructure based refractive index sensing and near-field enhancement suitable for surface enhanced spectroscopy. Three kinds of excitonic nanostructures were considered - a TDBC-PVA thin film supporting surface exciton polariton (SEP), a TDBC-PVA nanosphere possessing localized surface exciton (LSE), and a square lattice of similar nanospheres manifesting excitonic surface lattice resonance (ESLR). The effect of molecular concentration was studied by varying the oscillator strength (f) and the Lorentzian broadening (γ) of the TDBC-PVA material. The performance in sensing and spectroscopy was evaluated in terms of sensitivity, figure of merit, near-field intensity enhancement, Purcell enhancement, and field confinement. Our numerical findings revealed that most of the performance parameters showed a rise in their values when the oscillator strength was increased without any additional Lorentzian broadening. However, when the broadening was considered, the parameter values dropped implying a counteracting effect. Such outcome indicates that one can tune the optical performance of an excitonic system through its molecular concentration which is not possible in typical plasmonic systems. Moreover, different surface excitonic modes showed different degrees of tunability and equivalency in performance when compared to metals (silver and gold).

In line with our results on various excitonic systems, we can infer that to achieve an efficient performance from these systems, one should aim a molecular concentration corresponds to a large value of f . In practice, however, this approach might incur formation of molecular aggregates at extremely high concentration and thereby, induces challenge to maintain a relatively small value for γ within the broadening tolerance. Such limitation can be mitigated by selecting a molecule possessing strong transition dipole moment with narrow spectral linewidth since then a large f can be achieved with comparatively low molecular concentration while maintaining a small value of γ . Therefore, we can conclude that excitonic systems offer an extra degree of tunability via molecular concentration and are a promising alternative for plasmonics. Our comprehensive study provides key information to develop such alternative systems for organic nanophotonics.

Appendix

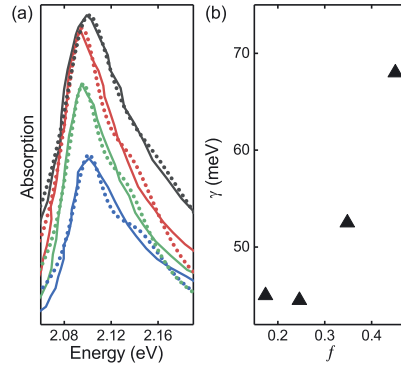


Fig. 7. (a) experimental (solid curves) and fitted (dotted curves) absorption spectra of TDBC J-aggregate thin films with increasing concentration. The experimental (solid curves) spectra are reproduced from Ref. [44]. (b) Lorentz linewidth (γ) as a function of oscillator strength (f) where the values for γ are directly from Ref. [44] while the values for f are obtained by fitting the absorption spectra reported in (a).

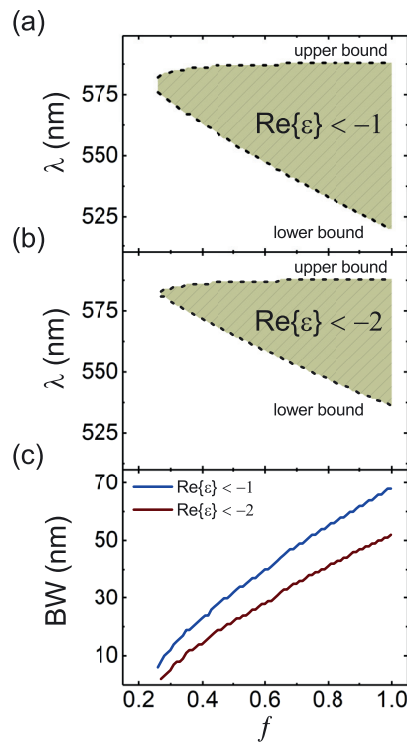


Fig. 8. Negative $Re\{\epsilon\}$ regime of TDBC-PVA system. Wavelength (λ) regions (shaded areas) as a function of oscillator strength (f) where $|Im\{\epsilon\}| < |Re\{\epsilon\}|$ with (a) $Re\{\epsilon\} < -1$ and (b) $Re\{\epsilon\} < -2$. (c) Spectral bandwidth of the surface excitonic modes as a function of f where the bandwidth (BW) is calculated as the difference between the upper and lower bounds shown as black dashed lines in (a)-(b).

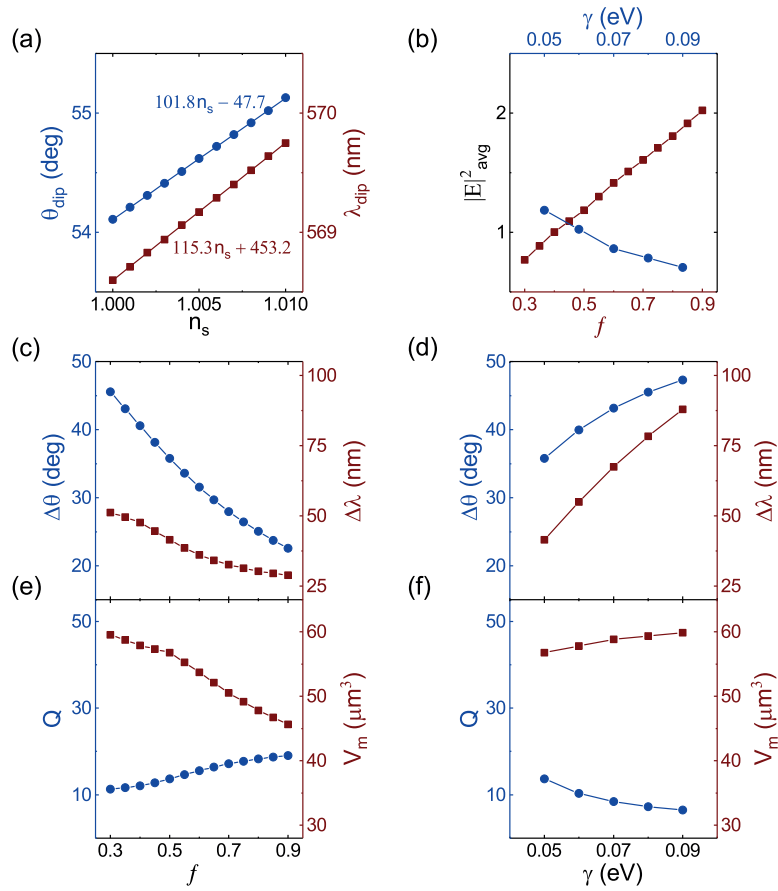


Fig. 9. Properties of the surface exciton polariton (SEP) mode of a 60 nm thick TDBC-PVA film under the Kretschmann configuration. (a) Calibration curves for refractive index (RI) sensing, i.e., reflection minimum (θ_{dip} and λ_{dip}) as a function of the RI of sensing medium (n_s). Linear fits on θ_{dip} and λ_{dip} are performed to calculate the sensitivities as the slopes of the fitted lines. (b) Average near-field intensity enhancement ($|E|^2_{avg}$) as a function of oscillator strength (f) and Lorentz linewidth (γ). Angular ($\Delta\theta$) and spectral ($\Delta\lambda$) full width at half maximum (FWHM) as a function of (c) f , and (d) γ . The quality factor (Q) and mode volume (V_m) as a function of (e) f , and (f) γ . In (b)-(f), f is varied with $\gamma = 0.05$ eV and γ is varied with $f = 0.5$. In (a) and (c)-(f), the blue and red vertical axes correspond to the blue and red curves, respectively. In (b), the blue and red horizontal axes correspond to the blue and red curves, respectively. In all figures, the blue circles and the red squares on the curves of corresponding color depict the discrete data points.

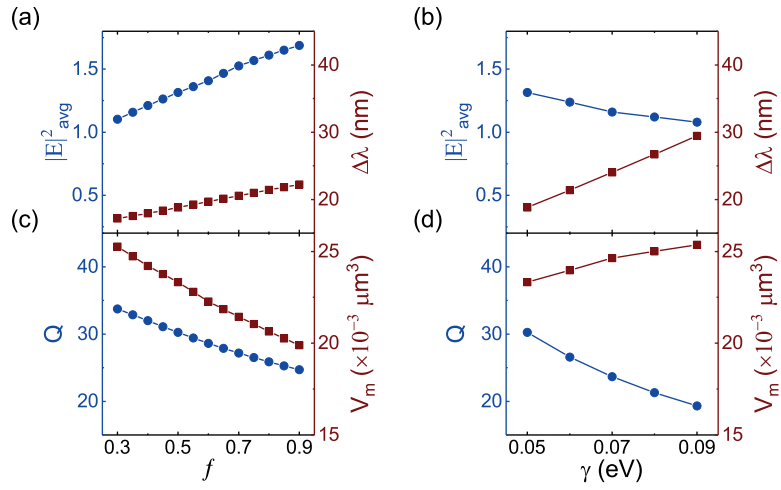


Fig. 10. Properties of the localized surface exciton (LSE) mode of a 100 nm TDBC-PVA nanosphere. Average near-field intensity enhancement ($|E|_{avg}^2$) and spectral full width at half maximum (FWHM) ($\Delta\lambda$) as a function of (a) oscillator strength (f), and (b) Lorentz linewidth (γ). The quality factor (Q) and mode volume (V_m) as a function of (c) f , and (d) γ . In all cases, f is varied with $\gamma = 0.05$ eV and γ is varied with $f = 0.5$. In all figures, the blue and red vertical axes correspond to the blue and red curves, respectively, while the blue circles and the red squares on the curves of corresponding color depict the discrete data points.

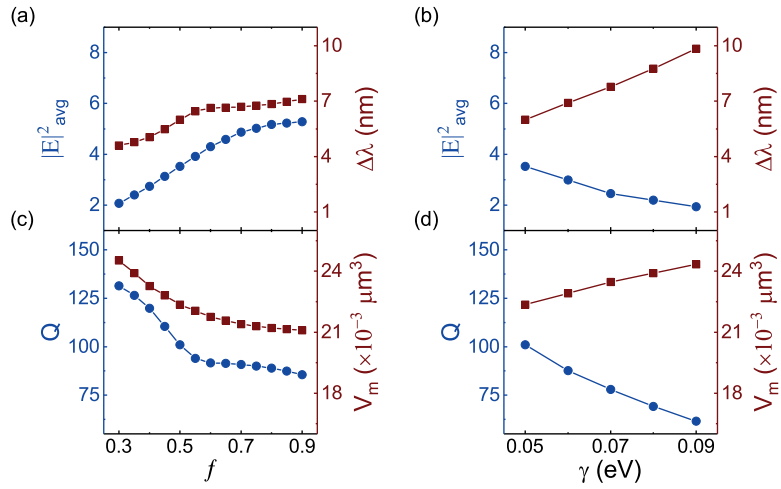


Fig. 11. Properties of the excitonic surface lattice resonance (ESLR) mode of a 400×400 square lattice of 100 nm TDBC-PVA nanospheres with a lattice period of 400 nm. Average near-field intensity enhancement ($|E|_{avg}^2$) and spectral full width at half maximum (FWHM) ($\Delta\lambda$) as a function of (a) oscillator strength (f), and (b) Lorentz linewidth (γ). The quality factor (Q) and mode volume (V_m) as a function of (c) f , and (d) γ . In all cases, f is varied with $\gamma = 0.05$ eV and γ is varied with $f = 0.5$. In all figures, the blue and red vertical axes correspond to the blue and red curves, respectively, while the blue circles and the red squares on the curves of corresponding color depict the discrete data points.

Table 1. Comparison between - surface plasmon polariton (SPP) and surface exciton polariton (SEP); localized surface plasmon (LSP) and localized surface exciton (LSE); plasmonic surface lattice resonance (PSLR) and excitonic surface lattice resonance (ESLR). The comparison is in terms of - angular (S_θ) and spectral (S_λ) sensitivities; angular (F_θ) and spectral (F_λ) figure of merits; maximum ($|E|_{max}^2$) and average ($|E|_{avg}^2$) of near-field intensity enhancement; quality factor (Q) and mode volume (V_m); Purcell enhancement (Φ_P) and field-confinement (Φ_C).

| | Ag | Au | TDBC-PVA |
|--|-----------------|-----------------|-------------|
| Parameters | SPP | SPP | SEP |
| S_θ (deg/RIU) | 210, 216 [78] | 64, 74 [31] | 84-109 |
| S_λ (nm/RIU) | 2051, 2000 [79] | 2711, 1600 [79] | 71-184 |
| F_θ (RIU ⁻¹) | 113 | 29 | 2-5 |
| F_λ (RIU ⁻¹) | 120 | 42 | 1-6 |
| $ E _{max}^2$ | 75 | 65 | 3-14 |
| $ E _{avg}^2$ | 8 | 8 | 1-2 |
| Q | 26 | 9 | 7-19 |
| V_m (μm^3) | 29 | 85 | 45-60 |
| Φ_P ($\times 10^{-2} \mu\text{m}^{-3}$) | 91 | 11 | 11-42 |
| Φ_C ($\times 10^{-2} \mu\text{m}^{-3/2}$) | 19 | 11 | 13-15 |
| Parameters | LSP | LSP | LSE |
| S_λ (nm/RIU) | 209, 160 [79] | 204, 203 [79] | 24-63 |
| F_λ (RIU ⁻¹) | 2 | 2 | 1-3 |
| $ E _{max}^2$ | 47 | 17 | 9-28 |
| $ E _{avg}^2$ | 2 | 2 | 1-2 |
| Q | 4 | 6 | 19-34 |
| V_m ($\times 10^{-3} \mu\text{m}^3$) | 16 | 25 | 20-25 |
| Φ_P (μm^{-3}) | 267 | 254 | 761-1335 |
| Φ_C ($\mu\text{m}^{-3/2}$) | 8 | 6 | 6-7 |
| Parameters | PSLR | PSLR | ESLR |
| S_λ (nm/RIU) | 433, 450 [80] | 440, 450 [80] | 321-353 |
| F_λ (RIU ⁻¹) | 20 | 14 | 35-70 |
| $ E _{max}^2$ | 360 | 128 | 14-54 |
| $ E _{avg}^2$ | 17 | 8 | 2-5 |
| Q | 29 | 21 | 62-132 |
| V_m ($\times 10^{-3} \mu\text{m}^3$) | 15 | 12 | 21-25 |
| Φ_P (μm^{-3}) | 1973 | 1707 | 2528-5359 |
| Φ_C ($\mu\text{m}^{-3/2}$) | 8 | 9 | 6-7 |

Funding. Academy of Finland (289947, 323995).

Acknowledgments. The authors would like to thank Academy of Finland under the grant nos. 289947 and 323995 for financial support of this project.

Disclosures. The authors declare no conflicts of interest.

Data availability. Data underlying the results presented in this paper are not publicly available at this time but may be obtained from the authors upon reasonable request.

References

1. S. A. Maier, *Plasmonics: Fundamentals and Applications* (Springer, 2007).

2. S. Enoch and N. Bonod, *Plasmonics: From Basics to Advanced Topics* (Springer, 2012).
3. T. V. Shahbazyan and M. I. Stockman, *Plasmonics: Theory and Applications* (Springer, 2013).
4. W. L. Barnes, A. Dereux, and T. W. Ebbesen, "Surface plasmon subwavelength optics," *Nature* **424**(6950), 824–830 (2003).
5. K. A. Willets and R. P. Van Duyne, "Localized surface plasmon resonance spectroscopy and sensing," *Annu. Rev. Phys. Chem.* **58**(1), 267–297 (2007).
6. V. G. Kravets, A. V. Kabashin, W. L. Barnes, and A. N. Grigorenko, "Plasmonic surface lattice resonances: a review of properties and applications," *Chem. Rev.* **118**(12), 5912–5951 (2018).
7. J. Homola, *Surface Plasmon Resonance Based Sensors* (Springer, 2006).
8. Y.-T. Long and C. Jing, *Localized Surface Plasmon Resonance Based Nanobiosensors* (Springer, 2014).
9. B. Špačková and J. Homola, "Sensing properties of lattice resonances of 2D metal nanoparticle arrays: an analytical model," *Opt. Express* **21**(22), 27490–27502 (2013).
10. J. Homola, "Surface plasmon resonance sensors for detection of chemical and biological species," *Chem. Rev.* **108**(2), 462–493 (2008).
11. P. Offermans, M. C. Schaafsma, S. R. K. Rodriguez, Y. Zhang, M. Crego-Calama, S. H. Brongersma, and J. G. Rivas, "Universal scaling of the figure of merit of plasmonic sensors," *ACS Nano* **5**(6), 5151–5157 (2011).
12. A. Dutta, T. Nuutinen, K. Alam, A. Matikainen, P. Li, E. Hulkko, J. J. Toppari, H. Lipsanen, and G. Kang, "Fabrication-friendly polarization-sensitive plasmonic grating for optimal surface-enhanced Raman spectroscopy," *J. Eur. Opt. Soc.-Rapid Publ.* **16**(1), 22 (2020).
13. A. Dutta, K. Alam, T. Nuutinen, E. Hulkko, P. Karvinen, M. Kuittinen, J. J. Toppari, and E. M. Vartiainen, "Influence of Fano resonance on SERS enhancement in Fano-plasmonic oligomers," *Opt. Express* **27**(21), 30031–30043 (2019).
14. A. Dutta, A. Matikainen, S. Andoh, and T. Nuutinen, "SERS activity of photoreduced silver chloride crystals," *AIP Conf. Proc.* **2220**, 050004 (2020).
15. F. Laux, N. Bonod, and D. Gérard, "Single emitter fluorescence enhancement with surface lattice resonances," *J. Phys. Chem. C* **121**(24), 13280–13289 (2017).
16. S. A. Maier, "Plasmonic field enhancement and SERS in the effective mode volume picture," *Opt. Express* **14**(5), 1957–1964 (2006).
17. Z.-J. Yang, T. J. Antosiewicz, and T. Shegai, "Role of material loss and mode volume of plasmonic nanocavities for strong plasmon-exciton interactions," *Opt. Express* **24**(18), 20373–20381 (2016).
18. A. Dutta and E. M. Vartiainen, "Spatial localization of hotspots in Fano-resonant plasmonic oligomers for surface-enhanced coherent anti-Stokes Raman scattering," *J. Eur. Opt. Soc.-Rapid Publ.* **16**(1), 8 (2020).
19. H. Yu, Y. Peng, Y. Yang, and Z.-Y. Li, "Plasmon-enhanced light-matter interactions and applications," *npj Comput. Mater.* **5**(1), 45 (2019).
20. J.-F. Li, C.-Y. Li, and R. F. Aroca, "Plasmon-enhanced fluorescence spectroscopy," *Chem. Soc. Rev.* **46**(13), 3962–3979 (2017).
21. J. Langer, J. de Aberasturi, and J. Aizpurua, *et al.*, "Present and future of surface-enhanced Raman scattering," *ACS Nano* **14**(1), 28–117 (2020).
22. F. Neubrech, C. Huck, K. Weber, A. Pucci, and H. Giessen, "Surface-enhanced infrared spectroscopy using resonant nanoantennas," *Chem. Rev.* **117**(7), 5110–5145 (2017).
23. S. Baeva, O. Hakamaa, G. Groenhof, T. T. Heikkilä, and J. J. Toppari, "Dynamics of strongly coupled modes between surface plasmon polaritons and photoactive molecules: the effect of the Stokes shift," *ACS Photonics* **4**(1), 28–37 (2017).
24. A. E. Schlather, N. Large, A. S. Urban, P. Nordlander, and N. J. Halas, "Near-field mediated plexcitonic coupling and giant Rabi splitting in individual metallic dimers," *Nano Lett.* **13**(7), 3281–3286 (2013).
25. A. I. Väkeväinen, R. J. Moerland, H. T. Rekola, A.-P. Eskelinen, J.-P. Martikainen, D.-H. Kim, and P. Törmä, "Plasmonic surface lattice resonances at the strong coupling regime," *Nano Lett.* **14**(4), 1721–1727 (2014).
26. L. Gu, J. Livenere, G. Zhu, E. E. Narimanov, and M. A. Noginov, "Quest for organic plasmonics," *Appl. Phys. Lett.* **103**(2), 021104 (2013).
27. M. J. Gentile, S. Núñez-Sánchez, and W. L. Barnes, "Optical field-enhancement and subwavelength field-confinement using excitonic nanostructures," *Nano Lett.* **14**(5), 2339–2344 (2014).
28. R. Yu, L. M. Liz-Marzán, and F. J. García de Abajo, "Universal analytical modeling of plasmonic nanoparticles," *Chem. Soc. Rev.* **46**(22), 6710–6724 (2017).
29. D. Barchiesi and T. Grosjes, "Fitting the optical constants of gold, silver, chromium, titanium, and aluminum in the visible bandwidth," *J. Nanophotonics* **8**(1), 083097 (2014).
30. K. Takatori, T. Okamoto, K. Ishibashi, and R. Micheletto, "Surface exciton polaritons supported by a J-aggregate-dye/air interface at room temperature," *Opt. Lett.* **42**(19), 3876–3879 (2017).
31. Y. Xu, L. Wu, and L. K. Ang, "Surface exciton polaritons: a promising mechanism for refractive-index sensing," *Phys. Rev. Appl.* **12**(2), 024029 (2019).
32. M. J. Gentile, S. A. R. Horsley, and W. L. Barnes, "Localized exciton-polariton modes in dye-doped nanospheres: a quantum approach," *J. Opt.* **18**(1), 015001 (2016).
33. M. J. Gentile and W. L. Barnes, "Hybridised exciton-polariton resonances in core-shell nanoparticles," *J. Opt.* **19**(3), 035003 (2017).

34. A. D. Humphrey, M. J. Gentile, and W. L. Barnes, "Excitonic surface lattice resonances," *J. Opt.* **18**(8), 085004 (2016).
35. A. Cacciola, C. Triolo, O. D. Stefano, A. Genco, M. Mazzeo, R. Saija, S. Patanè, and S. Savasta, "Subdiffraction light concentration by J-aggregate nanostructures," *ACS Photonics* **2**(7), 971–979 (2015).
36. S. Baieva, T. K. Hakala, and J. J. Toppari, "Strong coupling between surface plasmon polaritons and sulforhodamine 101 dye," *Nanoscale Res. Lett.* **7**(1), 191 (2012).
37. A. Dutta, V. Tiainen, H. A. Qureshi, L. Duarte, and J. J. Toppari, "Modeling optical constants from the absorption of organic thin films using a modified Lorentz oscillator model," *Opt. Mater. Express* **12**(7), 2855–2869 (2022).
38. B. Valeur and M. N. Berberan-Santos, *Molecular Fluorescence: Principles and Applications* (Wiley-VCH, 2012).
39. A. Canales, D. G. Baranov, T. J. Antosiewicz, and T. Shegai, "Abundance of cavity-free polaritonic states in resonant materials and nanostructures," *J. Chem. Phys.* **154**(2), 024701 (2021).
40. W. J. Tan, P. A. Thomas, I. J. Luxmoore, and W. L. Barnes, "Single vs double anti-crossing in the strong coupling between surface plasmons and molecular excitons," *J. Chem. Phys.* **154**(2), 024704 (2021).
41. G. Zengin, G. Johansson, P. Johansson, T. J. Antosiewicz, M. Käll, and T. Shegai, "Approaching the strong coupling limit in single plasmonic nanorods interacting with J-aggregates," *Sci. Rep.* **3**(1), 3074 (2013).
42. D. M. Coles, P. Michetti, C. Clark, A. M. Adawi, and D. G. Lidzey, "Temperature dependence of the upper-branch polariton population in an organic semiconductor microcavity," *Phys. Rev. B* **84**(20), 205214 (2011).
43. K. Das, J. Dey, M. S. Verma, M. Kumar, and M. Chandra, "Probing the role of oscillator strength and charge of exciton forming molecular J-aggregates in controlling nanoscale plasmon–exciton interactions," *Phys. Chem. Chem. Phys.* **22**(36), 20499–20506 (2020).
44. M. S. Bradley, J. R. Tischler, and V. Bulović, "Layer-by-layer J-aggregate thin films with a peak absorption constant of 10^6 cm^{-1} ," *Adv. Mater.* **17**(15), 1881–1886 (2005).
45. T. G. Mackay and A. Lakhtakia, *The Transfer-Matrix Method in Electromagnetics and Optics* (Morgan and Claypool, 2020).
46. K. J. Pascoe, *Reflectivity and Transmissivity Through Layered, Lossy Media: A User-Friendly Approach* (Wright Patterson Air Force Base, 2001).
47. K. Sayood, *Learning Programming Using MATLAB* (Morgan and Claypool, 2006).
48. <https://www.mathworks.com/products/matlab.html>.
49. L. C. Oliveira, A. M. N. Lima, C. Thirstrup, and H. F. Neff, *Surface Plasmon Resonance Sensors* (Springer, 2019).
50. K. Takagi, S. V. Nair, R. Watanabe, K. Seto, T. Kobayashi, and E. Tokunaga, "Surface plasmon polariton resonance of gold, silver, and copper studied in the Kretschmann geometry: dependence on wavelength, angle of incidence, and film thickness," *J. Phys. Soc. Jpn.* **86**(12), 124721 (2017).
51. I. Chambouleyron and J. M. Martínez, "Optical properties of dielectric and semiconductor thin films," in *Handbook of Thin Films*, H. S. Nalwa, ed. (Academic Press, 2002).
52. S. D. Gedney, *Introduction to the Finite-Difference Time-Domain (FDTD) Method for Electromagnetics* (Morgan and Claypool, 2011).
53. <https://www.ansys.com/products/photonics/fdtd>.
54. K. J. Vahala, "Optical microcavities," *Nature* **424**(6950), 839–846 (2003).
55. A. Dutta, V. Tiainen, and J. J. Toppari, "Optimizing geometry of low-Q all-metal Fabry-Pérot microcavity for fluorescence spectroscopy," *IOPSciNotes* **2**(1), 015205 (2021).
56. M. S. Rider and W. L. Barnes, "Something from nothing: linking molecules with virtual light," *Contemp. Phys.* **62**(4), 217–232 (2021).
57. <https://optics.ansys.com/hc/en-us/articles/360034395374>.
58. C. F. Bohren and D. R. Huffman, *Absorption and Scattering of Light by Small Particles* (Wiley-VCH, 1998).
59. G. Baffou, *Thermoplasmonics: Heating Metal Nanoparticles Using Light* (Cambridge University Press, 2017).
60. M. Quinten, *Optical Properties of Nanoparticle Systems: Mie and Beyond* (Wiley-VCH, 2011).
61. A. Trügler, *Optical Properties of Metallic Nanoparticles* (Springer, 2016).
62. K. Travis and J. Guck, "Scattering from single nanoparticles: Mie theory revisited," *Biophys. Rev. Lett.* **01**(02), 179–207 (2006).
63. A. Dutta, V. Tiainen, and J. J. Toppari, "Numerical study on the limit of quasi-static approximation for plasmonic nanosphere," *AIP Conf. Proc.* **2220**, 050012 (2020).
64. W. L. Barnes, "Particle plasmons: why shape matters," *Am. J. Phys.* **84**(8), 593–601 (2016).
65. S. T. Holder, C. Estévez-Varela, I. Pastoriza-Santos, M. Lopez-García, R. Oulton, and S. Núñez-Sánchez, "Bio-inspired building blocks for all-organic metamaterials from visible to near-infrared," *Nanophotonics* **12**(2), 307–318 (2023).
66. S. Chen, E. S. H. Kang, M. S. Chaharsoughi, V. Stanishev, P. Kühne, H. Sun, C. Wang, M. Fahlman, S. Fabiano, V. Darakchieva, and M. P. Jonsson, "Conductive polymer nanoantennas for dynamic organic plasmonics," *Nat. Nanotechnol.* **15**(1), 35–40 (2020).
67. D. Khlopin, F. Laux, W. P. Wardley, J. Martin, G. A. Wurtz, J. Plain, N. Bonod, A. V. Zayats, W. Dickson, and D. Gérard, "Lattice modes and plasmonic linewidth engineering in gold and aluminum nanoparticle arrays," *J. Opt. Soc. Am. B* **34**(3), 691–700 (2017).
68. B. Auguie, X. M. Bendaña, W. L. Barnes, and F. J. García de Abajo, "Diffractive arrays of gold nanoparticles near an interface: critical role of the substrate," *Phys. Rev. B* **82**(15), 155447 (2010).

69. S. Zou, N. Janel, and G. C. Schatz, "Silver nanoparticle array structures that produce remarkably narrow plasmon lineshapes," *J. Chem. Phys.* **120**(23), 10871–10875 (2004).
70. S. Zou and G. C. Schatz, "Narrow plasmonic/photonic extinction and scattering line shapes for one and two dimensional silver nanoparticle arrays," *J. Chem. Phys.* **121**(24), 12606–12612 (2004).
71. C. Cherqui, M. R. Bourgeois, D. Wang, and G. C. Schatz, "Plasmonic surface lattice resonances: theory and computation," *Acc. Chem. Res.* **52**(9), 2548–2558 (2019).
72. R. Adato, A. A. Yanik, C.-H. Wu, G. Shvets, and H. Altug, "Radiative engineering of plasmon lifetimes in embedded nanoantenna arrays," *Opt. Express* **18**(5), 4526–4537 (2010).
73. B. Augu e and W. L. Barnes, "Collective resonances in gold nanoparticle arrays," *Phys. Rev. Lett.* **101**(14), 143902 (2008).
74. A. D. Humphrey and W. L. Barnes, "Plasmonic surface lattice resonances on arrays of different lattice symmetry," *Phys. Rev. B* **90**(7), 075404 (2014).
75. A. D. Humphrey and W. L. Barnes, "Plasmonic surface lattice resonances in arrays of metallic nanoparticle dimers," *J. Opt.* **18**(3), 035005 (2016).
76. S. Zou and G. C. Schatz, "Theoretical studies of plasmon resonances in one-dimensional nanoparticle chains: narrow lineshapes with tunable widths," *Nanotechnology* **17**(11), 2813–2820 (2006).
77. P. B. Johnson and R. W. Christy, "Optical constants of the noble metals," *Phys. Rev. B* **6**(12), 4370–4379 (1972).
78. A. H. M. Almwagani, S. K. Awasthi, A. Mehaney, G. A. Ali, H. A. Elsayed, H. Sayed, and A. M. Ahmed, "A theoretical approach for a new design of an ultrasensitive angular plasmonic chemical sensor using black phosphorus and aluminum oxide architecture," *RSC Adv.* **13**(24), 16154–16164 (2023).
79. Y. Xu, P. Bai, X. Zhou, Y. Akimov, C. E. Png, L.-K. Ang, W. Knoll, and L. Wu, "Optical refractive index sensors with plasmonic and photonic structures: promising and inconvenient truth," *Adv. Opt. Mater.* **7**(9), 1801433 (2019).
80. A. Minopoli, A. Acunzo, B. D. Ventura, and R. Velotta, "Nanostructured surfaces as plasmonic biosensors: a review," *Adv. Mater. Interfaces* **9**(2), 2101133 (2022).

PVIII

**WEAK AND STRONG COUPLING PROPERTIES OF SURFACE
EXCITONS**

by

A. Dutta and J. J. Toppari,

ChemRxiv, **Preprint**, 10.26434/chemrxiv-2023-ldwcs (2023).

Reproduced with kind permission of all the authors.

Weak and Strong Coupling Properties of Surface Excitons

Arpan Dutta* and J. Jussi Toppari†
Nanoscience Center and Department of Physics
University of Jyväskylä, P.O. Box 35, FI-40014, Finland

With high enough doping concentrations organic dye doped polymer materials exhibit negative real part of the permittivity within an energy range just above their material absorption, incurring surface exciton modes at these energies. Here, we report how such modes can be used to realize strong light-matter coupling with photoactive molecules. Our simulations reveal that surface excitons can facilitate strong coupling in terms of induced transparency, however, the polaritons may not be visible in the absorption since they can easily be located outside of the narrow negative permittivity regime. Moreover, we show that the surface exciton modes cannot couple strongly with the surface plasmons. Our findings shed light on the weak and strong coupling properties of surface excitons.

Polymer materials doped with organic dyes possessing Frenkel excitons are an important class of excitonic materials in modern resonant nanophotonics [1–10]. If the doping concentration is high enough, the real part of the dielectric function ($\Re\{\epsilon(\omega)\}$) of such excitonic materials becomes negative within an energy regime just above the material absorption [1, 2]. This negative $\Re\{\epsilon(\omega)\}$ regime can sustain surface exciton (SE) modes that are analogous to the surface plasmon (SP) modes in plasmonic metallic systems [1, 2, 5–11]. Eventually, like SP modes, such SE modes can be exploited in refractive-index sensing [6, 11] and in near-field enhanced spectroscopy [10, 11]. Moreover, these SE modes possess lower material losses compared to SP modes [1] and unlike SPs, their optical performance can be tuned by varying the doping concentration [11].

In this letter, we numerically investigate the performance of the SE modes when employed in strong light-matter coupling, and compare this to a similar case of SP modes. We further examine the coupling between SE and SP modes to explore light coupling properties of SEs.

To facilitate strong light-matter coupling, we consider a core-shell geometry as shown in Fig. 1. The core radius (r_{core}) is considered to be 50 nm while the shell thickness (t_{shell}) is taken as 25 nm leading to a shell outer radius (r_{shell}) of 75 nm. The complex-dispersive dielectric functions of the core and shell materials are $\epsilon_{core}(\omega)$ and $\epsilon_{shell}(\omega)$, respectively.

At first, we consider a gold (Au) core with a generic dye shell to study strong light-matter coupling between organic molecules and the SP mode as a reference case. The dielectric function of the Au core ($\epsilon_{core}(\omega)$) is obtained from the literature [12] while the same for the dye shell ($\epsilon_{shell}(\omega)$) is modelled using the Lorentz oscillator model (LOM) [2, 11].

In LOM, the dielectric function is expressed as

$$\epsilon(E) = \epsilon_{\infty} + \frac{fE_0^2}{(E_0^2 - E^2 - i\gamma E)}, \quad (1)$$

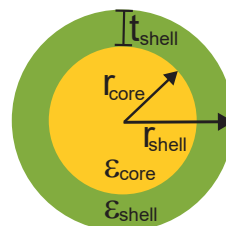


FIG. 1. Core-shell nanoparticle geometry. The core radius (r_{core}) is considered as 50 nm while the shell thickness (t_{shell}) is taken as 25 nm. The shell outer radius (r_{shell}) is thus 75 nm. The complex-dispersive dielectric functions of the core and shell materials are $\epsilon_{core}(\omega)$ and $\epsilon_{shell}(\omega)$, respectively.

where $E = \hbar\omega$ is the energy, ϵ_{∞} is the dielectric constant of the host polymer, f is the oscillator strength of the molecular absorption having E_0 as its spectral peak position and γ as its spectral linewidth. For the generic dye shell, we consider $\epsilon_{\infty} = 1.45^2$ and $\gamma = 0.1$ eV since these numbers correspond well to the realistic dyes [13]. The spectral peak E_0 is set to 2.28 eV to have a spectral match with the absorption maximum of the SP mode of the gold core (E_c). The change in molecular concentration of the shell is modelled by varying f (f_{dye}) as 0.01, 0.03, 0.05, 0.10, 0.15, and 0.20.

The optical properties of such core-shell nanoparticle is calculated using Mie theory [14] implemented in MATLAB [15] since the nanoparticle size is beyond the quasi-static limit [16]. We examine the absorption (absorption efficiency, *i.e.*, absorption cross-sections normalized by geometrical cross-section) of the core-shell system since signature of strong coupling is more clearly manifested in that than in the scattering or extinction [17, 18]. The black and red curves in Fig. 2(a) show the absorption of the plain dye shell and sole Au core, respectively, with a spectral tuning of the dye at $E_c = 2.28$ eV. For the coupled system, an increase in f_{dye} incurs a rise in the energy splitting, *i.e.*, an increase in the energy separation between the upper (UP) and lower (LP) polariton branches as shown in Fig. 2(a). Such finding is consistent with the earlier reports on plasmon-molecule strong cou-

* arpan.a.dutta@jyu.fi

† j.jussi.toppari@jyu.fi

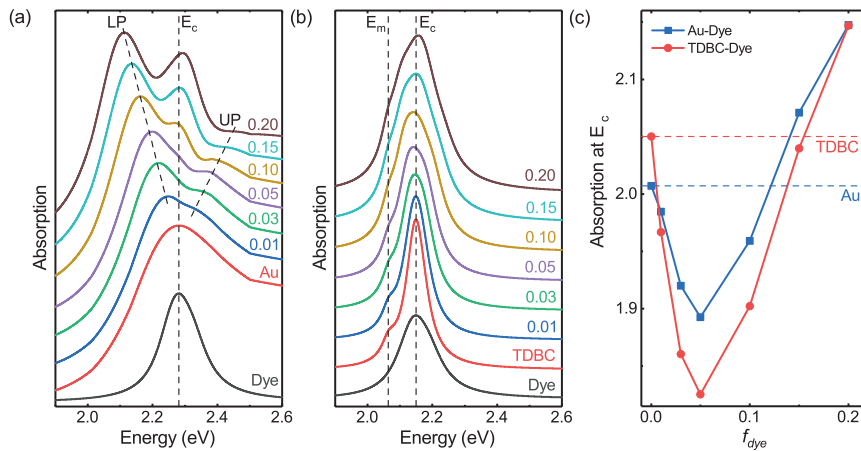


FIG. 2. (a) Absorption spectra of generic dye shell (black), Au core (red), and the core-shell coupled system for different values of f_{dye} (0.01, 0.03, 0.05, 0.10, 0.15, and 0.20) and for $\gamma = 0.1$ eV. The spectra are shifted vertically for clarity. The absorption of the dye shell is spectrally tuned to the same as the Au core absorption maximum, *i.e.*, $E_0 = E_c = 2.28$ eV (vertical dashed line). The lower (LP) and upper (UP) polariton branches are shown by the tilted black dashed lines. (b) Absorption spectra of generic dye shell (black), TDBC core (red), and the core-shell coupled system with the same γ and f_{dye} values as in (a). The spectra are shifted vertically for clarity. The SE mode of the TDBC core ($E_m = 2.08$ eV) and the material absorption of TDBC ($E_c = 2.15$ eV) are shown by the vertical dashed black lines. The absorption of the dye shell is spectrally tuned with E_c . (c) Absorption at E_c for Au core-dye shell ($E_c = 2.28$ eV) and TDBC core-dye shell ($E_c = 2.15$ eV) coupled systems as a function of f_{dye} . The blue and red horizontal dashed lines show the core absorption for Au and TDBC, respectively. The blue squares and red circles on the curves of corresponding color depict the discrete data points. In (a)-(c), absorption means absorption efficiency, *i.e.*, absorption cross-sections normalized by geometrical cross-section.

pling in core-shell systems [13, 17–20]. In Fig. 2(a), we also see that for high values of f_{dye} (0.10, 0.15, and 0.20), an absorption peak reappears around E_c . The presence of this third peak is due to the absorption of the non-hybridized molecular excitons when the exciton number (*i.e.*, f_{dye}) is high [21].

Now, let us assume a fully organic core-shell system having an excitonic core possessing SE mode and a generic dye shell. To study the strong light-matter coupling between organic molecules and the SE mode, we consider the TDBC J-aggregate as the core material since TDBC nanostructures are shown to support SE modes at room temperature [2, 5–11]. It is worth to highlight here that even though both core and shell are now made of organic materials modelled by Eq. (1), the TDBC core possesses a negative $\Re\{\epsilon(\omega)\}$ regime and hence, supports a SE mode along with its molecular absorption. However, the generic dye shell has only its molecular absorption and no such SE mode since its $\Re\{\epsilon(\omega)\}$ is always positive.

We chose the LOM parameters for the TDBC core ($\epsilon_{core}(\omega)$) as $\epsilon_\infty = 1.45^2$, $\gamma = 0.05$ eV, $f = 0.5$, and $E_0 = 2.08$ eV to be consistent with the existing literature [13]. The red curve in Fig. 2(b) shows the absorption of such excitonic core having the SE mode as a strong peak at $E_c = 2.15$ eV and the material absorption of TDBC as a shoulder peak at $E_m = 2.08$ eV. To have a spectral match with the SE mode (E_c) of the TDBC core, the E_0

for the generic dye shell is set to 2.15 eV with $\gamma = 0.1$ eV and with the same ϵ_∞ as in core. The change in molecular concentration of the shell is modelled by varying the f in Eq. (1) for the shell (*i.e.*, f_{dye}) similar to the case of Au core. The black curve in Fig. 2(b) shows the shell absorption having a spectral tuning with the SE mode of the TDBC core at $E_c = 2.15$ eV.

Considering the fact that SEs provide field-confinement and field-enhancement analogous to SPs [2, 7, 8, 10, 11], one should expect strong coupling between the SE mode of the TDBC core and the generic dye shell resulting in an emergence of polariton peaks in the absorption of the coupled system. However, with an increase in f_{dye} , no such energy splitting is found for the coupled system as one can see in Fig. 2(b). The absorption around E_c is only slightly broadened as the f_{dye} increases. Apparently, such outcome hints that unlike SPs, SE mode might not be able to facilitate strong coupling.

To have a closer look, we calculate the absorption of the coupled system at E_c as a function of f_{dye} in the cases of Au core (SP) and TDBC core (SE) as reported in Fig. 2(c). For both coupled systems, the absorption at E_c drops at first due to the energy-splitting induced transparency [13] and then rises due to the appearance of nonhybridized molecular excitons when the exciton number, *i.e.*, f_{dye} is high enough [21]. It is interesting that the coupling between organic molecules and the SE mode

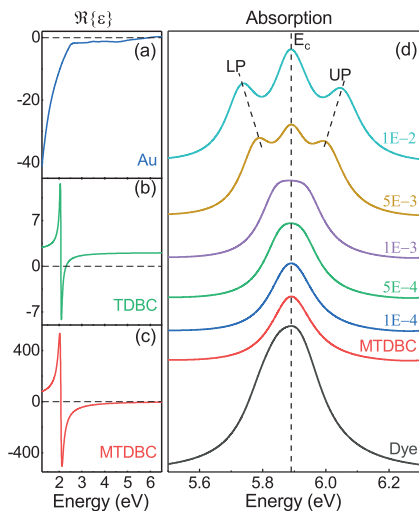


FIG. 3. Real part of the dielectric function ($\Re\{\epsilon(\omega)\}$) for (a) Au, (b) TDBC, and (c) MTDBC as a function of energy. (d) Absorption spectra of generic dye shell (black), MTDBC core (red), and the core-shell coupled system for different values of f_{dye} (0.0001, 0.0005, 0.001, 0.005, and 0.01). The spectra are vertically shifted for clarity. The absorption of the dye shell is spectrally tuned to match the SE mode energy of the MTDBC core, *i.e.*, $E_0 = E_c = 5.9$ eV (vertical dashed line). The lower (LP) and upper (UP) polariton branches are shown by the tilted black dashed lines. In the figure, absorption means absorption efficiency, *i.e.*, absorption cross-sections normalized by geometrical cross-section.

shows a trend similar to the case of plasmon-molecule coupling. Such result indicates that SE modes can facilitate strong coupling even though the polaritons are not visible in the absorption spectra of the coupled system.

The SE modes in excitonic (TDBC) nanostructures can outperform SP modes in their plasmonic (Au) analogs in terms of field-confinement (quality factor and mode volume) and coupling strength [11]. Here also, the quality factor [22] of the SE mode is higher than that of the SP mode as one can see by comparing the red curves in Figs. 2(a) and 2(b). Consequently, the SE mode provides deeper transparency at E_c , *i.e.*, stronger coupling compared to the SP mode, as depicted in Fig. 2(c).

To understand the absence of polaritons in the absorption of the TDBC core-dye shell system we compare $\Re\{\epsilon(\omega)\}$ spectra of Au and TDBC reported in Figs. 3(a) and 3(b), respectively. The negative regime of $\Re\{\epsilon(\omega)\}$ for Au is very broad and thus can support the SP mode and the polaritons around it over the spectral range of interest. Eventually, the polaritons and the induced transparency are clearly visible in the absorption spectra. For TDBC, the negative regime of $\Re\{\epsilon(\omega)\}$ is extremely narrow. We argue that such narrow regime can only support the SE mode and the induced transparency caused by it while the polaritons lie outside that regime and hence, are

not visible in the absorption. To validate our argument we consider a modified TDBC (MTDBC) material modelled by Eq. 1 with a huge oscillator strength of $f = 50$ and $\gamma = 0.1$ eV while all other LOM parameters are kept identical with the TDBC. Such a large value of f yields a very broad negative regime of $\Re\{\epsilon(\omega)\}$ for MTDBC like in the case of Au as shown in Fig. 3(c). It is important to note here that our MTDBC material is unrealistic for J-aggregates and used here only as a proof of concept.

Now, let's consider a MTDBC core having the same geometry as Fig. 1. The geometry is kept the same to be able to directly compare the absorption efficiencies. However, the higher f and thus the more negative $\epsilon_{core}(\omega)$ pushes the energy of the SE mode to $E_c = 5.9$ eV as shown by the black curve in Fig. 3(d). The absorption of the generic dye shell is spectrally tuned with E_c as illustrated by the black curve in Fig. 3(d) for LOM parameters: $\epsilon_\infty = 1.45^2$, $\gamma = 0.1$ eV, $E_0 = 5.9$ eV, and a varying f (f_{dye} as 0.0001, 0.0005, 0.001, 0.005, and 0.01). Note that due to increased confinement of the SE mode of the MTDBC, the system reaches the strong coupling limit already with much lower molecular absorption, *i.e.*, lower values of f_{dye} . From Fig. 3(d) it is clear that for the coupled system, an increase in f_{dye} incurs a flat top profile (transparency) at E_c in the beginning (f_{dye} from 0.0001 to 0.001). However, for higher values of f_{dye} (0.005 and 0.01), the polariton branches emerge along with a peak at E_c due to nonhybridized molecular excitons at high exciton numbers [21]. Such finding clearly confirms our argument that SE modes can facilitate strong coupling but the polaritons might not be visible in the absorption due to the extremely narrow negative $\Re\{\epsilon(\omega)\}$ regime of excitonic materials.

To further explore light coupling properties of SEs, we examine the coupling between SE and SP modes. To do so, we consider again the same system as in the beginning, *i.e.*, the Au core having a SP mode at $E_c = 2.28$ eV and a TDBC shell, but now the shell is possessing SE modes. The LOM parameters for the TDBC shell ($\epsilon_{shell}(\omega)$) are identical with that of the previously discussed TDBC core. A plain TDBC shell with an inert core (dielectric) yields two SE modes (E_{L1} and E_{L2}) manifested as sharp peaks along with its material absorption (E_m) in the absorption spectrum as shown by the green curve in Fig. 4(a). The origin of these two SE modes (E_{L1} and E_{L2}) comes from the interaction (Fano-type hybridization) between two individual SE modes present at the inner and outer surfaces of the TDBC shell [8]. However, if the core is absorbing (blue curve in Fig. 4(a)), like the SP mode of the Au core, these two SE modes (E_{L1} and E_{L2}) merge leading to a single broad peak as shown by the red curve in Fig. 4(a).

Since the SP mode (E_c) of the Au core cannot be changed without changing the geometry, we vary the material absorption (E_m) of the TDBC shell to study the effect of the energy difference between the SP mode and the SE modes (E_{L1} and E_{L2}). In other words, we vary the $E_m = E_0$ in Eq. (1) for TDBC shell, as 1.9 eV, 2 eV,

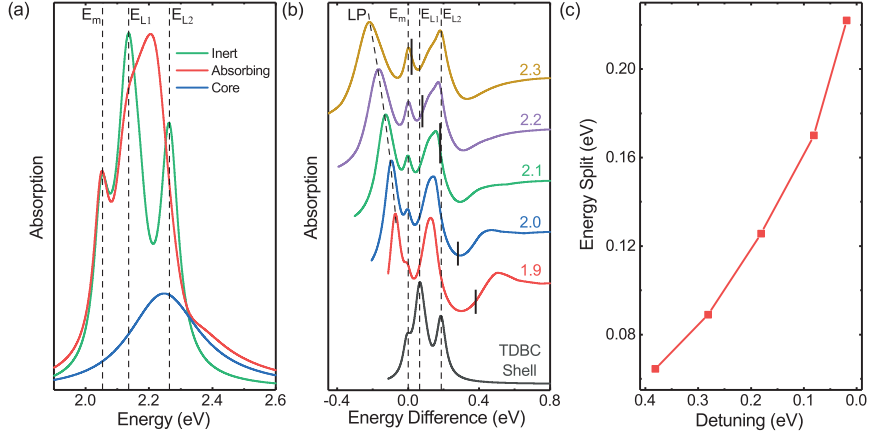


FIG. 4. (a) Absorption spectra of TDBC shell possessing two SE modes (E_{L1} and E_{L2}) along with the material absorption (E_m), when located around an inert dielectric core (green curve). An absorbing core along with the shown absorption (blue curve) yield merging of the two SE modes (red curve). (b) Absorption spectra as a function of energy difference ($E - E_m$) for the TDBC shell and the Au core-TDBC shell system for different values of E_m (1.9 eV, 2 eV, 2.1 eV, 2.2 eV, and 2.3 eV). On each curve (except the black one), the thick black vertical line represents the position of the SP mode of the Au core ($E_c = 2.28$ eV) on the energy difference scale. In (a)-(b), two SE modes of the TDBC shell (E_{L1} and E_{L2}) and the material absorption of TDBC (E_m) are shown by the vertical dashed black lines while in (b), the lower (LP) polariton branch is shown by the tilted black dashed line. In the figures, absorption means absorption efficiency, *i.e.*, absorption cross-sections normalized by geometrical cross-section. (c) Energy splitting ($E_m - E_{LP}$) as a function of detuning ($E_c - E_m$) where the red squares on the red curve depict the discrete data points.

2.1 eV, 2.2 eV, and 2.3 eV to attain different amounts of detunings ($E_c - E_m$). In Fig. 4(b), the black curve shows the position of E_{L1} , E_{L2} , and E_m on the energy difference scale centered at the material absorption of the TDBC shell ($E - E_m$). All other curves in the figure show the absorption of Au core-TDBC shell system as the function of the energy difference from the material absorption ($E - E_m$) for different values of E_m (1.9 eV, 2 eV, 2.1 eV, 2.2 eV, and 2.3 eV). On each curve in Fig. 4(b) (except the black one), the thick black vertical line represents the position of the SP mode of the Au core ($E_c = 2.28$ eV) on the energy difference scale. From the figure it is clear that for $E_m = 2.1$ eV (green curve), E_{L2} and E_c are spectrally tuned. For $E_m = 2.2$ eV (violet curve), E_{L1} and E_c are spectrally tuned while for $E_m = 2.3$ eV (yellow curve), E_m and E_c are spectrally tuned. For E_m as 1.9 eV and 2 eV (red and blue curves), only the broad tail of the SP mode partially overlaps with E_{L1} , E_{L2} , and E_c .

From the absorption of the coupled system we can infer that in all cases (E_m as 1.9 eV, 2 eV, 2.1 eV, 2.2 eV, and 2.3 eV), E_{L1} and E_{L2} merge into a single broad peak due to the presence of an absorbing Au core like the case reported in Fig. 4(a) (red curve). In addition to the features present in TDBC shell, shown in Fig. 4(a), all the absorption curves of the coupled system (Fig. 4(b)) show a clear peak at energies lower than the material absorption (E_m). This peak moves as a function of the detuning between E_m and E_c , and its separation from

E_m increases as the detuning decreases as shown in Fig. 4(c). This clearly indicates that the additional peak is the LP formed by the strong coupling between the Au core E_c and the material absorption E_m as in the case of Fig. 2. Like in that case, the UP is not well present here either, due to Au absorption and in particular due to interference by the SE modes. Such outcome indicates that SE modes (E_{L1} and E_{L2}) can only weakly couple with the SP mode (E_c) while the strong coupling happens only between the material absorption (E_m) and the SP mode (E_c).

It is worth to highlight here that SP and SE modes can be considered as the so-called resonator modes used to realize strong light-matter coupling. Strong coupling between two resonator modes such as microcavity mode strongly coupled to plasmons [23] and strong coupling between two different kinds of plasmonic modes [24] have been recently realized. In this regard, light coupling properties of SE modes drastically differ from SP modes since strong coupling between SE and SP resonator modes is not possible as we show in Fig. 4.

To further validate our claim we consider a scenario where, unlike in the core-shell system, the SE and the SP resonator modes are not geometrically coupled. To do so, we consider a dimer system where a plasmonic nanoantenna (Au nanobar) interacts with an excitonic nanoantenna (TDBC nanosphere) as schematically shown in the top left corner of Fig. 5. The dimensions of the Au nanobar in x , y , and z directions are L_x , L_y , and L_z , respec-

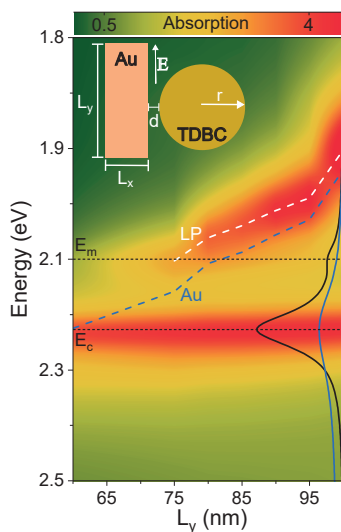


FIG. 5. Absorption of the dimer system consisting of a Au nanobar and a TDBC nanosphere (as shown in the schematic in top left corner) plotted as a contour map. The dimensions of the Au nanobar in x , y , and z directions are L_x (width), L_y (length), and L_z (thickness), respectively, where $L_x = 30$ nm and $L_z = 50$ nm. The L_y is varied from 60 nm to 100 nm with a 5 nm increment. The radius (r) of the TDBC nanosphere is 50 nm and the nanosphere is 10 nm away from the nanobar, *i.e.*, $d = 10$ nm. The dimer is excited by a plane wave (normal incidence) polarized along L_y as shown by the alignment (white arrow) of the electric-field vector (\mathbf{E}). In the contour map, the black and blue curves on the right represent absorption of the TDBC nanosphere and the Au nanobar with $L_y = 60$ nm, respectively. The SE mode of the TDBC nanosphere (E_c) and the material absorption of TDBC (E_m) are shown by the horizontal dashed black lines. The blue and white dashed lines depict the dispersion of the SP mode in Au nanobar and the lower polariton (LP) branch originated due to strong coupling of E_m with the SP mode, respectively. In the figure, absorption means absorption efficiency, *i.e.*, absorption cross-sections normalized by geometrical cross-section.

tively. We consider $L_x = 30$ nm (width) and $L_z = 50$ nm (thickness) while L_y (length) is varied. The radius (r) of the TDBC nanosphere is taken as 50 nm and the nanosphere is kept 10 nm away from the nanobar, *i.e.*, $d = 10$ nm. The optical response of the dimer system for a plane wave excitation (normal incidence) polarized along L_y , as shown in the schematic, is computed by the finite-difference time-domain (FDTD) method [25] implemented in Lumerical [26].

The absorption spectrum of the TDBC nanosphere is presented by the black curve on the right side of Fig. 5. Like the TDBC core in the previous case (red curve in Fig. 2(b)), the TDBC nanosphere supports a SE mode (E_c) as a main absorption peak along with its material

absorption (E_m) as a shoulder peak. The absorption spectrum of the Au nanobar for $L_y = 60$ nm is also depicted on the right side of Fig. 5 as a blue curve and it is spectrally tuned with the SE mode (E_c). We vary L_y (60 nm to 100 nm with a 5 nm increment) to shift the absorption peak of the nanobar from E_c to E_m , *i.e.*, to span through the entire absorption spectrum of the TDBC nanosphere. The dispersion of the SP mode of Au nanobar with respect to L_y is shown by the blue dashed line in Fig. 5.

The absorption of the coupled (dimer) system plotted as a contour map in Fig. 5 reveals that no energy splitting is found when the SP mode is tuned with the SE mode (E_c). The energy splitting is only found when the SP mode is tuned with the material absorption (E_m) of TDBC and as a consequence, a polariton branch (LP) emerges as shown by the white dashed line in Fig. 5. Such outcome is in agreement with the results reported in Fig. 4 and again confirms our claim that the strong coupling happens only between the material absorption and SPs. Interestingly, in Fig. 5, we do not see any upper polariton branch and only the LP branch (white dashed line) is visible. That is most probably because the upper polaritons are spectrally overlapping with the SE mode (E_c).

In conclusion, we have studied the performance of the SE mode when employed to realize strong light-matter coupling. We considered a core-shell nanoparticle system having a TDBC core possessing SE mode with a generic dye shell and compared it with the identical core-shell geometry consisting similar dye shell with a gold core (SP mode). Our Mie calculations revealed that SE modes can facilitate strong coupling in terms of induced transparency, however, the polaritons are not visible in the absorption due to an extremely narrow negative $\Re\{\epsilon(\omega)\}$ regime of excitonic materials. Moreover, as a resonator mode, SEs provide deeper transparency and stronger coupling compared to SPs.

We further examined the coupling between SE and SP modes to explore the light coupling properties of SEs. On one hand, we considered a core-shell nanoparticle system consisting a Au core having a SP mode and a TDBC shell possessing SE modes. On the other hand, we modelled a dimer system where the SP mode of a Au nanobar is coupled with the SE mode of a TDBC nanosphere. In both cases, our numerical findings showed that SE modes can only weakly couple with the SP mode, while the strong coupling happens between the excitonic material absorption and SPs. Furthermore, when the material absorption and a SP mode are strongly coupled, the SE mode can overlap with the polariton and overrun it. Our findings provide key information on the weak and strong coupling properties of SEs and hence, important in the context of developing novel excitonic devices for organic nanophotonics.

We wish to acknowledge the support from Academy of Finland (289947, 323995) for funding.

-
- [1] L. Gu, J. Livenere, G. Zhu, E. E. Narimanov, and M. A. Noginov, Quest for organic plasmonics, *Appl. Phys. Lett.* **103**, 021104 (2013).
- [2] M. J. Gentile, S. Núñez-Sánchez, and W. L. Barnes, Optical field-enhancement and subwavelength field-confinement using excitonic nanostructures, *Nano Lett.* **14**, 2339 (2014).
- [3] A. Canales, D. G. Baranov, T. J. Antosiewicz, and T. Shegai, Abundance of cavity-free polaritonic states in resonant materials and nanostructures, *J. Chem. Phys.* **154**, 024701 (2021).
- [4] W. J. Tan, P. A. Thomas, I. J. Luxmoore, and W. L. Barnes, Single vs double anti-crossing in the strong coupling between surface plasmons and molecular excitons, *J. Chem. Phys.* **154**, 024704 (2021).
- [5] K. Takatori, T. Okamoto, K. Ishibashi, and R. Micheletto, Surface exciton polaritons supported by a J-aggregate-dye/air interface at room temperature, *Opt. Lett.* **42**, 3876 (2017).
- [6] Y. Xu, L. Wu, and L. K. Ang, Surface exciton polaritons: a promising mechanism for refractive-index sensing, *Phys. Rev. Applied* **12**, 024029 (2019).
- [7] M. J. Gentile, S. A. R. Horsley, and W. L. Barnes, Localized exciton-polariton modes in dye-doped nanospheres: a quantum approach, *J. Opt.* **18**, 015001 (2016).
- [8] M. J. Gentile and W. L. Barnes, Hybridised exciton-polariton resonances in core-shell nanoparticles, *J. Opt.* **19**, 035003 (2017).
- [9] A. D. Humphrey, M. J. Gentile, and W. L. Barnes, Excitonic surface lattice resonances, *J. Opt.* **18**, 085004 (2016).
- [10] A. Cacciola, C. Triolo, O. D. Stefano, A. Genco, M. Mazzeo, R. Saija, S. Patanè, and S. Savasta, Subdiffraction light concentration by J-aggregate nanostructures, *ACS Photonics* **2**, 971 (2015).
- [11] A. Dutta and J. J. Toppari, 10.26434/chemrxiv-2023-7qkch.
- [12] P. B. Johnson and R. W. Christy, Optical constants of the noble metals, *Phys. Rev. B* **6**, 4370 (1972).
- [13] G. Zengin, G. Johansson, P. Johansson, T. J. Antosiewicz, M. Käll, and T. Shegai, Approaching the strong coupling limit in single plasmonic nanorods interacting with J-aggregates, *Sci. Rep.* **3**, 3074 (2013).
- [14] C. F. Bohren and D. R. Huffman, *Absorption and Scattering of Light by Small Particles* (Wiley-VCH, 1998).
- [15] <https://www.mathworks.com/products/matlab.html>.
- [16] A. Dutta, V. Tiainen, and J. J. Toppari, Numerical study on the limit of quasi-static approximation for plasmonic nanosphere, *AIP Conf. Proc.* **2220**, 050012 (2020).
- [17] T. J. Antosiewicz, S. P. Apell, and T. Shegai, Plasmon-exciton interactions in a core-shell geometry: from enhanced absorption to strong coupling, *ACS Photonics* **1**, 454 (2014).
- [18] F. Stete, W. Koopman, and M. Bargheer, Signatures of strong coupling on nanoparticles: revealing absorption anticrossing by tuning the dielectric environment, *ACS Photonics* **4**, 1669 (2017).
- [19] G. Zengin, T. Gschneidtnr, R. Verre, L. Shao, T. J. Antosiewicz, K. Moth-Poulsen, M. Käll, and T. Shegai, Evaluating conditions for strong coupling between nanoparticle plasmons and organic dyes using scattering and absorption spectroscopy, *J. Phys. Chem. C* **120**, 20588 (2016).
- [20] F. Stete, P. Schoßau, M. Bargheer, and W. Koopman, Size-dependent coupling of hybrid core-shell nanorods: toward single-emitter strong-coupling, *J. Phys. Chem. C* **122**, 17976 (2018).
- [21] W. Li, R. Liu, and X. Wang, Anomalous spectral response of plasmon-exciton strong coupling beyond J-C model, *Results Phys.* **31**, 105064 (2021).
- [22] A. Dutta, V. Tiainen, and J. J. Toppari, Optimizing geometry of low-Q all-metal Fabry-Pérot microcavity for fluorescence spectroscopy, *IOPSciNotes* **2**, 015205 (2021).
- [23] D. G. Baranov, B. Munkhbat, E. Zhukova, A. Bisht, A. Canales, B. Rousseaux, G. Johansson, T. J. Antosiewicz, and T. Shegai, Ultrastrong coupling between nanoparticle plasmons and cavity photons at ambient conditions, *Nat. Commun.* **11**, 2715 (2020).
- [24] B. C. Yildiz, M. Habib, A. R. Rashed, and H. Caglayan, Hybridized plasmon modes in a system of metal thin film-nanodisk array, *J. Appl. Phys.* **126**, 113104 (2019).
- [25] S. D. Gedney, *Introduction to the Finite-Difference Time-Domain (FDTD) Method for Electromagnetics* (Morgan and Claypool, 2011).
- [26] <https://www.ansys.com/products/photonics/fdtd>.